AUBURN UNIVERSITY

SAMUEL GINN
COLLEGE OF ENGINEERING

Research Report No. 2 for ALDOT Project 930-832

IMPROVING CAMBER PREDICTIONS FOR PRESTRESSED CONCRETE GIRDERS: PART 2 OF 2

Submitted to

The Alabama Department of Transportation

Prepared by

David M. Mante, Robert W. Barnes, Anton K. Schindler
Andric Hofrichter, Levent Isbiliroglu

October 2019

Highway Research Center
Harbert Engineering Center
Auburn, Alabama 36849

www.eng.auburn.edu/research/centers/hrc.html

1. Report No. ALDOT 930-832-2	**2. Government Accession No.**	**3. Recipient Catalog No.**
4 Title and Subtitle Improving Camber Predictions for Prestressed Girders: Part 2 of 2		**5 Report Date** October 2019 **6 Performing Organization Code**
7. Author(s) David M. Mante, Robert W. Barnes, Anton K. Schindler Andric Hofrichter, Levent Isbiliroglu		**8 Performing Organization Report No.** ALDOT 930-832-2
9 Performing Organization Name and Address Highway Research Center Department of Civil Engineering 238 Harbert Engineering Center Auburn, AL 36849		**10 Work Unit No. (TRAIS)** **11 Contract or Grant No.**
12 Sponsoring Agency Name and Address Alabama Department of Transportation 1409 Coliseum Boulevard Montgomery, Alabama 36130-3050		**13 Type of Report and Period Covered** Technical Report **14 Sponsoring Agency Code**

15 Supplementary Notes

Research performed in cooperation with the Alabama Department of Transportation

16 Abstract

In precast, prestressed concrete construction, the eccentricity of the prestressing force typically results in a net upward girder deflection known as camber. Camber is first observed at the time of prestress transfer and tends to increase thereafter as a function of time-dependent material properties. While accurately predicted levels of camber are desirable to concrete bridge construction, inaccuracies in design camber estimates can result in construction difficulties and the need to modify bridge designs to ensure proper girder fit. In order to mitigate such troublesome issues, the Alabama Department of Transportation (ALDOT) sponsored this investigation to develop a suggested procedure for use during girder design to more accurately predict pre-erection camber in precast, prestressed concrete bridge girders. In support of this objective, various laboratory and field studies were conducted exploring relevant regionally-variable concrete material properties (e.g. concrete compressive strength, concrete unit stiffness, and creep and shrinkage behavior) as well as the effect of transient environmental conditions on girder camber. Relying on the conclusions of these laboratory and field studies, a revised camber prediction procedure was developed, implemented in a user-friendly computer software (*ALCAMBER v1.0*) and validated by comparison to multiple design and production cycles of ALDOT precast, prestressed concrete bridge girders.

17 Key Words Bridge, deflection, camber, overstrength, elastic modulus, time-dependent, creep and shrinkage, thermal effects		**18 Distribution Statement** No restrictions. This document is available to the public through the National Technical Information Service, Springfield, Virginia 22161	
19 Security Classification (of this report) Unclassified	**20 Security Classification (of this report)** Unclassified	**21 No. of pages** 264	**22 Price**

DISCLAIMERS

The contents of this report reflect the views of the authors, who are responsible for the facts and the accuracy of the data presented herein. The contents do not necessarily reflect the official views or policies of Auburn University or the Federal Highway Administration. This report does not constitute a standard, specification, or regulation.

NOT INTENDED FOR CONSTRUCTION, BIDDING, OR PERMIT PURPOSES

Robert W. Barnes, Ph.D., P.E.
Anton K. Schindler, Ph.D., P.E.
Research Supervisors

ACKNOWLEDGEMENTS

Material contained herein was obtained in connection with a research project ALDOT 930-601, conducted by the Auburn University Highway Research Center. Funding for the project was provided by the Alabama Department of Transportation (ALDOT) with donations received from BASF Corporation, Holcim Inc., Elkem Materials, and CEMEX. The funding, cooperation, and assistance of many individuals from each of these organizations are gratefully acknowledged. The authors would like to acknowledge the various contributions of the following individuals:

Tim Colquitt, ALDOT, State Bridge Engineer
Buddy Black, ALDOT, State Bridge Engineer (*Retired)*
Drew Waldrop, ALDOT, Concrete/Cement Engineer
Keith Hegler, ALDOT, Field Inspection Team
Nathan Emmerich, Forterra
Frankie Smith, Forterra, Plant Manager
Dwayne Hamby, Forterra, Engineering Manager
Don Theobald, Gulf Coast Prestress, Engineering Manager
Larry Nicely, Gulf Coast Prestress, Plant Manager

ABSTRACT

In precast, prestressed concrete construction, the eccentricity of the prestressing force typically results in a net upward girder deflection known as camber. Camber is first observed at the time of prestress transfer and tends to increase thereafter as a function of time-dependent material properties. While accurately predicted levels of camber are desirable to concrete bridge construction, inaccuracies in design camber estimates can result in construction difficulties and the need to modify bridge designs to ensure proper girder fit. In order to mitigate such troublesome issues, the Alabama Department of Transportation (ALDOT) sponsored this investigation to develop a suggested procedure for use during girder design to more accurately predict pre-erection camber in precast, prestressed concrete bridge girders. In support of this objective, various laboratory and field studies were conducted exploring relevant regionally-variable concrete material properties (e.g. concrete compressive strength, concrete unit stiffness, and creep and shrinkage behavior) as well as the effect of transient environmental conditions on girder camber. Relying on the conclusions of these laboratory and field studies, a revised camber prediction procedure was developed, implemented in a user-friendly computer software (*ALCAMBER v1.0*) and validated by comparison to multiple design and production cycles of ALDOT precast, prestressed concrete bridge girders.

TABLE OF CONTENTS

LIST OF TABLES

LIST OF FIGURES

Chapter 7: Creep and Shrinkage Behavior of Alabama Precast, Prestressed Concretes

7.1 Introduction

Creep and shrinkage are major contributing factors to the time-dependent growth of initial elastic camber in precast, prestressed concrete girders. The magnitude of long-term deformations due to creep and shrinkage can be several times the elastic deformations in concrete structures (Bazant and Panula 1980). Concrete creep is the primary factor responsible for camber growth over time, while concrete shrinkage plays a secondary role in reducing the effective prestress force over time, thereby acting to mitigate the effect of creep.

The focus of this research investigation is limited to accurately predicting the camber behavior of precast, prestressed concrete girders up until the time of deck placement. For structural design purposes, ALDOT assumes girders will be installed approximately 60 days following production (ALDOT 2014), while the ALDOT construction specifications suggests that an appropriate upper-bound estimate is 120 days (ALDOT 2010). The 60-day design assumption of ALDOT is in agreement with the assumption of Martin (1977) used in developing the PCI multiplier method. For the laboratory phase of this research study, the measurement of time-dependent material properties was extended to 250 days (approximately 8 months), roughly double the upper-bound assumption provided by ALDOT for girder installation time. For a duration of loading of 250 days, it is estimated that roughly 70–75 percent of the ultimate time-dependent deformations will have occurred (Troxell, Raphael, and Davis 1958).

The research effort detailed herein is intended to provide useful results for designers of precast, prestressed concrete bridge girders by focusing on design-friendly relationships. Available prediction models for creep and shrinkage require varying degrees of detailed input variables. Therefore, when selecting the creep and shrinkage prediction models considered in this study, an effort was made to examine only those models appropriate for use by designer engineers at the time of preliminary girder design—before detailed information is known regarding concrete mixture proportions or constituent

materials. In the event that a model requires inputs not likely to be precisely known at the time of design (e.g. air content, slump, cement content, etc.), an average value, as reflected in Chapter 4 of this report, may be used by design engineers. Additionally, recognizing that ALDOT has transitioned fully to the use of the AASHTO LRFD Bridge Design Specifications, it is preferable that the final recommendations of this section be compatible with the provisions of that design specification, if possible.

7.1.1 Chapter Objectives

The primary objective of the research described in this chapter was to evaluate the early-age time-dependent deformational behavior (namely creep and shrinkage) of typical Alabama girder concretes in order to recommend appropriate prediction equations for use at the time of preliminary girder design. Tasks completed in support of this primary objective include the following:

- Evaluate the effect of regionally available coarse aggregates on pre-erection time-dependent deformational behavior;
- Evaluate the effect of varying the age at loading on pre-erection early-age time-dependent deformational behavior;
- Evaluate the effect of the use of varying supplementary cementing material (SCMs) on pre-erection time-dependent deformational behavior; and
- Compare time-dependent deformational behavior predicted by available design models to observed material behavior and determine any warranted adjustments.

7.1.2 Chapter Outline

This chapter begins with a brief background discussion of creep and shrinkage behavior in concrete including general definitions, primary factors contributing to each, and available code-based prediction equations appropriate for use at the preliminary design phase. Then, an experimental creep and shrinkage testing program is detailed. Next, various post-processing techniques are applied to the raw experimental results including detection and removal of flawed measurements, determination of experimental precision and investigation of the repeatability of results, and a discussion on uncontrolled thermal effects. Finally, a comprehensive analysis of experimental results is presented in support of the primary chapter objective.

7.2 Background

As noted by Adam and Taha (2011), the modeling of creep and shrinkage behavior of concrete has been among the most challenging problems in recent concrete history. While it is relatively clear that both phenomena are related to the movement of water within concrete elements, the specific mechanisms behind creep and shrinkage are still very much debated. The focus of this chapter remains on the predictability of creep and shrinkage in typical precast, prestressed concretes–without specific consideration of the mechanisms behind these phenomena. This section introduces terminology related to creep and shrinkage behavior, before presenting a general review of some primary factors affecting the magnitude of these time-dependent changes. Next, three particular factors (coarse aggregate type, SCM type, and concrete age at loading) are explored in depth. Finally, the creep and shrinkage prediction equations evaluated and calibrated in this study are briefly presented.

7.2.1 Terminology

ACI Committee 209 (2008) defines creep as the time-dependent increase of strain in hardened concrete subjected to a sustained stress. The total observed creep consists of both the basic creep component (creep occurring under conditions of no moisture movement to or from the environment) and drying creep (the portion of creep when moisture movement to or from the environment is allowed to occur). For practical design purposes, it is unnecessary to differentiate between basic creep and drying creep. Laboratory evaluation of creep and shrinkage in concrete cylinders is performed in accordance with the *Standard Test Method for Creep of Concrete in Compression* (ASTM C512 2002). The two most common metrics of time-dependent load-induced deformational behavior are the creep coefficient and compliance. The creep coefficient, most commonly denoted by v_t, is defined as the ratio of the observed creep strain to the initial strain and is a function of concrete age at loading, t_i, and duration of loading, t (ACI Committee 209 2005). An ultimate creep coefficient of 2.5 for a particular concrete means that it is expected that ultimate displacement will be 2.5 times the magnitude of the initially observed elastic displacement. An equation relating (1) stress applied at time of loading, (2) concrete elastic modulus at time of loading, and (3) concrete creep coefficient to (4) total load-induced strain (for a given duration of loading) is shown in Equation 7-1.

$$\varepsilon_{load-induced}(t,t_i) = \frac{\sigma_{applied}}{E_c}\left[1+\nu_t(t,t_i)\right] \quad (7\text{-}1)$$

where

t = duration of loading;

t_i = concrete age at loading;

$\sigma_{applied}$ = stress applied at time of loading;

E_c = elastic modulus of concrete at time of loading;

$\nu_t(t,t_i)$ = creep coefficient for a considered duration of loading, t; and

$\frac{\sigma_{applied}}{E_c}$ = initial elastic strain upon loading.

The other common metric for describing time-dependent load-induced deformational behavior is compliance, most commonly denoted as J. ACI Committee 209 (2008) defines compliance as "the total load-induced strain (elastic strain plus creep strain) [for a considered duration of loading, t,]…per unit stress caused by a unit uniaxial sustained load since loading age." Dividing the total load-induced strain, $\varepsilon_{load-induced}(t,t_i)$, (Equation 7-1) by the stress applied at time of loading, $\sigma_{applied}$, and simplifying yields

$$J(t,t_i) = \frac{\left[1+\nu_t(t,t_i)\right]}{E_c} \quad (7\text{-}2)$$

where

$J(t,t_i)$ = compliance for a considered loading duration and age at loading.

Rearranging Equation 7-2, the creep coefficient, ν_t, can be solved for as a function of compliance and elastic modulus at the time of loading

$$\nu_t(t,t_i) = E_c J(t,t_i) - 1 \quad (7\text{-}3)$$

The primary difference between the two presented metrics of time-dependent deformation is that while the creep coefficient describes time-dependent behavior as a ratio of the creep deformation to the initial elastic deformation, compliance includes the initial elastic deformation and therefore describes the total

load-induced deformational behavior (both elastic and time-dependent). For design purposes, the distinction between creep coefficient and compliance is inconsequential, as Equations 7-2 and 7-3 (along with an "expected" value of E_c) allow designers to translate freely between these two parameters of time-dependent deformations.

Practically speaking, it is not possible during creep testing to differentiate between the portion of the observed early deformation attributed to instantaneous elastic strain and that portion attributed to early creep effects (ACI Committee 209 2008). While the creep coefficient parameter is particularly sensitive to intrinsic errors in early testing, compliance, by nature of it being normalized to the applied stress, tends to be a more measurable metric of time-dependent deformation. In this research effort, compliance is used as the primary metric for creep behavior with the understanding that, as long as the elastic modulus of a given concrete is known (or predicted accurately) at the time of prestress transfer, one can freely transition between creep coefficient and compliance. Hubler, Wender, and Bazant (2015) have endorsed the use of the compliance metric for the reporting of all experimental creep and shrinkage work in lieu of the creep coefficient.

Shrinkage is defined as the time-dependent decrease in volume of an unloaded, hardened concrete specimen (ACI Committee 209 2008). Typically measured in dimensionless strain units, the total shrinkage consists of the drying shrinkage (due to moisture loss from the concrete), autogenous shrinkage (due to self-desiccation of cement), and carbonation shrinkage (due to carbonation of various cement hydration products). For design purposes, it is not necessary to differentiate among these sources of shrinkage as long as the net result can be satisfactorily predicted. Shrinkage is typically measured as part of creep testing conducted in accordance with the requirements of ASTM C512-02 or independently in concrete standard rectangular prism testing conducted in accordance with the requirements of the *Standard Test Method for Length Change of Hardened Hydraulic-Cement Mortar and Concrete* (ASTM C157 2008).

7.2.2 Primary Factors Affecting Creep

ACI Committee 209 (ACI Committee 209 2005) outlines three major groups of factors known to affect creep including (1) mixture proportions, (2) environment, and (3) construction and structural design. Each

of these groupings is briefly discussed in this section prior to a more in-depth review of three specific parameters explored as part of the experimental work presented later in this chapter. More comprehensive reviews of the factors affecting creep are given by *Factors Affecting Shrinkage and Creep of Hardened Concrete* (ACI Committee 209 2005) and He (2013).

Although the mechanisms behind creep are not fully understood, it is the general consensus that creep behavior is governed by the properties of the cement paste and the quantity and properties of aggregate within a concrete mixture. Generally speaking, a concrete mixture with increased aggregate volume (and corresponding reduced paste content) will tend to exhibit less creep than a high paste content mixture (ACI Committee 209 2005). Similarly, stiffer aggregates tend to more effectively restrain time-dependent deformational behavior and, therefore, result in less creep. It is also clear that increased water content of a mixture and increased air content both correlate to increased creep. Finally, the presence of various supplementary cementing materials (SCMs) within a mixture has also been found to affect creep magnitude (ACI Committee 209 2005). Two of the above-referenced parameters (aggregate type and SCM use) are discussed in more detail in the subsequent sections.

The next major grouping of factors known to affect creep behavior is the environment in which concrete is cast, cured, and loaded. The magnitude of creep is particularly sensitive to the relative humidity conditions of the concrete sample. Increased relative humidity correlates to slower creep development and less ultimate creep (ACI Committee 209 2005). Creep is also very much temperature-dependent with higher temperatures being generally correlating to increased rates of creep development (ACI Committee 216 2014). In terms of the testing conducted in this report, the above environmental factors are generally well-controlled in accordance with the requirements of ASTM C512-02 and, therefore, are not intended as experimental variables in this work.

Finally, various construction and structural design practices are also known to be primary factors affecting creep of concrete. First, the magnitude of the applied stress linearly correlated to the creep response for values up to approximately 40–60 percent of ultimate compressive strength (ACI Committee 209 2005). The size and shape of the concrete element (particularly the volume-to-surface-area ratio) is another key factor. Thinner concrete sections, tending to more-easily allow moisture loss to the surrounding environment, typically experience more creep than thicker concrete sections. Creep

behavior is also sensitive to the duration and type of curing for a given concrete. Generally, an increased period of moist curing is correlated to lower creep development, while steam-curing is known to reduce the ultimate creep magnitude by up to 30 percent (ACI Committee 209 2005). Finally, age at loading is also important, with concretes loaded at later ages generally exhibiting less overall creep. While the majority of the construction and structural practices reviewed above are fairly well-controlled within precast, prestressed concrete construction, the variation of age at loading (time to prestress release) is quite variable (as discussed in Section 4.5.2) and, therefore, investigated as a primary factor in the experimental work of this report.

7.2.2.1 Coarse Aggregate Type

In the earliest available published work on the topic, Davis and Davis (1931) concluded that the aggregate type had a significant effect on the magnitude of observed creep in loaded concrete specimens. By controlling for aggregate-cement ratio, water-cement ratio, and applied stress among mixtures prepared with varying aggregate mixtures, Davis and Davis (1931) concluded that limestone and quartz aggregates tended to limit the magnitude of long-term creep deformation, while sandstone and basalt aggregates contributed to greater long-term creep. As shown in Figure 7-1, it was reported that the use of sandstone aggregates tended to cause roughly double the magnitude of time-dependent creep as compared to limestone aggregates.

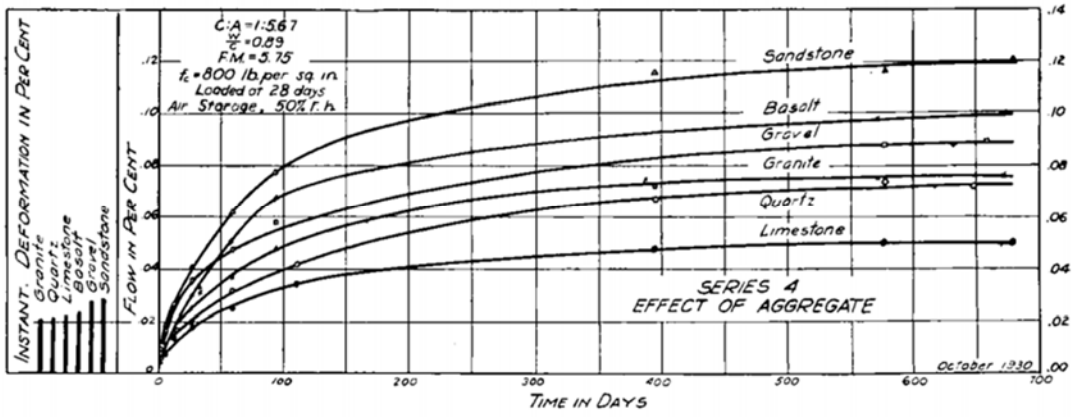

Figure 7-1: Findings of Davis and Davis (1931) Regarding Effect of Aggregate on Creep Behavior

A follow-up study by Troxell, Raphael, and Davis (1958) confirmed the same findings for an extended measurement period of up to 30 years. Neville (2013) explains that the observed differences in creep

behavior for varying aggregates are primarily due to differing aggregate stiffness. As creep is a phenomenon that manifests within the paste phase, stiffer aggregates likely better restrain the bulk concrete against the external manifestation of creep behavior. The explanation proposed by Neville has generally been accepted and recently affirmed by other researchers (He [2013], Liu and Tia [2012]). The experimental program detailed in this chapter allows for direct comparisons among creep behavior of concretes made with three coarse aggregate types.

7.2.2.2 Use of Supplementary Cementing Materials (SCMs)

There is little consensus among researchers on the effect of the use of supplementary cementing materials (SCMs) on the creep behavior of concrete. While the work of various researchers is reviewed in this section, it is important to note that there is a relatively large amount of variation intrinsic to the testing of creep in hardened concrete. Neville (2013) attributes the great variety in research findings (and corresponding lack of consensus on this issue) to a failure by some researchers to recognize the intrinsic limitations of creep testing, namely those of experimental precision and repeatability of results. This topic is discussed further in Section 7.4.3, where experimental precisions are determined for the creep testing described in this report.

ACI 209R.1 (ACI Committee 209 2005) notes that the use of slag cement in concrete generally causes a decrease in the basic creep component, but causes little change in total observed creep. Brooks (1999), whose earlier work is the primary reference for ACI 209R.1 on this topic, later contended that for increasingly large substitution percentages, slag cement replacement causes a distinct decrease in total creep. Similarly, Levy, Barnes, and Schindler (2010) observed a reduction in creep for concretes containing slag cement. Conversely, Chern and Chan (1989) and He (2013) found that increasingly large slag cement replacement caused an increase in total creep. Tia, Liu, and Brown (2005) concluded that the creep coefficient of concrete with slag was generally less than that for a comparable fly ash mixture.

With regards to the effect of fly ash on the creep of hardened concrete, there are somewhat more consistent results reported. ACI 209R.1 (ACI Committee 209 2005) contends that there is a net reduction in observed creep for concrete mixtures using a substitution percentage of more than 10 percent. This

recommendation is in agreement with the previous work of Brooks (1999), Ghosh and Timusk (1981), and Lane and Best (1982) —although contrary to the work of He (2013).

ACI 209R.1 (ACI Committee 209 2005) cites a general increase in the creep tendency of concrete for silica fume replacements of less than 7.5 percent. Conversely, Brooks (1999) and Khatri and Sirivivatnanon (1995) observed a net reduction in creep behavior for replacements of cement with silica fume of less than 15 percent, with a net increase in creep behavior noted for percentage substitutions exceeding 15 percent.

7.2.2.3 Age at Loading

ACI 209.R1 (ACI Committee 209 2005), citing early work by L'Hermite, contends that there is a net decrease in creep for increasing concrete age at load application, but provides little guidance for age at loading of less than seven days. Keske (2014) observed a reduction in creep for specimens loaded at a chronological age of 365 days as compared to specimens loaded at typical prestress release ages (18-24 hours)—further finding that the age at loading provisions of various prediction models satisfactorily predicted the observed reduction due to age at loading over this extreme range. There appears to be no previous research work that explicitly explores the effect of different ages at loading for very early ages (i.e. an attempt to differentiate between 18 and 24 hours creep responses) perhaps, in part, due to a combination of (1) the difficulty in identifying a significant difference given the inherent variability in creep testing results and (2) difficulties in conducting creep testing that isolates age at loading from other inherently-related parameters (e.g. compressive strength at loading, maturity at loading, etc.).

7.2.3 Primary Factors Affecting Shrinkage

The three major groups of factors affecting creep discussed above are also applicable to concrete shrinkage and include (1) mixture proportions, (2) environment, and (3) design and construction practices. Again, each grouping is briefly discussed in this section with a more in-depth review of the three primary factors examined in this research project to follow.

ACI Committee 209 (2005) states the most important factor affecting the potential shrinkage of a given concrete is the total volume of aggregate present in the mixture. Similar to the theory previously discussed for creep, the relatively stiff aggregate acts to restrain the shrinkage tendency that originates

primarily in the cement paste. The increasing size of aggregate in a given concrete mixture can also affects shrinkage by dictating a decrease in required paste content for a given workability and, therefore, a corresponding reduction in observed shrinkage. Increasing water content of a mixture generally corresponds to increased shrinkage as more pore water is available within the concrete. The effect of SCMs on concrete shrinkage is somewhat unclear and is discussed in more detailed in subsequent sections.

Concrete shrinkage is especially sensitive to environmental changes in relative humidity and temperature, with decreased shrinkage observed for concrete stored in elevated humidity conditions and an increase in both the time-rate and ultimate shrinkage of concrete subjected to elevated temperatures (ACI Committee 209 2008). Environmental variables were closely controlled (in accordance with applicable testing standards) in the shrinkage testing conducted in this study.

The final grouping of factors affecting shrinkage of concrete according to ACI 209.R1 is design and construction factors. Generally speaking, extended periods of moist curing reduce the expected amount of drying shrinkage. The use of steam curing can significantly reduce drying shrinkage by as much as 30 percent (ACI Committee 209 2005). Finally, the size and shape of the concrete element influence the rate and magnitude of shrinkage. Larger and thicker members typically experience a slower rate of moisture loss, and therefore a corresponding lower rate of shrinkage development and less ultimate shrinkage.

7.2.3.1 Aggregate Type

The effect of aggregate type on shrinkage is virtually identical to the effect discussed previously for creep with similar behavior again reported by Davis and Davis (1931) and confirmed by Troxell et al. (1958). Generally speaking, stiffer aggregates examined corresponded to reduced rates and ultimate values of concrete shrinkage.

7.2.3.2 Use of Supplementary Cementing Materials (SCMs)

ACI 209.1R (ACI Committee 209 2005) notes that at high replacement values, the use of slag cement may result in increased shrinkage. Work by Khatri and Sirivivatnanon (1995), Chern and Chan (1989), and He (2013) provide similar conclusions. However, as a result of a review of seven studies, Brooks

(1999) concluded that the magnitude of concrete shrinkage for a given concrete is largely unaffected by the use of slag cement partial replacement. More recently, Aly and Sanjayan (2008) showed that concrete mixtures containing slag cement exhibit an expansion during curing, which leads to less total shrinkage than mixtures not containing slag cement.

ACI 209.R1 (ACI Committee 209 2005), Brooks (1999), and Lane and Best (1982) agree that the use of fly ash in concrete causes no appreciable change in shrinkage characteristics. While the work of Ghosh and Timusk (1981) provides partial agreement for moderate percent substitutions of fly ash, they also observed lower ultimate shrinkage values corresponding to high fly ash replacement percentages. He (2013) found that shrinkage tends to decrease for substitution percentages of up to 30 percent.

Research work exploring the effect of silica fume usage in concrete is largely inconclusive. ACI 209.R1 notes that at low percent replacement (less than 7.5 percent), a decrease in shrinkage should be expected. Khatri and Sirivivatnanon (1995) found that silica fume replacement generally caused a higher early rate of shrinkage, but a lesser ultimate value when compared to control mixtures. Brooks (1999) concluded that shrinkage behavior remained largely unaffected by the use of silica fume replacement.

7.2.4 Available Creep Prediction Equations

In this research effort, creep prediction equations were selected on the basis of ease of use for designers of precast, prestressed concrete elements. Previous related work by Schrantz (2010) and Isbiliroglu (2014) considered the design-friendly prediction models of the following: (1) AASHTO LRFD Bridge Specifications (hereafter termed “AASHTO 2014 method”), (2) ACI 209R-92 (hereafter termed “ACI 209 method”) and (3) the *fib* Model Code 2010 method (hereafter termed “Model Code 2010 method”). This section briefly introduces the basic form of each model and highlights the recommendations of previous researchers regarding the use of each model. Readers interested in the intricacies of prediction model application are referred to the primary reference for each model (i.e. AASHTO [2014], ACI 209R [2008], or *fib* Model Code [2010]) or to the previous work of Keske (2014) and Ellis (2012) for a more thorough comparison of each model than is presented here.

7.2.4.1 AASHTO 2014

The most current of the AASHTO LRFD Bridge Design Specification (AASHTO 2014) contains a relatively simple creep prediction model based on the work of Huo et al. (2001), Al-Omaishi (2001), Tadros et al. (2003), and Collins and Mitchell (1991). The prediction model uses a series of factors to modify an ultimate creep coefficient of 1.9 as shown in Equation 7-4.

$$\psi(t,t_i) = 1.9k_s k_{hc} k_f k_{td} t_i^{-0.118} \quad (7\text{-}4)$$

where

k_s = factor for the effect of the volume-to-surface ratio of the component;

k_{hc} = humidity factor for creep;

k_f = factor for the effect of concrete strength;

k_{td} = time-development factor; and

t_i = chronological age accelerated cured concrete at time of load application (days).

While the time index above, t_i, relies on chronological time (and also assumes accelerated curing conditions), the time factor, t, nested within the time-development factor, k_{td}, recommends the use of the maturity (in days) to express the temperature-adjusted time duration of loading. Previous research work by Rizkalla et al. (2011), Keske (2014), Hinkle (2006), and Tadros et al. (2011) endorse the use of this prediction model for use in predicting the time-dependent behavior of precast, prestressed concrete flexural elements. Rosa et al. (2007) also endorse the use of this method, although suggest a modification factor of 1.4 be used to amplify the predicted result to provide more accurate results for typical WSDOT concretes.

7.2.4.2 ACI 209

ACI Committee 209 (2008) first adopted a consensus creep prediction model in 1992. An assumed creep coefficient is modified by a series of parameters as shown in Equation 7-5.

$$v_t = \left(2.35 \cdot \gamma_{la} \cdot \gamma_{\lambda} \cdot \gamma_{vs} \cdot \gamma_{\psi} \cdot \gamma_s \cdot \gamma_a\right)\left(\frac{t^{0.60}}{10 + t^{0.60}}\right) \quad (7\text{-}5)$$

where

γ_{la} = loading age correction factor;

γ_{λ} = ambient relative humidity correction factor;

γ_{vs} = volume-surface ratio correction factor;

γ_{ψ} = fine aggregate percentage factor;

γ_{s} = slump correction factor;

γ_{a} = air content correction factor; and

t = time after loading (days).

The use of the ACI 209 method for predicting creep behavior in precast, prestressed concrete elements was endorsed in experimental findings of French and O'Neill (2012), while Stallings et al. (2003) found that this method tended to over-predict creep behavior for high-performance concrete if a measured slump (post-HRWRA) is used in the slump correction factor, γ_{s}.

7.2.4.3 *fib* Model Code 2010

The Model Code 2010 (fib 2010) creep prediction equation is the most complex of the three prediction models considered in this work. A notional creep coefficient is first computed as the sum of the basic and drying creep components, before being modified by a time-development factor as shown in Equation 7-6.

$$\varphi = \varphi_0 \cdot \beta_c(t, t_0) \tag{7-6}$$

φ_0 = notional creep coefficient; and

$\beta_c(t, t_0)$ = time-development coefficient.

Computation of the notional creep coefficient, φ_0, requires knowledge of the following parameters: (1) ambient relative humidity, (2) notional size of member, (3) mean 28-day compressive strength, (4)

concrete strength class, and (5) the temperature and cement type adjusted age[1] of concrete at loading. Computation of the time-development coefficient, $\beta_c(t,t_0)$, requires above parameters 1–3 as well as the duration of loading expressed as unadjusted chronological time. The Model Code 2010 method is especially lengthy in formulation, and thus, is not included here in its entirety.

7.2.5 Available Shrinkage Prediction Equations

Typical design practice dictates that provisions of the same model (or governing specification) be used for the computation of creep and shrinkage behavior of concrete for design of a given project. Accordingly, the concrete shrinkage prediction methods corresponding to the three previously considered creep models are briefly outlined in this section.

7.2.5.1 AASHTO 2014

The AASHTO 2014 (AASHTO 2014) model relies on an assumed ultimate shrinkage value of 480 microstrain, that is then modified by applicable factors as shown in Equation 7-7.

$$\varepsilon_{sh} = k_s k_{hs} k_f k_{td} 0.48(10^{-3}) \quad (7\text{-}7)$$

where

k_s = factor for the effect of the volume-to-surface ratio of the component;

k_{hs} = humidity factor for shrinkage;

k_f = factor for the effect of concrete strength; and

k_{td} = time-development factor.

AASHTO (2014) specifies that for concrete exposed to drying before five days of curing have elapsed, the shrinkage determined by Equation 7-7 should be increased by 20 percent. Schrantz (2012) and Isbiliroglu (2014) adapted the above recommendation (suspected as intended for non-accelerated cured concrete) for accelerated-cured concrete by computing an approximate corresponding age of first drying of 17 hours (5/7 days). In discussing the development of their AASHTO shrinkage provisions, Al-Omaishi

[1] Hofrichter (2014) showed that the equivalent-age relationship contained in the *fib* Model Code 2010 parallels the equivalent-age maturity method of ASTM C1074 - calibrated for a datum temperature of 20°C and activation energy of 33.2 kJ/mol.

et al. (2009) offer no clarification on the applicability of the 20 percent shrinkage increase for accelerated-cured concrete. Practically speaking, implementation of the above requirement for accelerated-cured concrete is questionable because (1) the curing temperature (and therefore, the rate of maturity development) of accelerated-cured concrete is not uniform over time as it is for non-accelerated concrete, (2) therefore, the growth in maturity of a non-accelerated cured concrete for a given non-accelerated curing period (e.g. days 5 to 6) is a different proportion of the overall maturity than the corresponding maturity growth of an accelerated cured concrete occurring over a similar accelerated curing period (e.g. 17 to 20.5 hours), and (3) the piecewise formulation of the provision (as opposed to a smoother equation-based transition) does not match the expectation of observed behavior. Due to the lack of clarity regarding the applicability of the 20 percent shrinkage amplification and the rarity with which it is applicable in regional precast, prestressed concrete production, it is neither used in the analyses of this report nor recommended for use in camber prediction procedures.

7.2.5.2 ACI 209

The ACI 209 shrinkage prediction model (ACI Committee 209 2008) employs a similar approach to the AASHTO 2014 method, by modifying an assumed ultimate value of 780 microstrain as shown in Equation 7-8.

$$\left(\varepsilon_{sh}\right)_t = \left(780 \cdot 10^{-6} \cdot \gamma_\lambda \cdot \gamma_{vs} \cdot \gamma_\psi \cdot \gamma_s \cdot \gamma_c \cdot \gamma_a\right)\left(\frac{t}{55+t}\right) \tag{7-8}$$

where

γ_λ = ambient relative humidity correction factor;

γ_{vs} = volume-surface ratio correction factor;

γ_ψ = fine aggregate percentage correction factor;

γ_s = slump correction factor;

γ_c = cement content correction factor;

γ_a = air content correction factor; and

t = chronological days after loading (days).

7.2.5.3 *fib* Model Code 2010

The Model Code 2010 method for shrinkage prediction is again the most complex of the three considered methods, relying on independent computation of the relative contributions of both autogenous and drying shrinkage as shown in Equation 7-9.

$$\varepsilon_{cs}(t,t_s) = \varepsilon_{cas}(t) + \varepsilon_{cds}(t,t_s) \quad (7\text{-}9)$$

where

$\varepsilon_{cas}(t)$ = autogenous shrinkage component and

$\varepsilon_{cds}(t,t_s)$ = drying shrinkage component.

Time inputs nested within the above expression (concrete age at start of drying and duration of drying) exclusively use chronological time in contrast to those inputs of Equation 7-4 relying on temperature-adjusted time. Computation of the autogenous shrinkage component requires knowledge of (1) mean compressive strength at 28 days, (2) type of cement, and (3) concrete age in days. The time-development of autogenous shrinkage as predicted by MC 2010 is independent of the duration of curing and starts at the time of initial concrete production rather than at the time of first drying. This distinction results in the need to subtract the portion of autogenous shrinkage occurring prior to first measurement when comparisons are made to experimental work. Computation of the drying shrinkage component requires knowledge of (1) concrete age in days, (2) concrete age at the beginning of drying, (3) mean compressive strength at 28 days, (4) ambient relative humidity, (5) cement type, and (6) notional side of member.

7.3 Experimental Program

This section describes the experimental program conducted to explore the creep and shrinkage behavior of concrete mixtures typical of the Alabama precast, prestressed bridge girder industry. First, a brief summary of work is presented, followed by a discussion of the various candidate mixtures examined. Next, the accelerated curing procedures used in this work are reviewed—including the computation of equivalent age maturities for each trial run. Then, fresh and hardened concrete properties, as relevant to

this effort and later use in candidate creep prediction models, are presented. Finally, the experimental procedures for testing the creep and shrinkage behavior of cylindrical specimens and the shrinkage behavior of rectangular prismatic specimens are discussed.

7.3.1 Summary of Work

In this laboratory study, six concrete mixtures were proportioned to represent mixtures typical of Alabama precast, prestressed work. These six mixtures included three regional coarse aggregates and three varying combinations of supplementary cementing materials (SCMs) in typical substitution percentages. By maintaining a uniform 18-hour compressive strength, paste content, and sand-to-total aggregate ratio (by volume) for all mixtures, certain key variables of interest were isolated. Sampled cylindrical specimens were then exposed to accelerated curing practices mimicking those of accelerated curing methods used in precast, prestressed production, while rectangular prismatic specimens were exposed to standard curing conditions. After the completion of the initial curing period (either 18 or 24 hours), cylindrical specimens were tested in accordance with ASTM C512-02 (ASTM 2002) to evaluate the creep and shrinkage behavior of each mixture for two ages at loading for a period of 250 days. Concurrently, rectangular prismatic specimens were tested in accordance with ASTM C157-08 (ASTM 2008) to also evaluate shrinkage behavior also for a period of 250 days. To ensure the precision and repeatability of results, the first three tests were duplicated.

7.3.2 Concrete Mixtures

The laboratory work presented in this chapter was performed concurrently with the laboratory work previously detailed in Chapter 6 of this report. Accordingly, the six trial mixtures included in this testing program are those detailed in Table 6-1, reproduced here for convenience. Each of these six mixtures is characterized by identical sand/total aggregate ratio (by volume), total paste content, and 18-hour strength. Three of these mixtures, the DL-III, CL-III, and GG-III mixtures are identical mixtures with exception of differing coarse aggregates. The three remaining mixtures, the DL-SL, DL-FA, and DL-FA/SF, each utilize an identical coarse aggregate, but include different substitutions of SCMs.

Table 6-1: Laboratory Phase Concrete Mixture Proportions

Mixture ID	Type III Cement (pcy)	Grade 120 Slag Cement (pcy)	Class F Fly Ash (pcy)	Silica Fume (pcy)	Water (pcy)	*w/cm*	Coarse Agg. SSD (pcy)	Fine Agg. SSD (pcy)	*sand/total agg. (volume)*	*total agg. vol. (%)*	*paste vol.* (ft^3/cy)	HRWRA (oz/cwt)	HSA (oz/cwt)
DL-III	878	0	0	0	281	0.32	1,860	1,048	0.37	64	9.0	7.50	1
CL-III	878	0	0	0	281	0.32	1,860	1,048	0.37	64	9.0	7.75	1
GG-III	878	0	0	0	281	0.32	1,823	1,038	0.37	64	9.0	7.50	1
DL-SL	746	130 (15%)	0	0	278	0.32	1,860	1,048	0.37	64	9.0	6.75	1
DL-FA	754	0	132 (15%)	0	262	0.30	1,860	1,048	0.37	64	9.0	7.50	1
DL-FA/SF	606	0	142 (18%)	63 (8%)	276	0.34	1,860	1,048	0.37	64	9.0	7.75	1

Notes:

1. Percent substitutions noted for supplementary cementing materials (SCMs) are by weight of total cementitious materials.
2. HRWRA = Glenium 7700 and HSA = Masterset Delvo.

7.3.3 Accelerated Curing Procedures

While briefly discussed previously in Section 6.3.1.4, this section more completely details the accelerated curing procedures used for cylindrical specimens in this portion of the work and also describes the computation of the various metrics of maturity necessary for inclusion in the candidate creep and shrinkage prediction models summarized earlier in this chapter. While all three models require some metric of age at loading, the *fib* Model Code 2010 is the only model explicitly requiring the use of maturity for computation of creep and shrinkage, as computed herein.

As previously discussed in Chapter 6, two ages of simulated prestress release were selected based on the historic data set compiled by Hofrichter (2014) documenting the chronological time to prestress release for 1,917 girder concrete placement events. These two chronological ages were 18.0 hours (the approximate average of the primary peak of Figure 4-10) and 24.0 hours (an upper-bound value capturing 99.5 percent of the data of the same primary peak). The complete temperature history for each of fifteen tests through the time of loading is shown in Figure 7-2.

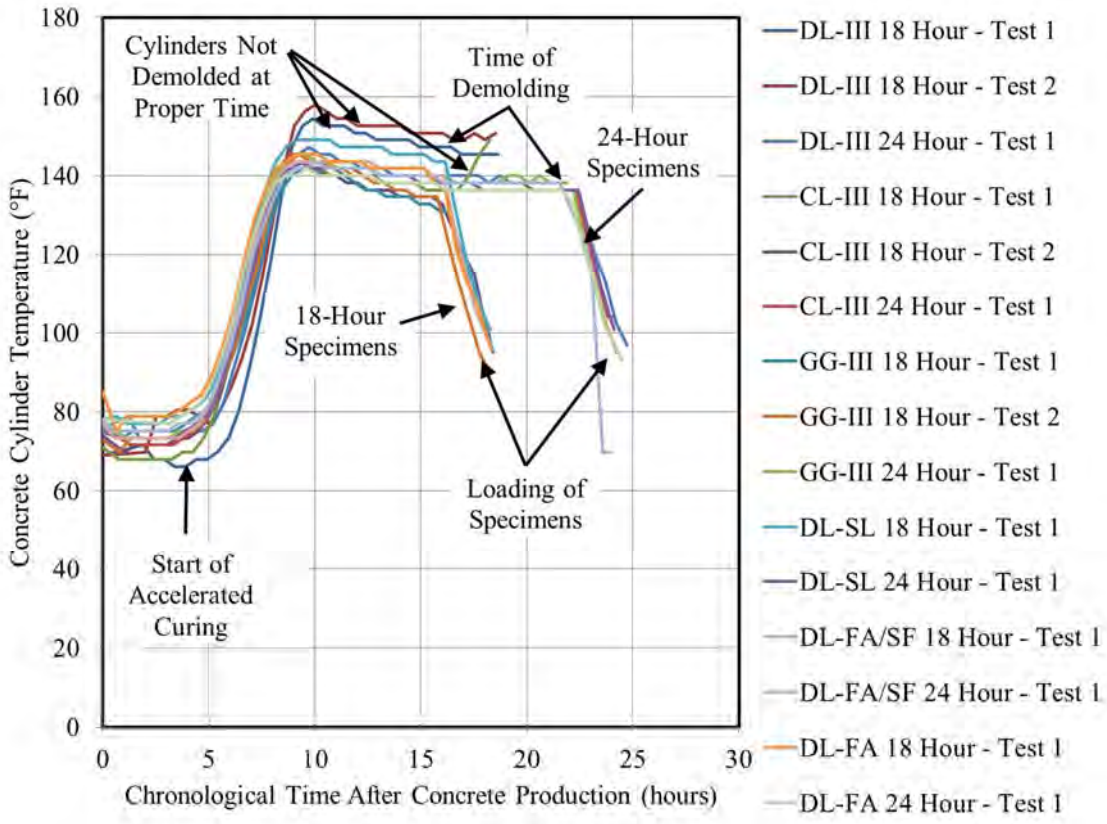

Figure 7-2: Temperature History for Laboratory Tests

As shown, the accelerated curing treatment began four hours after concrete production with curing temperature linearly increasing at an hourly rate of approximately 20.5°F up to a maximum temperature of approximately 150°F. Then, specimens were demolded and prepared for testing in accordance with ASTM C512-02. During the period after demolding and prior to testing, specimens were exposed to ambient laboratory conditions (68-70°F) and allowed to cool accordingly. In three tests (DL-III 18 Hour Test 1+2 and CL-III 18 Hour Test 1), the companion thermocouple cylinders used to record temperature were not demolded at the proper time, as represented in Figure 7-2 by the roughly horizontal lines immediately prior to loading for these three tests. For this reason, the computed maturity for the DL-SL 18 Hour Test 1 was used as a typical 18-hour loading maturity for each of the three tests noted above.

The temperature profiles shown in Figure 7-2 were used to compute two metrics of maturity necessary for creep and shrinkage prediction models. First, the equivalent-age maturity was computed for each test in accordance with *fib* Model Code 2010. Computed values for the equivalent age at the time of loading are shown in the third column of Table 7-1 for each test. Next, to include the effect of

cement type and curing temperature as required by the provisions of the *fib* Model Code 2010, the adjusted equivalent-age maturity was computed for each test as shown in the fourth column of Table 7-1.

Table 7-1: Equivalent-Ages at Time of Loading by Test

Test ID	Chronological Age at Loading (days)	Equivalent Age[b] At Loading (days)	Adjusted Equivalent Age[c] of Loading (days)
DL-III 18 Hour – Test 1	0.78	3.0[a]	7.6
DL-III 18 Hour – Test 2	0.77	3.0[a]	7.6
DL-III 24 Hour – Test 1	1.03	4.0	8.9
CL-III 18 Hour – Test 1	0.76	3.0[a]	7.6
CL-III 18 Hour – Test 2	0.76	2.5	7.0
CL-III 24 Hour – Test 1	1.00	3.9	8.8
GG-III 18 Hour – Test 1	0.77	2.5	7.0
GG-III 18 Hour – Test 2	0.76	2.5	7.0
GG-III 24 Hour – Test 1	1.01	3.9	8.8
DL-SL 18 Hour – Test 1	0.76	3.0	7.7
DL-SL 24 Hour – Test 1	1.00	3.8	8.7
DL-FA/SF 18 Hour – Test 1	0.76	2.7	7.3
DL-FA/SF 24 Hour – Test 1	1.00	3.8	8.7
DL-FA 18 Hour – Test 1	0.76	2.8	7.4
DL-FA 24 Hour – Test 1	1.02	3.8	8.7

Notes: [a] = DL-SL 18 Hour – Test 1 temperature profile used;
[b] = Computed in accordance with *fib* MC 2010 (datum temperature = 20°C and AE = 33.2 kJ/mol); and
[c] = Computed in accordance with *fib* MC 2010 accounting for cement type.

7.3.4 Fresh Concrete Properties

For each of fifteen tests, fresh concrete temperature, slump, and air content were measured as shown in Table 7-2. The fresh concrete temperature for each test was used in the computation of the equivalent-age maturities computed in Section 7.3.3 for the time period between initial mixing of concrete and the time of cylinder sampling.

Table 7-2: Fresh Concrete Properties by Test

Test ID	Temperature (°F)	Slump (in.)	Air Content (%)
DL-III 18 Hour – Test 1	69	9.0	2.5
DL-III 18 Hour – Test 2	69	8.0	3.0
DL-III 24 Hour – Test 1	76	8.0	2.5
CL-III 18 Hour – Test 1	71	9.0	3.0
CL-III 18 Hour – Test 2	74	8.0	3.6
CL-III 24 Hour – Test 1	75	8.25	2.8
GG-III 18 Hour – Test 1	75.5	8.5	3.0
GG-III 18 Hour – Test 2	73	9.0	3.9
GG-III 24 Hour – Test 1	77	8.50	2.5
DL-SL 18 Hour – Test 1	76	8.0	2.8
DL-SL 24 Hour – Test 1	75	8.0	2.5
DL-FA/SF 18 Hour – Test 1	77	8.5	5.0
DL-FA/SF 24 Hour – Test 1	78	8.0	4.0
DL-FA 18 Hour – Test 1	78	8.5	2.9
DL-FA 24 Hour – Test 1	78	7.5	2.8

7.3.5 Hardened Concrete Properties

For each of 15 tests, concrete compressive strength and elastic modulus at the time of loading were tested in accordance with ASTM C39 (ASTM 2010) and ASTM C469 (ASTM 2010), respectively. Results for each test are shown in Table 7-3.

Table 7-3: Hardened Concrete Properties by Test

Test ID	Compressive Strength, f_c, at Loading (psi)	Elastic Modulus, E_c, at Loading (ksi)	Compressive Strength, f_c, at 28 Days (psi)
DL-III 18 Hour – Test 1	6,420	5,700	9,900
DL-III 18 Hour – Test 2	6,520	5,600	9,910
DL-III 24 Hour – Test 1	6,900	6,350	9,010
CL-III 18 Hour – Test 1	6,610	5,700	9,520
CL-III 18 Hour – Test 2	6,170	5,750	9,010
CL-III 24 Hour – Test 1	7,220	6,100	9,640
GG-III 18 Hour – Test 1	7,400	3,700	10,070
GG-III 18 Hour – Test 2	6,850	3,500	9,650
GG-III 24 Hour – Test 1	7,940	3,900	10,440
DL-SL 18 Hour – Test 1	6,870	6,600	10,080
DL-SL 24 Hour – Test 1	7,260	6,400	9,860
DL-FA/SF 18 Hour – Test 1	6,900	6,050	9,850
DL-FA/SF 24 Hour – Test 1	7,270	6,100	9,800
DL-FA 18 Hour – Test 1	6,860	6,100	10,240
DL-FA 24 Hour – Test 1	7,360	6,100	10,200

7.3.6 Creep and Shrinkage Testing Procedures

Creep and shrinkage testing was conducted in accordance with the general requirements of the *Standard Test Method for Creep of Concrete in Compression,* ASTM C512-02. Testing in accordance with this specification requires the application of a sustained stress equal to 40 percent of the compressive strength at the time of loading and monitoring specimens for long-term changes in strain. In absence of specification requirements or guidance, the following experimental procedures were selected to tailor creep and shrinkage testing efforts to regional precast, prestressed industry practices:

- Due to the early age of testing, the use of sulfur capping was impractical and instead, the ends of cylindrical specimens were ground flat and true with an automated diamond grinder intended for use on concrete cylinders;
- Two ages at loading (18 hours and 24 hours) and an accelerated curing protocol were used in this research program to simulate both the average loading maturity observed in the field and an upper-bound value;
- The accelerated curing protocol was terminated roughly two hours prior to creep frame loading to allow preparation of the specimens (demolding, grinding, and *DEMEC* application). During this time period, the specimens were exposed to ambient temperature, but maintained in a moist enclosure;

- The elevated temperature of cylinders at the time of loading was recorded throughout the early life of the test—until the specimens reached ambient specified temperature conditions;
- In addition to the testing of compressive strength immediately prior to the time of loading as required by ASTM C512-02, the elastic modulus was tested at the time of loading in accordance with ASTM C469;
- Creep and shrinkage testing was performed for a period of 250 days, well in excess of the anticipated pre-service life of bridge girder; and
- Demountable mechanical (*DEMEC)* strain gages were used to monitor both concrete cylinder strains and also tension in the steel bars of creep loading frames. *DEMEC* gages were used to monitor steel bar strains to preclude long-term drift associated with electrical-resistance strain gages.

A detailed narrative of creep and shrinkage testing procedures in accordance with ASTM C512-02 is described in previous work of Ellis (2012) and Kavanaugh (2008), who each previously conducted creep and shrinkage testing using identical apparatuses to those used in this experimental effort. Key steps in the creep testing procedure are shown in Figure 7-3.

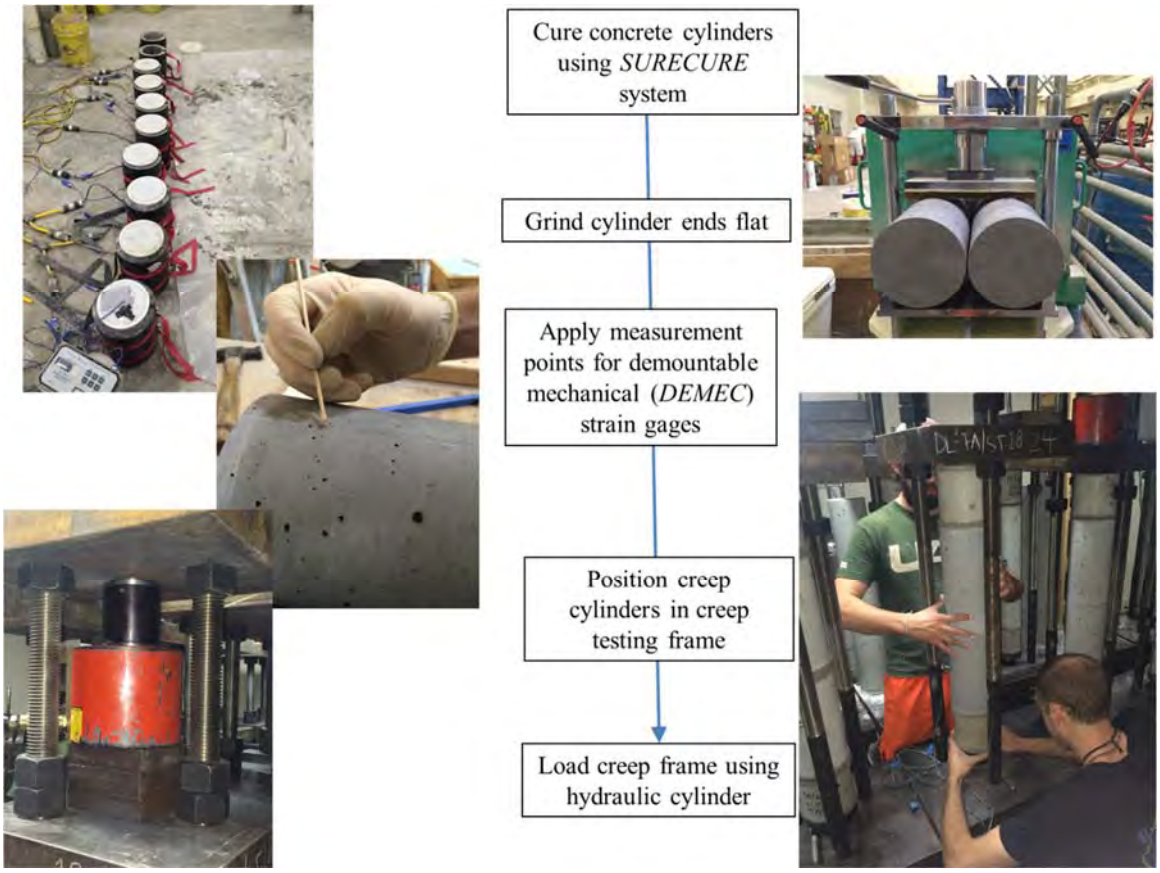

Figure 7-3: Creep Testing Procedure

7.3.7 Shrinkage Testing Procedures

In addition to the shrinkage testing performed on accelerated cured cylindrical specimens detailed above, shrinkage properties were also evaluated for each candidate concrete mixture using standard-cured concrete rectangular prisms in accordance with the requirements of ASTM C157-08. In absence of specification requirements or guidance, the following experimental procedure adjustment was selected to best tailor shrinkage testing efforts to regional precast, prestressed industry practices:

- Benchmark shrinkage readings were first recorded upon exposure to ambient conditions at the end of an initial standard curing period of 7 days. A value of 7 days was selected to coincide with the default assumptions for the length of initial standard (non-accelerated) curing period as reflected in the ACI 209 and AASHTO 2014 shrinkage prediction models.

7.4 Post-Processing of Measured Data

This section details various post-processing efforts aimed at affirming the accuracy of recorded data, determining the experimental precision of the laboratory creep and shrinkage testing setup, and accounting for temperature effects at the time of loading. The full experimental data set resulting from the creep and shrinkage testing efforts of this research study is presented in Section 7.5; only limited results related to the topic of this section are included here.

7.4.1 Detection and Removal of Climate Control System Failures

As discussed earlier in this chapter, creep and shrinkage behavior of concrete is extremely sensitive to environmental factors, namely temperature and relative humidity. For this reason, ASTM C512-02 and ASTM C157-08 each require strict control over temperature and relative humidity throughout the duration of testing. Ambient temperature during testing must be 73.4 ± 1.5°F, while relative humidity is permitted to range from 46-54 percent. Due to the extended period of testing (250 days) conducted in this research effort, brief failures of the climate control system were inevitable due to power outages and unexpected malfunctions of the climate control system. The date and time of all climate control system malfunctions were noted and repairs were completed expediently. Nonetheless, various failures of the climate control system did compromise certain measurements throughout the course of the project. An iterative procedure (as detailed in Mante [2016]) was developed for the detection and removal of data points that were compromised by documented failures of the climate control system.

7.4.2 Determination of Experimental Precision for Creep and Shrinkage Testing of Cylindrical Specimens

It is important to determine the experimental precision of the creep and shrinkage testing of cylindrical specimens conducted in this research effort to allow for accurate analysis of experimental data. Without a clear understanding of the precision and repeatability of the experimental methods used herein, it may not be possible to attribute observed variation to the key variables of interest (i.e. age at loading, coarse aggregate type, and SCM use) instead of to intrinsic variability of the test method. This section focuses on determining an approximate level of experimental precision for cylindrical specimen testing that is used in the subsequent data analysis efforts of this chapter. Readers should note that this effort is

necessary because of the limited availability of data (n=1 or n=2 at best for given variable combination) precludes the use of inferential statistics. The first portion of this section focuses on systematically determining the experimental precision for compliance of cylindrical specimens, while the later portions focus on estimating the experimental precision for shrinkage testing of cylindrical concrete specimens.

ASTM C512-02 notes that the results of two properly conducted creep and shrinkage tests by the same operator on material cast from different batches should not differ by more than 13 percent of their average (ASTM 2002). The computed compliance, J, for each of three duplicate tests conducted in this experimental effort is shown in Figure 7-4. As shown, the results of duplicate tests qualitatively appear quite similar, with each set of tests satisfying the precision statement noted above (a maximum variation from average of 6 percent is observed for the GG-III tests).

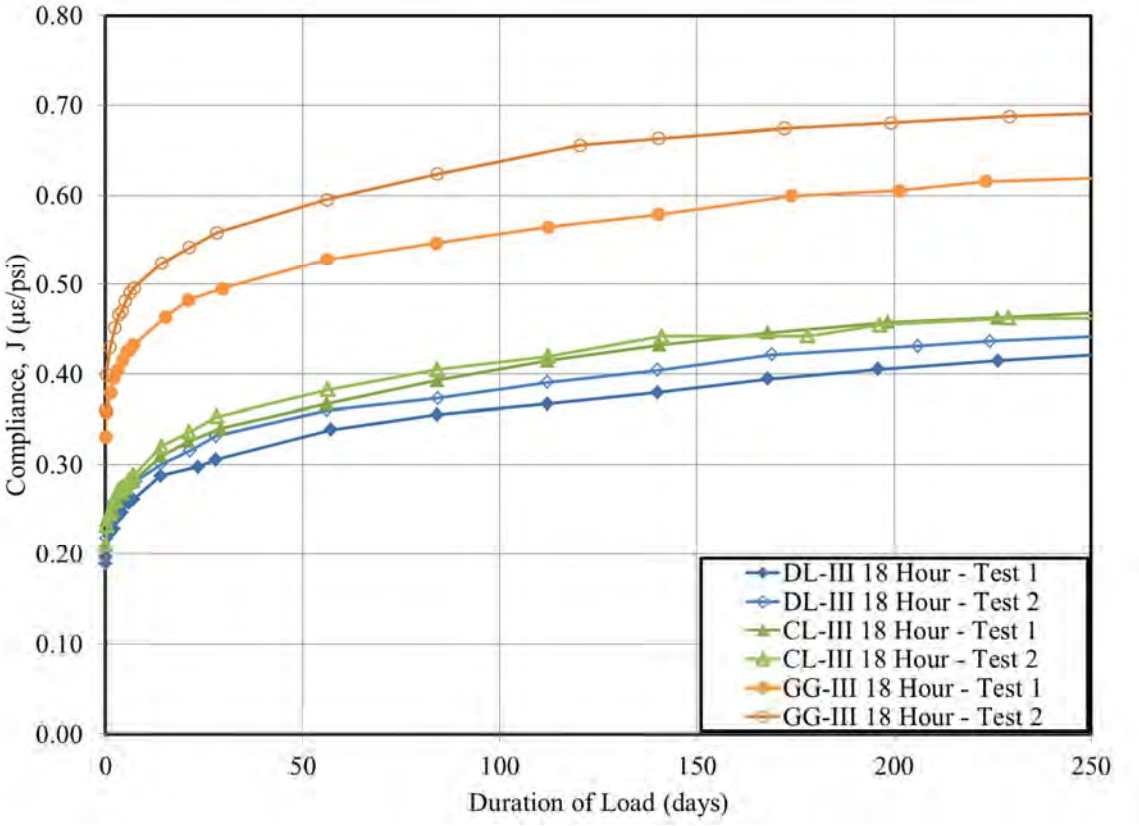

Figure 7-4: Compliance Behavior of Duplicate Tests

The compliance data of Figure 7-4 is displayed in tabulated form for four key ages in Table 7-4. The ages of interest include the following times: (1) immediately after loading, (2) lower-bound girder erection estimate = 60 days, (3) upper-bound girder erection estimate = 120 days, and (4) 250 days. As shown,

the duplicate tests for the DL-III concrete exhibit a uniform difference between subsequent tests of 0.02 με/psi at all considered ages, while the CL-III tests exhibit a similar uniform difference of 0.01 με/psi between subsequent verification tests. For the dolomitic limestone mixtures considered in this effort, a precision of 0.02 με/psi is assumed for analysis purposes—that is, any measured compliance value is assumed to be precise to within ± 0.02 με/psi for a given test[2].

[2] Without knowing which of two duplicate loading cycles is most accurate, it was not possible to compute a percent difference between measured values. Instead, the difference between values is selected as a measure of experimental precision.

Table 7-4: Compliance Behavior of Duplicate Tests

Test ID	Initial Compliance, *J*, (με/psi)	Difference Between Duplicate Tests (με/psi)	60-Day Compliance, *J*, (με/psi)	Difference Between Duplicate Tests (με/psi)	120-Day Compliance, *J*, (με/psi)	Difference Between Duplicate Tests (με/psi)	250-Day Compliance, *J*, (με/psi)	Difference Between Duplicate Tests (με/psi)
DL-III 18 Hour – Test 1	0.19	0.00	0.34	**0.02**	0.37	**0.02**	0.42	**0.02**
DL-III 18 Hour – Test 2	0.19		0.36		0.39		0.44	
CL-III 18 Hour – Test 1	0.21	0.00	0.37	0.01	0.41	0.01	0.47	0.01
CL-III 18 Hour – Test 2	0.21		0.38		0.42		0.46	
GG-III 18 Hour – Test 1	0.33	0.03	0.53	0.07	0.56	**0.10**	0.62	0.07
GG-II 18 Hour – Test 2	0.36		0.60		0.66		0.69	

Note: Approximate error derived from instrument precision = 0.003 με/psi.

Conversely, the difference between the two GG-III duplicate tests is more pronounced, ranging from 0.03 to 0.10 με/psi at various ages. At first consideration, it is tempting to assume experimental difficulties may be to blame for the larger observed differences between duplicate tests. However, no apparent anomalies were detected within either loading frame. Given that (1) the observed variation for the GG-III duplicate tests remains well within the precision of the test, (2) the GG-III mixture exhibited unexpectedly low stiffness (perhaps due to high levels of deleterious substances), and (3) one of the GG-III tests appears to exhibit an uncharacteristically high early rate of compliance, the computed precision values of 0.03 to 0.10 με/psi is used to evaluate the GG-III tests in the remainder of this report.

A similar procedure was used to determine the experimental precision for shrinkage testing of cylindrical specimens. A graph of experimental results for the duplicate shrinkage tests is shown in Figure 7-5, with values at key ages displayed in Table 7-5. By the nature of testing early-age accelerated-cured concrete specimens, there is slight variability in the temperature of specimens at the age at loading, which increases the variability of measured results. This topic is discussed more thoroughly in Section 7.4.5.

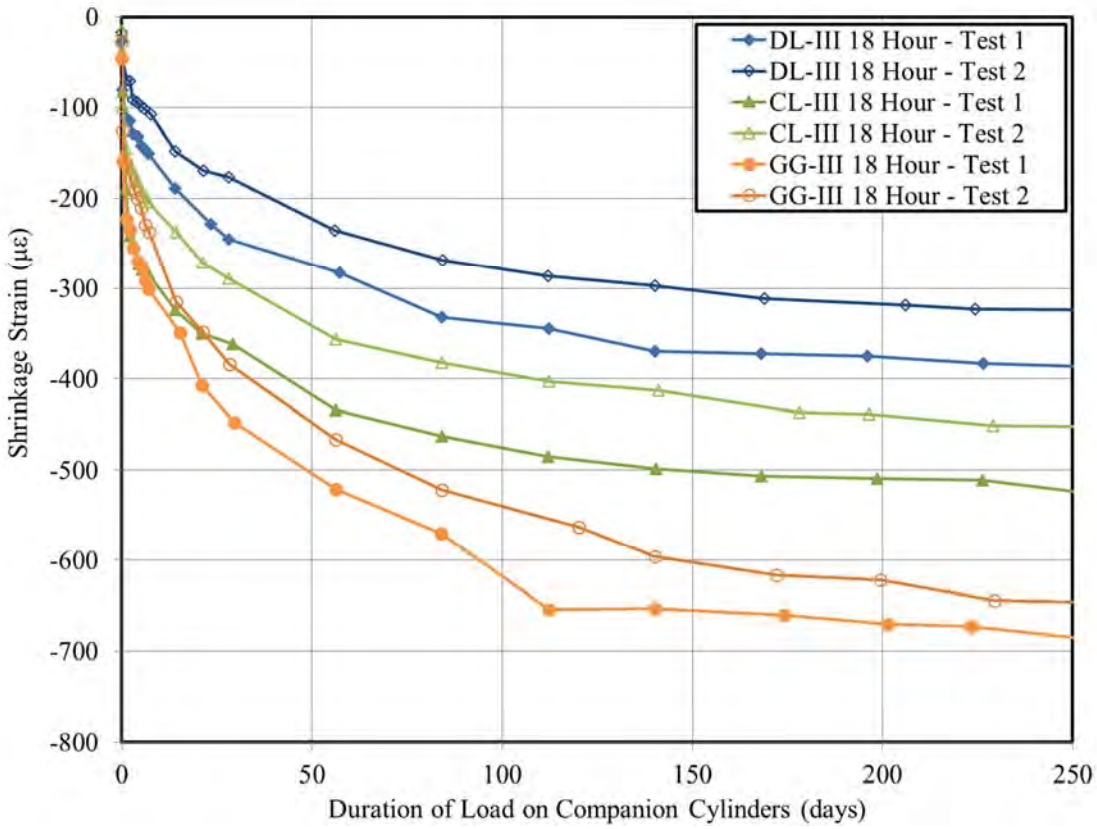

Figure 7-5: Cylinder Shrinkage Behavior of Duplicate Tests

Table 7-5: Cylinder Shrinkage Behavior of Duplicate Tests

Test ID	Initial Shrinkage[a], (με)	Difference Between Duplicate Tests (με)	60-Day Shrinkage, (με)	Difference Between Duplicate Tests (με)	120-Day Shrinkage, (με)	Difference Between Duplicate Tests (με)	250-Day Shrinkage, (με)	Difference Between Duplicate Tests (με)
DL-III 18 Hour - Test 1	-27	9	-288	48	-352	63	-386	62
DL-III 18 Hour – Test 2	-18		-240		-289		-324	
CL-III 18 Hour – Test 1	-39	23	-438	78	-489	84	-524	**90**
CL-III 18 Hour – Test 2	-16		-360		-405		-452	
GG-III 18 Hour – Test 1	-46	17	-528	54	-653	**90**	-685	39
GG-II 18 Hour – Test 2	-29		-474		-563		-646	

[a] = Initial shrinkage is the measured shrinkage occurring between pre-loading and post-loading and is predominately due to the cooling of specimens (as is discussed in Section 7.4.4).

Note: Approximate error from instrument precision = 8 με.

Examining the data of Table 7-5, a maximum difference between duplicate tests of 90 με is observed and an approximate average value of 60 με exceeds all but four of the shown differences. This value serves as an average precision for the cylinder shrinkage testing conducted in this study, although engineering judgment is also used to identify possible significant trends in experimental data.

7.4.3 Determination of Experimental Precision for Rectangular Shrinkage Prism Testing

The experimental precision for rectangular shrinkage prism testing was determined in similar fashion to above using the experimental results shown in Figure 7-6 and Table 7-6. Despite the rectangular shrinkage prism data exhibiting more distinct and clear clustering of experimental results, the precisions between duplicate tests are similar to those of cylindrical specimens. In this case, three tests are available for the DL-III and GG-III sample groups due to the identical treatment of rectangular shrinkage prisms regardless of 18- or 24-hour age at loading. The CL-III sample group contains only two tests due to experimental difficulties with the rectangular prisms from the CL-III 18 Hour – Test 2. As shown in Table 7-6, a maximum difference between duplicate results of 92 με is observed for the DL-III tests, while the average value of observed difference lingers again around 70 με. This value serves as an average precision for the rectangular prism shrinkage testing conducted in this study, although engineering judgment may also be used to identify possible significant trends in experimental data. For typical design values of prestressing strand modulus of elasticity and jacking stresses, a variation of 140 με (±70 με) in unrestrained shrinkage corresponds to less than a 2 percent change in the effective prestress force, thereby having a small effect on computed camber values.

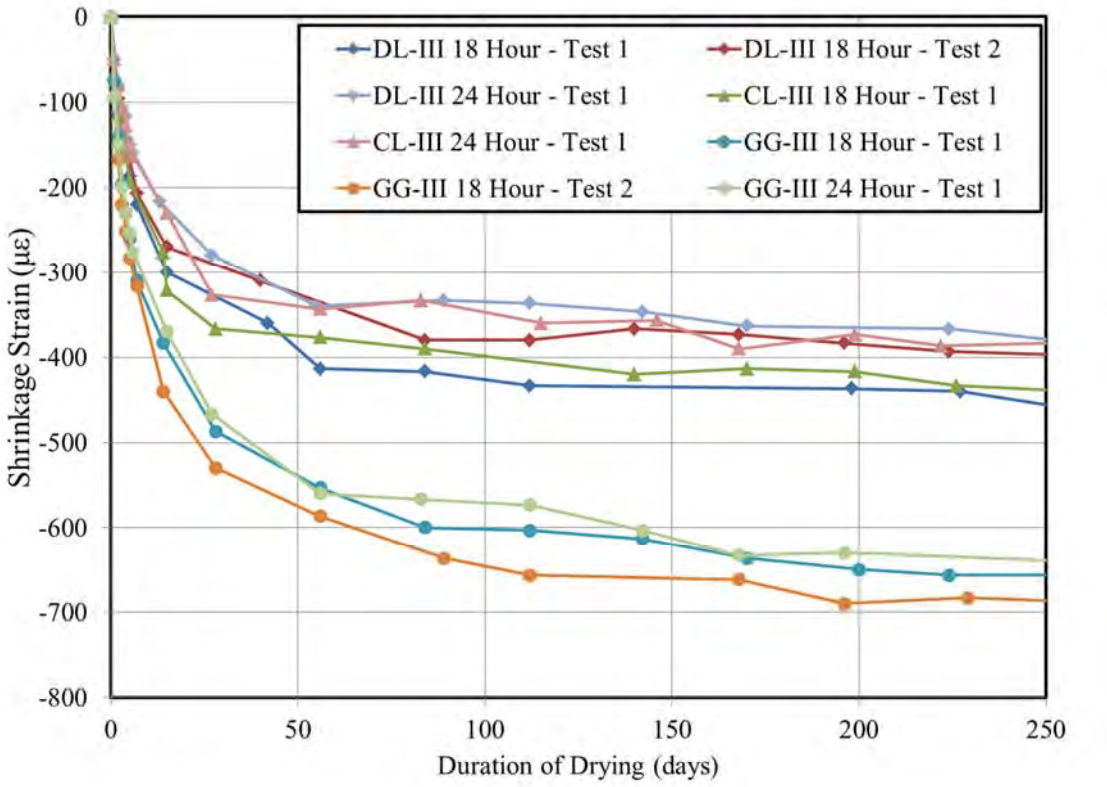

Figure 7-6: Rectangular Prism Shrinkage Behavior for Duplicate Tests

Table 7-6: Rectangular Prism Shrinkage Behavior of Duplicate Tests

Test ID	1-Day Shrinkage, (με)	Max. Difference Among Duplicate Tests (με)	60-Day Shrinkage, (με)	Max. Difference Among Duplicate Tests (με)	120-Day Shrinkage, (με)	Max. Difference Among Duplicate Tests (με)	250-Day Shrinkage, (με)	Max. Difference Among Duplicate Tests (με)
DL-III 18 Hour - Test 1	-73	23	-414	75	-432	**92**	-456	77
DL-III 18 Hour – Test 2	-50		-341		-376		-396	
DL-III 24 Hour – Test 1	-50		-339		-340		-379	
CL-III 18 Hour – Test 1	-67	17	-379	37	-409	50	-438	55
CL-III 24 Hour – Test 1	-50		-342		-359		-383	
GG-III 18 Hour – Test 1	-77	16	-560	33	-606	77	-657	47
GG-III 18 Hour – Test 2	-93		-593		-658		-687	
GG-III 24 Hour – Test 1	-93		-561		-581		-640	

Note: Approximate error from instrument precision = 10 με.

7.4.4 Effect of Concrete Temperature at Loading

As noted by ACI Committee 209 (2008) any effects of thermal strain should be avoided entirely or otherwise removed from measured creep and shrinkage data. By virtue of the early concrete age at loading and accelerated curing methods typical of precast, prestressed concrete construction, it is unavoidable that elevated temperatures be present at the time of loading in both field-testing and laboratory-testing efforts. Previous researchers most often ignore the presence of thermal strains at and immediately following loading and, therefore, reported shrinkage values measured on cylindrical specimens actually represent a combination of shrinkage strains and thermal strains. Conveniently, because these shrinkage and thermal strains are subtracted from the loaded cylinders, compliance is unaffected by the presence of these thermal strains. Kelly, Bradberry, and Breen (1987) attempted to manually remove the effect of thermal strains at the time of loading from measured cylinder shrinkage strains—although their methods relied on an assumed coefficient of thermal expansion for typical precast, prestressed concretes. Without precisely knowing the coefficient of thermal expansion (CTE) of the concrete at loading (which is expected to be a function of moisture content), precise decoupling of shrinkage strains and thermal strains is not possible.

In this research project, the decision was made to disregard the effect of thermal strains at and immediately following the time of loading in laboratory testing for the following reasons:

- The thermal strains observed and induced in this research effort simulated those likely present during field-fabrication and thus, should be included in design predictions of shrinkage[3];
- Nearly all previous researchers conducting creep and shrinkage testing of precast, prestressed concretes have similarly ignored the presence of the effect of early thermal strains in their reported shrinkage results;
- ACI 209 (2008) notes that the rate of creep and shrinkage are temperature-dependent, thereby suggesting that the superposition method used by Kelly et al. (1987) may not fully remove the influence of temperature on experimental measurements; and

[3] ACI 209 (2008) notes that no prediction method can yield better results than testing actual materials under conditions similar to those expected in the field.

- Coefficient of thermal expansion (CTE) values as required for the superposition method used by Kelly at al. (1987) are difficult to estimate accurately at the time (and moisture state) at loading.

In addition to the above practical reasons, a more theoretical justification for the decision to neglect the presence of thermal strains in shrinkage measurements is offered herein. The intent of this experimental effort is to evaluate the effect of various material properties (either assumed, expected, or known) on the camber of precast, prestressed concrete girders. In computing camber, the effect of shrinkage is assumed to act uniformly on a given cross section as is discussed in Chapter 9 (i.e. unrestrained shrinkage strains do not vary with girder height). In accordance with this assumption, a uniform shrinkage will not tend to directly influence the magnitude of camber in a precast, prestressed girder. Instead, concrete shrinkage behavior tends to induce only minor changes to camber due to (1) eccentric restraint of reinforcement and (2) by reducing the effective prestressing force of the element (as is discussed and clarified in Chapter 8). For this reason, it seems permissible and perhaps even advantageous to include the effect of early thermal strains in measured shrinkage values.

7.5 Presentation and Analysis of Results

This report section first broadly presents the experimental results of the creep and shrinkage testing conducted as part of this effort. Then, the relative effect of each of the three main variables of interest (coarse aggregate type, age at loading, and SCM usage) is explored, while using the previously computed experimental precisions to identify significant results. Next, three candidate creep and shrinkage prediction models are implemented and compared to experimental behavior. Finally, the three candidate creep and shrinkage prediction models are modified (calibrated) by the use of a multiplier to yield most accurate results for typical regional concretes.

7.5.1 Compliance

As previously mentioned, the preferred metric for time-dependent load-induced deformation in this report is compliance. Compliance, as presented in this section, is computed directly from the following measured parameters: (1) the total strain of creep specimens after loading at a given time, (2) the total strain of companion shrinkage specimens after loading at a given time, and (3) the magnitude of the applied load. Due to the large amount of data generated from the experimental efforts of this chapter,

visualization of data in a clear and concise manner is somewhat challenging. Graphical depictions of compliance curves are selected as the preferred metric of data display, with selected values shown in tabulated form as required for quantitative comparisons. Where tabulated values are used to analyze and compare data, the following important durations of load are again used: 60 days, 120 days, and 250 days.

7.5.1.1 Presentation of Measured Results

Compliance results for each of 15 tests included in this project are displayed in Figure 7-7, grouped by coarse aggregate type for clarity. As shown, compliance results from the crushed granite concrete mixture appear distinctly separate from the dolomitic limestone mixtures and are thus considered a separate group for the remainder of data visualization purposes.

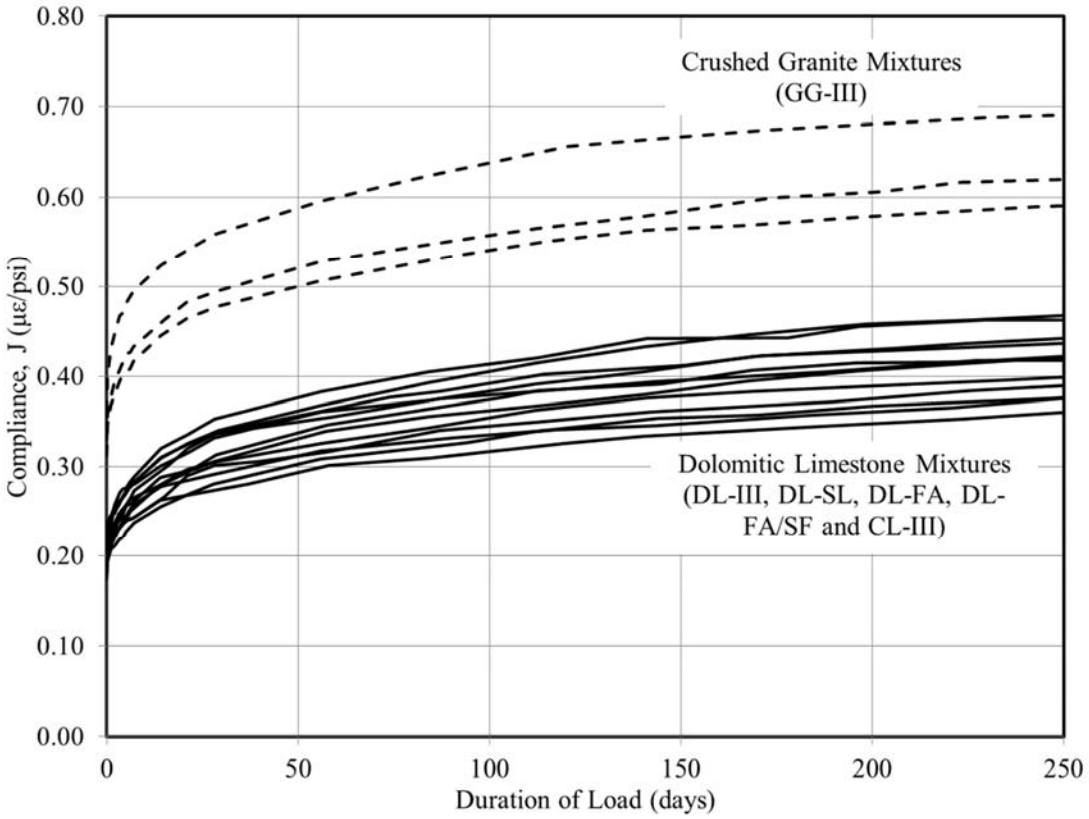

Figure 7-7: Compliance Results by Aggregate Type

For each of the above subgroups, results of the no-SCM variant (i.e. GG-III, DL-III, and CL-III) tests are displayed in Figures 7-8 and 7-9, identified by age at loading. For convenience in preliminary comparisons of each subgroup, dashed lines identify 18-hour tests and solid lines denote 24-hour tests.

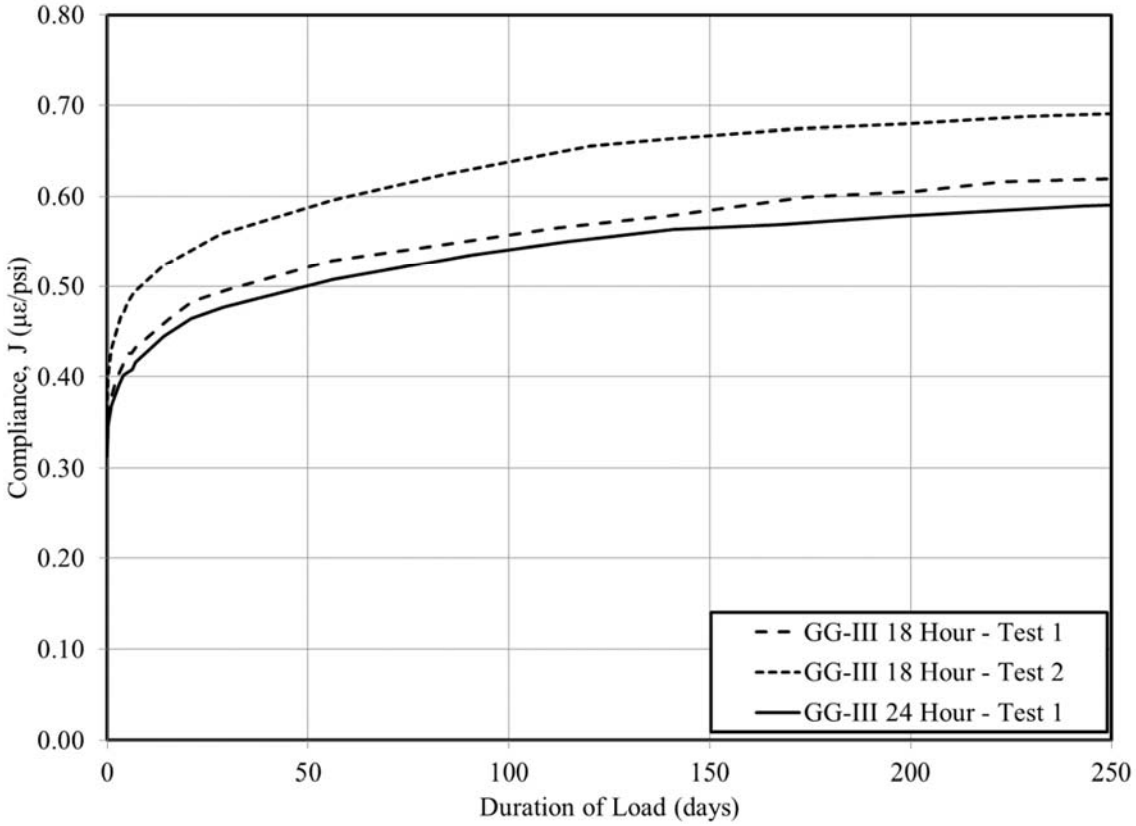

Figure 7-8: Compliance for No-SCM Variant Crushed Granite Tests

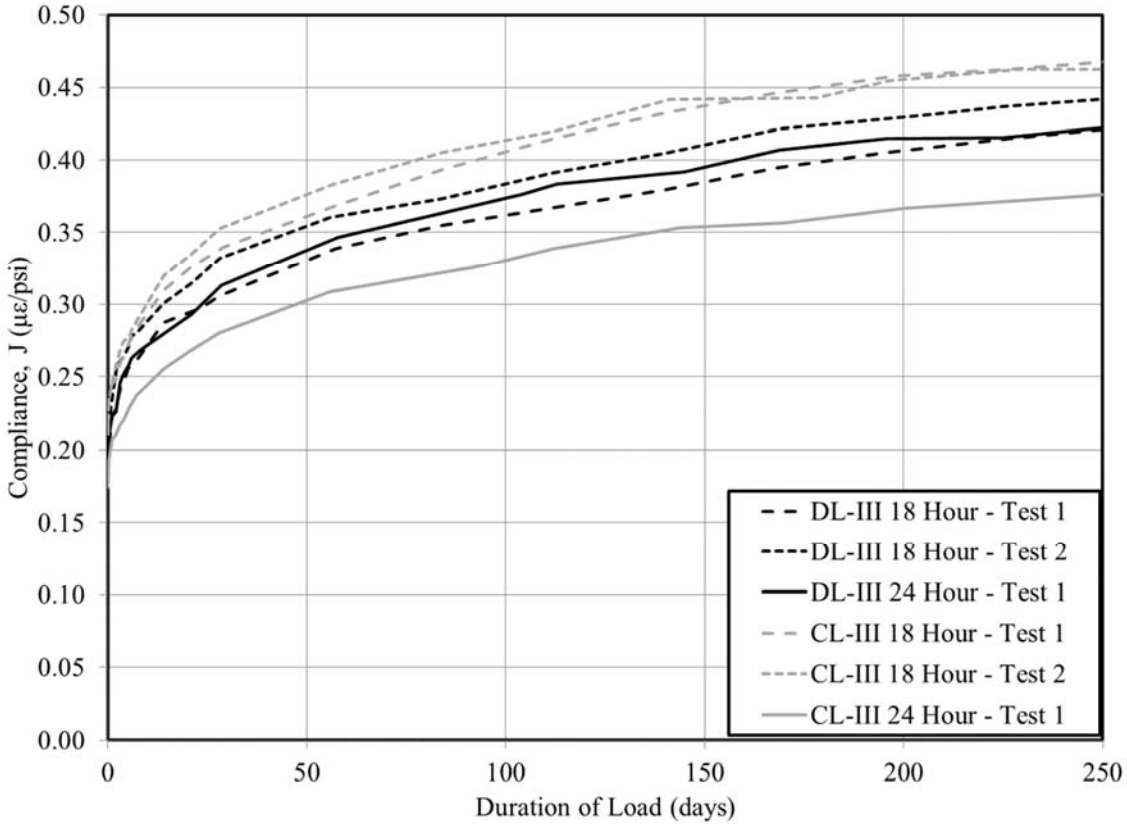

Figure 7-9: Compliance for No-SCM Variant Dolomitic Limestone Tests

Figures 7-8 and 7-9 collectively depict nine of the fifteen total tests conducted as part of this research effort. The remaining six tests represent the SCM variants and are displayed in Figure 7-10, along with the companion dolomitic limestone no-SCM variants for comparison.

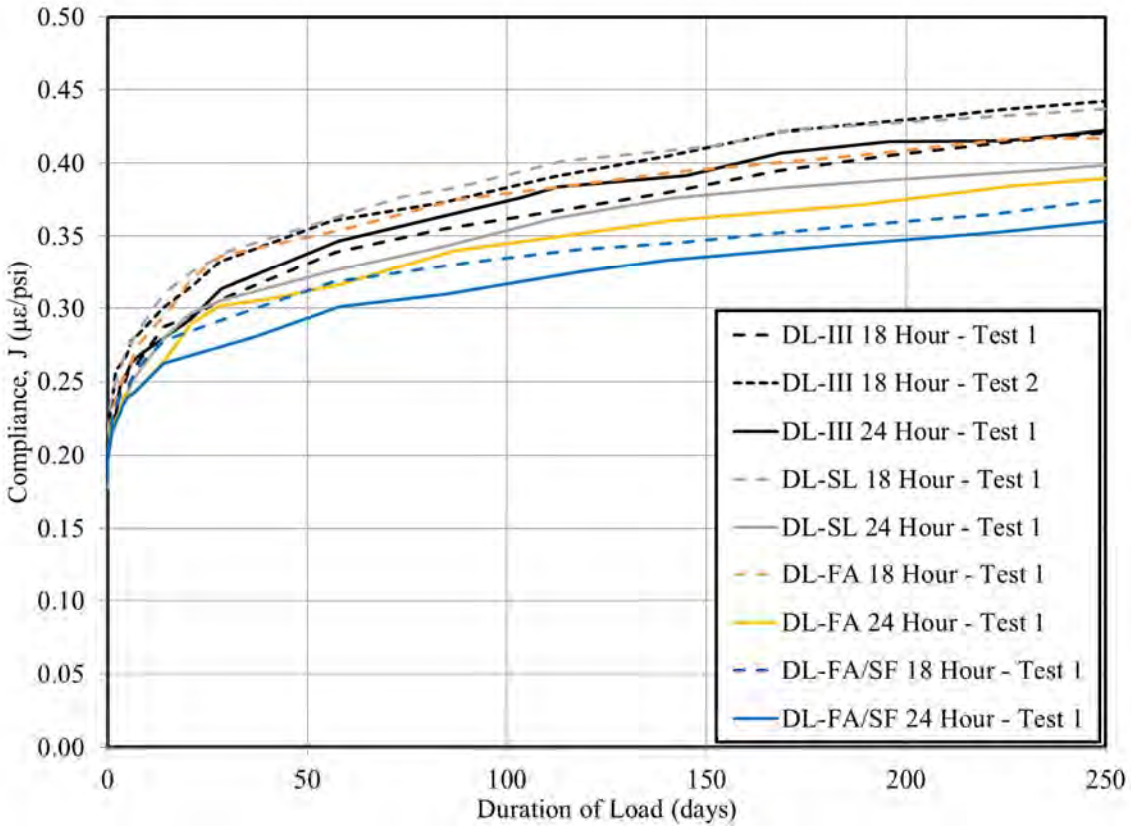

Figure 7-10: SCM-Variant Dolomitic Limestone Tests

Although the above figures display the experimental data set in the most convenient subgrouping for analysis purposes, the complete unsorted data set is also shown in Figure 7-11 for reference.

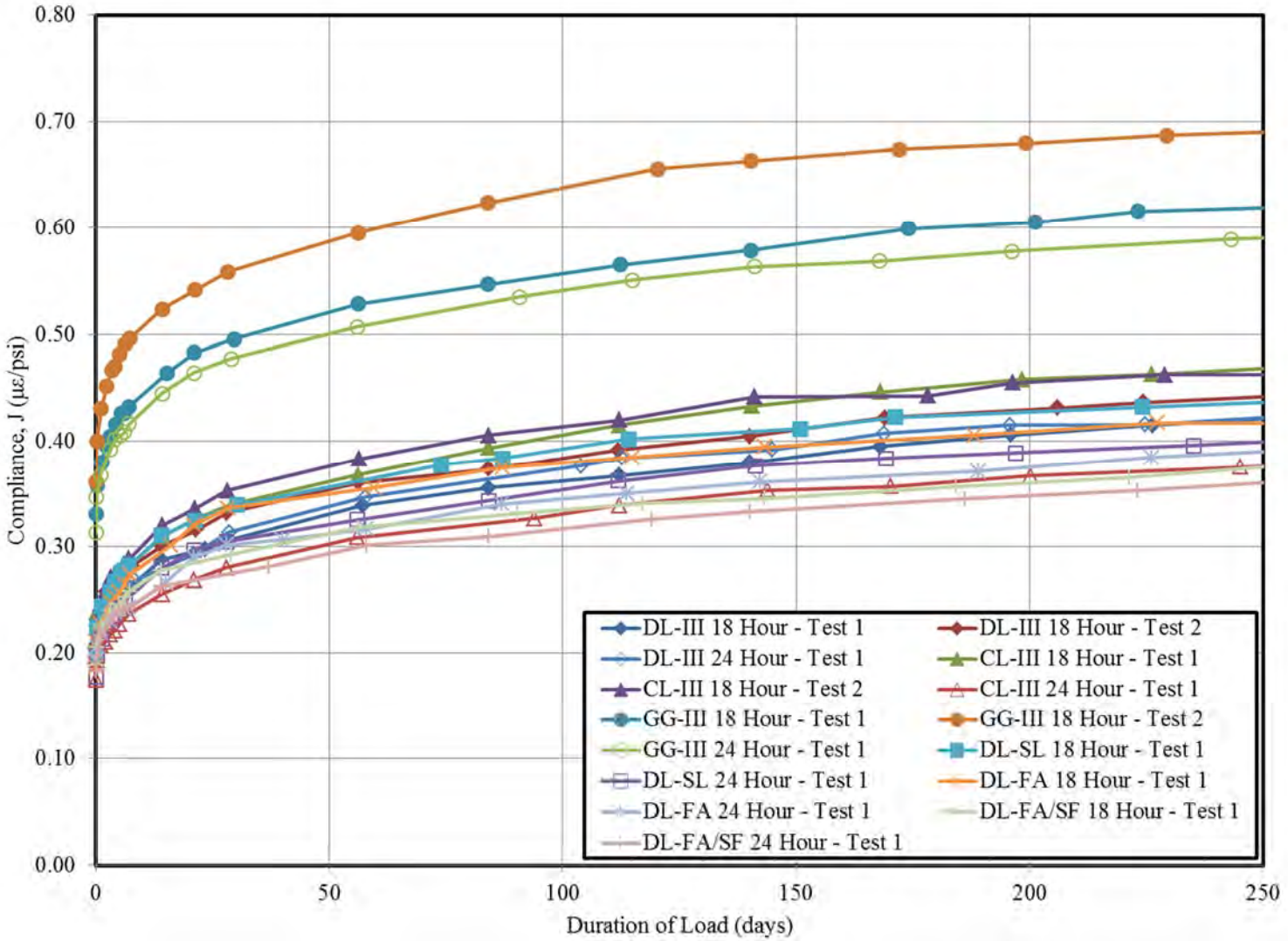

Figure 7-11: Unsorted Creep and Shrinkage Experimental Data Set

7.5.1.2 Effect of Coarse Aggregate Type

To isolate any potential effect of coarse aggregate type on compliance, it is most reasonable to compare only the no-SCM experimental variants (DL-III, CL-III, and GG-III) for each of two ages at loading, independently. Significant trends in experimental data are first identified by the use of error bands corresponding to the experimental precisions determined in Section 7.4.2. Then, tabulated results are presented as necessary to quantify significant trends. Compliance results for each of the three no-SCM variants for an age at loading of 18 hours are shown in Figure 7-12.

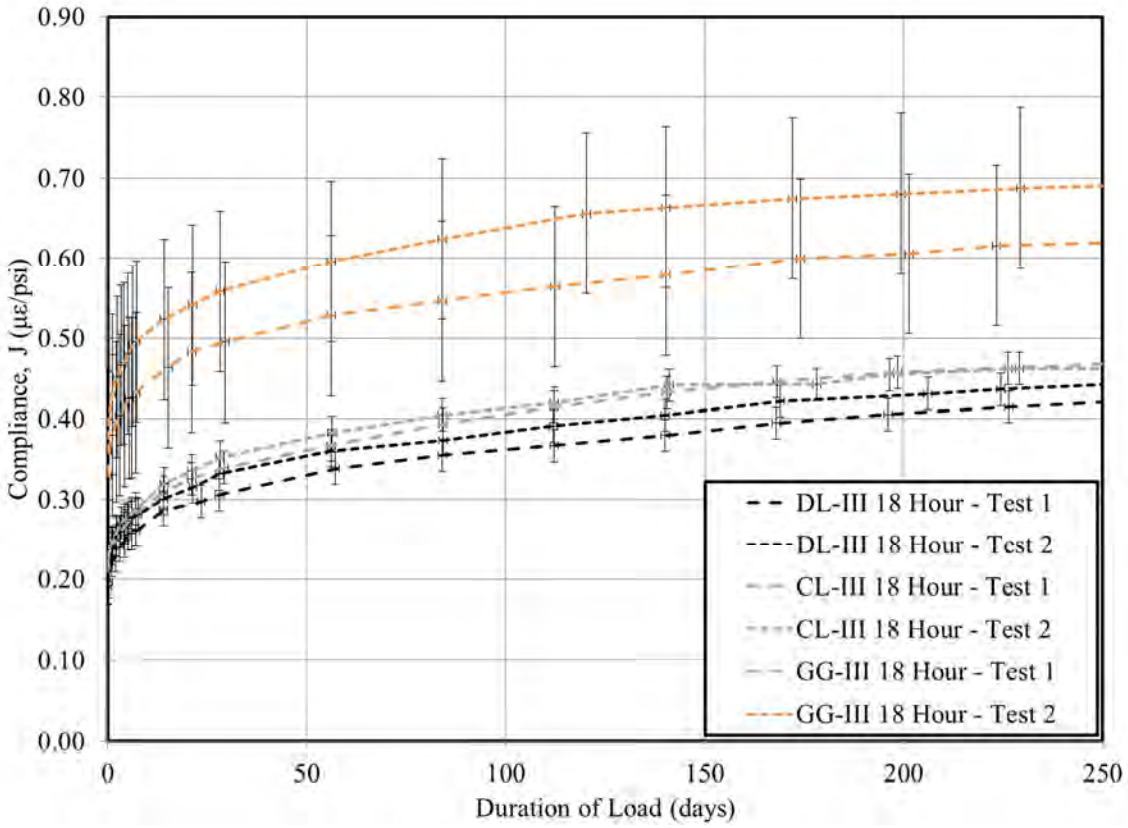

Figure 7-12: Compliance by Aggregate Type for 18 Hour Tests

Error bands are also shown denoting the experimental precisions of ±0.02 με/psi and ±0.10 με/psi for dolomitic limestone and crushed granite tests, respectively. No significant difference in compliance is detectable between the two considered dolomitic limestone mixtures for an age at loading of 18 hours. Conversely, however, there is a significant difference between the dolomitic limestone mixtures (represented by four tests) and the crushed granite mixtures (represented by two tests). Tabulated values for selected 18-hour age at loading data are shown in Table 7-7.

Table 7-7: Effect of Aggregate Type on Compliance for 18 Hour Loading

Test ID	Initial Compliance[a], *J*, (με/psi)	60-Day Compliance, *J*, (με/psi)	120-Day Compliance, *J*, (με/psi)	250-Day Compliance, *J*, (με/psi)
DL-III 18 Hour - Test 1	0.19	0.34	0.37	0.42
DL-III 18 Hour – Test 2	0.19	0.36	0.39	0.44
CL-III 18 Hour – Test 1	0.21	0.37	0.41	0.47
CL-III 18 Hour – Test 2	0.21	0.38	0.42	0.46
Dolomitic Limestone Average	**0.20**	**0.36**	**0.40**	**0.45**
GG-III 18 Hour – Test 1	0.33	0.53	0.56	0.62
GG-II 18 Hour – Test 2	0.36	0.60	0.66	0.69
Crushed Granite Average	**0.35**	**0.57**	**0.61**	**0.66**

Note: [a] Corresponds to the compliance at the end of load application.

The crushed granite mixtures exhibited substantially increased compliance when compared to the dolomitic limestone mixtures. On average, the observed compliance for the crushed granite mixtures exceeded the dolomitic limestone mixtures by 58 percent. Similar conclusions follow for the compliance behavior by aggregate for the 24-hour tests shown in Figure 7-13 and Table 7-8. In this case, the average observed compliance for the crushed granite mixtures exceeded the dolomitic limestone mixtures by 55 percent.

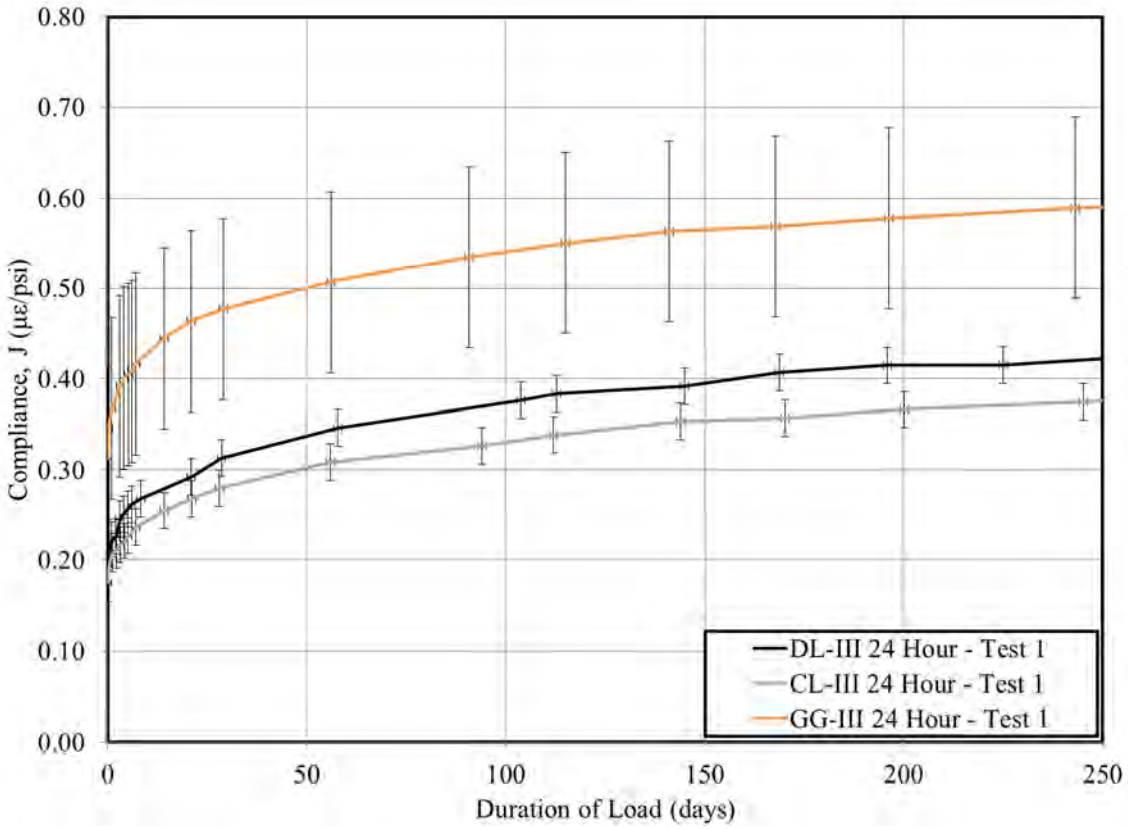

Figure 7-13: Compliance by Aggregate Type for 24 Hour Tests

Table 7-8: Effect of Aggregate Type on Compliance for 24 Hour Loading

Test ID	Initial Compliance[a], *J*, (με/psi)	60-Day Compliance, *J*, (με/psi)	120-Day Compliance, *J*, (με/psi)	250-Day Compliance, *J*, (με/psi)
DL-III 24 Hour - Test 1	0.20	0.35	0.38	0.42
CL-III 24 Hour – Test 1	0.17	0.31	0.34	0.38
Dolomitic Limestone Average	**0.19**	**0.33**	**0.36**	**0.40**
GG-III 24 Hour – Test 1	0.31	0.51	0.55	0.59
Crushed Granite Average	**0.31**	**0.51**	**0.55**	**0.59**

Note: [a] Corresponds to the compliance at the end of load application.

7.5.1.3 Effect of Age at Loading

In order to isolate the effect of age at loading on compliance behavior, each of the six candidate mixtures (unless already shown to be substantially similar as in the case of the DL-III and CL-III) must be independently evaluated using the previously determined experimental precisions. The compliance behavior for the crushed granite tests conducted at ages at loading of 18 and 24 hours are shown in Figure 7-14.

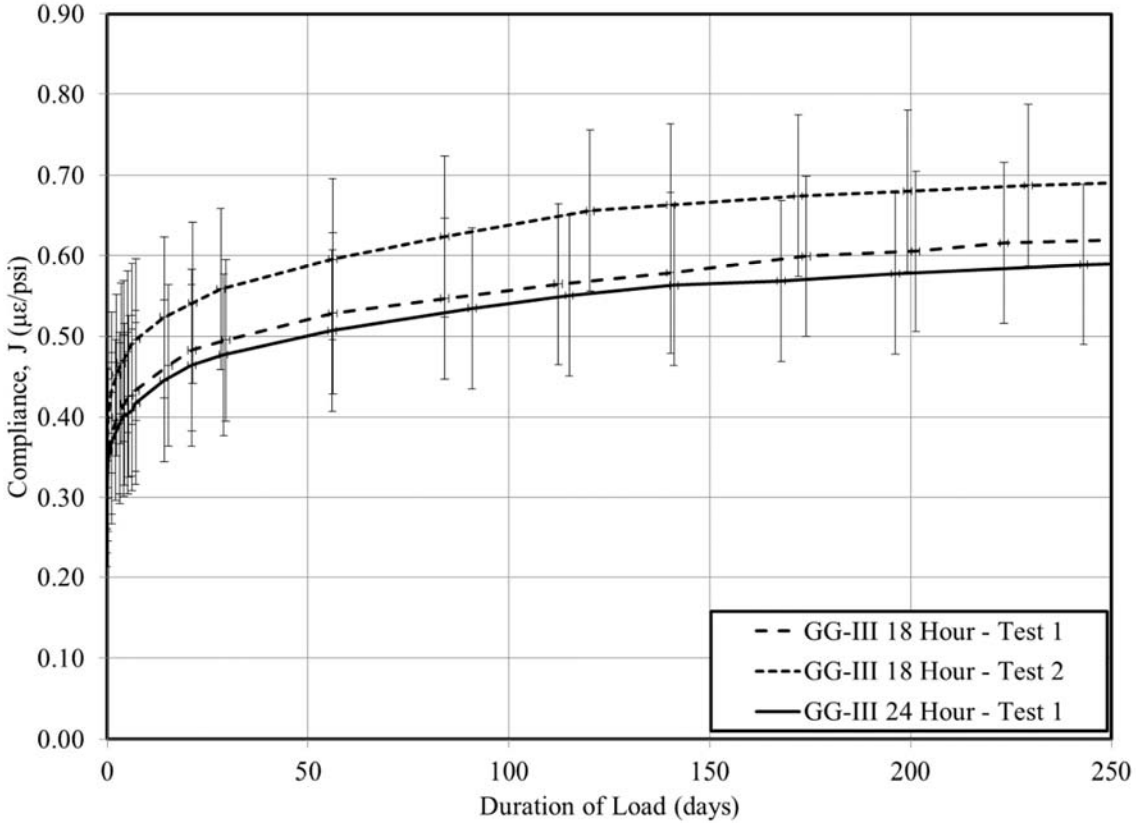

Figure 7-14: Compliance Behavior of Crushed Granite Tests by Age at Loading

As demonstrated by the overlapping error bands, there is no clearly discernable effect of age at loading on compliance behavior for the crushed granite mixtures included in this study. However, although still formally within the precision of the testing program, the 24-hour age at loading tended to exhibit slightly less compliance than the 18-hour ages. Similar conclusions are evident from the no-SCM dolomitic limestone tests shown in Figure 7-15. (Although the error bands of the CL-III 18-hour tests do not overlap the CL-III 24-hour tests, they do overlap the DL-III 24-hour test, which Section 7.5.1.2 affirmed was largely the same as the CL-III 24-hour test.)

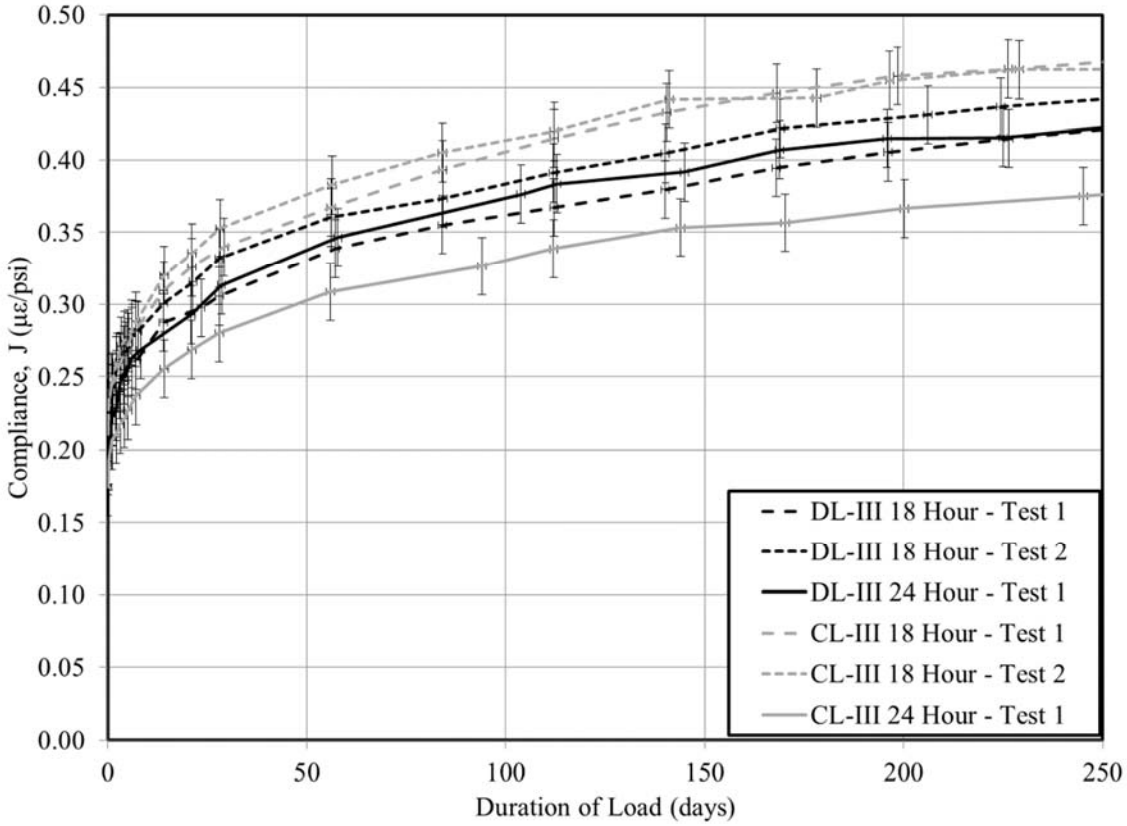

Figure 7-15: Compliance Behavior of No-SCM Variant Dolomitic Limestone Tests by Age at Loading

Again, despite the precision of the experimental program prohibiting the detection of a significant effect of varying ages at loading, all tests with exception of DL-III 18 Hour – Test 1 exhibited the trend that later ages of loading correspond to reduced compliance. Finally, the compliance behavior for each of the SCM-variant tests is shown in Figure 7-16. Similarly, no clear effect of age at loading is detected, although the trend of reduced compliance behavior for later ages at loading is again affirmed.

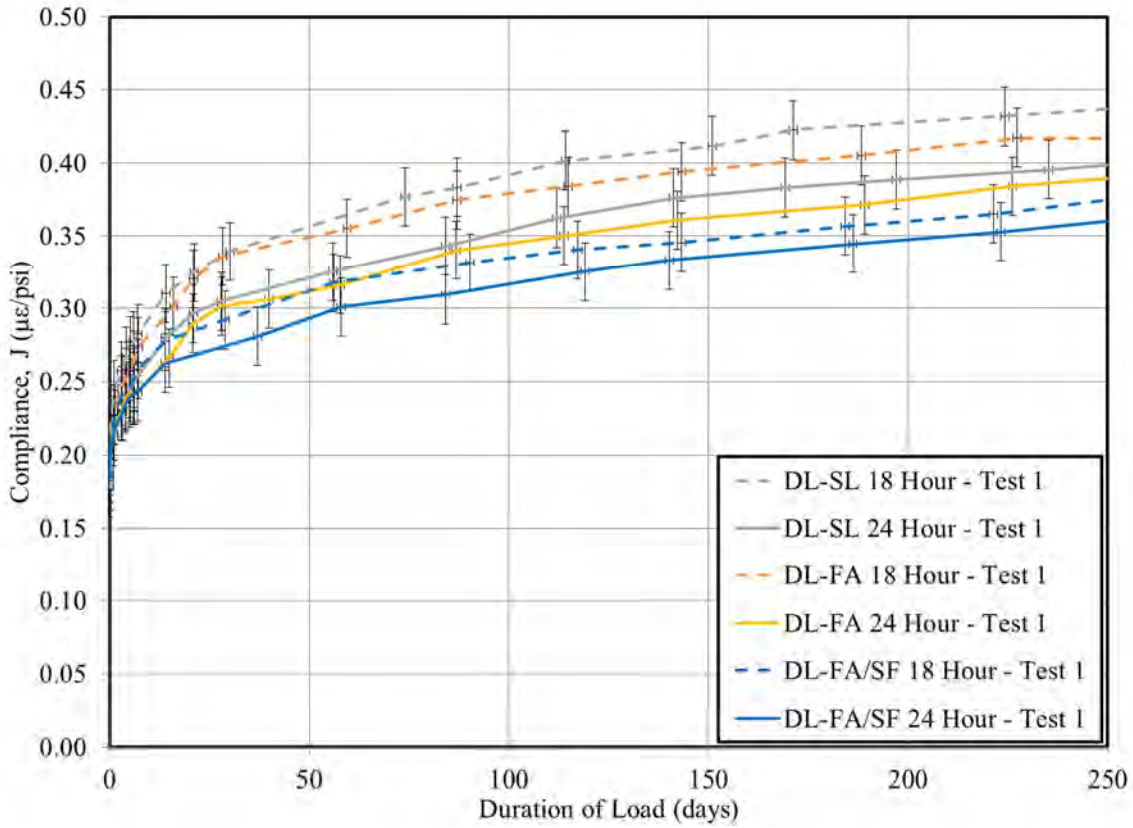

Figure 7-16: Compliance Behavior for SCM-Variant Dolomitic Limestone Tests by Age at Loading

Despite the precision of the creep and shrinkage testing conducted as part of this research effort being better than values included in the precision and bias statement of ASTM C512-02, an effect of age at loading on observed compliance was not detectable for a six hour time difference (18 hour versus 24 hour). In fact, the AASHTO 2014 model predicts a mere 3.5 percent decrease in the computed creep coefficient for an increase in age at loading from 18 hours to 24 hours. Similarly, the 2010 Model Code predicts a 2.9 percent decrease in the computed creep coefficient (for a corresponding shift in adjusted equivalent age from 7.0 to 9.0 days).

7.5.1.4 Effect of Supplementary Cementing Materials (SCMs)

A similar analysis was conducted to explore the potential effect of the use of supplementary cementing materials (SCMs) on compliance, with results shown in Figure 7-17.

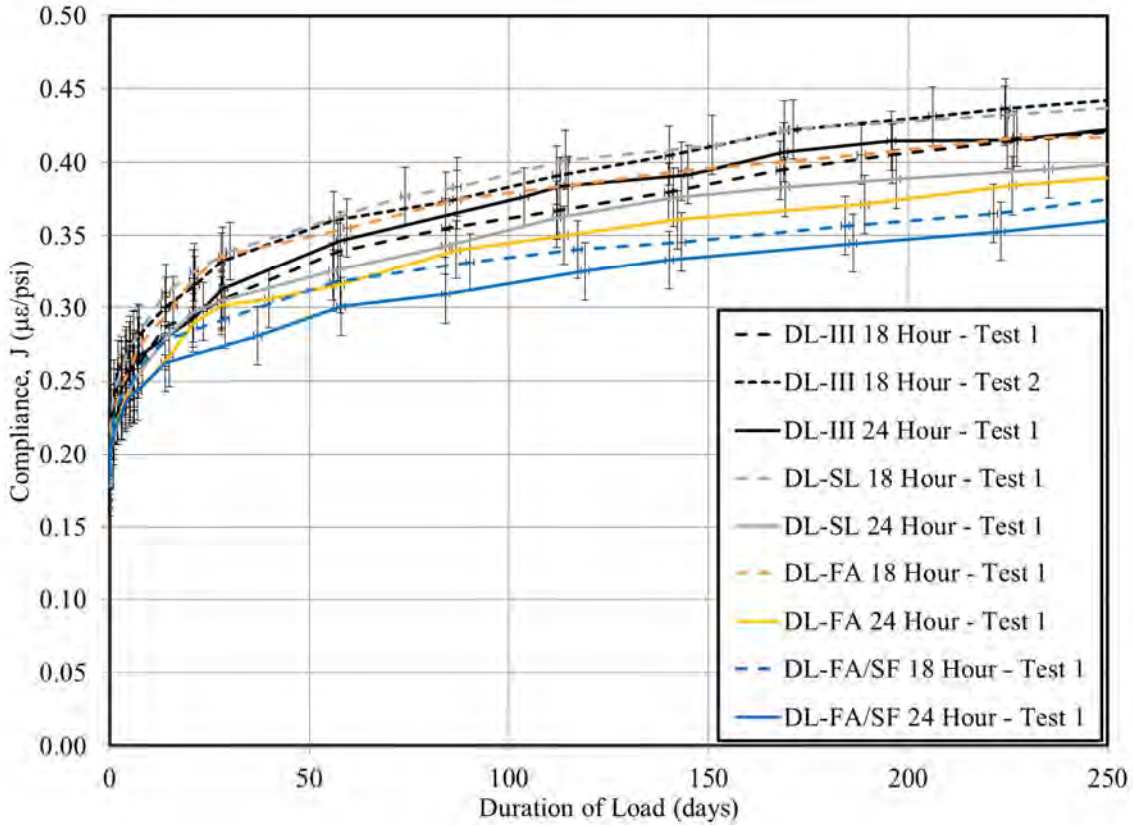

Figure 7-17: Compliance Behavior for All Dolomitic Limestone Tests by Age at Loading

As shown, the DL-SL and DL-FA tests are likely not significantly different from the no-SCM variant experimental control tests. These conclusions are largely in agreement with previous findings, (Section 7.2.2.2) which noted that the use of slag cement tends to have a negligible effect on total observed creep behavior and the influence of fly ash varies by previous researcher. However, despite approaching limits of experimental precision, the overall average of the DL-FA tests exhibited less creep than the overall average of the DL-III tests, perhaps suggesting a small reduction in creep behavior for the fly ash substitution percentage (15 percent) utilized in this research effort. In contrast to the above discussion, tests of the ternary mixture, DL-FA/SF, exhibited a clearly reduced magnitude of compliance through the testing period. Tabulated values are displayed in Table 7-9.

Table 7-9: Effect of SCM Usage on Compliance

Test ID	Initial Compliance[a], *J*, (με/psi)	60-Day Compliance, *J*, (με/psi)	120-Day Compliance, *J*, (με/psi)	250-Day Compliance, *J*, (με/psi)
DL-III 18 Hour - Test 1	0.19	0.34	0.37	0.42
DL-III 18 Hour - Test 2	0.19	0.36	0.39	0.44
DL-III 24 Hour - Test 1	0.20	0.35	0.38	0.42
No-SCM Variant Average	**0.19**	**0.35**	**0.38**	**0.43**
DL-FA/SF 18 Hour – Test 1	0.19	0.32	0.34	0.38
DL-FA/SF 24 Hour – Test 1	0.18	0.30	0.33	0.36
Fly Ash / Silica Fume Ternary Average	**0.19**	**0.31**	**0.34**	**0.37**

Note: [a] Corresponds to the compliance at the end of load application.

From the data presented in Table 7-9, the use of fly ash and silica fume in ternary mixtures in the substitution percentages utilized in this study (18 percent and 8 percent, respectively) was associated with an average reduction of between 9-12 percent in observed compliance behavior. This conclusion is in agreement with the previous work of Brooks (1999) and Khatri and Sirivivatnanon (1995), who also observed a net reduction in creep behavior for mixtures using silica fume in percent replacements less than 15 percent.

7.5.1.5 Application of Candidate Prediction Models

The three candidate creep prediction models previously described in Section 7.2.4 were implemented for each test to generate predictions of creep coefficients using the assumptions and inputs as summarized in Table 7-10. Then, the initial elastic strain was computed for each test using the measured value of the induced creep frame load and (2) the measured value of elastic modulus at the time of loading as tested by ASTM C469-10. Finally, using the computed initial elastic strain and creep coefficient, compliance was computed for each test. Typical results for a dolomitic limestone test are shown in Figure 7-18, with Mante (2016) containing a similar plot for each of the 15 tests.

Table 7-10: Creep Prediction Model Summary of Inputs

AASHTO 2014		ACI 209		Model Code 2010	
Input	***Justification***	***Input***	***Justification***	***Input***	***Justification***
Relative humidity = 50 percent	ASTM C512-02	Relative humidity = 50 percent	ASTM C512-02	Relative humidity = 50 percent	ASTM C512-02
Volume-to-surface ratio = 1.5	Computed excluding cylinder ends not exposed to atmosphere	Volume-to-surface ratio = 1.5	Computed excluding cylinder ends not exposed to atmosphere	Cement and temperature –adjusted age at loading	Table 7-1
Chronological age at loading	Table 7-1	Slump = 0.5 in.	Assumed pre-admixture slump in agreement with Keske (2014) and Ellis (2012)	28-day measured compressive strength	Table 7-3
Compressive strength at loading	Table 7-3	Sand-to-aggregate weight ratio	Computed from Table 6-1	Notional size = 76.2 mm.	Computed by MC 2010 provisions.
		Cement factor	Assumed total powder content , Table 6-1	Rapid-hardening high-strength cement assumed	In accordance with Keske (2014) and recommendations of ACI 209 (2008).
		Air content	Table 7-2		

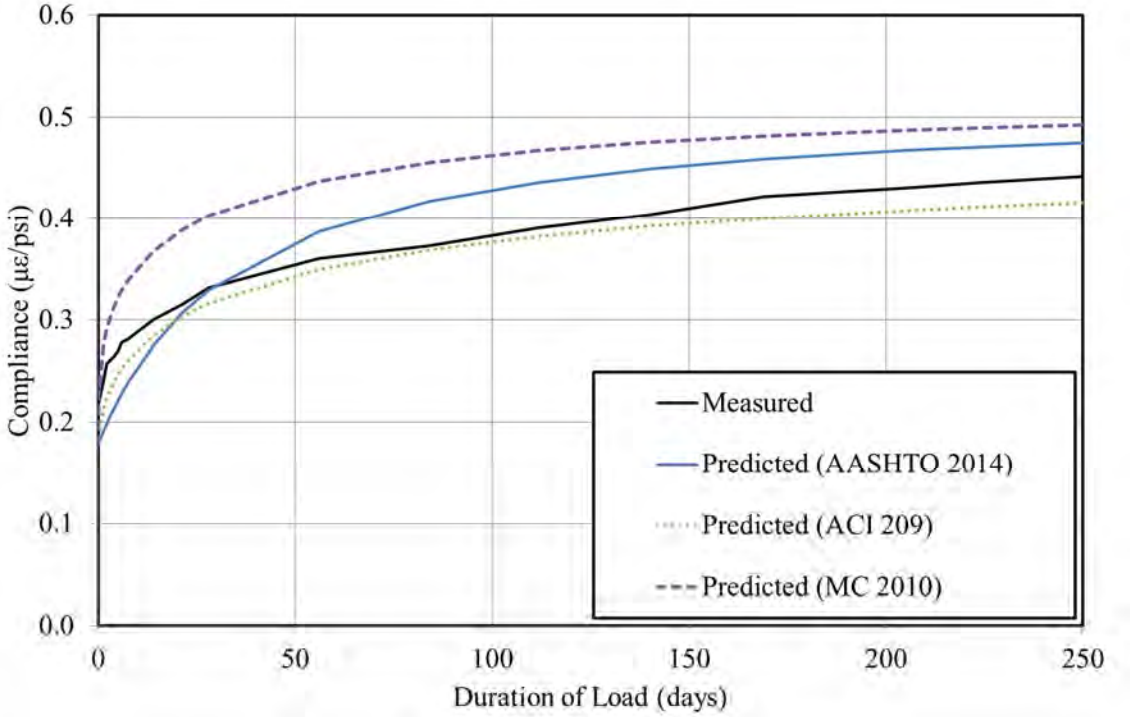

Figure 7-18: Comparison between Experimental Results and Unadjusted Prediction Models for Compliance of a Typical Dolomitic Limestone Test.

In general, for dolomitic limestone concrete mixtures, it appears that the MC 2010 prediction model most frequently tends to over-predict compliance for early ages (less than 100 days), whereas, the AASHTO 2014 and ACI 209 models show relatively good agreement with experimental results at these early ages. For later ages (up to 250 days), the three prediction models yield largely similar results, approaching the precision of the experimental testing conducted in this study. The relative accuracy of each prediction model is explored systematically in the following section.

7.5.1.6 Relative Goodness-of-Fit

As noted by ACI 209.2R (2008), there exists no consensus as to a preferred analytical technique for evaluating the relative goodness-of-fit of prediction models to measured data. Due to the nonlinear measurement timing required by ASTM C512, conventional methods such as the sum-of-squares error are prone to excessive bias and, therefore, are not preferred. In this section, a technique proposed by Bazant and Panula, as summarized in Appendix B of ACI 209.2R (2008), is used as the preferred scalar metric of goodness-of-fit. Previous similar work by Keske (2014) also utilized this analysis technique.

The basic premise of the analytical technique employed herein is the computation of a time-weighted coefficient of variation, denoted as ϖ_j, intended to evaluate the accuracy of the prediction models in terms of the relative sizes of the squared residuals and outcome values. By grouping data points into logarithmic decades (0 to 9.9 days, 10 to 99.9 days, etc.) and assigning relative weight to each decade based on the number of measurements, the potential for bias from a disproportionate number of early-age measurements is minimized. In general, lower ϖ_j values correspond to improved correlation between predicted and measured data, with a perfect correlation represented by $\varpi_j = 0$ percent. For reference, the range of ϖ_j values reflected in ACI 209.2R (2008) for various endorsed creep prediction models (as compared to experimental compliance data from the RILEM database) is from 23 to 58 percent. Therefore, any ϖ_j value less than 23 percent for compliance reflects an exceptional fit. The details of the application of this procedure are given in Appendix B of ACI 209.2R (2008). Computed values for the coefficient of variation, ϖ_j, for each test of this study are shown in Table 7-11, with the most accurate prediction model noted in bold for each test. The overall coefficient of deviation, ϖ_{BP}, proposed by ACI 209.2R (2008) for all tests within this study is also shown in Table 7-11.

Table 7-11: Relative Goodness-of-Fit of Unadjusted Candidate Prediction Models to Experimental Data for Compliance

	Coefficient of Variation, ϖ_j (%)		
Test ID	**AASHTO 2014**	**ACI 209**	**Model Code 2010**
DL-III 18 Hour - Test 1	13.5	**3.5**	23.0
DL-III 18 Hour - Test 2	11.6	**6.2**	18.6
DL-III 24 Hour - Test 1	**12.2**	13.3	14.0
CL-III 18 Hour - Test 1	**10.1**	11.7	14.7
CL-III 18 Hour - Test 2	**11.4**	13.5	16.0
CL-III 24 Hour - Test 1	10.7	**3.8**	27.7
GG-III 18 Hour - Test 1	13.3	**7.0**	22.5
GG-III 18 Hour - Test 2	14.6	**11.1**	17.2
GG-III 24 Hour - Test 1	12.1	**7.8**	15.6
DL-SL 18 Hour - Test 1	18.3	21.3	**5.0**
DL-SL 24 Hour - Test 1	10.6	**9.8**	11.9
DL-FA/SF 18 Hour - Test 1	15.9	**6.1**	26.9
DL-FA/SF 24 Hour - Test 1	15.2	**7.9**	29.2
DL-FA 18 Hour - Test 1	11.0	11.1	**10.0**
DL-FA 24 Hour - Test 1	9.5	**4.6**	18.9
Overall Average	12.7	**9.3**	18.1
Overall Coefficient of Variation, ϖ_{BP} (%)	12.9	**10.3**	19.2

As shown, all unadjusted creep prediction models reflect fairly good fits of experimental results, with a maximum ϖ_j value of 29.2 percent. For the tests conducted in this project, the unadjusted ACI 209 creep prediction model tended to yield the most accurate results with an overall coefficient of variation, ϖ_{BP}, of 10.3 percent, followed next by the AASHTO 2014 and Model Code 2010 models with overall coefficients of variation of 12.9 and 19.2 percent, respectively.

7.5.1.7 Optimization of Prediction Models to Measured Data

To optimize each prediction model to reflect the results of each test, a creep coefficient modification factor was introduced into the prediction models. For each model and test, a value for the creep coefficient modification factor was determined iteratively using a GRG nonlinear solver to minimize the corresponding coefficient of variation, ϖ_j. This analysis method essentially minimized the difference between predicted and measured compliance by means of varying the predicted creep coefficient.

Computed creep coefficient modification factors for each test and candidate prediction model are summarized in Table 7-12.

Table 7-12: Creep Coefficient Modification Factors to Calibrate Candidate Prediction Equations to Experimental Data

	Modification Factor		
Test	**AASHTO 2014**	**ACI 209**	**Model Code 2010**
DL-III 18 Hour - Test 1	0.83	1.03	0.70
DL-III 18 Hour - Test 2	0.89	1.09	0.75
DL-III 24 Hour - Test 1	1.12	1.27	0.81
CL-III 18 Hour - Test 1	1.01	1.23	0.81
CL-III 18 Hour - Test 2	1.00	1.28	0.79
CL-III 24 Hour - Test 1	0.85	0.94	0.65
GG-III 18 Hour - Test 1	0.89	1.01	0.69
GG-III 18 Hour - Test 2	0.95	1.15	0.76
GG-III 24 Hour - Test 1	0.99	1.03	0.77
DL-SL 18 Hour - Test 1	1.24	1.48	1.04
DL-SL 24 Hour - Test 1	1.07	1.18	0.84
DL-FA/SF 18 Hour - Test 1	0.80	0.96	0.65
DL-FA/SF 24 Hour - Test 1	0.80	0.89	0.62
DL-FA 18 Hour - Test 1	1.02	1.21	0.86
DL-FA 24 Hour - Test 1	0.93	1.02	0.73
Overall Average	**0.96**	**1.12**	**0.76**
Overall Range	**0.44**	**0.59**	**0.42**
Average of Mixtures Similar to Current Regional Mixtures (DL-SL+DL-FA/SF)	0.98	1.13	0.79
Overall Average Excluding DL-FA/SF	0.98	1.15	0.78
Average for DL-FA/SF	0.80	0.93	0.64

As shown, each of the three candidate prediction models requires different average creep coefficient modification factors to provide a best fit to experimental data. The overall average modification factor for the AASHTO 2014 model is closest to 1.0. The Model Code 2010 model requires an overall average factor of 0.76 to yield most accurate results, while the ACI 209 model requires an average factor of 1.12. An average modification factor is also computed including only those mixtures most similar to current ALDOT precast, prestressed concrete mixtures (DL-SL and DL-FA/SF), although, the modification factor values similar to the overall averages for each model. Also computed are average adjustment factors after segregating the ternary mixture due to the significant difference found in Section 7.5.1.4. Here, the

overall average for the AASHTO 2014 model creep coefficient modification factor is closer to 1.0, while the suggested correction factor for the ternary mixture is 0.80.

For each test included in this study, the creep coefficient modification factors of Table 7-12 were used to re-compute compliance (i.e. a factor of 0.83 was applied to the creep coefficient predicted using the AASHTO 2014 model with inputs from DL-III 18 hour – Test 1). Graphical comparisons between these adjusted prediction models and experimental data are included in Mante (2016) for each test, with a typical result for dolomitic limestone mixtures shown below in Figure 7-19.

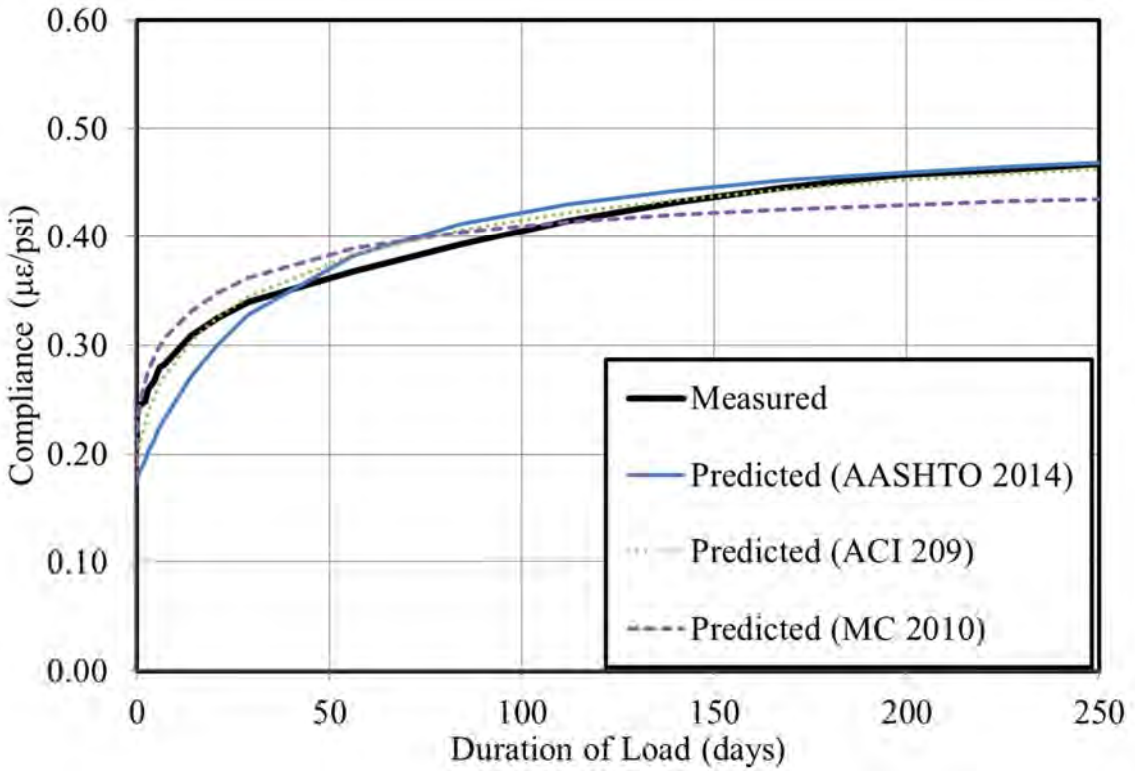

Figure 7-19: Comparison between Experimental Results and Adjusted Prediction Models for Compliance of a Typical Dolomitic Limestone Test.

Similarly to those computed in Section 7.5.1.6 for unadjusted prediction models, revised coefficients of variation for the adjusted models for each test are summarized in Table 7-13.

Table 7-13: Relative Goodness-of-Fit of Adjusted Candidate Prediction Models to Experimental Data

	Coefficient of Variation, ϖ_j (%)		
Test ID	**AASHTO 2014**	**ACI 209**	**Model Code 2010**
DL-III 18 Hour - Test 1	8.4	**3.3**	6.0
DL-III 18 Hour - Test 2	9.8	**4.2**	4.9
DL-III 24 Hour - Test 1	10.7	5.5	**5.3**
CL-III 18 Hour - Test 1	10.0	**5.0**	6.4
CL-III 18 Hour - Test 2	11.4	5.1	**4.5**
CL-III 24 Hour - Test 1	6.3	**2.4**	5.5
GG-III 18 Hour - Test 1	11.9	7.0	**3.5**
GG-III 18 Hour - Test 2	14.4	8.9	**3.7**
GG-III 24 Hour - Test 1	12.0	7.7	**3.8**
DL-SL 18 Hour - Test 1	14.3	8.2	**4.3**
DL-SL 24 Hour - Test 1	10.0	**4.7**	4.8
DL-FA/SF 18 Hour - Test 1	10.5	5.7	**3.2**
DL-FA/SF 24 Hour - Test 1	9.3	4.9	**3.9**
DL-FA 18 Hour - Test 1	11.0	5.5	**3.7**
DL-FA 24 Hour - Test 1	8.8	**4.5**	4.8
Overall Average	10.6	5.5	**4.6**
Overall Coefficient of Variation, ϖ_{BP} (%)	10.8	5.8	**4.7**

As demonstrated by the lowest average coefficient of variation, ϖ_j, the adjusted Model Code 2010 method provides the best fit of experimental data. This is somewhat expected as this model is by far the most complex of the three considered models. Next most accurate is the ACI 209 method, which is the second most complex model, requiring certain concrete mixture-specific inputs (i.e. air content and slump). Finally, the AASHTO 2014 model exhibited the least accurate results of the adjusted models, with an accuracy only slightly improved as compared to the unadjusted AASHTO 2014 model.

7.5.1.8 Design Recommendations

ACI 209.2R (2008) notes that measured creep testing results should, at best, be expected to match prediction models within ±20 percent, while the AASHTO LRFD Bridge Design Specifications (2014) suggest agreement between measured and predicted responses within ±50 percent is typical. Given that agreement of all three unadjusted candidate models is well within the expected range of variation, it can be concluded that the unadjusted creep prediction models provide acceptable agreement for the

purposes of camber prediction during initial girder design. Of the unadjusted models, the AASHTO LRFD model is preferable due to its agreement with the experimental data of this study and the simplicity of implementation during the girder design phase. When more refined estimates of girder creep development are desired after a concrete mixture selection is made, (i.e. producer verifications of camber predictions) use of the appropriate creep coefficient modification factor, as summarized in Table 7-14, is recommended.

Table 7-14: Design Recommendations for Creep Coefficient Modification Factors

	Proposed Creep Coefficient Modification Factors	
Prediction Model	**When ternary mixtures are used**	**For all other mixture compositions (or unknown)**
AASHTO LRFD	**0.80**	1.00
ACI 209[b]	**0.95**	**1.15**
Model Code 2010[c]	**0.65**	**0.80**

[a] = Ternary mixtures refer to those mixtures containing fly ash and silica fume.
[b] = Requires mixture-specific input parameters including fine aggregate percent, slump, air content.
[c] = Requires estimate of adjusted maturity at the time of prestress transfer.

Implementation of the ACI 209 model or Model Code 2010 with creep coefficient modification factors as summarized in Table 7-14 yield predictions of similar accuracy and therefore, the prediction model choice is left to designer preference.

7.5.2 Cylinder and Rectangular Prism Shrinkage

This section presents and analyzes the results of the shrinkage testing including both shrinkage of cylindrical specimens (conducted in accordance with ASTM C512-02) and concrete rectangular prisms (in accordance with ASTM C157-08). As previously discussed, the relative influence of concrete shrinkage on the camber of prestressed concrete girders is significantly less than the influence of creep. Accordingly, the discussions and analysis of this section are slightly more abbreviated than those of Section 7.5.1, with less effort devoted to identifying trends in results approaching the limits of experimental precisions. The purpose of the shrinkage testing performed on cylindrical specimens was primarily to provide a means to decouple the effects of creep behavior from early-life temperature effects and shrinkage behavior—not necessary to provide comparisons among experimental tests and variables. For this purpose, the rectangular prism shrinkage testing efforts provide more repeatable and accurate results as is evident in the following sections.

7.5.2.1 Presentation of Measured Results

The full data sets representing the shrinkage testing conducted in this effort are shown in Figures 7-20 and 7-21 for cylindrical specimens and rectangular prismatic specimens, respectively. For cylindrical specimens, the horizontal axis (time) reflects duration of load (days) because readings were taken during creep testing and a small portion of the shrinkage occurred prior to first reading. For rectangular shrinkage prism results, the horizontal axis reflects actual duration of drying (days) because the first measurement of shrinkage was taken immediately upon removal from curing conditions.

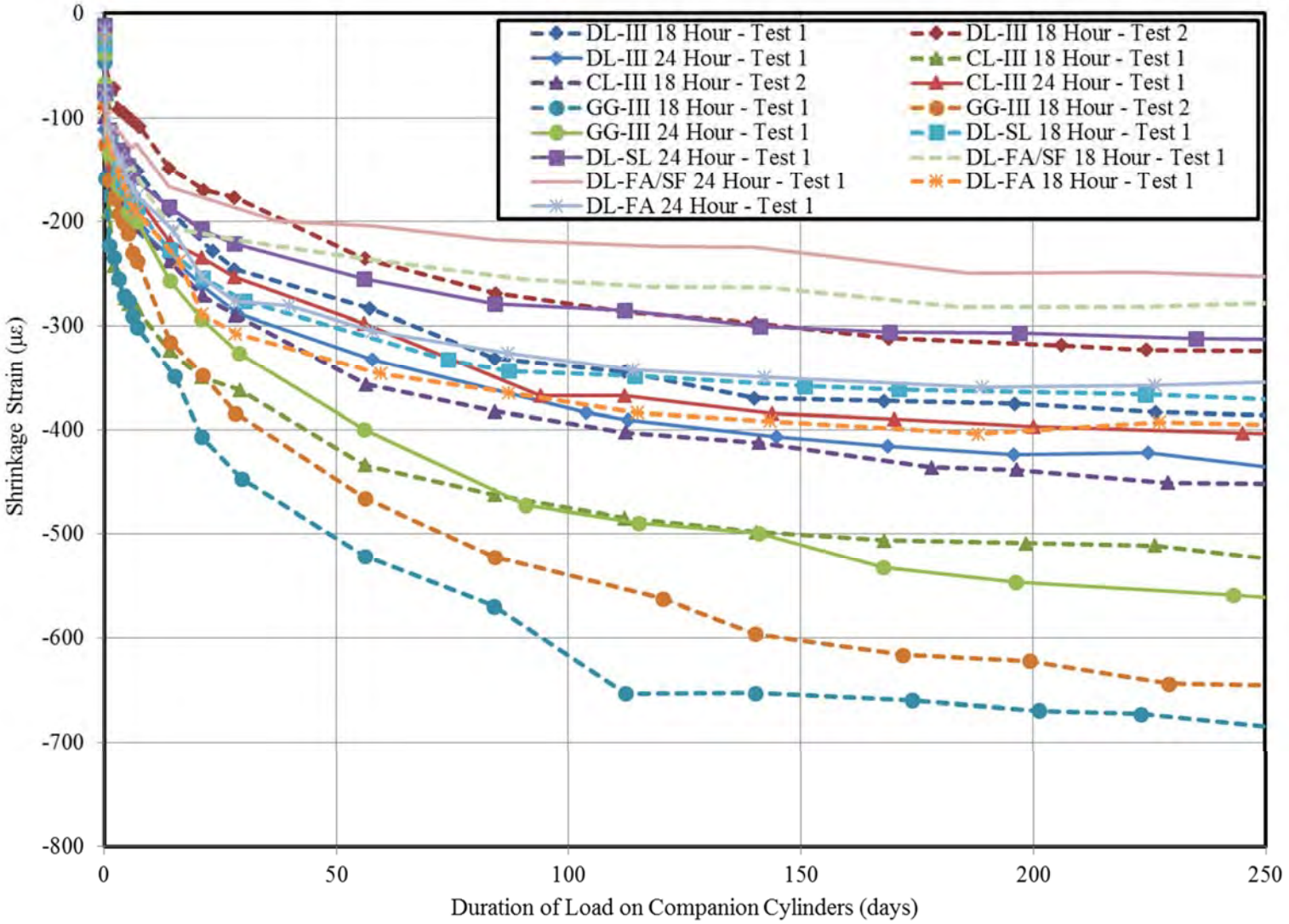

Figure 7-20: Shrinkage Test Results for Cylindrical Specimens

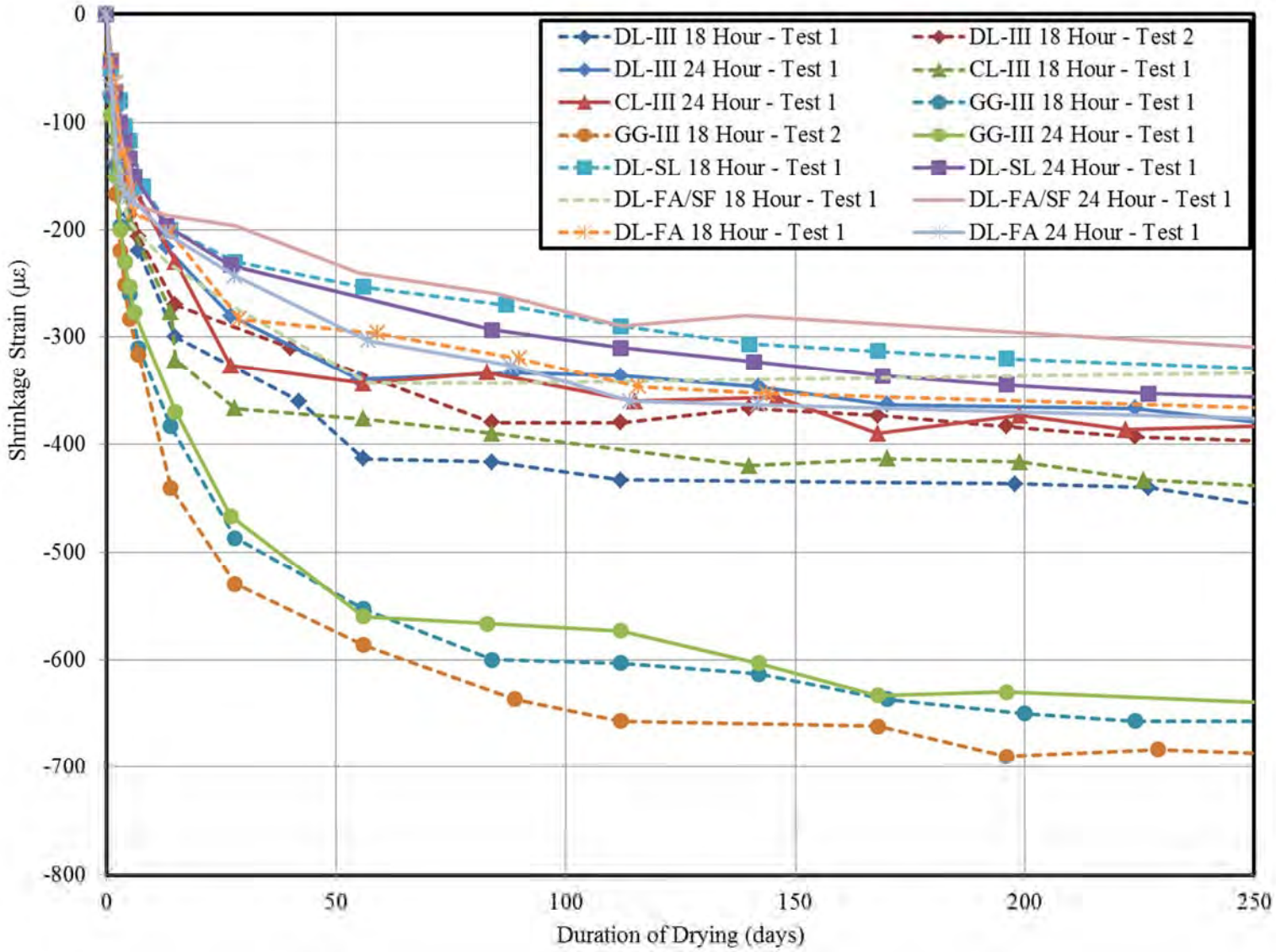

Figure 7-21: Shrinkage Test Results for Rectangular Prismatic Specimens

Dashed lines in Figures 7-20 and 7-21 denote 18-hour tests. As demonstrated by the more distinct clustering of repeated tests in Figure 7-21 than in Figure 7-20, there appears to be more variability in the testing results for cylindrical specimens as compared to rectangular prismatic specimens, likely due to (1) the unavoidable inclusion of early thermal effects in benchmark cylindrical specimen readings and (2) the use of different measuring equipment (*DEMEC* gage versus standard length comparator) for each type of specimen. The following sections describe analyses aimed at identifying significant trends among the three key variables of interest (coarse aggregate type, age at loading, and use of SCMs). Analytical procedures are similar to those of Section 7.5.1 except the appropriate experimental precisions as determined in Sections 7.4.2 and 7.4.3 are used to identify significant trends.

7.5.2.2 Effect of Coarse Aggregate Type

Similar to the previous compliance analysis, the no-SCM variants were compared for each of two ages at loading, independently. Errors bands in this analysis use an average experimental precision value of ±70 με. Cylinder shrinkage testing results, grouped by coarse aggregate type, are shown for the 18-hour age at loading in Figure 7-22. While there appears to be no clear difference between the DL-III and CL-III tests, both CL-III 18-hour tests are located below the DL-III 18-hour tests, possibly suggesting an increased shrinkage tendency. The GG-III mixtures appear to demonstrate more shrinkage as compared to the DL-III and CL-III mixtures, although the difference approaches the experimental precision.

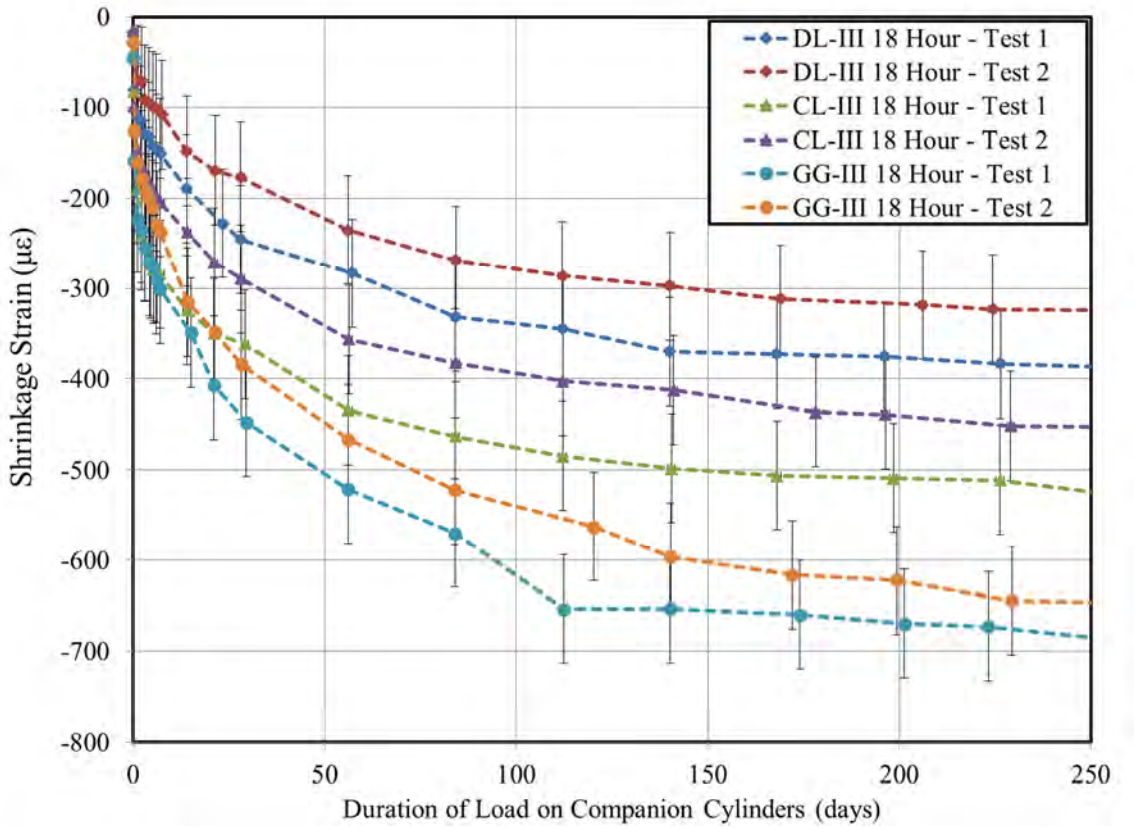

Figure 7-22: Cylinder Shrinkage by Aggregate Type for 18 Hour Tests

Similar results for rectangular prism specimens are shown in Figure 7-23. Here, no differences are detectable among DL-III and CL-III tests, although a significant increased shrinkage tendency is discovered for the GG-III tests when compared to dolomitic limestone tests. Identical results are found when considering shrinkage results from the 24-hour age at loading, as shown in Figures 7-24 and 7-25 for cylinders and rectangular prisms, respectively. Tabulated values used to quantify these qualitatively-identified trends are shown in Table 7-15.

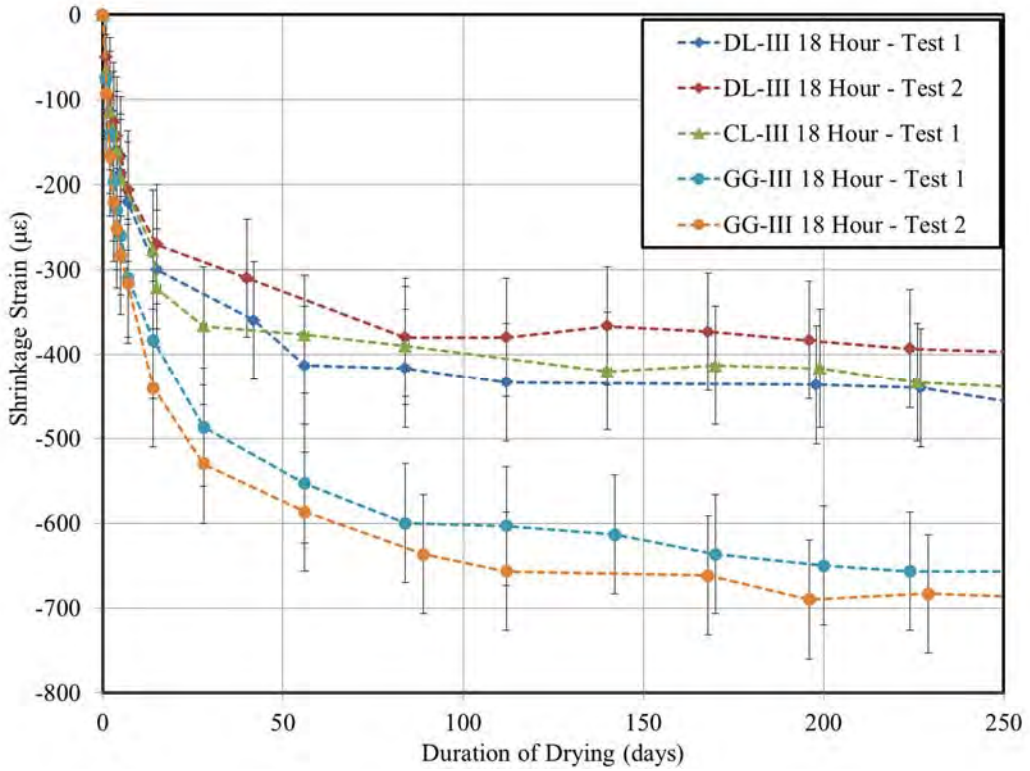

Figure 7-23: Rectangular Prism Shrinkage by Aggregate Type for 18 Hour Tests

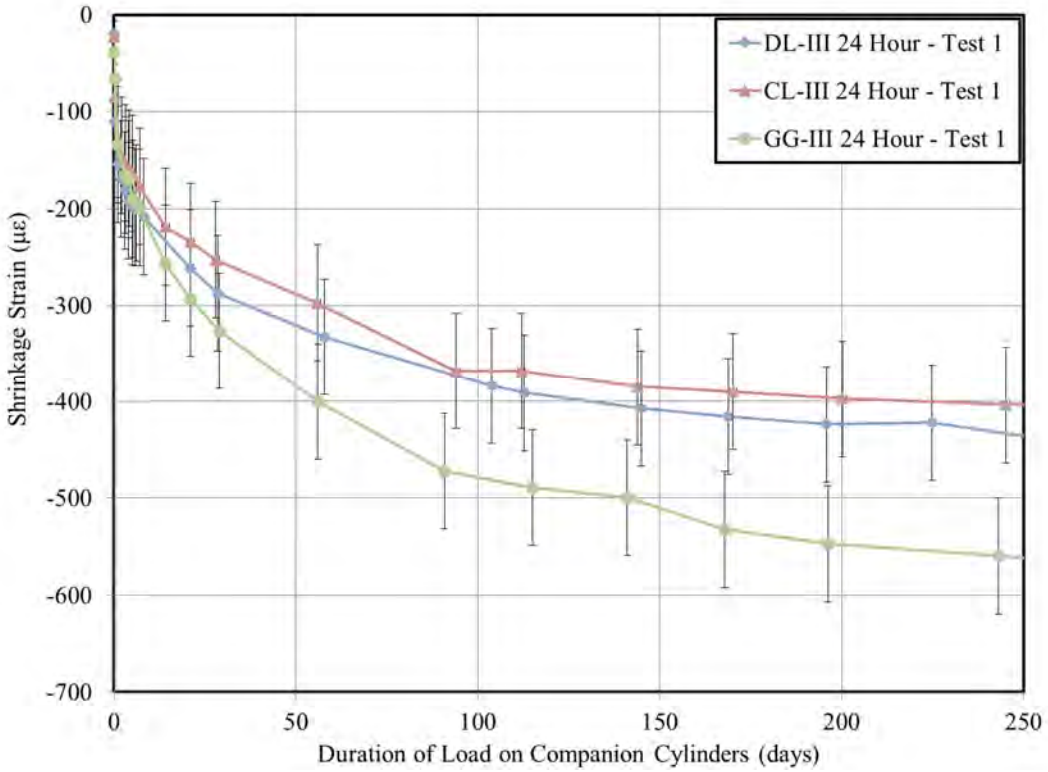

Figure 7-24: Cylinder Shrinkage by Aggregate Type for 24 Hour Tests

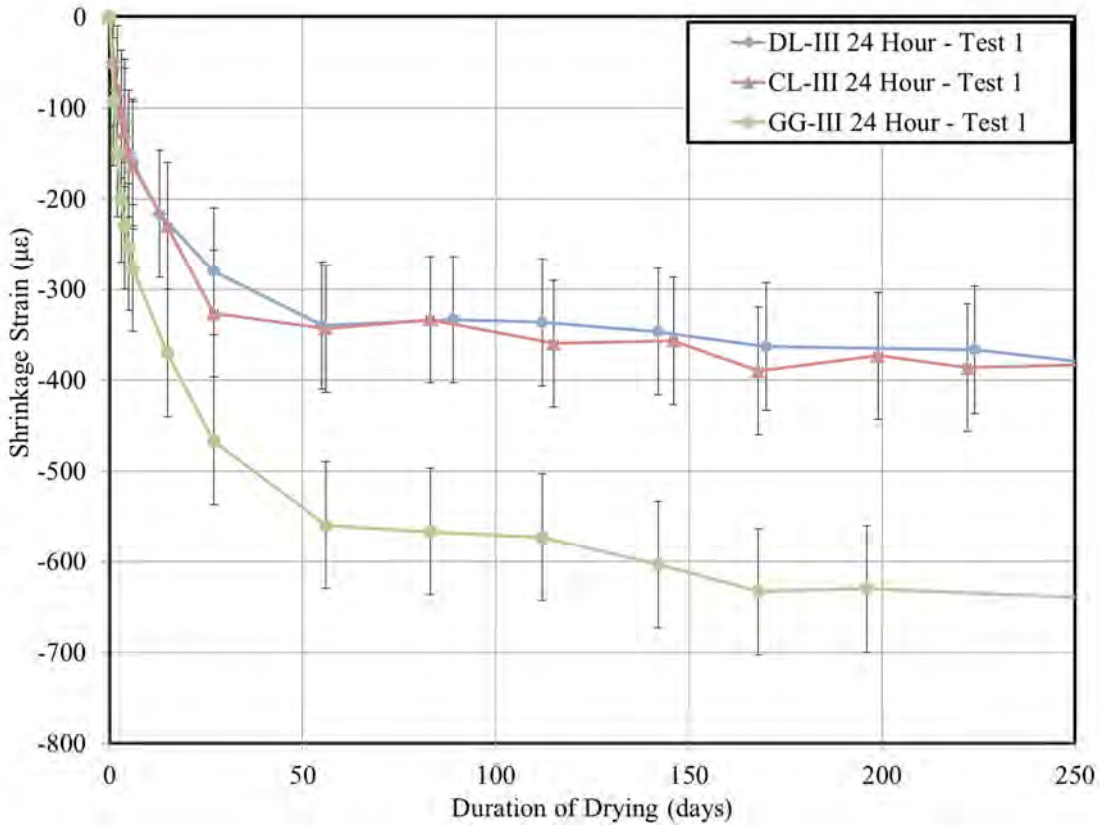

Figure 7-25: Rectangular Prism Shrinkage by Aggregate Type for 24 Hour Tests

Table 7-15: Effect of Aggregate Type on Shrinkage Behavior for 18 and 24 Hour Tests

Test ID	Initial[a] (or 1-Day) Shrinkage, (με)		60-Day Shrinkage, (με)		120-Day Shrinkage, (με)		250-Day Shrinkage, (με)	
	Cylinder	Prism[b]	Cylinder	Prism[b]	Cylinder	Prism[b]	Cylinder	Prism[b]
DL-III 18 Hour – Test 1	-27	-73	-288	-414	-352	-433	-386	-457
DL-III 18 Hour – Test 2	-18	-50	-239	-342	-289	-376	-324	-397
CL-III 18 Hour – Test 1	-39	-67	-438	-379	-488	-409	-525	-438
CL-III 18 Hour – Test 2	-16	n/a	-361	n/a	-405	n/a	-452	n/a
Dolomitic Limestone 18 Hour Average	**-25**	**-63**	**-332**	**-378**	**-384**	**-406**	**-422**	**-431**
GG-III 18 Hour – Test 1	-46	-77	-528	-560	-654	-606	-685	-657
GG-III 18 Hour – Test 2	-29	-93	-474	-593	-563	-658	-646	-687
Crushed Granite 18 Hour Average	**-38**	**-85**	**-501**	**-577**	**-609**	**-632**	**-666**	**-672**
DL-III 24 Hour – Test 1	-20	-50	-335	-339	-395	-340	-436	-380
CL-III 24 Hour – Test 1	-23	-50	-304	-341	-372	-359	-404	-384
Dolomitic Limestone 24 Hour Average	**-22**	**-50**	**-320**	**-340**	**-384**	**-350**	**-420**	**-382**
GG-II 24 Hour – Test 1	-38	-93	-408	-561	-491	-581	-562	-640
Crushed Granite 24 Hour Average	**-38**	**-93**	**-408**	**-561**	**-491**	**-581**	**-562**	**-640**

[a] = For cylindrical specimens, initial shrinkage reflects predominately cooling effects during loading. For prismatic specimens, 1-day shrinkage values are reported.

[b] = Prism specimens received uniform curing treatment and timing to exposure regardless of the age at loading designation of the associated test.

For the 18-hour age at loading, the GG-III cylindrical specimens exhibited a 50 percent net increase in shrinkage when compared to the dolomitic limestone tests, while the rectangular prismatic specimens exhibited a similar 53 percent increase. For the 24-hour age at loading, the GG-III cylindrical specimens showed roughly 40 percent net increased shrinkage as compared to dolomitic limestone specimens, whereas the GG-III prismatic specimens exhibited a substantially greater increase of over 70 percent. These results are generally in agreement with the discussion of Section 7.2.3.1 affirming that less stiff aggregates allow more shrinkage, likely due to their reduced ability to restrain the shrinkage tendency of the cement paste.

7.5.2.3 Effect of Age at Loading

When analyzing results for the effect of age at loading, it is important to recall that rectangular prism specimens received uniform curing treatment and duration regardless of the age at loading designation of the associated test. Therefore, the effect of age at loading is only able to be examined through analysis of cylindrical specimen results. Cylinder shrinkage results, grouped by age at loading, are shown for the dolomitic limestone no-SCM variants in Figure 7-26. As shown, no discernable effect of age at loading is readily apparent, as the 18-hour tests for CL-III tests tend to exhibit increased shrinkage as compared to 24-hour tests, with the opposite trend occurring for DL-III tests. Conversely, cylinder shrinkage results for the GG-III tests and dolomitic limestone SCM-variant tests (shown in Figures 7-27 and 7-28, respectively) tend to suggest that the 18-hour tests may exhibit slightly increased shrinkage as compared to 24-hour tests. However, experimental precision prohibits the identification of a clear trend in this case.

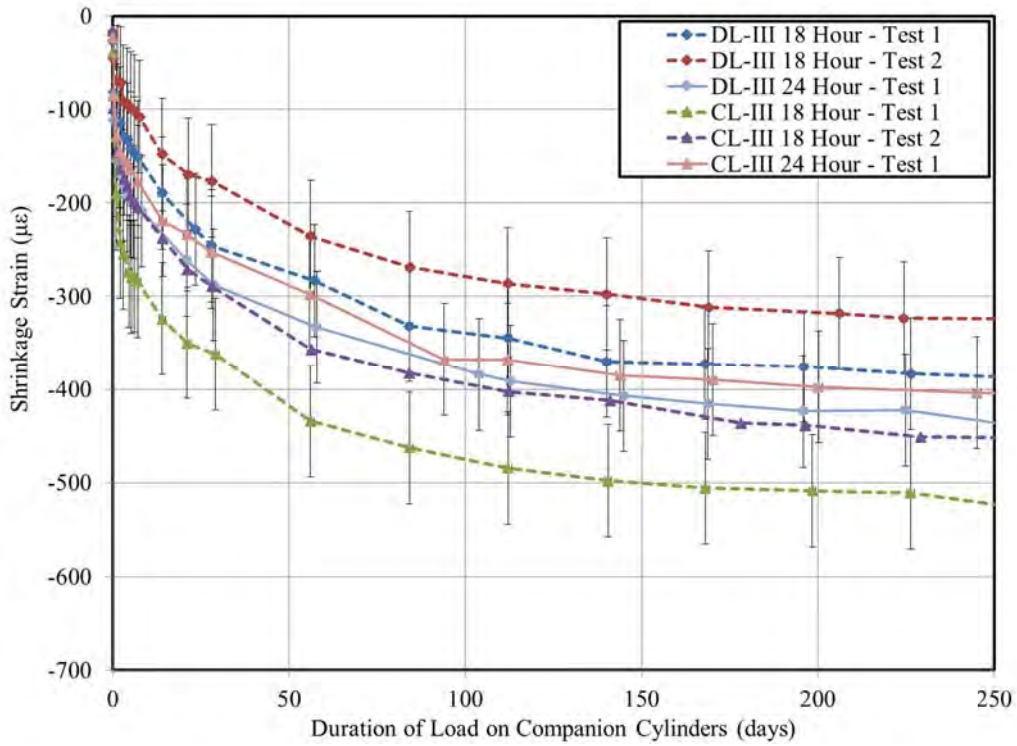

Figure 7-26: Cylinder Shrinkage Behavior of No-SCM Variant Dolomitic Limestone Tests by Age at Loading

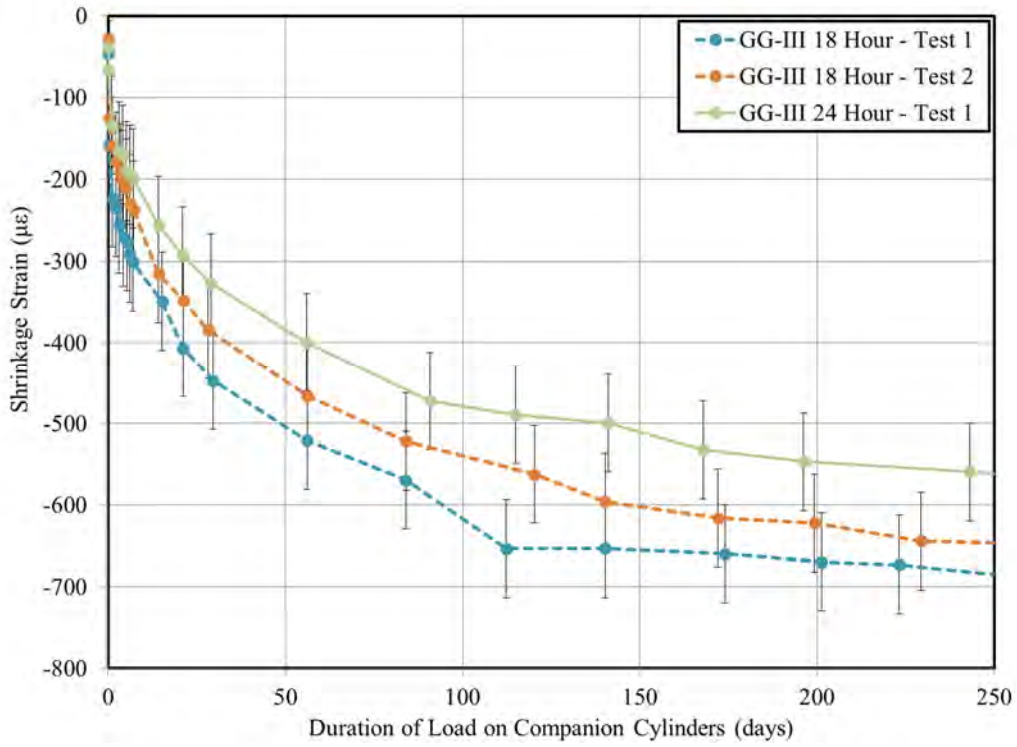

Figure 7-27: Cylinder Shrinkage Behavior of Crushed Granite Tests by Age at Loading

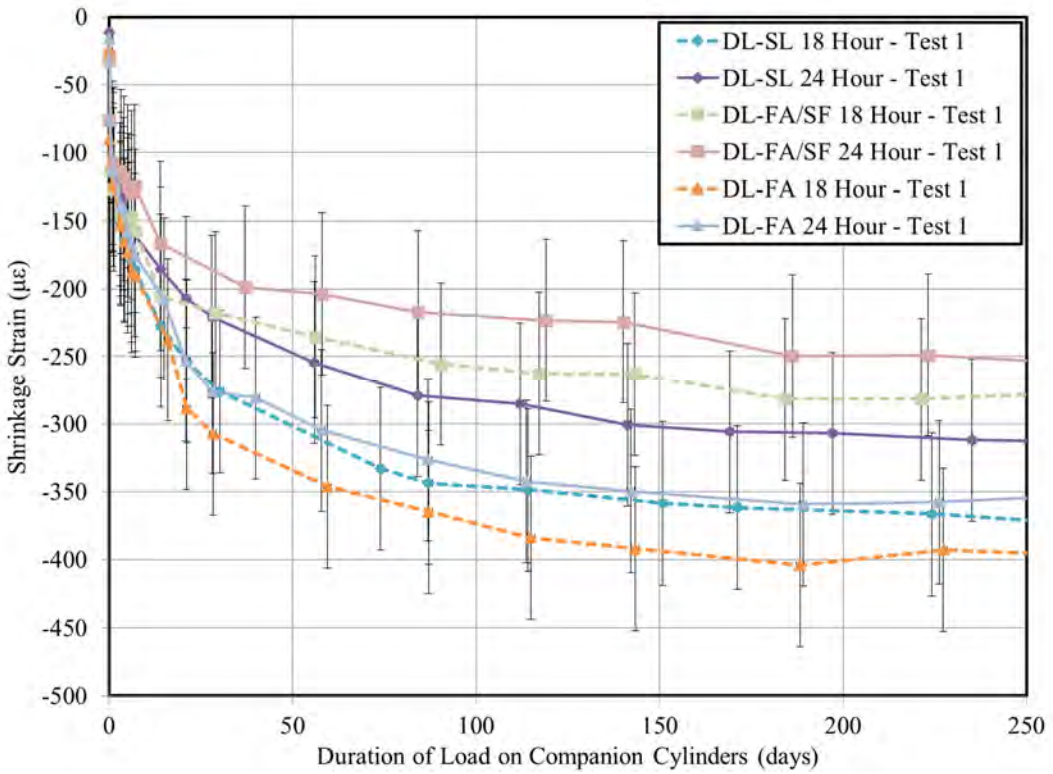

Figure 7-28: Cylinder Shrinkage Behavior of SCM-Variant Dolomitic Limestone Tests by Age at Loading

7.5.2.4 Effect of Supplementary Cementing Materials (SCMs)

Experimental shrinkage results are shown in Figure 7-29 and 7-30 for cylinder and rectangular prism specimens, respectively, along with the no-SCM variant experimental control tests for comparison. There exists no clearly discernable difference between the DL-III and DL-FA tests, suggesting that the effect of fly ash in the percent substitution used in this study is negligible. Similar results are seen for the slag cement mixtures (DL-SL), although a slight reduction in shrinkage of approximately the same order of experimental precision may be seen. Finally, results for the ternary mixture (DL-FA/SF) give the most evidence of a reduced shrinkage as compared to the no-SCM control (DL-III), although again, the observed reduction approaches the magnitude of the experimental precision.

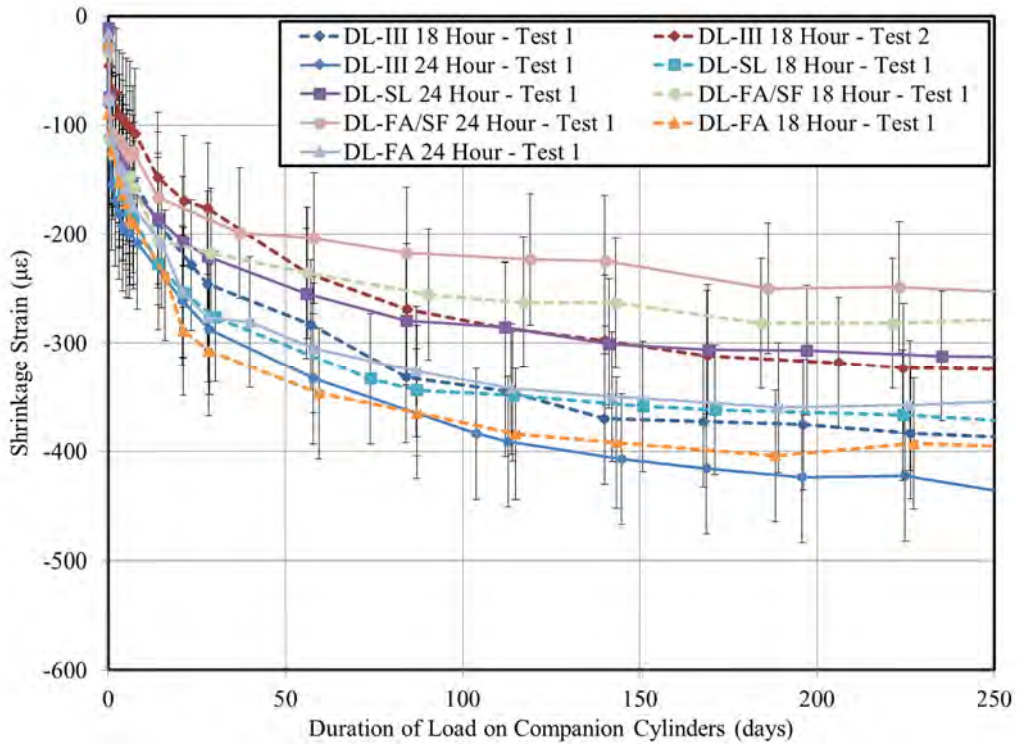

Figure 7-29: Cylinder Shrinkage Behavior of SCM-Variant Tests by Age at Loading

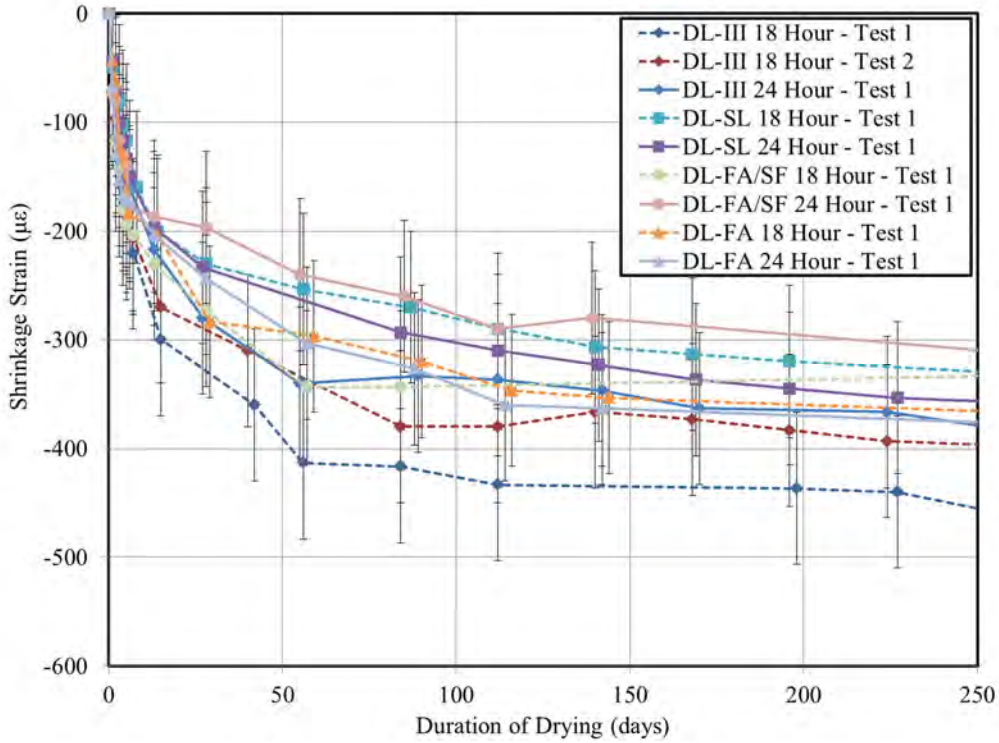

Figure 7-30: Rectangular Prism Shrinkage Behavior of SCM-Variant Tests by Age at Loading

Although more rigorous analytical techniques may be able better justify an observed difference in shrinkage behavior among tests, differences on the order reflected in experimental results (a total range of approximately 150 με) have a minimal effect on the magnitude of camber in prestressed concrete girders (as discussed in Section 7.4.3), and thus, are not of primary interest to the main objectives of this report.

7.5.2.5 Application of Candidate Prediction Models

The three candidate prediction models previously described in Section 7.2.5 were implemented for each test to generate predictions of shrinkage strains using the assumptions and inputs summarized in Table 7-16. Typical results for cylinder shrinkage and rectangular prism shrinkage are shown in Figures 7-31 and 7-32, respectively, with full results for each test available in Mante (2016). Major conclusions drawn from the plots are:

- Despite a slight tendency towards overprediction, cylinder and prism shrinkage predictions of the three candidate models are relatively accurate for the dolomitic limestone non-SCM variants;
- Predictions for the slag replacement and fly ash replacement mixtures tended to slightly exceed observed shrinkage behavior similarly in both cylinders and prisms;
- Predictions for the ternary mixture (fly ash and silica fume replacement) tended to substantially exceed observed shrinkage behavior in both cylinders and prisms; and
- Predictions for the crushed granite mixture tended to substantially underpredict observed response in both cylinders and prisms.

Table 7-16: Shrinkage Prediction Model Summary of Inputs

AASHTO 2014		ACI 209		Model Code 2010	
Input	***Justification***	***Input***	***Justification***	***Input***	***Justification***
Relative humidity = 50 percent	ASTM C512-02	Relative humidity = 50 percent	ASTM C512-02	Relative humidity = 50 percent	ASTM C512-02
Volume-to-surface ratio for cylinder = 1.5	Computed excluding cylinder ends not exposed to atmosphere	Volume-to-surface ratio = 1.5	Computed excluding cylinder ends not exposed to atmosphere	Cement and temperature – adjusted age at loading	Table 7-1
Volume-to-surface ratio for rectangular prism = 0.66	Computed including all six sides exposed to atmosphere	Volume-to-surface ratio for rectangular prism = 0.66	Computed including all six sides exposed to atmosphere	28-day measured compressive strength	Table 7-3
Chronological age at loading	Table 7-1	Slump = 0.5 in.	Assumed pre-admixture slump in agreement with Keske (2014) and Ellis (2012)	Notional size = 76.2 mm. for cylinders, = 38.1 mm. for rectangular prisms given ASTM C157 standard rectangular prism sizing.	Computed by MC 2010 provisions.
Compressive strength at loading	Table 7-3	Sand-to-aggregate weight ratio	Computed from Table 6-1	Rapid-hardening high-strength cement assumed	In accordance with Keske (2014) and recommendations of ACI 209 (2008).
		Cement factor	Assumed total powder content , Table 6-1	Concrete age at beginning of drying for rectangular prisms = 7 days	MC 2010 commentary notes chronological age to be used
		Air content	Table 7-2	Concrete age at beginning of drying for cylinders	Cylinder demolding occurred 2 hours prior to specimen loading time.
		Appropriate time-growth equation selected for 1-3 day steam cure or 7-day moist cure			

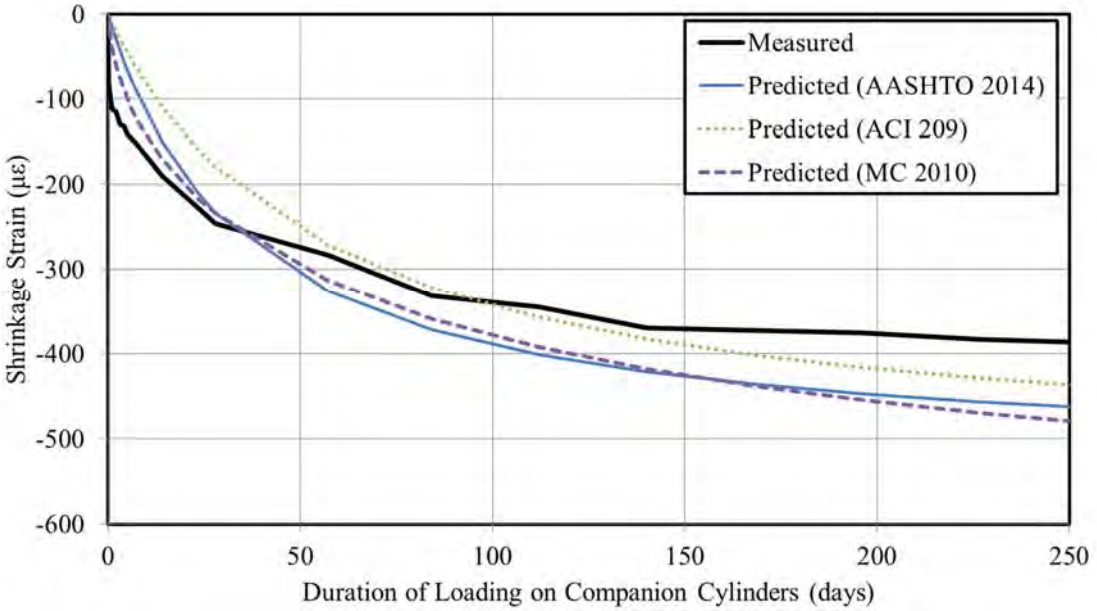

Figure 7-31: Comparison between Experimental Results and Prediction Models for Cylinder Shrinkage of Typical Dolomitic Limestone Test

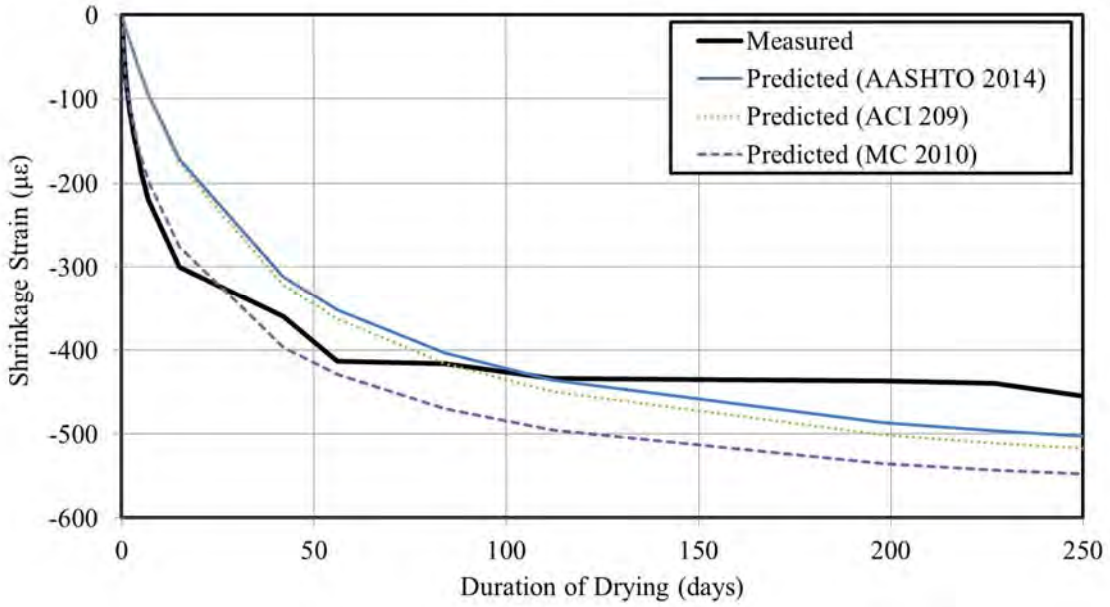

Figure 7-32: Comparison between Experimental Results and Prediction Models for Rectangular Prism Shrinkage of Typical Dolomitic Limestone Test

7.5.2.6 Relative Goodness-of-Fit

Similar to the discussion of Section 7.5.1.6, the time-weighted coefficient of variation, ϖ_j, is used as the preferred metric to evaluate goodness-of-fit. For reference, the general range of ϖ_j values reflected in ACI 209.2R (2008) for endorsed shrinkage prediction models range from 34 to 55 percent. Therefore,

any value less than 34 percent reflects an exceptional fit of a prediction model to experimental data. Computed values for the coefficients of variation for cylinder and rectangular prism shrinkage are shown in Table 7-17 for each test of this study. Also included is the overall coefficient of deviation, ϖ_{BP}, for each model.

Table 7-17: Relative Goodness-of-Fit of Unadjusted Candidate Prediction Models to Experimental Data

Test ID	Coefficient of Variation, ϖ_j (%)					
	AASHTO 2014		ACI 209		Model Code 2010	
	Cylinder	Prism	Cylinder	Prism	Cylinder	Prism
DL-III 18 Hour - Test 1	25.3	24.2	26.7	24.2	21.8	18.6
DL-III 18 Hour - Test 2	43.5	28.8	34.8	31.8	45.0	35.3
DL-III 24 Hour - Test 1	27.7	28.3	34.7	36.2	23.0	54.6
CL-III 18 Hour - Test 1	38.7	27.4	46.0	28.4	33.5	26.1
CL-III 18 Hour - Test 2	25.8	n/a	33.5	n/a	20.7	n/a
CL-III 24 Hour - Test 1	21.7	23.9	27.5	32.4	20.3	42.1
GG-III 18 Hour - Test 1	52.4	48.4	54.7	40.3	45.5	26.2
GG-III 18 Hour - Test 2	42.7	48.2	47.8	43.1	36.7	28.9
GG-III 24 Hour - Test 1	38.8	48.0	39.4	37.8	29.3	25.1
DL-SL 18 Hour - Test 1	27.3	45.8	32.9	57.2	26.9	72.0
DL-SL 24 Hour - Test 1	36.3	32.7	40.7	47.6	44.3	61.9
DL-FA/SF 18 Hour - Test 1	51.8	42.1	50.7	50.2	56.2	55.6
DL-FA/SF 24 Hour - Test 1	63.8	48.7	63.2	63.5	75.8	82.7
DL-FA 18 Hour - Test 1	26.0	31.0	33.3	39.5	24.7	46.5
DL-FA 24 Hour - Test 1	24.9	26.7	32.2	37.6	26.4	42.9
Overall Average	**36.4**	**36.0**	**39.9**	**40.7**	**35.3**	**44.2**
Overall Coefficient of Variation, ϖ_{BP} (%)	**38.4**	**37.3**	**41.2**	**42.0**	**38.4**	**47.9**

Of the unadjusted shrinkage prediction models considered in this effort, the AASHTO 2014 model represents the best combined fit with an overall coefficient of variation of 38.4 percent for cylinder

specimens and 37.3 percent for rectangular prisms. While the ACI 209 prediction model is the next most accurate for rectangular prismatic specimens, the Model Code 2010 prediction method proves approximately as accurate as the AASHTO model for cylinder specimens. Overall, the accuracy provided by the AASHTO 2014 model approaches the lower bound of the range cited by ACI Committee 209 (2008) and is therefore a reasonable estimate for girder design purposes.

7.5.2.7 Optimization of Prediction Models to Measured Data

A GRG nonlinear solver was used to calibrate the three considered prediction models to reflect experimental results by means of a shrinkage correction factor. In this analysis, the correction factor was applied directly to the shrinkage strain as predicted by a given model. By iterating the shrinkage correction factor in order to minimize the coefficient of variation, ϖ_j, values for the shrinkage correction factor, as shown in Table 7-18, were computed for each prediction model and test. Where the term "average of above" is used, the computed shrinkage correction factors for cylindrical and rectangular prismatic specimens were averaged[4]. After computing this factor for a given prediction method and test, shrinkage predictions were then recomputed including the shrinkage correction factor. Graphical comparisons between calibrated prediction models and experimental data are provided in Mante (2016).

[4] The analytical techniques of this section result in shrinkage correction factors for cylinders and rectangular shrinkage prisms—two types of specimens with different surface area to volume ratios. Although the surface area to volume ratio of 6"x12" cylinders more closely approach those of PCI girder shapes, the decision was made to average the computed shrinkage correction factors for a given test to reflect calibrations representing a variety of curing conditions (e.g. moist curing and accelerated curing).

Table 7-18: Shrinkage Modification Factors to Calibrate Candidate Prediction Equations to Experimental Data

Test ID	Shrinkage Modification Factors					
	AASHTO 2014		ACI 209		Model Code 2010	
	Cylinder	Prism	Cylinder	Prism	Cylinder	Prism
DL-III 18 Hour - Test 1	0.89	1.00	0.99	0.98	0.89	0.88
DL-III 18 Hour - Test 2	0.74	0.89	0.80	0.86	0.72	0.77
DL-III 24 Hour - Test 1	1.07	0.87	1.13	0.80	0.99	0.68
CL-III 18 Hour - Test 1	1.28	0.99	1.38	0.94	1.24	0.83
CL-III 18 Hour - Test 2	1.02	n/a	1.15	n/a	1.01	n/a
CL-III 24 Hour - Test 1	1.02	0.94	1.04	0.84	0.94	0.74
GG-III 18 Hour - Test 1	1.76	1.60	1.76	1.40	1.60	1.27
GG-III 18 Hour - Test 2	1.52	1.60	1.59	1.47	1.43	1.32
GG-III 24 Hour - Test 1	1.45	1.64	1.40	1.37	1.29	1.26
DL-SL 18 Hour - Test 1	0.94	0.74	0.99	0.68	0.91	0.61
DL-SL 24 Hour - Test 1	0.82	0.82	0.82	0.73	0.75	0.65
DL-FA/SF 18 Hour - Test 1	0.72	0.80	0.75	0.74	0.69	0.68
DL-FA/SF 24 Hour - Test 1	0.65	0.73	0.66	0.66	0.60	0.58
DL-FA 18 Hour - Test 1	1.03	0.85	1.07	0.78	0.99	0.72
DL-FA 24 Hour - Test 1	0.97	0.91	0.97	0.80	0.90	0.73
Overall Average	**1.06**	**1.03**	**1.10**	**0.93**	**1.00**	**0.84**
Average of Above	**1.04**		**1.02**		**0.92**	
Overall Range	**1.11**	**0.91**	**1.10**	**0.81**	**1.00**	**0.74**
Average of Mixtures Similar to Current Regional Mixtures (DL-SL+DL-FA/SF)	**0.78**	**0.77**	**0.81**	**0.70**	**0.74**	**0.63**
Average of Above	**0.78**		**0.75**		**0.68**	
Overall Average Excluding GG-III Tests	**0.93**	**0.87**	**0.98**	**0.80**	**0.89**	**0.72**
GG-III Tests Average	**1.58**	**1.61**	**1.58**	**1.41**	**1.44**	**1.28**
Average of Above	**1.6**		**1.5**		**1.4**	

In considering only the overall average of the shrinkage correction factors computed for all tests included in this effort, it appears that (1) no changes to shrinkage prediction equations are justified for AASHTO

LRFD and ACI 209 prediction models, and (2) a shrinkage modification factor of 0.90 may be appropriate for use with the Model Code 2010 method. However, upon closer inspection of the computed correction factors, it is apparent that in the overall average approach discussed above, the tendency to overpredict shrinkage for ternary mixtures tends to cancel with the tendency to underpredict shrinkage for the crushed granite mixtures. This effect becomes more evident when considering the average of the shrinkage correction factors for only those mixture types currently used in regional precast, prestressed production (DL-SL and DL-FA/SF). Here, average shrinkage correction factors of 0.78, 0.75, and 0.68 are computed for the AASHTO LRFD, ACI 209, and Model Code 2010 prediction methods, respectively. Isolating the GG-III tests from other results yields average shrinkage correction factors for crushed granites of 1.6, 1.5, and 1.4 for the AASHTO LRFD, ACI 209, and Model Code 2010 prediction models, respectively. The improved relative goodness-of-fits, computed for each of the tests using the shrinkage correction factors shown in Table 7-18, are presented in Table 7-19 (i.e. a shrinkage correction factor of 0.89 was applied to the AASHTO shrinkage prediction method for comparison to experimental data from DL-III -18 Hour Test 1 for cylindrical specimens).

Table 7-19: Relative Goodness-of-Fit of Adjusted Candidate Prediction Models to Experimental Data

Test ID	Coefficient of Variation, ϖ_j (%)					
	AASHTO 2014		ACI 209		Model Code 2010	
	Cylinder	Prism	Cylinder	Prism	Cylinder	Prism
DL-III 18 Hour - Test 1	21.5	24.2	26.6	24.0	16.7	10.0
DL-III 18 Hour - Test 2	16.0	25.8	21.4	25.8	11.0	11.5
DL-III 24 Hour - Test 1	26.7	22.6	32.4	23.3	23.0	8.8
CL-III 18 Hour - Test 1	31.0	27.4	36.3	27.6	26.4	13.7
CL-III 18 Hour - Test 2	25.7	n/a	30.6	n/a	20.6	n/a
CL-III 24 Hour - Test 1	21.6	22.7	27.2	23.9	19.1	10.7
GG-III 18 Hour - Test 1	22.8	21.5	29.2	23.1	19.3	8.0
GG-III 18 Hour - Test 2	18.8	23.6	24.7	24.2	14.4	9.4
GG-III 24 Hour - Test 1	16.0	20.0	23.2	22.6	14.2	7.9
DL-SL 18 Hour - Test 1	26.6	21.4	32.9	21.9	24.5	7.8
DL-SL 24 Hour - Test 1	27.1	21.3	33.7	22.6	26.8	7.0
DL-FA/SF 18 Hour - Test 1	33.2	33.0	38.6	33.7	29.7	19.2
DL-FA/SF 24 Hour - Test 1	29.7	26.6	35.4	27.6	28.3	13.4
DL-FA 18 Hour - Test 1	25.9	23.3	32.6	23.8	24.7	9.9
DL-FA 24 Hour - Test 1	24.7	24.3	32.0	25.4	23.5	11.3
Overall Average	**24.5**	**24.1**	**30.4**	**25.0**	**21.5**	**10.6**
Overall Coefficient of Variation, ϖ_{BP} (%)	**25.0**	**24.3**	**30.8**	**25.1**	**22.2**	**11.1**

Here, it becomes evident that with the exception of the Model Code 2010 shrinkage prism predictions, the accuracies of predictions furnished by all calibrated prediction models are similar.

7.5.2.8 Design Recommendations

Recommendations for shrinkage correction factors for use with the three shrinkage prediction models considered in this study are summarized in Table 7-20. For the purposes of preliminary girder design,

use of the AASHTO LRFD model is recommended due to its simplicity in application prior to concrete mixture selection.

Table 7-20: Design Recommendations for Shrinkage Modification Factors

	Proposed Shrinkage Modification Factors	
Prediction Model	**For use with slag and ternary[a] mixtures with limestone coarse aggregate (or unknown)**	**For use with crushed granite aggregate**
AASHTO LRFD	**0.80**	1.6
ACI 209[b]	0.75	1.5
Model Code 2010[c]	0.70	1.4

[a] = Ternary mixtures refer to those containing fly ash and silica fume.
[b] = Requires mixture-specific input parameters including fine aggregate percentage, cement content, slump, and air content.
[c] = Requires estimate of adjusted maturity at the time of prestress release and cement type.

For typical precast, prestressed concretes of the region (slag replacement or fly ash/silica fume replacement ternary mixtures) with limestone coarse aggregate, a shrinkage correction factor of 0.80 for use with the AASHTO LRFD prediction method is recommended at the time of initial girder design. This recommendation is in agreement with previous work of Keske (2014).

7.5.3 Comparison of Elastic Modulus as Computed from Creep Loading Frame to ASTM C469 Testing Results

An inevitable difficulty in conducting experimental creep testing is the tendency to "miss" a portion of the near-instantaneous creep behavior in experimental measurements due to the finite time period required for load application and recording measurements. Unfortunately, the rate of creep development is most active during this initial time period and thus, benchmark creep readings may be influenced by such errors. Recall, it is partially for this reason that compliance was selected as the preferred metric of time-dependent load-induced deformation in this report. By relying on compliance, the above-referenced error is confined to the first post-loading compliance value only, without being propagated through each measurement as would occur in the case of a computed creep coefficient.

For the experimental work reflected in this chapter, the elastic modulus was tested directly using companion cylinders in accordance with the requirements ASTM C469. However, an effective elastic modulus (as discussed in Section 7.4.2) was also computed from creep frame data using the measured values of applied stress and corresponding imposed deformation for each given test. Fundamentally, both methods of measuring concrete stiffness are similar, requiring imposing a load of 40 percent of the

compressive strength at time of loading and measuring associated deformation. However, ASTM C469 requires strict adherence to specified loading rates, while ASTM C512 does not specify required loading rates[5]. Values for the elastic modulus for each of the above methods are shown in Table 7-21, grouped by test. As shown by the comparison ratios, elastic modulus values computed from creep frame loading data are, on average, 14 percent lower than those tested in accordance with ASTM C469. Although somewhat puzzling at first consideration, this observed trend is in indeed in agreement with the discussion of the previous paragraph. Recognizing that (1) initial creep strain readings taken as close as practicable after creep frame loading inevitably represent the combined effect of initial elastic deformation and early creep behavior (i.e. recorded strain values are greater than if measurement was instantaneous) and (2) the applied stress is independent of the slight lag in measurement time, the value of elastic modulus computed from creep frame data (stress divided by strain) is expected to be less than that tested in accordance with ASTM C469. Also shown in Table 7-21 are initial compliance values, computed as the inverse of the measured elastic modulus for each given testing method. It is evident that despite the noted trend of a reduced apparent elastic modulus computed from creep frame data, these differences are hardly significant in initial compliance results for each testing method.

[5] The rate of loading for the creep testing performed in this work was similar to the loading rate specified by ASTM C469, with a given loading cycle for either method taking approximately 1-3 minutes.

Table 7-21: Comparison of Elastic Modulus Measurements by Test

Test ID	Elastic Modulus At Loading		E_{cf}/E_c	Compliance at Loading[a]	
	As Tested by ASTM C469, E_c (ksi)	As Computed from Creep Frame, $E_{c,f}$ (ksi)		$J_o = E_c^{-1}$ (με/psi)	$J_{o,f} = E_{c,f}^{-1}$ (με/psi)
DL-III 18 Hour - Test 1	5,700	5,300	0.93	0.18	0.19
DL-III 18 Hour - Test 2	5,600	5,300	0.95	0.18	0.19
DL-III 24 Hour - Test 1	6,350	5,100	0.80	0.16	0.20
CL-III 18 Hour - Test 1	5,700	4,700	0.82	0.18	0.21
CL-III 18 Hour - Test 2	5,750	4,750	0.83	0.17	0.21
CL-III 24 Hour - Test 1	6,100	5,750	0.94	0.16	0.17
GG-III 18 Hour - Test 1	3,700	3,050	0.82	0.27	0.33
GG-III 18 Hour - Test 2	3,500	2,800	0.80	0.29	0.36
GG-III 24 Hour - Test 1	3,900	3,200	0.82	0.26	0.31
DL-SL 18 Hour - Test 1	6,600	5,000	0.76	0.15	0.20
DL-SL 24 Hour - Test 1	6,400	5,650	0.88	0.16	0.18
DL-FA/SF 18 Hour - Test 1	6,050	5,300	0.88	0.17	0.19
DL-FA/SF 24 Hour - Test 1	6,100	5,500	0.90	0.16	0.18
DL-FA 18 Hour - Test 1	6,100	5,350	0.88	0.16	0.19
DL-FA 24 Hour - Test 1	6,100	5,200	0.85	0.16	0.19
Overall Average	-	-	**0.86**	-	-

[a] = Compliance at loading computed as inverse of elastic modulus at loading. $E_{c,f}^{-1}$ values correspond to those initial compliance values included in the analysis of Section 7.5.1.

7.6 Summary and Conclusions

7.6.1 Summary

In this laboratory study, six concrete mixtures were proportioned to represent mixtures typical of Alabama precast, prestressed girder production. These six mixtures included three regional coarse aggregates and three combinations of supplementary cementing materials (SCMs). A uniform 18-hour compressive strength, paste content, and sand-to-total aggregate ratio (by volume) were maintained for all mixtures. Sampled concrete cylinders were exposed to accelerated curing practices mimicking those of precast, prestressed plants, while rectangular prism specimens were exposed to standard curing conditions. At the completion of initial accelerated curing (either 18 or 24 hours), cylindrical specimens were tested in accordance with ASTM C512-02 (ASTM 2002) to determine creep and shrinkage behavior for a period of 250 days. Concurrently, ASTM C157-08 (ASTM 2008) tests were performed to determine shrinkage behavior for a period of 250 days. To ensure the precision and repeatability of results, the first three tests were duplicated. Trends were then identified in experimental results and comparisons were made between various prediction models—ultimately resulting in design recommendations to accurately predict time-dependent deformations of typical concretes within the study region.

7.6.2 Conclusions and Recommendations

The following are primary research findings relating to concrete creep:

1. No significant difference was detected for the two dolomitic limestone aggregates included in this study (DL-III and CL-III);
2. Concrete mixtures using crushed granite aggregate exhibited 55-58 percent more creep than corresponding dolomitic limestone mixtures. However, this difference is primarily due to the reduced elastic modulus of the crushed granite aggregate and is not attributable to a significant difference in time-dependent creep behavior;
3. Specimens loaded at 24 hours appeared to exhibit slightly reduced creep, although, approaching the limits of experimental precision;

4. The use of slag cement (15 percent substitution) had a negligible effect on creep, while the use of fly ash (15 percent substitution) may have caused a slight reduction in creep although again, approaching experimental precision;
5. The use of fly ash and silica fume (18 percent and 8 percent substitution, respectively) resulted in a reduced creep tendency of between 9-12 percent;
6. Of the unadjusted candidate creep prediction models, the ACI 209 and AASHTO 2014 models provided relatively accurate predictions for the concretes considered in this study, with BP coefficients of variation of 10.3 and 12.9, respectively;
7. For the purposes of camber prediction during initial girder design, the unadjusted AASHTO LRFD, ACI 209, and MC 2010 models predict creep behavior with reasonable accuracy for the concretes considered in this study. Of these models, the AASHTO LRFD is the simplest;
8. If a more refined estimate of creep is desired, the following creep coefficient modifications may be applied to the unadjusted models, with most accurate predictions offered by the Model Code 2010 method:

Table 7-22: Design Recommendations for Creep Coefficient Modification Factors

	Proposed Creep Coefficient Modification Factors	
Prediction Model	**When ternary mixtures are used**	**For all other mixture compositions (or unknown)**
AASHTO LRFD	**0.80**	1.00
ACI 209[b]	**0.95**	**1.15**
Model Code 2010[c]	**0.65**	**0.80**

[a] = Ternary mixtures refer to those mixtures containing fly ash and silica fume.
[b] = Requires mixture-specific input parameters including fine aggregate percent, slump, air content.
[c] = Requires estimate of adjusted maturity at the time of prestress transfer.

9. Elastic modulus, as computed from creep frame loadings in accordance with ASTM C512, tended to be 14 percent lower than those measured in companion cylinders by ASTM C469 at the time of loading—suggesting that a portion of the early creep is “missed” during typical ASTM C512 testing; and
10. The “missed” portion of early creep corresponds to negligible differences in compliance, and thus, affirms the preference to consider compliance as the primary metric of time-dependent load-induced deformation.

The following are primary research findings relating to concrete shrinkage behavior:

1. No significant difference in shrinkage behavior was detected for the two dolomitic limestones included in this study;
2. Crushed granite mixtures tended to exhibit between 40-70 percent increased shrinkage when compared to dolomitic limestone mixtures;
3. Specimens loaded at 18-hour ages exhibited a slightly increased shrinkage tendency, although approaching experimental precision;
4. No significant effect of fly ash or slag (for the substitution percentages used) on shrinkage behavior was detected;
5. The ternary mixture exhibited slightly decreased shrinkage, although approaching experimental precision;
6. Of the three unadjusted candidate prediction models, the AASHTO 2014 method is most accurate of the considered models with a BP coefficient of variation of 36 percent;
7. For most accurate prediction of concrete shrinkage, the following shrinkage modification factors are suggested for use with each prediction model:

8. **Table 7-20: Design Recommendations for Shrinkage Modification Factors**

	Proposed Shrinkage Modification Factors	
Prediction Model	**For use with slag and ternary[a] mixtures with limestone coarse aggregate (or unknown)**	**For use with crushed granite aggregate**
AASHTO LRFD	**0.80**	1.6
ACI 209[b]	0.75	1.5
Model Code 2010[c]	0.70	1.4

9. [a] = Ternary mixtures refer to those containing fly ash and silica fume.
10. [b] = Requires mixture-specific input parameters including fine aggregate percentage, cement content, slump, and air content.
11. [c] = Requires estimate of adjusted maturity at the time of prestress release and cement type.
12. The AASHTO LRFD method modified by the shrinkage modification factor of 0.80 is recommended for initial design in the absence of more detailed information.

The following summarize recommendations for future researchers:

1. The use of sound post-processing techniques to eliminate erroneous data points and to detect loading anomalies is encouraged;

2. Experimental precisions and repeatability of measurements should be determined by duplicate tests to allow identification of significant experimental results;
3. If conducting testing intended to simulate precast, prestressed concrete element production, an accelerated curing system should be used to introduce expected temperature profiles before and at the time of creep loading; and
4. The comparison of concrete elastic modulus as computed by loading frame data and also by testing of companion material testing can be used to affirm the soundness of testing procedures and validate the accuracy of benchmark readings.

Chapter 8: Effect of Diurnal Temperature Changes on Girder Camber

8.1 Introduction

After production, the introduction of nonuniform temperature variations along the height of hardened girders can induce transient changes in cross-sectional curvatures, thereby also causing relative changes to camber and other girder deflections. These nonuniform vertical temperature variations (also called profiles or gradients) are typically introduced in concrete girders by ambient conditions (temperature variations and differential solar radiation) and are collectively referred to as diurnal (daily) temperature variations.

Typical design predictions of girder deflections neglect the presence of these temperature-induced deflections, thereby assuming constant temperatures throughout structural elements. This practice is defensible for a variety of reasons including (1) difficulties in projecting future temperatures at a given time, (2) difficulties in precisely predicting the thermal response of materials (i.e. coefficient of thermal expansion) at various stages of construction, and (3) the relatively high computational cost of such analyses. Instead of explicitly accounting for these temperature-induced deflections in design computations, it is expected that appropriate levels of design or construction tolerance for camber are included in design documents to accommodate such transient changes in deformation.

This report addresses the topic of diurnal temperature-induced deformations in precast, prestressed girders in detail for a variety of reasons. By thoroughly understanding and validating the mechanism(s) of transient temperature-induced deformations, improved comparisons can be made among measured field cambers recorded under differing ambient conditions, and recommendations can be made regarding the anticipated degree of camber variation likely to be observed in field measurements due to transient temperature-induced effects.

This chapter describes an analytical and experimental exploration of the structural response of girders exposed to temperature changes. Measured results of a field investigation were used to

determine the “effective” or in-place coefficient of thermal expansion (CTE) of girder concrete. The analytical procedures utilized in this chapter are incorporated into the final analyses of Chapter 10.

8.1.1 Chapter Objectives

The primary objective of this chapter is to determine the effect that temperature variations in precast, prestressed concrete girders have on deformational behavior, and specifically on midspan camber. Tasks completed in support of the primary objective of this chapter include the following:

- Improve the implementation of an existing girder temperature-correction methodology;
- Conduct field testing to affirm and validate an existing temperature-correction procedure and recommend most efficient practices for future instrumentation in research applications (i.e. number and location of gages); and
- Identify rational deflection tolerances that reflect expected camber variations for girders in storage due to regionally-appropriate temperature conditions.

8.1.2 Chapter Outline

This chapter begins with a general discussion of the concept of a curvature-based temperature-correction algorithm—providing a thorough derivation of the governing mathematical equations and a description of algorithm refinements and improvements implemented as part of this research effort. Then, a summary of an in-plant experimental program consisting of the monitoring of internal concrete temperatures and various measures of induced deformational responses (i.e. concrete strains and girder deflections/end rotations) is presented. Next, results from each of three experimental tests are presented as necessary to affirm the soundness of recorded data and identify regional trends in girder temperature profiles. Then, an analysis is detailed aimed at (1) determination of an average effective coefficient of thermal expansion (CTE) for each field test, (2) comparison of observed cross-sectional and global deformational responses to predicted behavior, (3) implementation of various simplifications to the temperature-correction procedure utilized herein, and (4) determination of the approximate magnitude of expected variations in the prestressing force caused by temperature-induced girder deformations. Finally, the findings of the analyses of this chapter are relied on to determine appropriate tolerance limits for girder camber to account for the effect of transient temperature variations.

8.1.3 Exclusions

The focus of this chapter and the related experimental program is exploring the effect of transient diurnal temperature profiles on deformations of precast, prestressed concrete girders. Investigation of (1) early-age prestress losses due to temperature effects, (2) changes in the time-dependent rates of creep and/or shrinkage due to elevated temperatures, or (3) investigation of the effect of differential CTE of constituent materials is outside the scope of this investigation. These topics have been largely studied by others (Roller et al. 2003, French and O'Neill 2012, and Barr and Angomas 2010), who generally conclude that (1) the magnitude of early-age temperature losses is heavily dependent on regional construction practices and assumptions of the timing of steel to concrete bonding (which has not been extensively studied), (2) reductions in the prestressing force caused by early-age temperature losses are typically relatively small (between two to six percent of the initial jacking stress), and (3) the net variation in camber caused solely by temperature-induced prestressed force reductions is relatively small, limited to approximately 5 percent of the overall camber value in one parametric study (French and O'Neill 2012).

8.2 Curvature-Based Temperature-Correction Algorithm

The curvature-based temperature-correction algorithm employed in this report is derived directly from fundamental structural mechanics, specifically engineering beam theory and linear thermal expansion. The purpose of the temperature-correction algorithm is to compute the expected change in two key cross-sectional parameters, centroidal strain and curvature, corresponding to a given change in cross-sectional temperature profile. Most typically, this algorithm is used to compute the expected deformation associated with a change from a given (typically measured) cross-sectional temperature profile to a uniform vertical profile and, thus, the term "temperature-correction" is used. The key parameters, change in centroidal strain and change in curvature, are computed by balancing the thermal expansion tendencies within a cross section with any induced mechanical stresses (often called self-equilibrating stresses) to ultimately yield a linear strain profile in accordance with equilibrium and deformation constraints. While changes in cross-sectional curvature are of primary interest to this research effort due to their ability to directly induce changes to flexural deformations, cross-sectional centroidal strain was also evaluated.

8.2.1 Background

The use of temperature-correction procedures similar to that used in this report first appear in the literature in the mid-1980's as applicable to evaluating the effect of thermal gradients in concrete flexural members. Primary resources on this topic include a now withdrawn report by ACI Committee 435 titled *Report on Temperature-Induced Deflections of Reinforced Concrete Members* (ACI Committee 435 1997) and an NCHRP publication titled *Report 276: Thermal Effects in Concrete Bridge Superstructures* (Imbsen et al. 1985). Both of these reports contain similar derivations to those contained in Section 8.2.2 of this work, although each uses different notation, different sign conventions, and implements the basic concept somewhat differently. As is shown later in this chapter, the full application of the temperature-correction algorithm as implemented herein can be quite computationally expensive, likely explaining why early temperature-correction efforts employed simplifying approximations (i.e. only considering a single linear temperature profile) and, therefore, were less useful for a variety of temperature profiles than more recent temperature-correction efforts.

8.2.2 Assumptions and Derivation

Various governing assumptions allow the derivation of the curvature-based temperature correction used herein. These assumptions, as summarized from NCHRP Report 276 (1985) include the following: (1) constitutive materials are homogenous and exhibit isotropic behavior, (2) material properties are independent of temperature, (3) constitutive materials are governed by linear stress-strain and temperature-strain relations, (4) initially plane sections remain plane, and (5) temperature variations are only present with depth, but constant at all points of equal depth (i.e. no transverse gradients considered). A complete derivation, beginning with fundamental principles of structural mechanics is presented below:

Assume a sign convention that positive is downward from the elastic neutral axis with the zero point at the centroid location. At each depth (*y*) within a given cross section, the linear thermal strain, $\varepsilon_{th}(y)$, if not restrained, is given as

$$\varepsilon_{th}(y) = \alpha_T \cdot \Delta T(y) \tag{8-1}$$

where

α_T = coefficient of thermal expansion and

$\Delta T(y)$ = temperature at a given depth within cross section.

Expressed incrementally, Equation 8-1 becomes the following:

$$\Delta\varepsilon_{th}(y) = \alpha_T \cdot \Delta T(y) \tag{8-2}$$

The total strain at a given cross section, $\varepsilon_{tot}(y)$, can be expressed as

$$\varepsilon_{tot}(y) = \varepsilon_0 + \phi \cdot y \tag{8-3}$$

where

ε_0 = strain at the centroidal axis location for a given cross section,

ϕ = cross-sectional curvature, and

y = depth within a cross section.

Expressed incrementally:

$$\Delta\varepsilon_{tot}(y) = \Delta\varepsilon_0 + \Delta\phi \cdot y \tag{8-4}$$

The mechanical strain at a given cross section, $\Delta\varepsilon_{mech}(y)$, can be expressed as

$$\Delta\varepsilon_{mech}(y) = \frac{\Delta\sigma(y)}{E} \tag{8-5}$$

where

$\Delta\sigma(y)$ = change in stress at a given girder depth, and

E = modulus of elasticity of girder material.

The total strain in a cross section is the sum of the thermal and mechanical strain.

$$\Delta\varepsilon_{tot}(y) = \Delta\varepsilon_{th}(y) + \Delta\varepsilon_{mech}(y) \tag{8-6}$$

Substituting and solving for stress yields:

$$\Delta\sigma(y) = E\left[\Delta\varepsilon_{tot}(y) - \Delta\varepsilon_{th}(y)\right] \tag{8-7}$$

Substituting

$$\Delta\sigma(y) = E\left[\left(\Delta\varepsilon_0 + \Delta\phi \cdot y\right) - \left(\alpha_T \cdot \Delta T(y)\right)\right] \tag{8-8}$$

Imposing equilibrium for a given cross section in a beam with no change in axial force due to restraint:

$$0 = \int \Delta\sigma(y)dA = \int_A E\left(\left[\Delta\varepsilon_0 + \Delta\phi \cdot y\right] - \left[\alpha_T \cdot \Delta T(y)\right]\right)dA \tag{8-9}$$

Simplifying

$$0 = \int_A E\left(\Delta\varepsilon_0 + \Delta\phi \cdot y - \alpha_T \cdot \Delta T(y)\right)dA \tag{8-10}$$

Dividing into three separate integrals and simplifying:

$$0 = E\int_A \Delta\varepsilon_0 dA + E\int_A \left(\Delta\phi \cdot y\right)dA - E\int_A \left(\alpha_T \cdot \Delta T(y)\right)dA \tag{8-11}$$

By virtue of the centroidal axis where y=0, the second term equals zero.

$$0 = E\int_A \Delta\varepsilon_0 dA + 0 - E\int_A \left(\alpha_T \cdot \Delta T(y)\right)dA \tag{8-12}$$

Removing constants from integrals:

$$0 = E\Delta\varepsilon_0 \int_A dA - E\alpha_T \int_A \left(\Delta T(y)\right)dA \tag{8-13}$$

Recognizing that the first integral is equal to the cross-sectional area:

$$0 = E\Delta\varepsilon_0 A - E\alpha_T \int_A \left(\Delta T(y)\right)dA \tag{8-14}$$

Simplifying further yields the governing equation for change in centroidal strain:

$$\Delta\varepsilon_0 = \frac{\alpha_T}{A}\int_A \left(\Delta T(y)\right)dA \tag{8-15}$$

Modifying differential element, dA , to vary with width:

$$dA = dy \cdot w(y) \tag{8-16}$$

where

$w(y)$ = width at a given cross section at height y.

Substituting, yields the first governing equation:

$$\Delta\varepsilon_0 = \frac{\alpha_T}{A}\int_y \left(\Delta T(y)\right)w(y)dy \tag{8-17}$$

Similarly, the change in incremental curvature can be derived. Equations 8-1 through 8-8 are applicable and imposing moment equilibrium yields:

$$0 = \int y\Delta\sigma dA = \int_A yE\left(\left[\Delta\varepsilon_0 + \Delta\phi \cdot y\right] - \left[\alpha_T \cdot \Delta T(y)\right]\right)dA \tag{8-18}$$

Simplifying:

$$0 = \int_A yE\left(\Delta\varepsilon_0 + \Delta\phi \cdot y - \alpha_T \cdot \Delta T(y)\right)dA \tag{8-19}$$

Dividing into three separate integrals and simplifying:

$$0 = E\int_A \Delta\varepsilon_0 y dA + E\int_A \left(\Delta\phi \cdot y^2\right)dA - E\int_A \left(\alpha_T \cdot \Delta T(y)\right)y dA \tag{8-20}$$

By virtue of the centroidal axis where y=0, the first term now equals zero.

$$0 = 0 + E\int_A \left(\Delta\phi \cdot y^2\right)dA - E\int_A \left(\alpha_T \cdot \Delta T(y)\right)y dA \tag{8-21}$$

Simplifying the second and third terms and removing constants from integrals yields:

$$0 = E\Delta\phi\int_A \left(y^2\right)dA - E\alpha_T\int_A \left(\Delta T(y) \cdot y\right)dA \tag{8-22}$$

Recognizing that the first integral is the second moment of area (moment of inertia), I:

$$0 = E\Delta\phi I - E\alpha_T\int_A \left(\Delta T(y) \cdot y\right)dA \tag{8-23}$$

Solving for incremental curvature, $\Delta\phi$:

$$\Delta\phi = \frac{\alpha_T\int_A \left(\Delta T(y) \cdot y\right)dA}{I} \tag{8-24}$$

Simplifying and substituting yields the second governing equation:

$$\Delta\phi = \frac{\alpha_T}{I}\int_y \left(\Delta T(y) \cdot y \cdot w(y)\right)dy \tag{8-25}$$

The above two governing equations, Equation 8-17 and 8-25, jointly define the temperature-correction procedure employed in the remainder of this chapter. These equations are applicable to each cross section within a beam if unique temperature profiles are known for each girder cross section. By integrating Equation 8-25 for all cross sections within a girder, an incremental camber (i.e. the camber variation caused by the induced temperature profile) can be computed. Most typically, a single midspan

temperature profile is assumed to sufficiently represent the cross-sectional temperature profiles present at all other sections within a girder.

8.2.3 Related Previous Work by Others

After the initial appearance of curvature-based temperature-correction procedures in the literature in the mid-1980's, there was a relative absence of further developments and refinements of these procedures until the mid-2000's—apparently spurred by research interest in evaluating the accuracy of camber predictions in precast, prestressed concrete girders. First to implement temperature-correction procedures for the purpose of adjusting field measurements of camber in simple span concrete girders appears to be Cook and Bloomquist (2005) in their FDOT-sponsored effort to verify the accuracy of prefabrication camber estimates. Cook and Bloomquist implemented an analytical model based on the recommendations of NCHRP Report 276 and, in combination with (1) measurements of girder camber and concrete surface temperature profiles and (2) assumptions for the CTE of concrete, used this temperature-correction procedure to facilitate comparisons between predicted and measured camber in production girders.

Next to focus on temperature correction of precast, prestressed concrete girders was Barr et al. (2005), with similar results later republished by Barr and Angomas (2010). A portion of the work of Barr et al. explored the effect of in-service temperature variations and thus, a temperature-correction procedure similar to that used by Cook and Bloomquist (2005) was implemented. An effort was made to validate the temperature-correction procedure using field-gathered data, although it is not clear if an effort was made to calibrate the procedure (by means of an effective CTE or otherwise) or if standard values of thermal material properties were assumed. A similar implementation of a temperature-correction procedure was implemented by Lee (2010) in his analytical study. This work included a verification effort of the temperature-correction procedure using finite element modeling methods; typical values of concrete CTE were assumed in the absence of field measurements or calibrations.

A study by Rizkalla et al. (2011) also included a similar temperature-correction effort intended to modify field-measured girder cambers, except simplifying assumptions of linear temperature profiles were relied on. Rizkalla et al., using assumed values of concrete CTEs for this analytical work, concluded that

(1) temperature-correction procedures are somewhat unreliable, (2) to minimize error, field measurements should be taken at dawn, and (3) no adjustments were recommended due to the transient nature of temperature-induced changes to girder deformations.

Prior to the work contained in this report, four prior researchers also conducting work sponsored by ALDOT have implemented temperature-correction procedures similar to those discussed above. Johnson (2012) first derived a temperature-correction algorithm that served as a precursor to the derivations contained in Section 8.2.2 of this report. Included in Johnson's work were various assumptions to simplify the analysis including (1) a simplified cross-sectional shape and (2) assumptions of standard temperature profile shape given recorded values at four specific depths within a section. Next, Keske (2014) expanded on the prior efforts by (1) conducting laboratory testing to determine appropriate ranges of CTE for girder concretes (SCC and VC) and (2) expanding the applicability of Johnson's work to composite girders. Isbiliroglu (2014) implemented a similar temperature-correction procedure to evaluate historical testing results of noncomposite girders from four previous projects. Finally, Neal (2015), in concert with the work of Keske (2014), analytically determined values of an "effective" concrete coefficient of thermal expansion (CTE) that yielded best agreement between predicted and measured field responses of full-size girders. The joint work of Neal (2015) and Keske (2014) is most similar to the analytical techniques employed in this report, although the more detailed field instrumentation included in this effort allows for improved comparisons between predicted and measured field responses.

8.2.4 Algorithm Refinements and Improvements in this Work

A major objective of this report was to implement various algorithm refinements and improvements to address weaknesses of the studies referenced above. These refinements were focused in two areas: (1) improved understanding of regionally-induced temperature gradients, and (2) inclusion of actual girder cross-sectional widths without the use of simplifications.

In order to implement a temperature-correction procedure, it is first necessary to have a thorough understanding of the vertical temperature profiles induced in candidate girders. Previous work by others typically monitored temperature readings at certain key depths within a cross section and made

assumptions to define the temperature profile for other intermediate depths. In previous AUHRC research on this topic, the typical simplifying assumptions regarding temperature profiles are (1) a uniform temperature is assumed within the top flange, (2) a uniform temperature is assumed within the bottom flange and (3) a single linear gradient is assumed within the height of the web, not necessarily matching the top and bottom flange temperatures at the boundaries. An example of a fitted temperature profile from the previous work of Keske (2014) is shown in Figure 8-1. Given that only limited guidance is available in the literature regarding the likely shape of vertical temperature profiles in noncomposite precast, prestressed girder shapes (primarily from Lee 2010 and Kelly et al. 1987), the previous assumptions of ALDOT-sponsored researchers were logical.

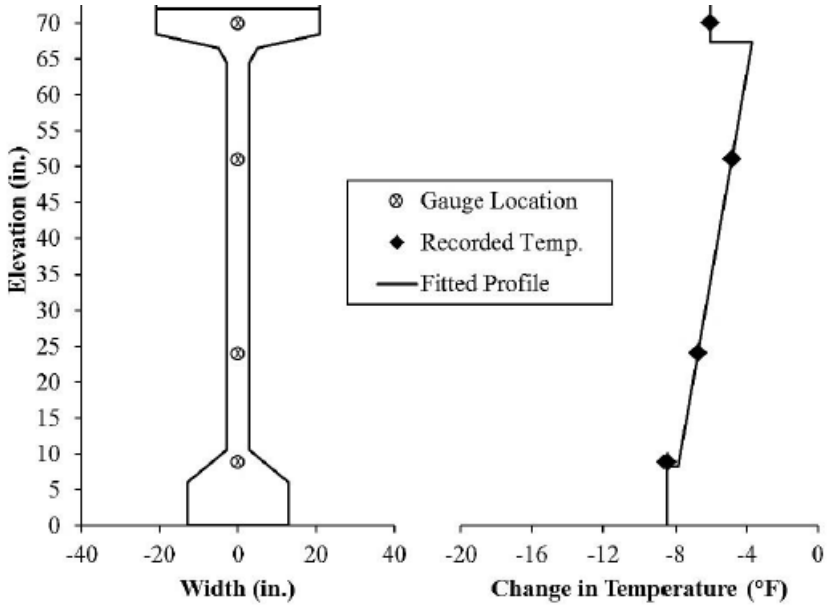

Figure 8-1: Fitted Temperature Profile from Keske (2014)

In the experimental effort detailed in this report, various girder cross sections were heavily instrumented with temperature sensors to more precisely characterize diurnal temperature profiles at different times. Accordingly, the revised implementation of the temperature-correction algorithm used in this project is capable of accepting a nearly unlimited number of vertical temperature measurements at different elevations. The algorithm linearly interpolates between adjacent temperature measurements along the height of the girder and also extrapolates linearly to the extreme top and bottom fibers using the nearest interpolated gradient as shown in Figure 8-2.

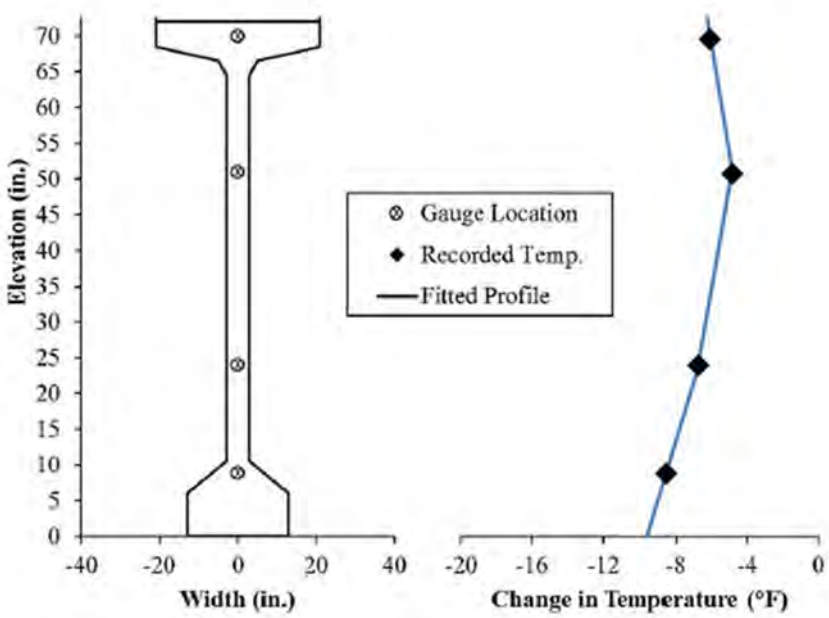

Figure 8-2: Fitted Temperature Profile of Revised Temperature-Correction Algorithm

The flexibility to accept varying numbers of temperature measurements along a girder height was advantageous in allowing the various analysis iterations conducted in Section 8.5 aimed at identifying best (and most efficient) girder instrumentation practices for future research implementation.

Another key improvement implemented in the temperature-correction algorithm used in this chapter was the ability to use true girder widths at any given height within a cross section. Previous work by ALDOT-sponsored researchers relied on a simplification of the bulb-tee girder shape by approximating the cross section as three rectangles with dimensions such that key cross-sectional geometric parameters (e.g. area and moment of inertia) were accurately preserved. In doing so, evaluation of the two integrals of Equation 8-17 and 8-25 is greatly simplified, although perhaps at a cost of computation accuracy. This magnitude of error introduced by the use of an equivalent cross section, as well as other previous assumptions, is explored thoroughly in Section 8.5 of this chapter.

While the inclusion of (1) the capability to accept additional temperature measurement inputs within a cross section and (2) the use of actual widths at all depths within a cross section were all welcomed improvements of the revised temperature-correction algorithm, these additions came at an increased computational cost. Where previous researchers were able to evaluate the dual integrals of Equations 8-17 and 8-25 relatively simply by approximate methods, the revised temperature-correction

algorithm demanded the use of numerical integration. In conducting the numerical integration for a single cross section, large matrices (at least as large as the number of vertical differential elements by the number of height-dependent parameters within Equation 8-17 and 8-25) become necessary. By virtue of these large matrices, it is challenging and computationally expensive to repeatedly evaluate numerical integrals for rapidly changing temperature profiles (e.g. to evaluate temperature-induced changes in deformations every two minutes for a 24-hour period). To address these challenges, the temperature-correction algorithm used herein was programmed as a series of layered functions in an engineering calculation software package. Structuring the algorithm as such facilitated the efficient post-processing of large amounts of field-gathered data, thereby allowing the breadth of the analyses offered later in this chapter. For reference, Mante (2016) contains samples of the layered functions used in the implementation of the temperature-correction algorithm.

8.3 Experimental Program

This section details the field experimental program conducted as part of this research effort to evaluate the effects of diurnal ambient temperature exposure on the deformations of three production girders during in-plant storage. First, a general overview of the experimental program is provided. Next, the experimental procedure is presented and additional details of each test are provided as required for subsequent analyses conducted later in this chapter. Finally, a comprehensive instrumentation plan is provided detailing both internal concrete and external instrumentation monitored during on-site testing.

8.3.1 Summary of Work

In this field monitoring study, the deformational responses of three hardened bulb-tee girders subjected to diurnal temperature profiles during in-plant storage were continuously monitored—at increments of two minutes—for a period of approximately 24 hours. During this testing period, temperature sensors (previously installed during girder production) monitored internal concrete temperatures at 15 depths within the midspan cross section and four depths within the 1/6-span cross section. In addition, various metrics of girder deformation (four internal concrete strains at midspan and 1/6-span cross sections, vertical deflection at three intermediate locations along each girder, and girder end rotations) were also monitored throughout each testing period.

8.3.2 Experimental Procedure and Field Test Details

The experimental procedure employed in this research effort had several steps:

- Prepare and bench test all sensors and data collection equipment utilized in this effort to verify sensor accuracy and compatibility of measurement ranges with anticipated field responses;
- Install internal girder sensors prior to and during initial girder production. Cap and protect protruding wires for later use;
- Identify candidate testing date(s) most likely to induce extreme diurnal temperature fluctuations[6] of girder concrete and coordinate field-availability with girder producers during these times;
- Approximately one week prior to performing each 24-hour in-plant test, coordinate relocation of candidate girder(s) from typical position in storage yard to a position of (a) relatively unobstructed solar exposure and (b) support conditions similar to those of final installation;
- Arrive on-site, install external girder sensors and connect all gages to data collection system; and
- Continuously monitor data collection effort throughout 24-hour testing period to ensure (a) shading of temperature-sensitive instrumentation from solar exposure, (b) protection of sensors from precipitation, (c) continuous power supply, and (d) proper operation of data collection system.

Details for each girder specimen and field test, as relevant to implementation of the temperature-correction algorithm herein, are displayed in Table 8-1 for each of three tests.

[6] In-plant tests were conducted during winter months due to both researcher/producer availability and the potential for extreme fluctuations of girder concrete temperatures due to diurnal exposures (i.e. colder nights and warmer days with unobstructed solar exposure).

Table 8-1: Test Details for 24-Hour In-Plant Tests

Test No.	Girder Shape	Girder Length[a]	Casting Date	Testing Date	Chronological Age of Girder at Testing (days)	Test Duration (hours)
1	BT-72	139'-5.7"	10/9/13	12/15/13-12/16/13	67	23.9
2	BT-72	137'-9.5"	7/24/13	12/17/13-12/18/13	146	32.1
3	BT-63	130'-0"	9/23/14	12/15/14-12/16/14	83	23.9

[a] = SI girder lengths are converted to English units.

8.3.3 Instrumentation Plan

In accordance with recommendations for the instrumentation of concrete girders provided by both FHWA Report SA-96-075 (Holt 1996) and previous AUHRC researchers (Johnson [2012] and Keske [2014]), an instrumentation plan was developed to support the experimental effort of this research phase. Instrumentation consisted of both internal and external girder sensors labelled according to the convention shown in Figure 8-3.

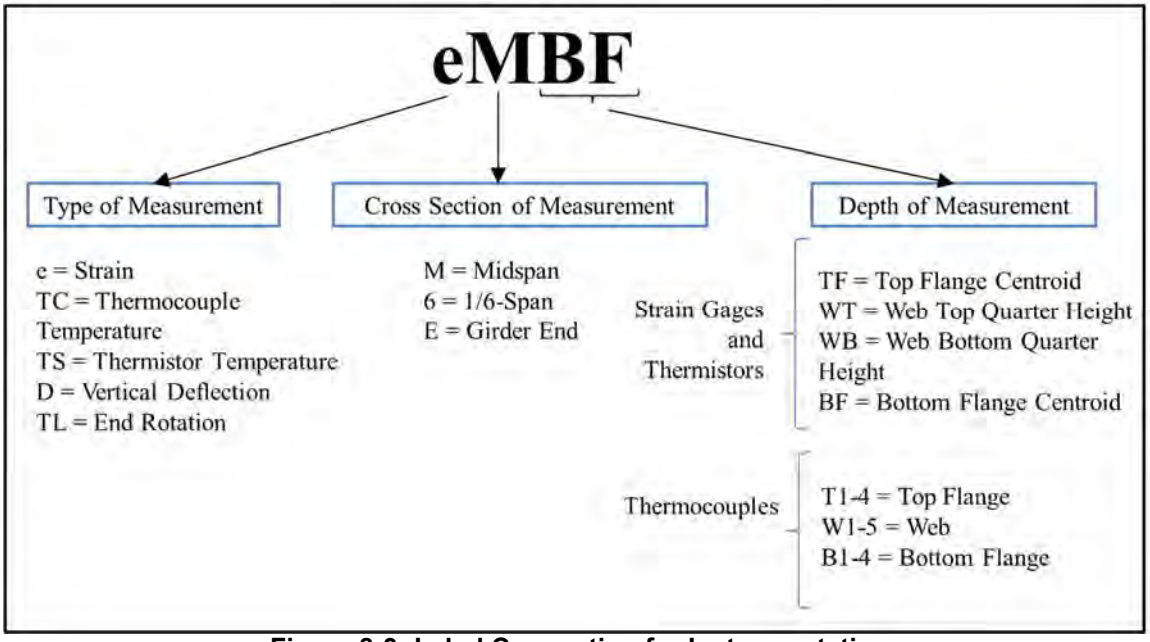

Figure 8-3: Label Convention for Instrumentation

Internal sensors installed at girder midspan consisted of both vibrating-wire strain gages (VWSGs) equipped with companion thermistors and Type T thermocouples positioned within girder concrete as shown in Figure 8-4. Vibrating-wire strain gages were installed at the approximate geometric centroids of the bottom and top flanges and at upper and lower quarter-points of the girder web height.

Type T thermocouple locations at the midspan cross section are also shown in Figure 8-3, consisting of either eleven or thirteen thermocouples dependent on the test. In selecting thermocouple positions, an effort was made to capture temperature profiles at changes in the cross-sectional width, as well as to concentrate sensors in areas expected to experience extreme temperature variations (i.e. extreme top and bottom fibers of girder).

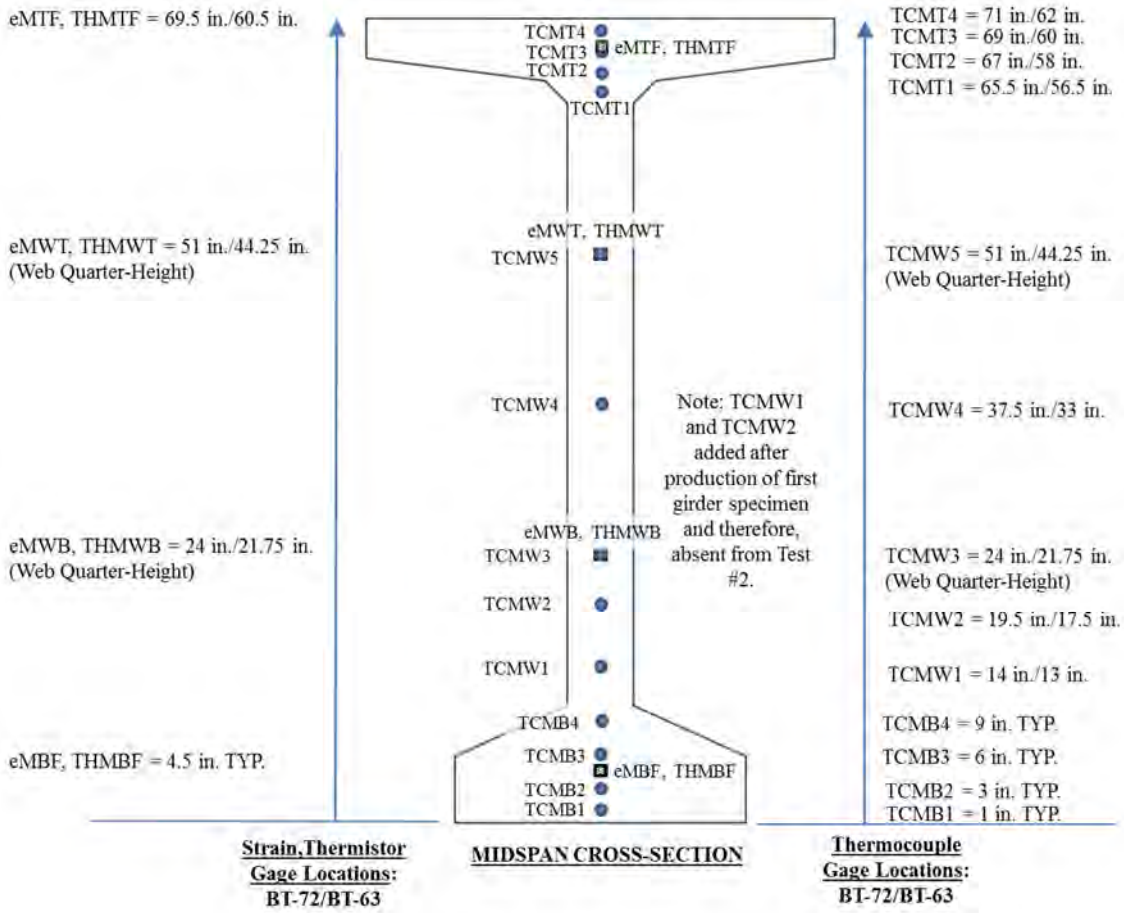

Figure 8-4: Typical Internal Instrumentation at Midspan Cross Section

Vibrating-wire strain gages were also installed at the 1/6-span cross section of girders specimens at similar depths. The primary purpose of these gages was to verify if different cross sections behaved similarly as hypothesized by the temperature-correction procedure for camber. The locations of the four additional 1/6-span gages are displayed in Figure 8-5.

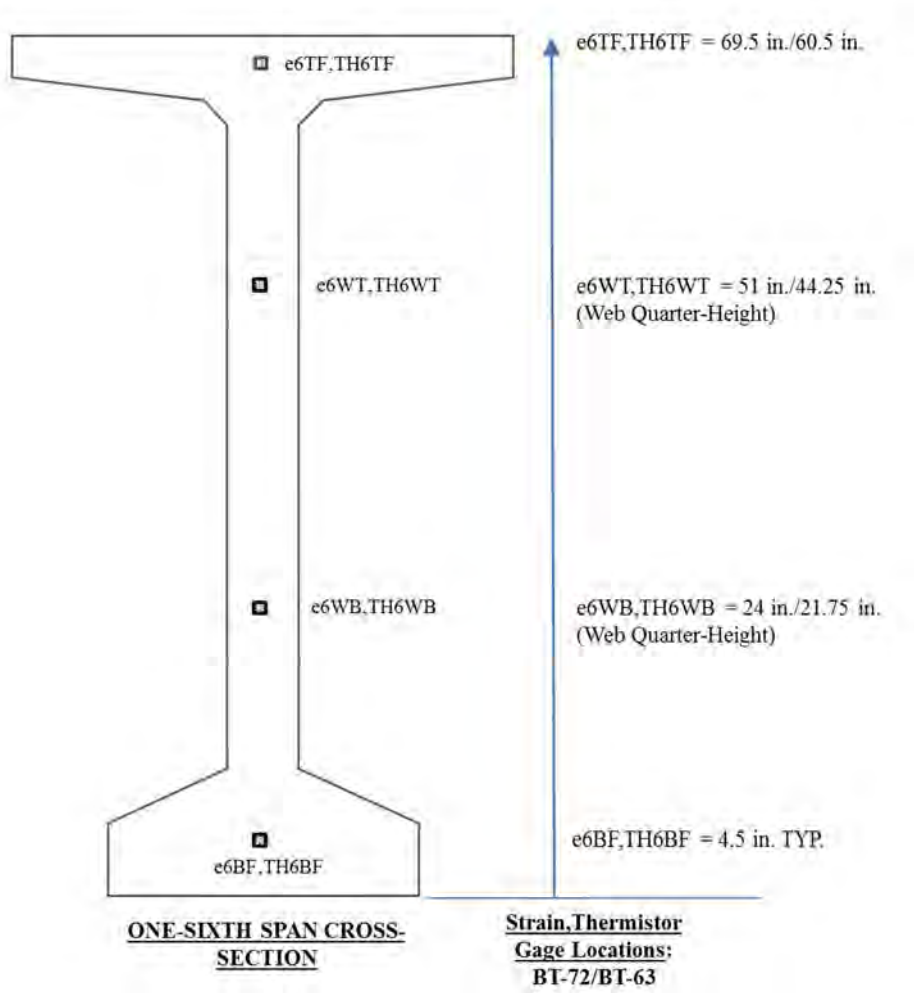

Figure 8-5: Typical Internal Instrumentation at 1/6-Span Cross Section

Both Figures 8-4 and 8-5 show the locations of internal gages measured from girder bottom for both specimen cross-sectional shapes included in this effort (BT-72 and BT-63 sections). A typical midspan installation of gages prior to concrete placement is shown in Figure 8-6.

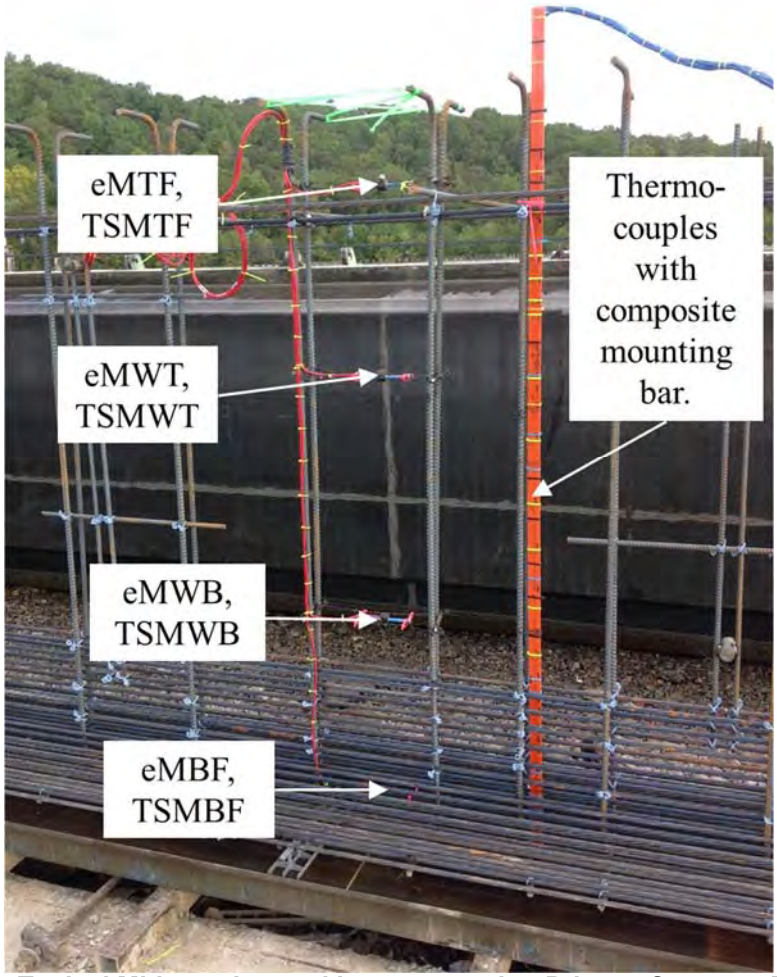

Figure 8-6: Typical Midspan Internal Instrumentation Prior to Concrete Placement

In contrast to the internal sensors which were installed during girder production, the external sensors were temporarily affixed to girder specimens during field monitoring. External sensors consisted of displacement gages attached to the girder bottom flange and tiltmeters affixed to the girder end as shown in Figure 8-7. A slightly modified spacing of the bottom-flange displacement gages was mistakenly used in Tests #1-2, but later corrected for Test #3.

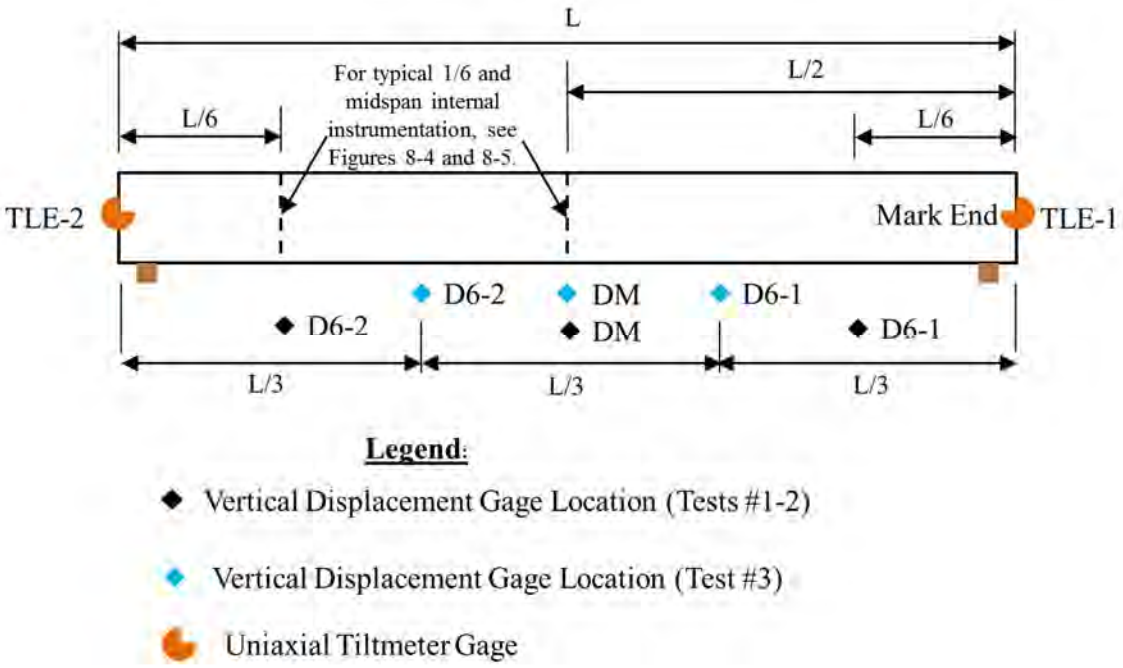

Figure 8-7: Typical Girder External Instrumentation for 24-Hour Tests

A typical 24-hour test in progress is shown in Figure 8-8 with all relevant instrumentation noted and the data acquisition vehicle also visible.

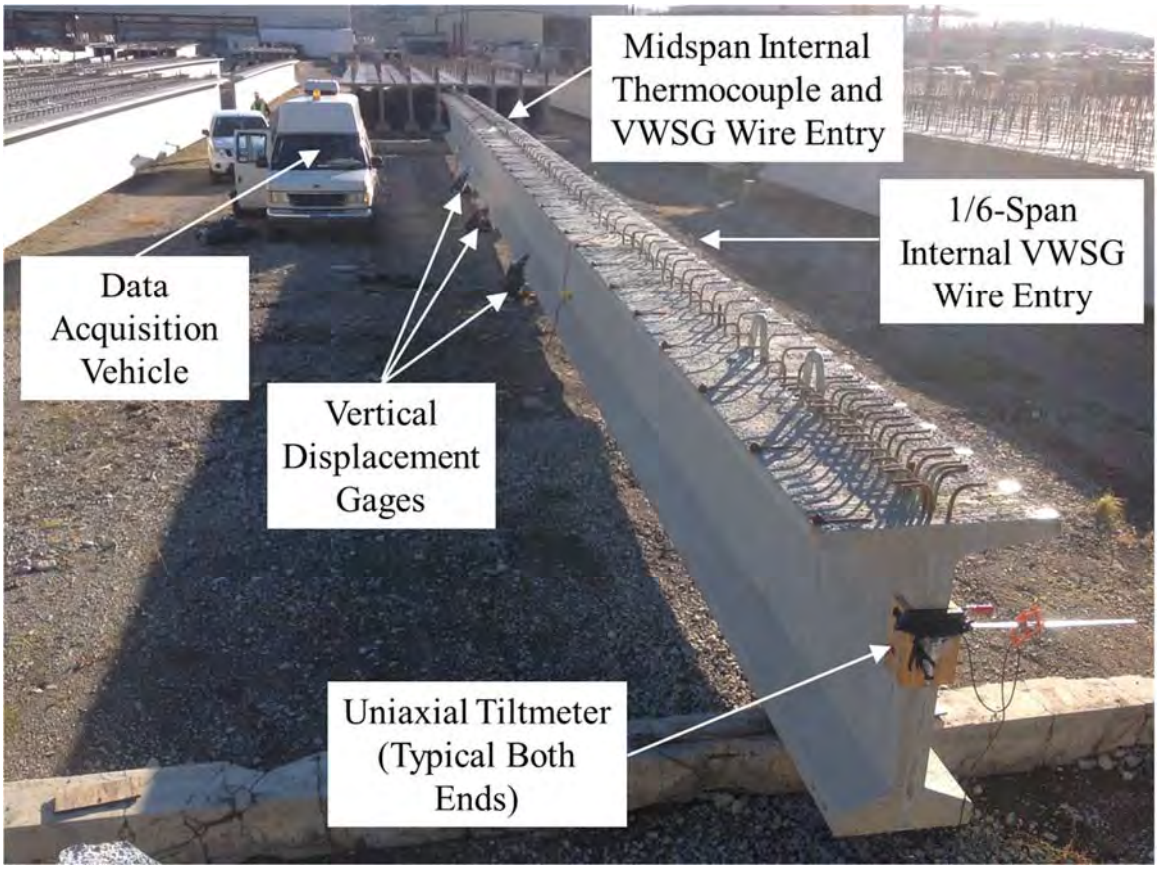

Figure 8-8: 24-Hour Test #3 in Progress

For data collection purposes, a custom data collection system was designed and assembled as shown in Figure 8-9. Key hardware features of the data collection system included (a) a battery backup capable of powering all instrumentation for the duration of each test, (b) a wireless link allowing real-time monitoring of experimental results from a mobile computer or tablet, (c) capability to monitor up to 32 VWSGs, (d) capability to monitor up to 32 thermocouple sensors, and (e) capability to monitor two tiltsensors.

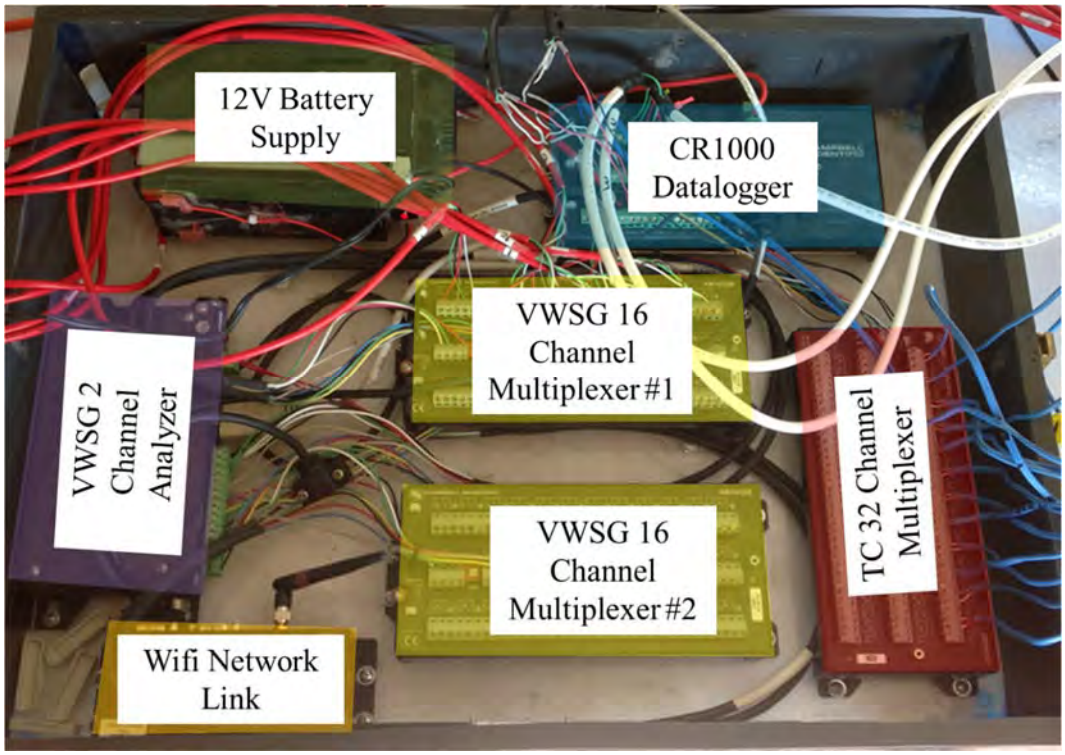

Figure 8-9: Typical Data Collection System for 24-Hour Tests

A custom sampling program was coded that monitored all sensors in 120-second intervals for the duration of each testing period. Details of both the data collection system components and the types/models of sensors used in this investigation are listed in Table 8-2.

Table 8-2: Sensor and Data Collection System Component Details

Type of Gage/Instrumentation	**Manufacturer and Model #**
Vibrating-Wire Strain Gage (VWSG) with Thermistor	Geokon 4200 Series
Draw Wire Displacement Sensor	Micro-Epsilon WDS-150-P60-CR-P
Type T Thermocouple	Varies
Data Collection System Components	**Campbell Scientific Model #**
Data Logger	CR1000
2-Channel Vibrating-Wire Spectrum Analyzer	AVW200
Three 16/32 Channel Multiplexers	AM16/32B
Wireless Network Link Interface	NL240

8.4 Presentation and Post-Processing of Raw Data

The purpose of this section is to present all data gathered as part of this experimental effort, while also detailing any post-processing efforts necessary to prepare the raw data for the analysis later described in Section 8.5 of this report. Major post-processing efforts included (a) detection and dismissal of flawed measurements, (b) examination of the linearity of measured strain profiles to confirm proper function and

positioning of internal strain gages, and (c) validation of duplicate measurements (i.e. examining similarities between adjacent thermistor and thermocouple gages). Then, various observations are offered on the magnitude and typical shapes of the diurnal temperature profiles observed in this study and previous research work by others.

8.4.1 Presentation of Raw Data by Test

Raw experimental results for Test #1 are displayed in Figures 8-10 through 8-13. Measured internal concrete temperatures at both midspan (all thermocouple and thermistor measurements) and 1/6-span (thermistor measurements) are shown in Figure 8-10. Also shown on this plot (and all other plots in this section) are the approximate timings of dawn and dusk during the test duration. For reference, the horizontal axis of all plots displayed herein begins at the start of the test (time t = 0) and extends through the duration of the test.

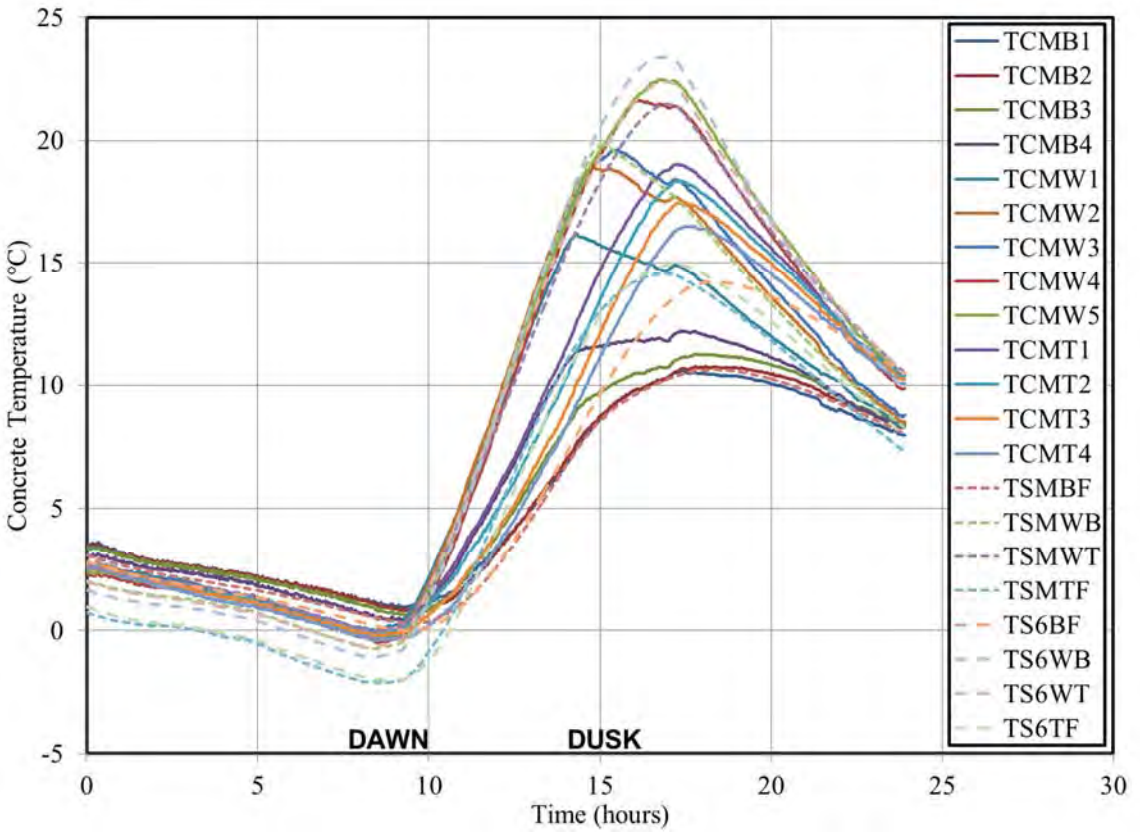

Figure 8-10: Test #1 Recorded Concrete Temperatures

Although Figure 8-10 conveniently displays all recorded temperature data from Test #1 in a single plot, the form of this plot is not conducive to the identification of specific trends within the recorded data set.

For this purpose, Section 8.4.3 later displays recorded temperature data in a more useful format to allow discussion and comment on recorded data. Changes in internal concrete strain at both midspan (eM-series) and 1/6-span (e6-series) for Test #1 are displayed in Figure 8-11. These strain values are unprocessed with the exception of the use of a manufacturer-specified gage temperature-correction factor and zeroing of readings with respect to the initial (t=0) reading.

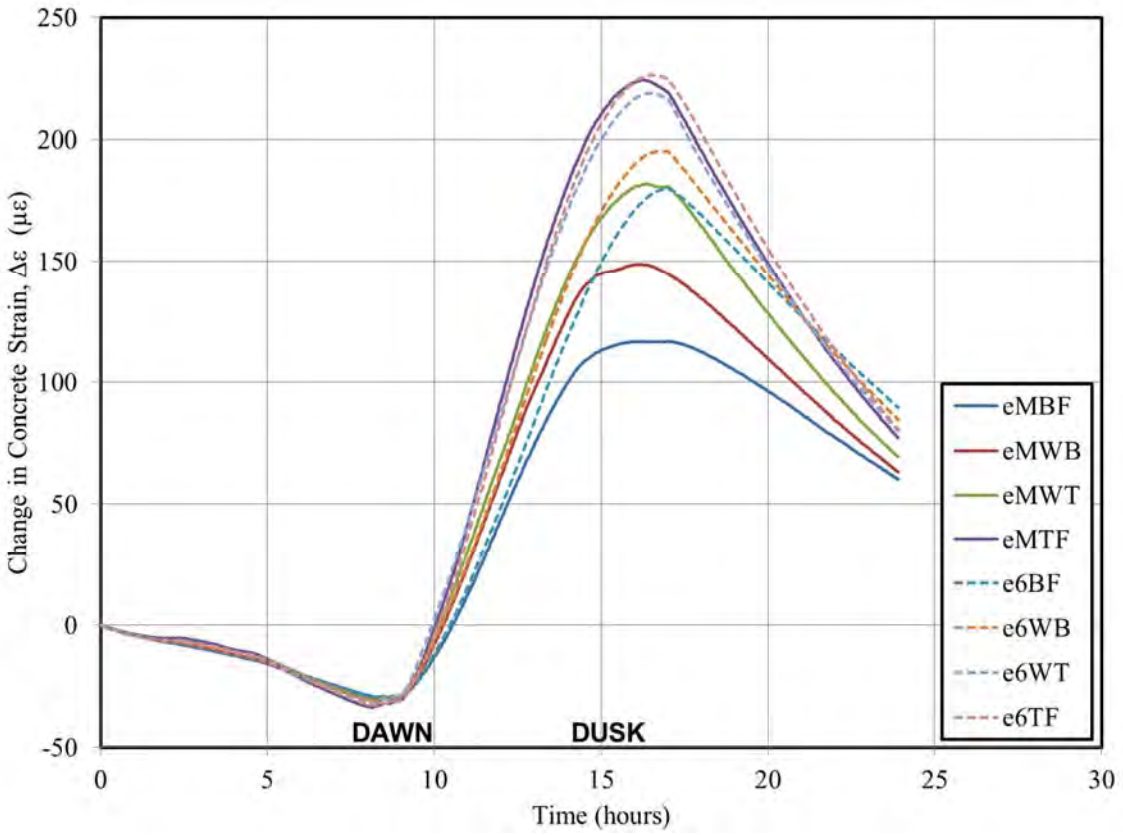

Figure 8-11: Test #1 Recorded Concrete Strains

Recorded vertical displacements for Test #1 are shown in Figure 8-12. As shown, the precision of the displacement sensors utilized in this investigation (approximately 0.01 inches) is visible in the plot. Girder response appears relatively symmetric with peak displacement values occurring at midspan as expected. Raw readings of girder end rotations are shown in Figure 8-13.

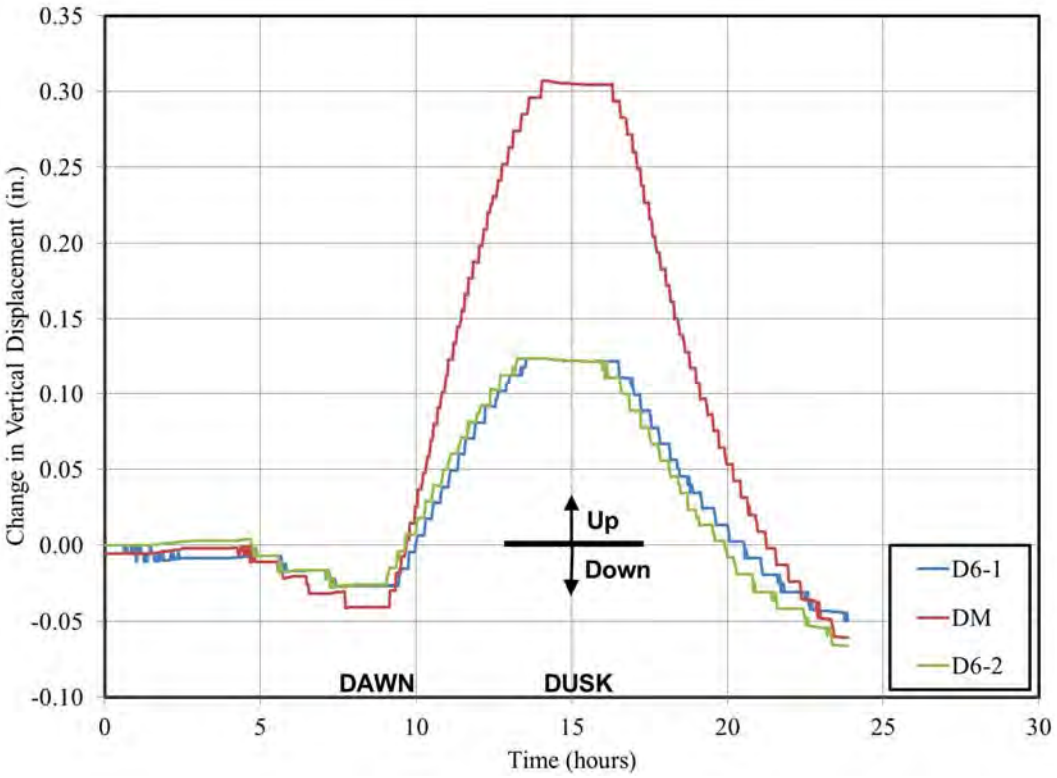

Figure 8-12: Test #1 Recorded Vertical Displacements

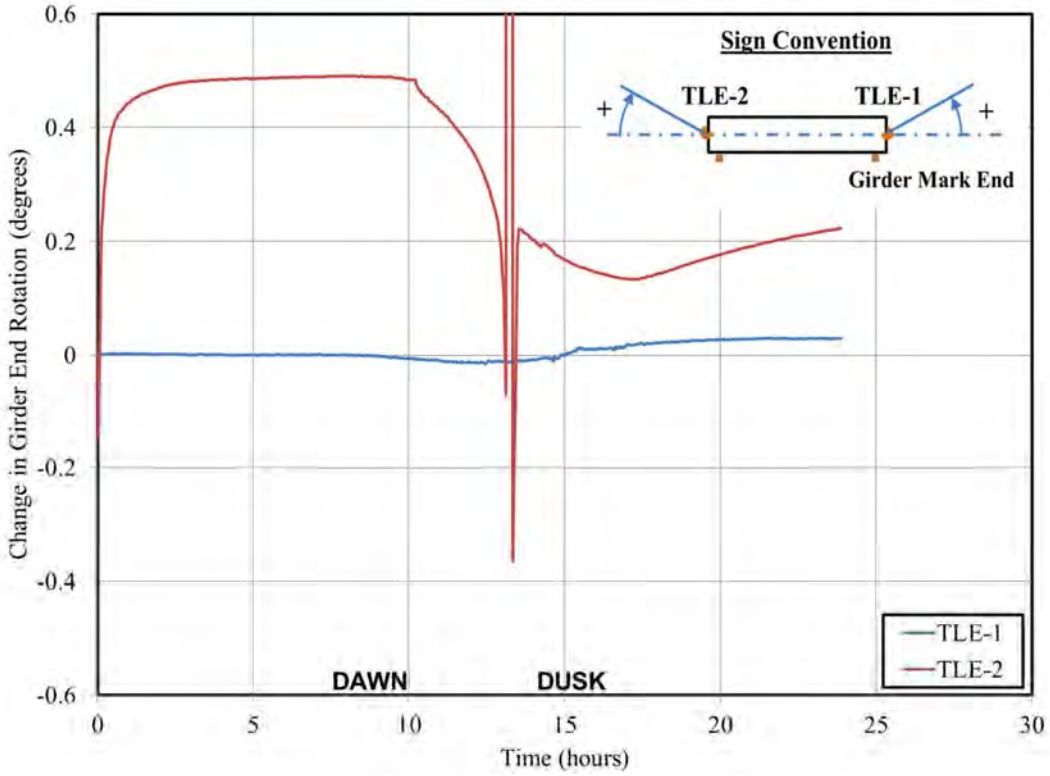

Figure 8-13: Test #1 Recorded Girder End Rotations

The readings from sensor TLE-2 were compromised as a result of the failure of an adhesive[7] used to affix sensor TLE-2 to the girder specimen. Additionally, close inspection of the girder end rotations recorded for sensor TLE-1 show disagreement with the observed vertical displacement trends of Figure 8-12. For instance, girder end rotation readings of gage TLE-1 fail to consistently return to benchmark values (t=0) at times when other measures of girder deformation (e.g. vertical deflection) return to zero (t=10 hours and t=20 hours)—suggesting an apparent drift of tiltmeter readings throughout the testing period. For this reason, the readings of the tiltmeters used in this investigation were found to be unreliable and despite being reported in this section, were omitted from remaining analyses. Similar results are shown in Figures 8-14 through 8-17 for Test #2. Recall, Test #2 utilized only 11 thermocouple sensors at midspan as opposed to the 13 sensors present in Tests #1 and 3.

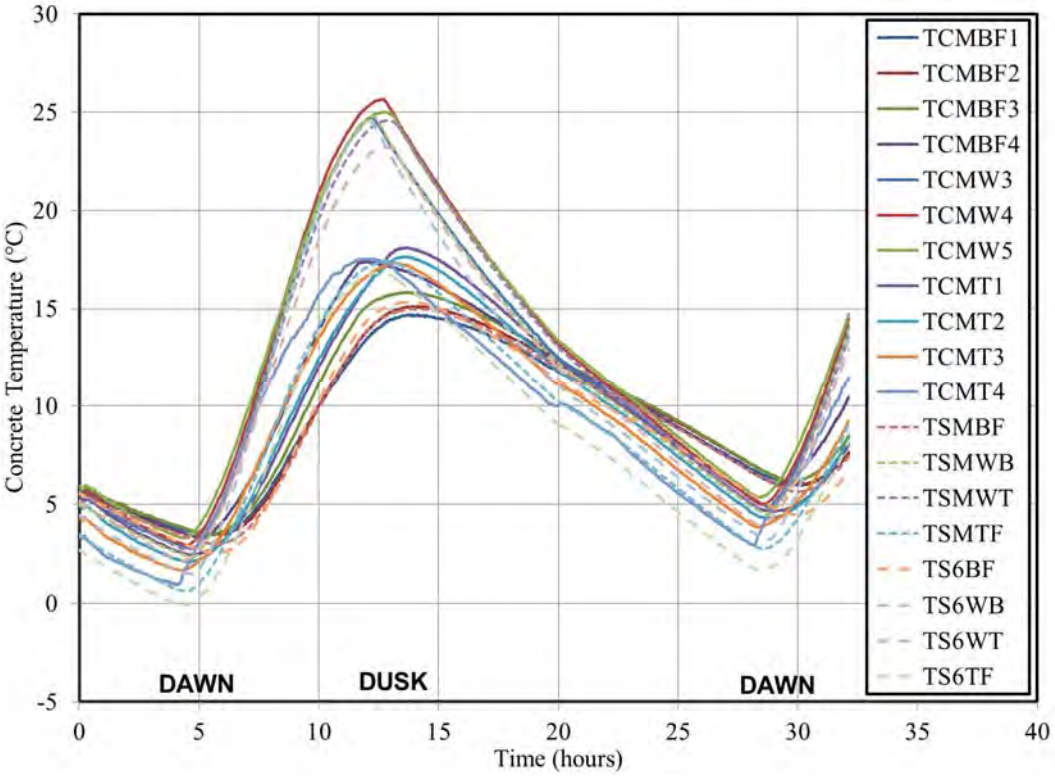

Figure 8-14: Test #2 Recorded Concrete Temperatures

[7] The epoxy used to attach the tiltmeter mounting bracket to the skewed girder web failed to sufficiently chemically activate due to below-freezing temperatures during test setup.

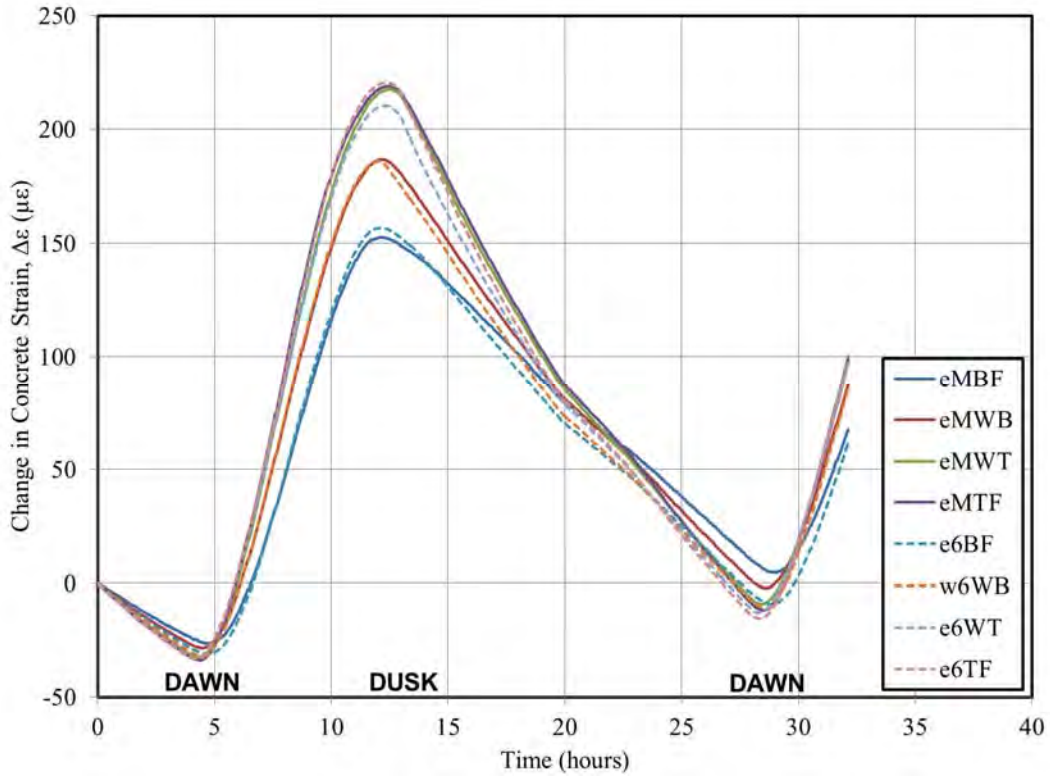

Figure 8-15: Test #2 Recorded Concrete Strains

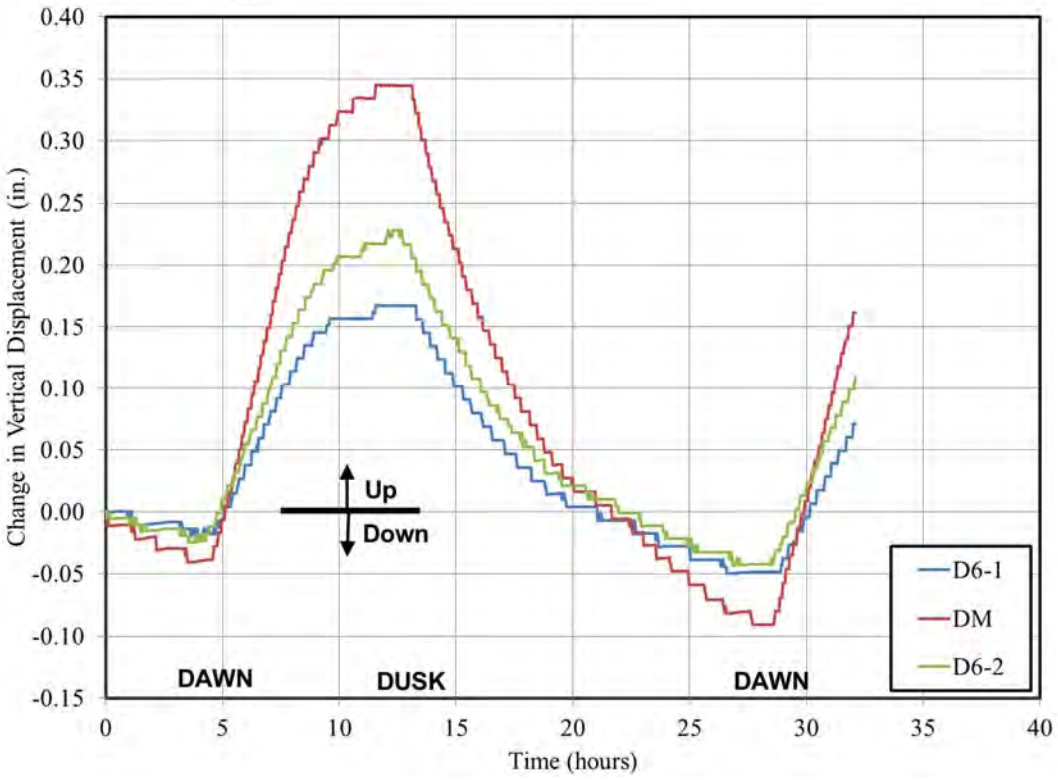

Figure 8-16: Test #2 Recorded Vertical Displacements

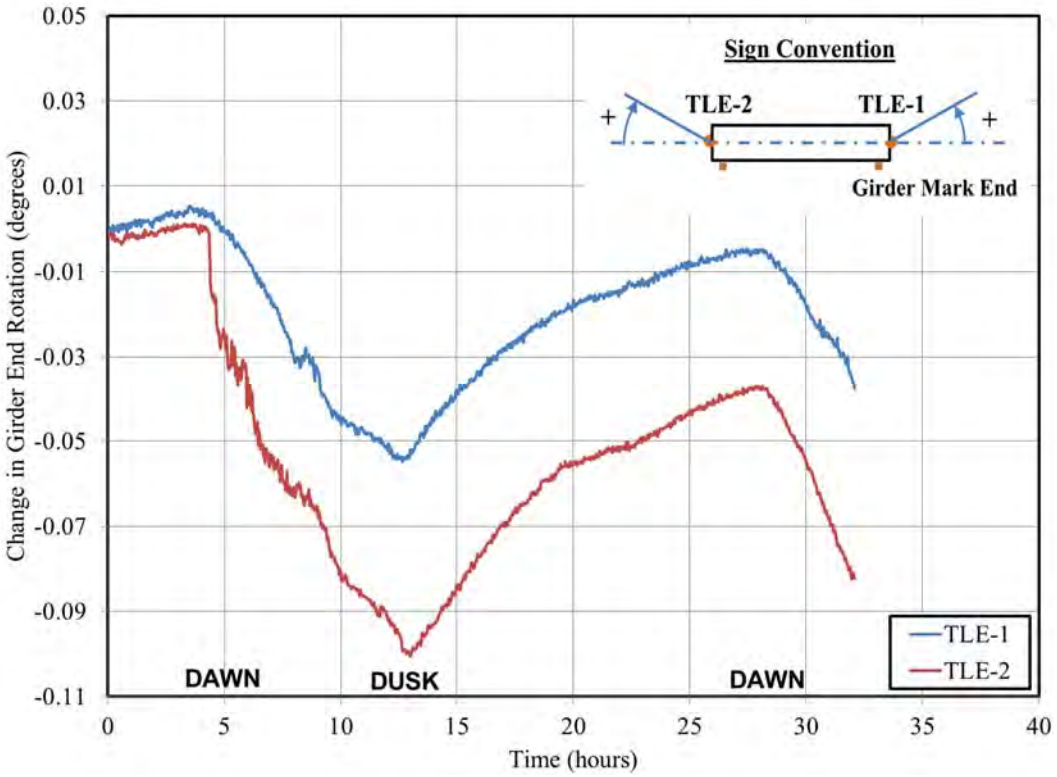

Figure 8-17: Test #2 Recorded Girder End Rotations

Similar plots are displayed in Figures 8-18 through 8-21 for Test #3. As noted on each plot, a change in the ambient weather conditions occurred approximately 5 hours into the test during Test #3 with the ambient temperature first slightly increasing, then rapidly decreasing 6°C in the five-hour period coinciding with testing hours 5 through 15. This weather change affords an opportunity to evaluate the accuracy of the temperature-correction procedure with respect to a change in ambient temperature independent of solar radiation.

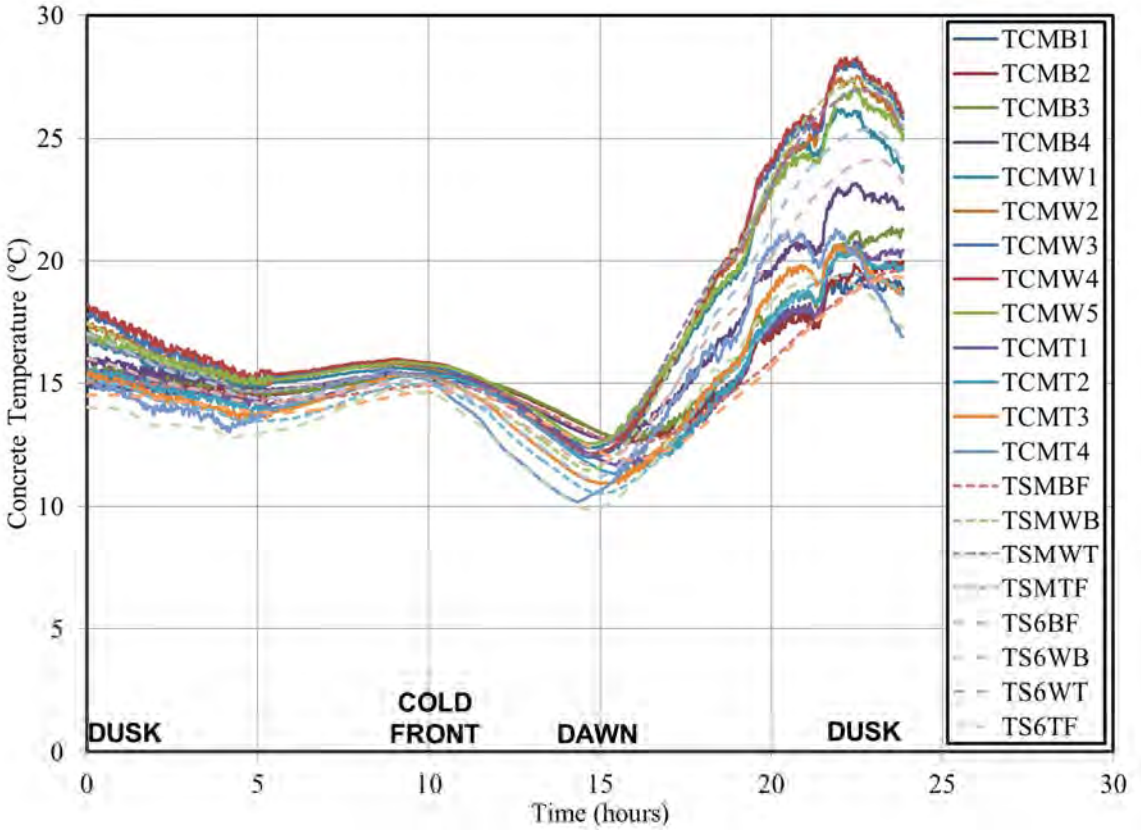

Figure 8-18: Test #3 Recorded Concrete Temperatures

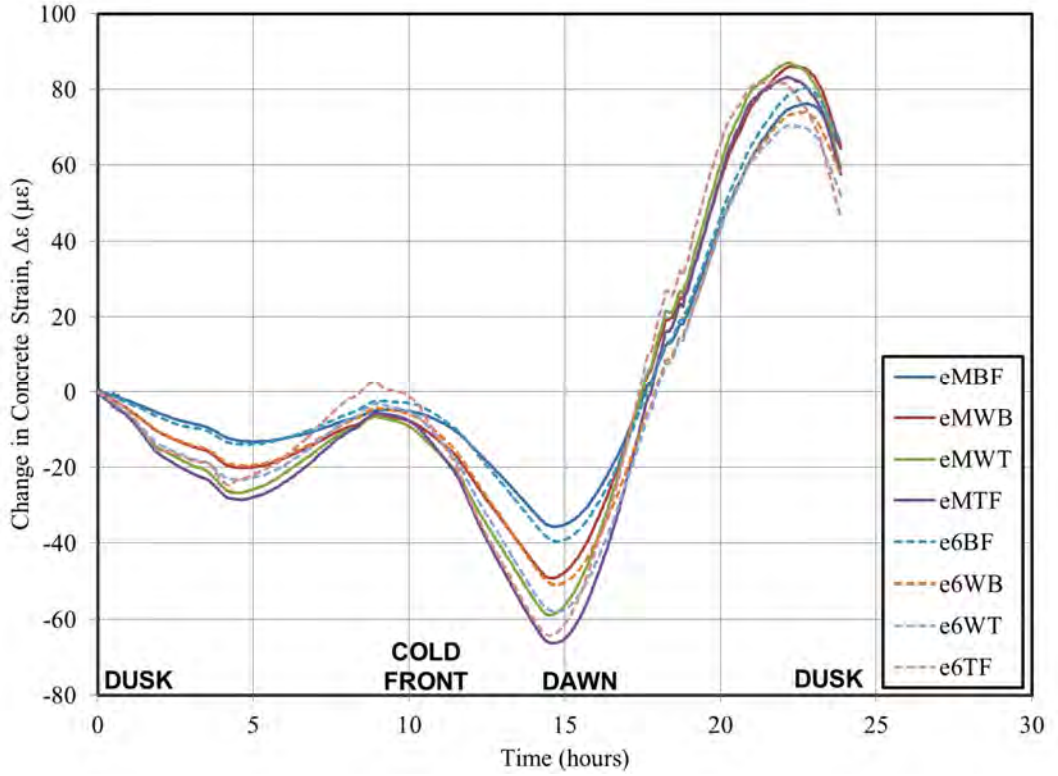

Figure 8-19: Test #3 Recorded Concrete Strains

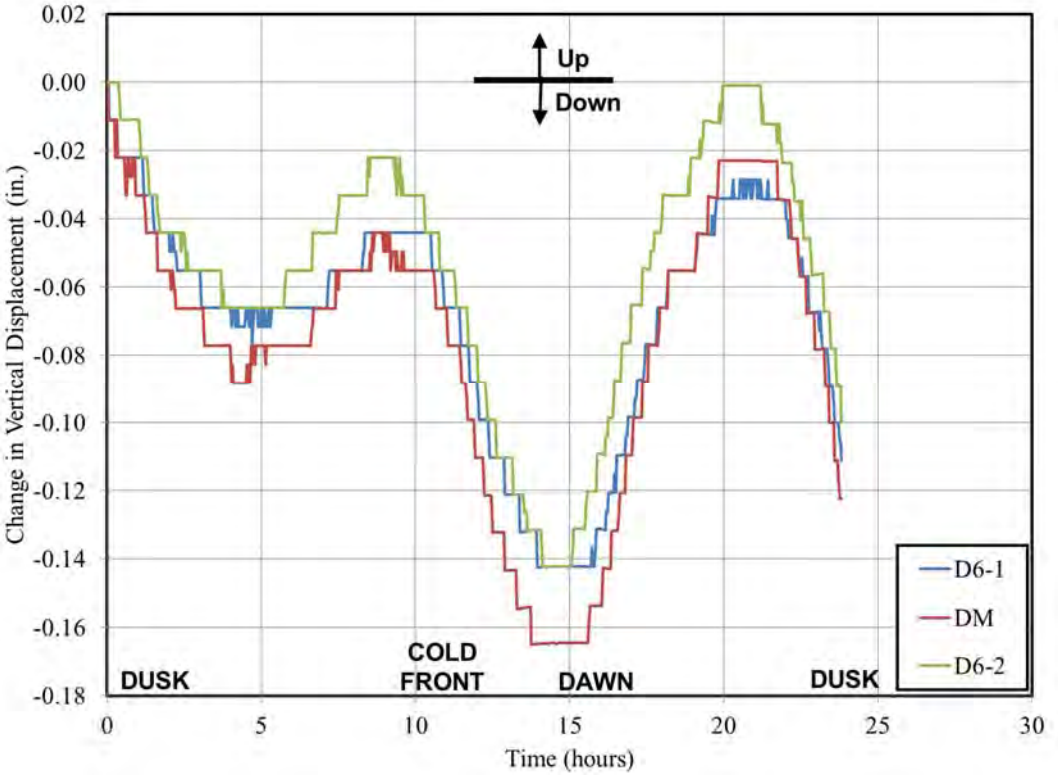

Figure 8-20: Test #3 Recorded Vertical Displacements

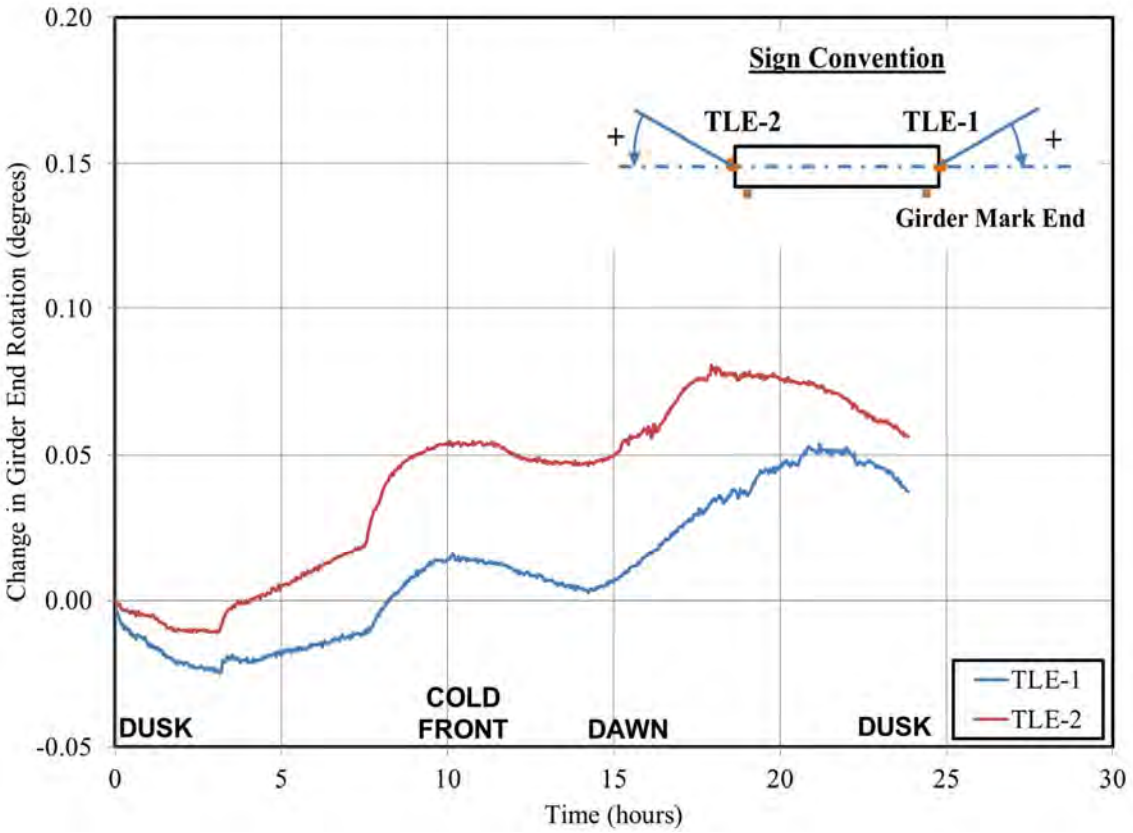

Figure 8-21: Test #3 Recorded Girder End Rotations

The following general observations are based on consideration of the raw data shown in Figures 8-10 through 8-21:

1. Tests #1 and 2 appear to have captured the most extreme temperature-induced deformational behavior, followed by Test #3;
2. Maximum observed fluctuations in internal concrete temperature of nearly 25°C (44°F) were recorded throughout Tests #1 and 2, with a maximum range within the cross section at a single time of roughly 15°C;
3. Maximum observed temperature-induced changes in internal concrete strains of approximately 250 microstrain were observed, with a maximum range within the cross section at a single time of roughly 120 microstrain;
4. Maximum observed temperature-induced changes to midspan displacement of approximately 0.45 inches were recorded;

5. With the exception of the readings of tilt sensors, a preliminary inspection of all readings does not warrant dismissal of any additional values; and
6. The deformational response of the girder, as manifested in external displacement measures, indicates relatively symmetric behavior of girder specimens in response to observed diurnal temperature profiles.

8.4.2 Validation of Recorded Data

During the placement of concrete in the fabrication of precast, prestressed concrete girders, there exists the potential for damage to internally-positioned sensors, primarily by shifting of gages by fresh concrete and incomplete consolidation in the vicinity of gages. Two methods were employed to validate the accuracy of recorded data: (1) confirmation of the linearity of recorded strain measurements across a cross-section depth, and (2) comparisons of readings from adjacent sensors.

A procedure was developed to confirm proper positioning and operation of the vibrating-wire strain gages installed during the fabrication of the three specimens included in this study. The basic premise of this method was to confirm the linearity of strain profiles induced during deformation. A convenient statistical metric for this purpose is the use of the coefficient of determination, R^2. In general, the coefficient of determination is an indicator of the proportion of the observed variation accounted for by a fitted statistical model. In the application used herein, a linear model was fitted to measured strain values (recorded at four depths within a girder) and a corresponding value of R^2 was then computed. For reference, values approaching 1.0 indicate an exceptionally good linear fit of experimental data. While relatively simple in application, a complication of this analysis procedure arises for experimental data sets representing vertical (or nearly vertical) lines. In this case, the dependent variable, strain, does not vary as a function of the independent variable, height within girder. For this reason, the coefficient of determination is not a valid indicator of the goodness-of-fit of a linear model for vertical lines. To avoid this complication, it was decided to compute the coefficient of determination of linear fit at only a single time for each set of readings—the time of maximum temperature-induced curvature. Values of the coefficient of determination for these situations are summarized in Table 8-3 and also depicted graphically in Figure 8-22.

Table 8-3: Verification of Linearity of Installed Strain Gages

	R^2 of Linear Fit to Measured Strain Readings at Time of Maximum Temperature-Induced Curvature	
Test #	**Midspan**	**1/6-Span**
1	0.99	0.97
2	0.93	0.98
3	0.98	0.98

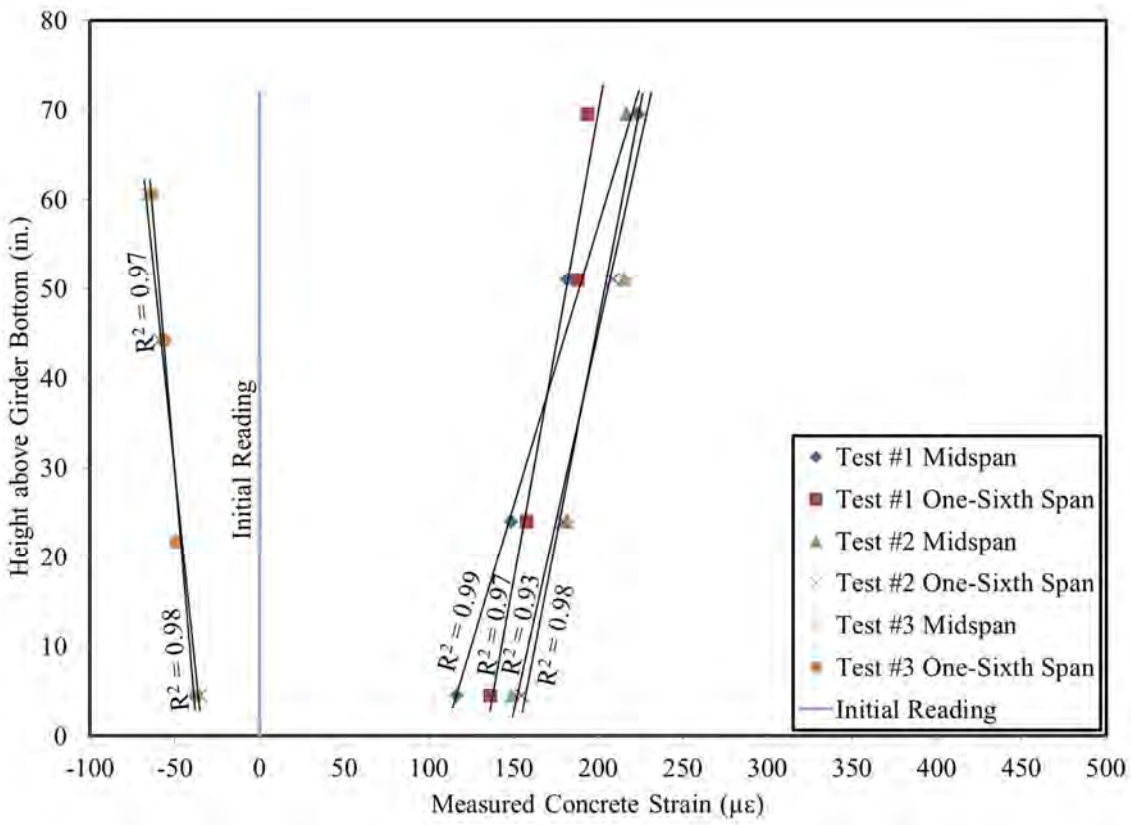

Figure 8-22: Verification of Linearity of Installed Strain Gages

As shown in Figure 8-22, the linear fit of Test #2 midspan data represents the poorest fit, with an R^2 value of 0.925. After a thorough review of site notes, photographs, and gage readings during concrete placement, it became apparent that the top midspan gage (eMTF) may have shifted during concrete placement as a result of the failure of reinforcement ties during girder fabrication. The observed failure, as illustrated in Figure 8-23, resulted from the following mechanism: (a) researchers instructed plant staff to avoid placing concrete directly on to gages to avoid damage, (b) plant staff accommodated the request, resulting in an area void of concrete within the two stirrup bays containing gages, (c) as concrete attempted to flow inward to fill the void during internal vibration, stirrup ties connecting the stirrup to the

prestressing strands failed to resist the unbalanced lateral force applied by the concrete, resulting in (d) rotation of the stirrup as shown. During placement, an attempt was made to reposition the stirrup after the unintentional relocation, although the top vibrating-wire strain gage may not have been returned to its intended location.

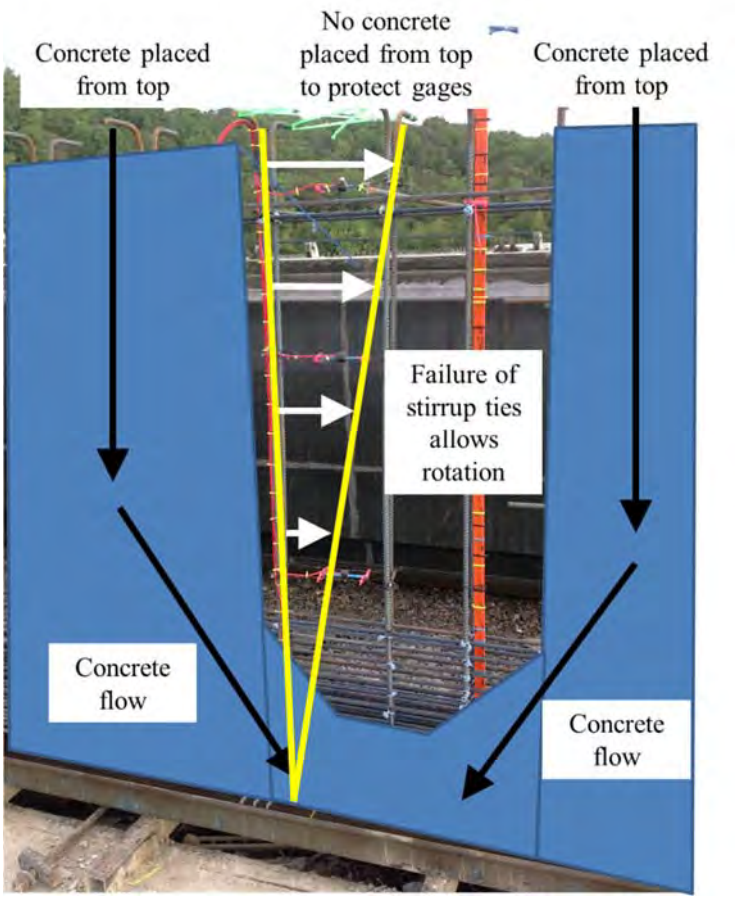

Figure 8-23: Observed Failure Mechanism of Midspan Gages

To avoid failures in future gage installations, the research team (1) separated the location of the vibrating-wire strain gage assembly from the location of the thermocouple assembly by at least 2–3 stirrup bays to allow concrete placement from above between the gage assemblies (thereby, reducing hydrostatic pressure differentials) and (2) inserted timber dunnage as shown in Figure 8-24 to shield installed gages from overhead concrete placement and prevent lateral translation of stirrups. Future researchers placing gages within girders are advised to consider a similar system to reduce the incidence of damaged gages during concrete placement.

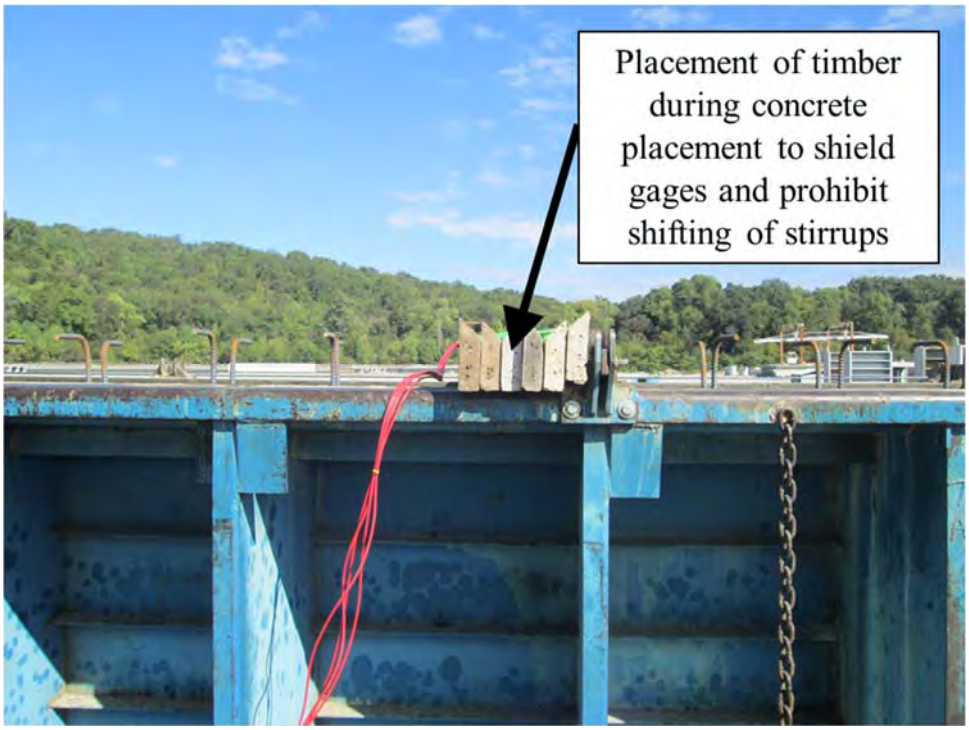

Figure 8-24: Placement of Timber to Avoid Gage Damage during Concrete Placement

Despite the coefficient of determination determined for the linear regression of Test #2 midspan strain measurements being somewhat less than for other similar tests and locations, preservation of the reading from the eMTF gage did cause a substantial change in the results of subsequent analyses performed in this chapter and, therefore, for completeness this reading is included in the remaining analyses of this chapter.

In order to confirm proper positioning and operation of installed thermocouple sensors, a more simple analysis method was used than that detailed above for strain measurements. By directly comparing readings of adjacent sensors, that is, sensors of different types positioned at similar locations, the validity of measured field temperature data was evaluated. Comparisons of temperature measurements recorded by both thermocouples and thermistors are displayed in Figures 8-25 through 8-27.

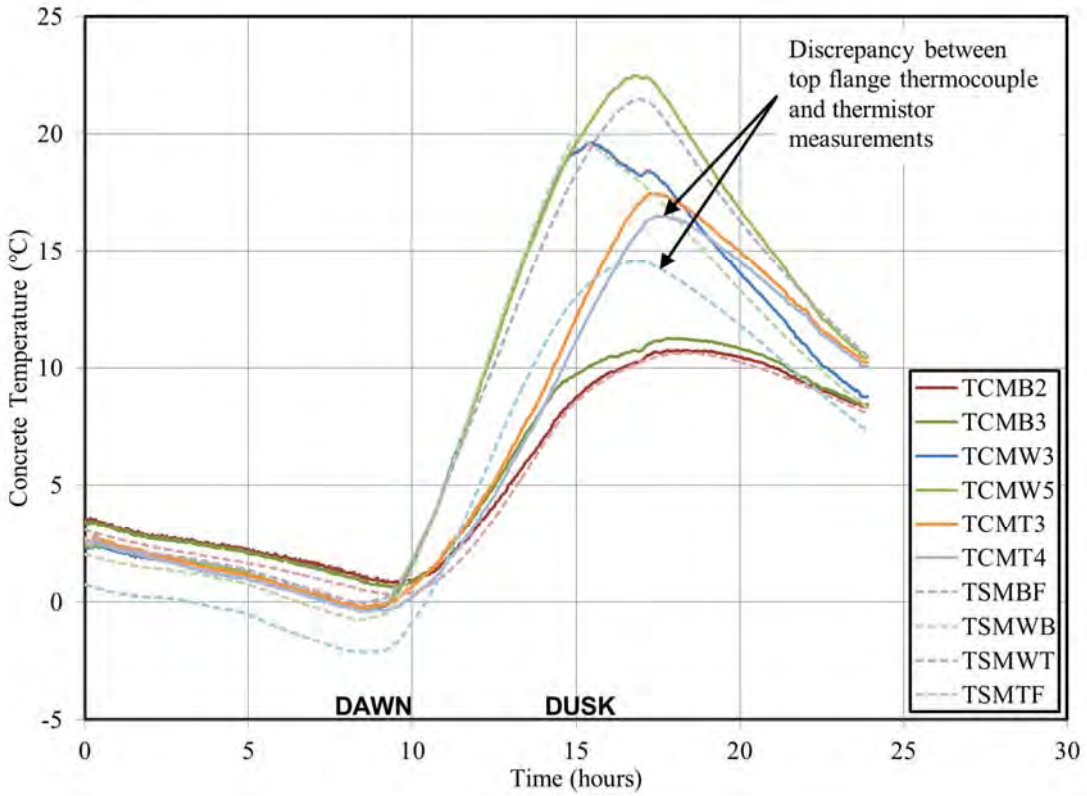

Figure 8-25: Test #1 Measured Temperatures

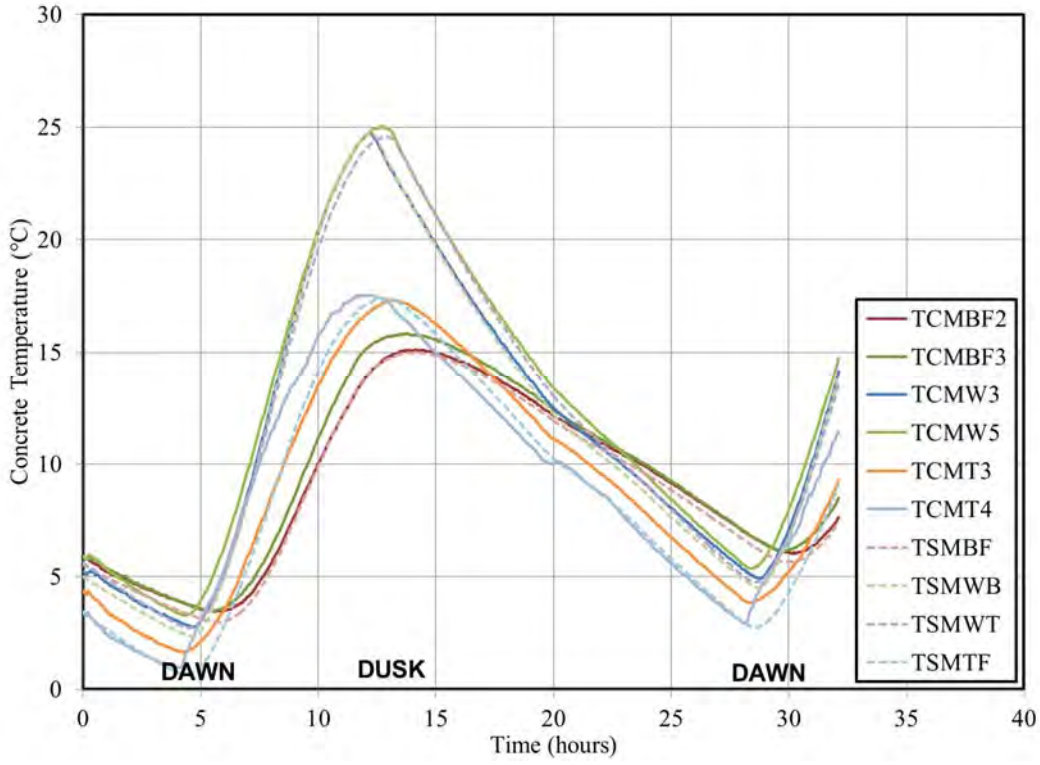

Figure 8-26: Test #2 Measured Temperatures

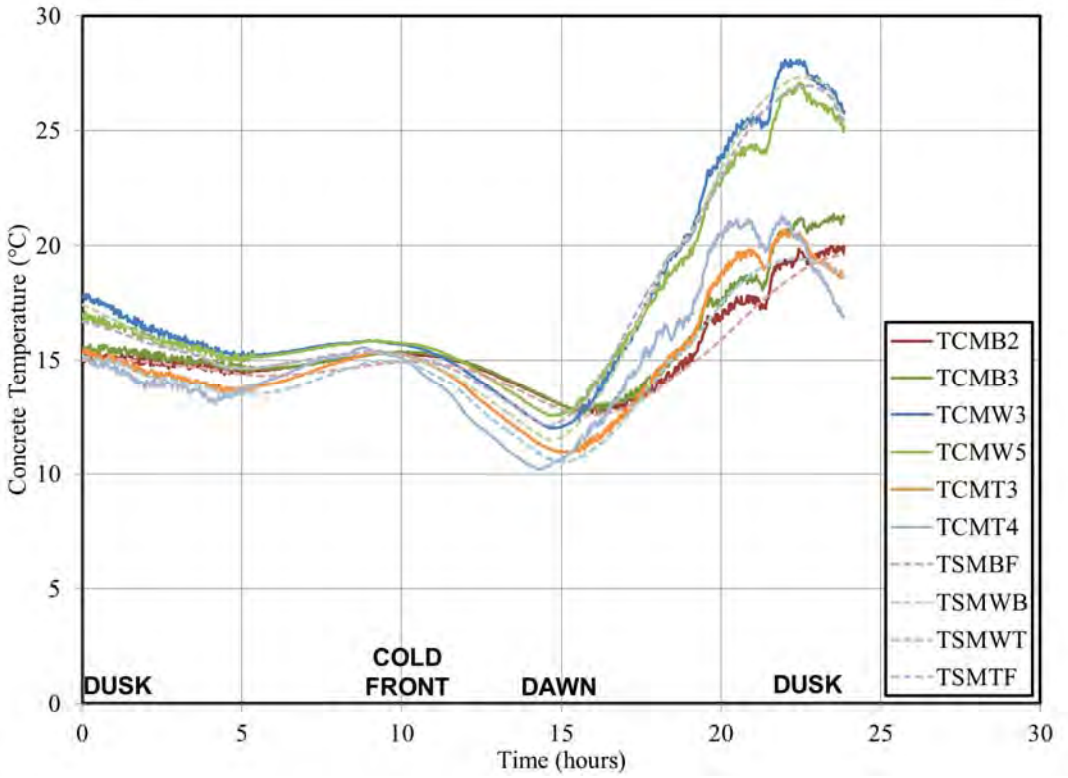

Figure 8-27: Test #3 Measured Temperatures

Readings of gage TSMBF are expected to fall between readings of gages TCMB2 and TCMB3, readings of gage TSMWB and TSMWT are expected be nearly identical to readings of TCMW3 and TCMW5, respectively, and readings of gage TSMTF are expected to fall between readings of TCMT3 and TCMT4. In general, agreement among measured temperature results was largely as expected, although there did exist a suspicious discrepancy among the top flange readings (TSMTF, TCMT3, and TCMT4) in Test #1. In addition, an analysis of the thermocouple sensor readings from Test #3 shows that at various times within the test, increased electrical noise was detected in the sensor signals. While this increased noise does not appear to compromise the results, this noise appears only during operation of the on-site computer and thus is likely a result of interference caused by either the AC adapter wiring of the laptop computer or the RS232 data transfer cable. For reference, a photograph of the test setup inside the mobile laboratory, with possible sources of electrical interference labelled, is shown in Figure 8-28. Future researchers conducting similar on-site testing are advised to not only confirm sensor readings are within expected ranges after experimental setup, but also to evaluate a series of continuous measurements to identify any electrical interference presence in sensor signals.

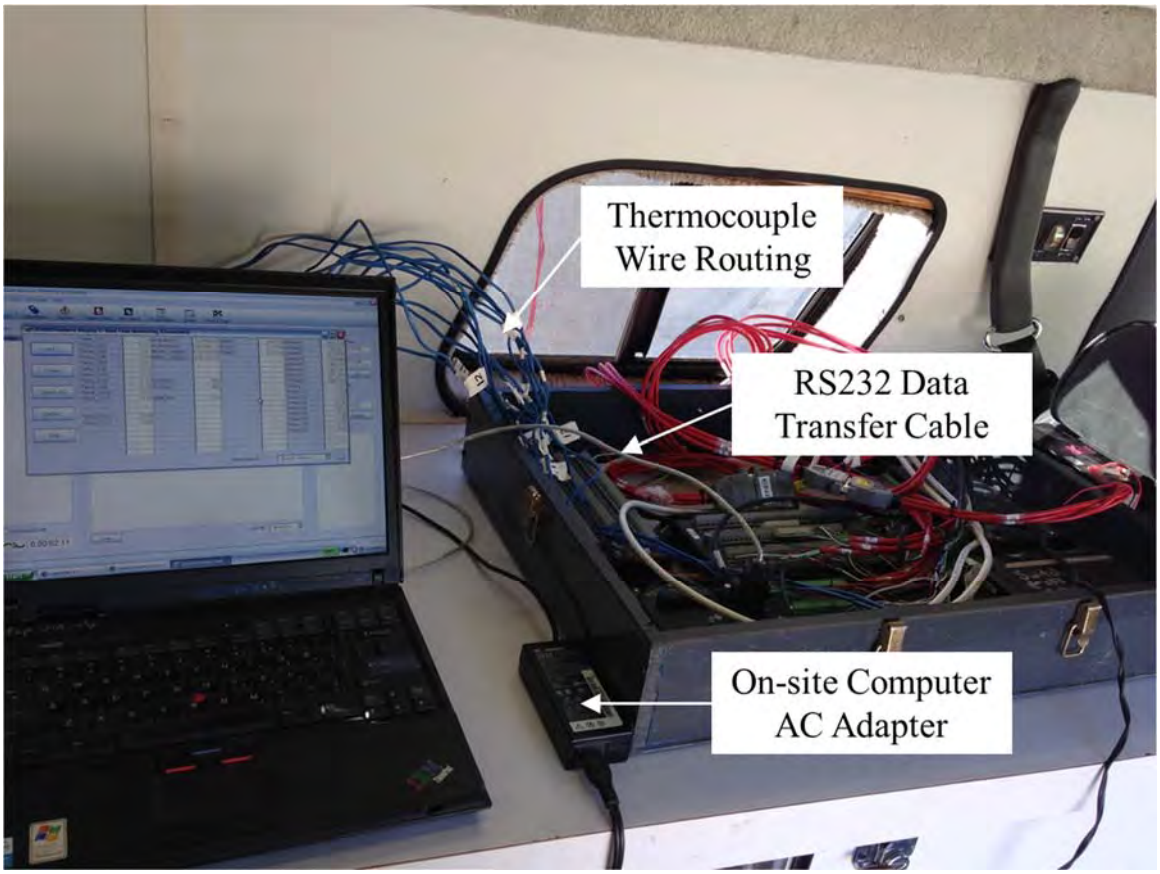

Figure 8-28: Data Acquisition Setup for Test #3

8.4.3 Discussion of Observed Vertical Temperature Profiles

The visualizations of the measured internal concrete temperature data contained in Figures 8-10, 8-14, and 8-18 are not ideal for identification of vertical temperature profiles within girders at various times throughout each test. For this purpose, the data of these figures are displayed in a somewhat more convenient form in this section. Then, a discussion summarizing the observed trends in experimental data is presented and comparisons are made to previous work by others.

For each test, three separate plots are presented, reflecting (1) midspan thermocouple gages, (2) midspan VWSG thermistor gages, and (3) 1/6-span VWSG thermistor gages. Results of Test #1 are shown in Figure 8-29 through 8-31. The vertical axis of each plot represents elevation within the girder cross section, while the horizontal axis displays internal concrete temperature at a given location. For each hour of the test duration, the internal vertical temperature profile is displayed. Arrows and key hours of timing within the test are shown overlayed on each plot to help clarify the progression of vertical temperature profiles as a function of time. To progress chronologically through the data presented in

Figure 8-29 through 8-31, readers should use the following steps: (a) begin at the time t=0 hours, proceeding left to t=8 hours by following solid lines, (b) proceed right following dashed lines until t=17 hours is reached, and finally, (c) proceed left following solid lines until test completion (t=24 hours). Similar plots detailing the recorded temperature readings of Tests #2 and 3 are shown in Figures 8-32 through 8-34 and Figures 8-35 through 8-37, respectively. Trends similar to those identified in Test #1 are seen for Test #2. The results of Test #3, as shown in Figures 8-35 through 8-37, are somewhat more difficult to interpret because four temperature reversals (as shown on superimposed arrows) occur during this test.

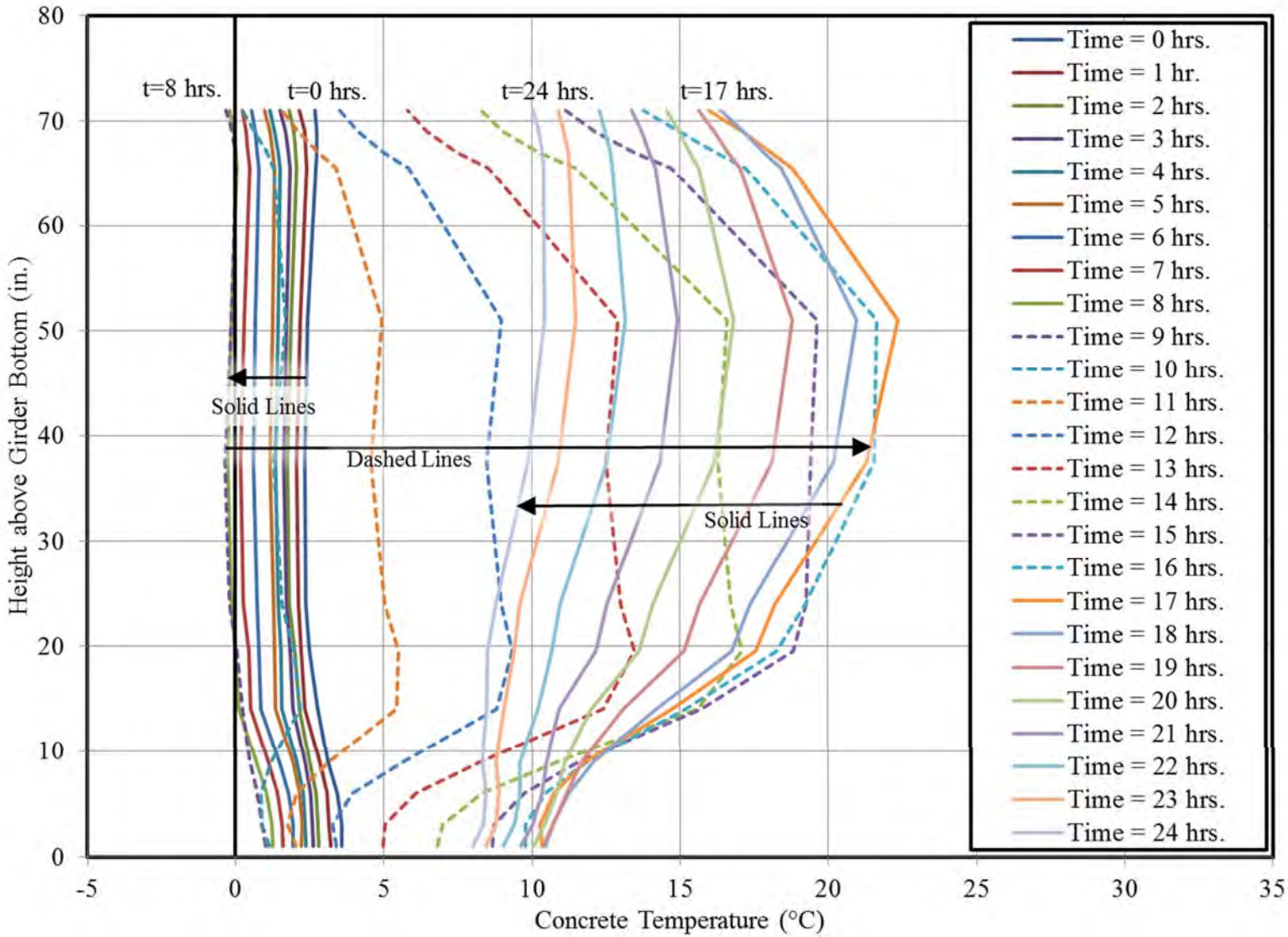

Figure 8-29: Midspan Thermocouple Results (TCM-Series) for Test #1

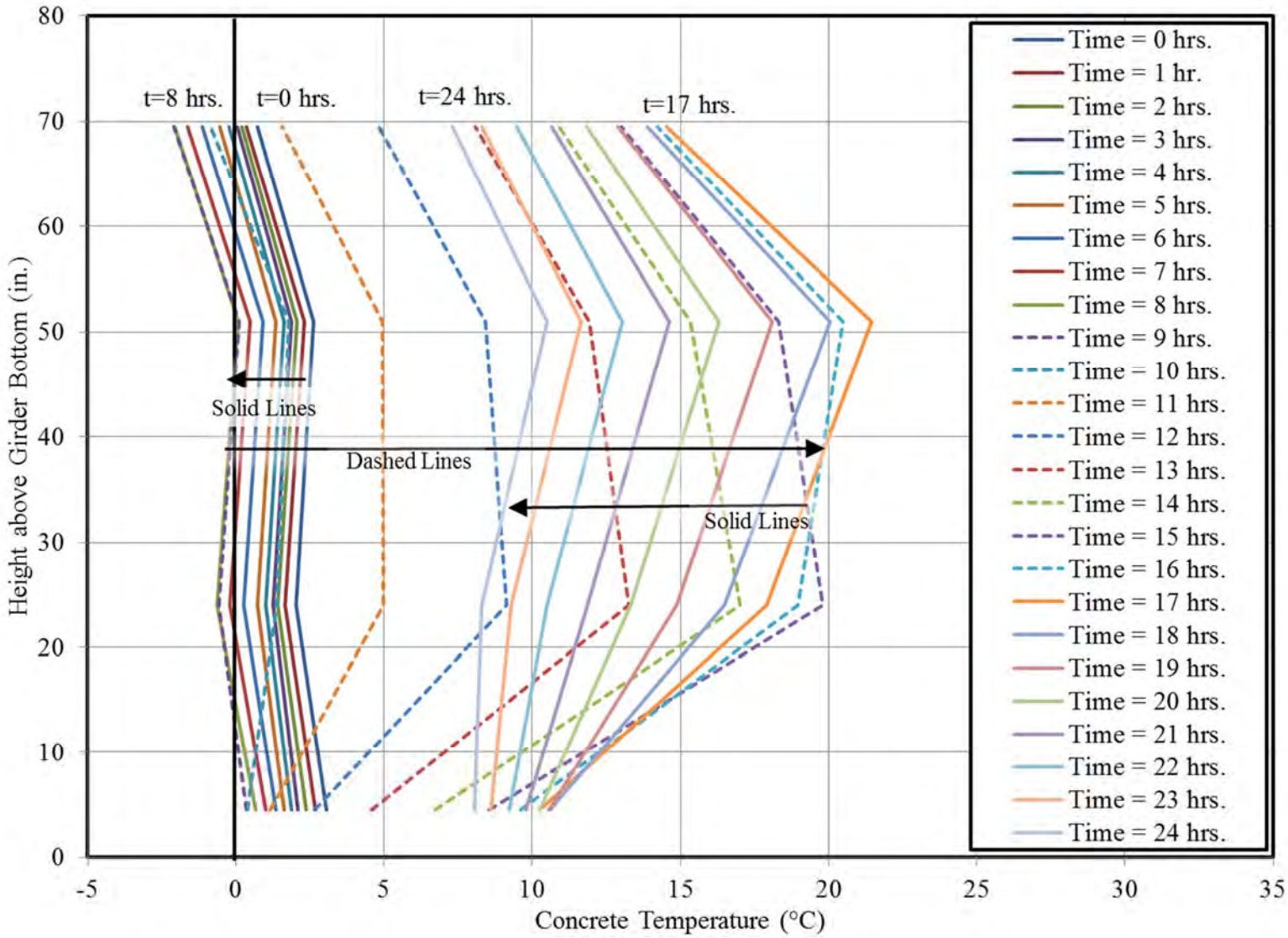

Figure 8-30: Midspan Thermistor (TSM-Series) Results for Test #1

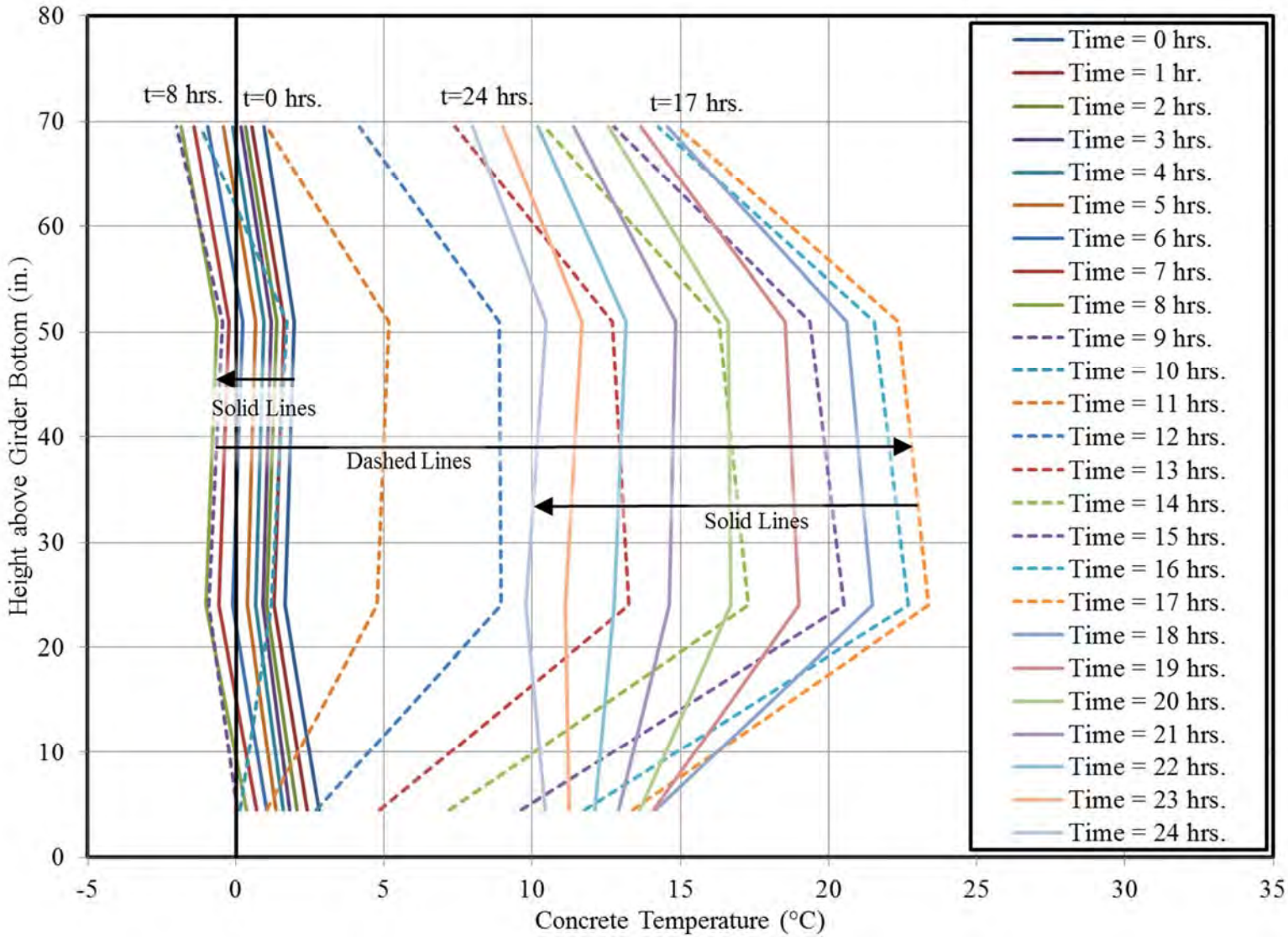

Figure 8-31: 1/6-Span Span Thermistor (TS6-Series) Results for Test #1

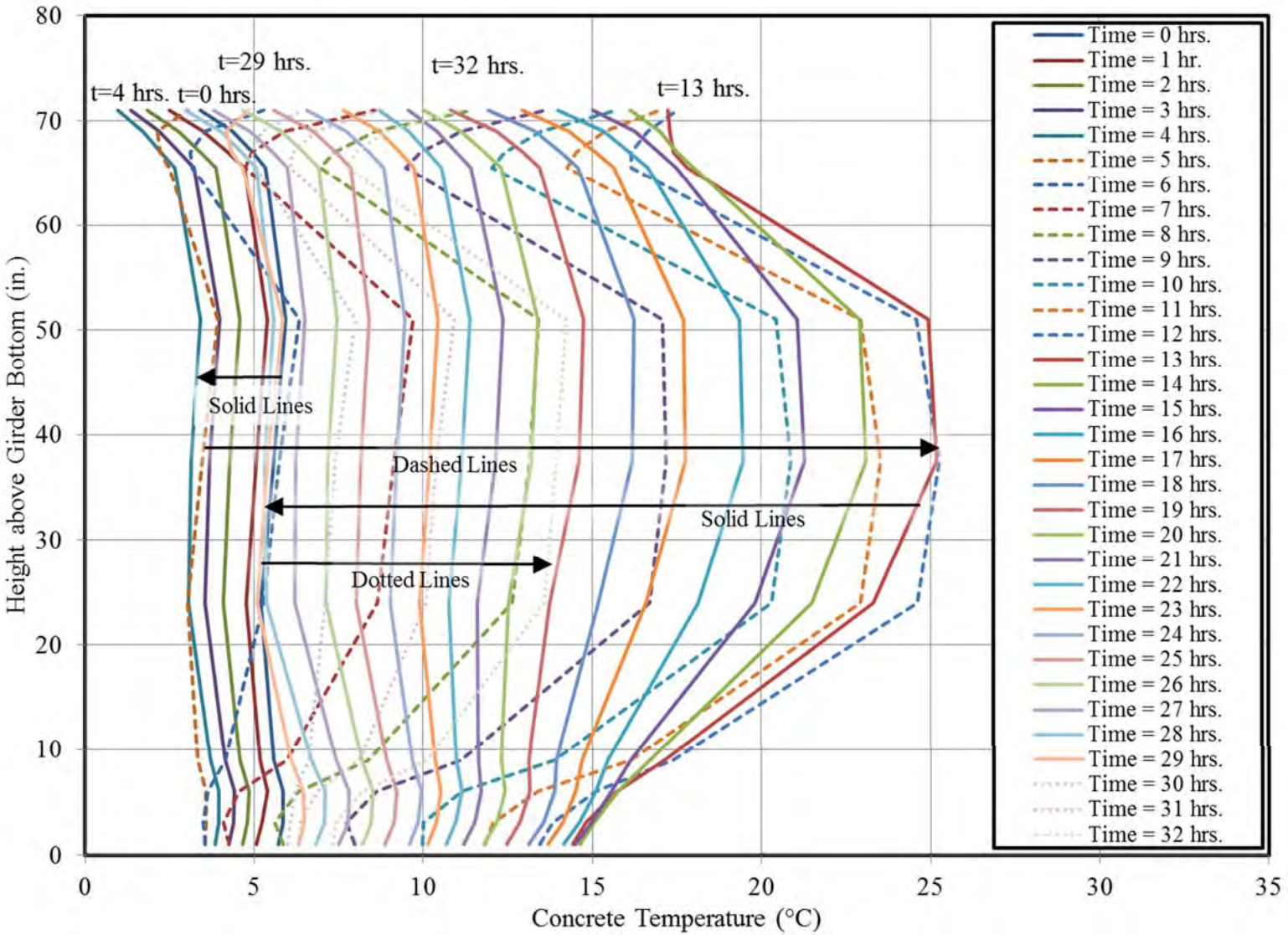

Figure 8-32: Midspan Thermocouple (TCM-Series) Results for Test #2

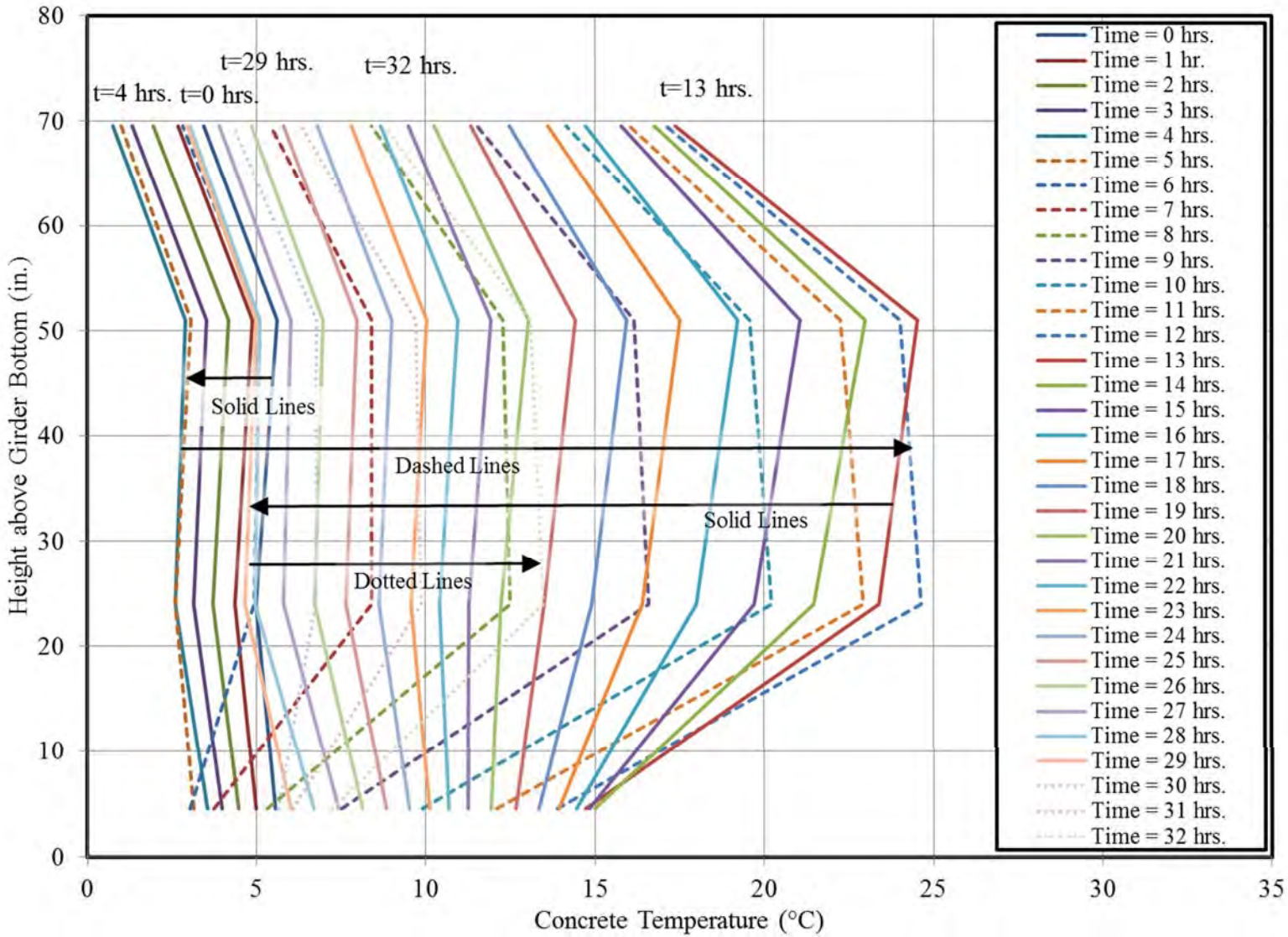

Figure 8-33: Midspan Thermistor (TSM-Series) Results for Test #2

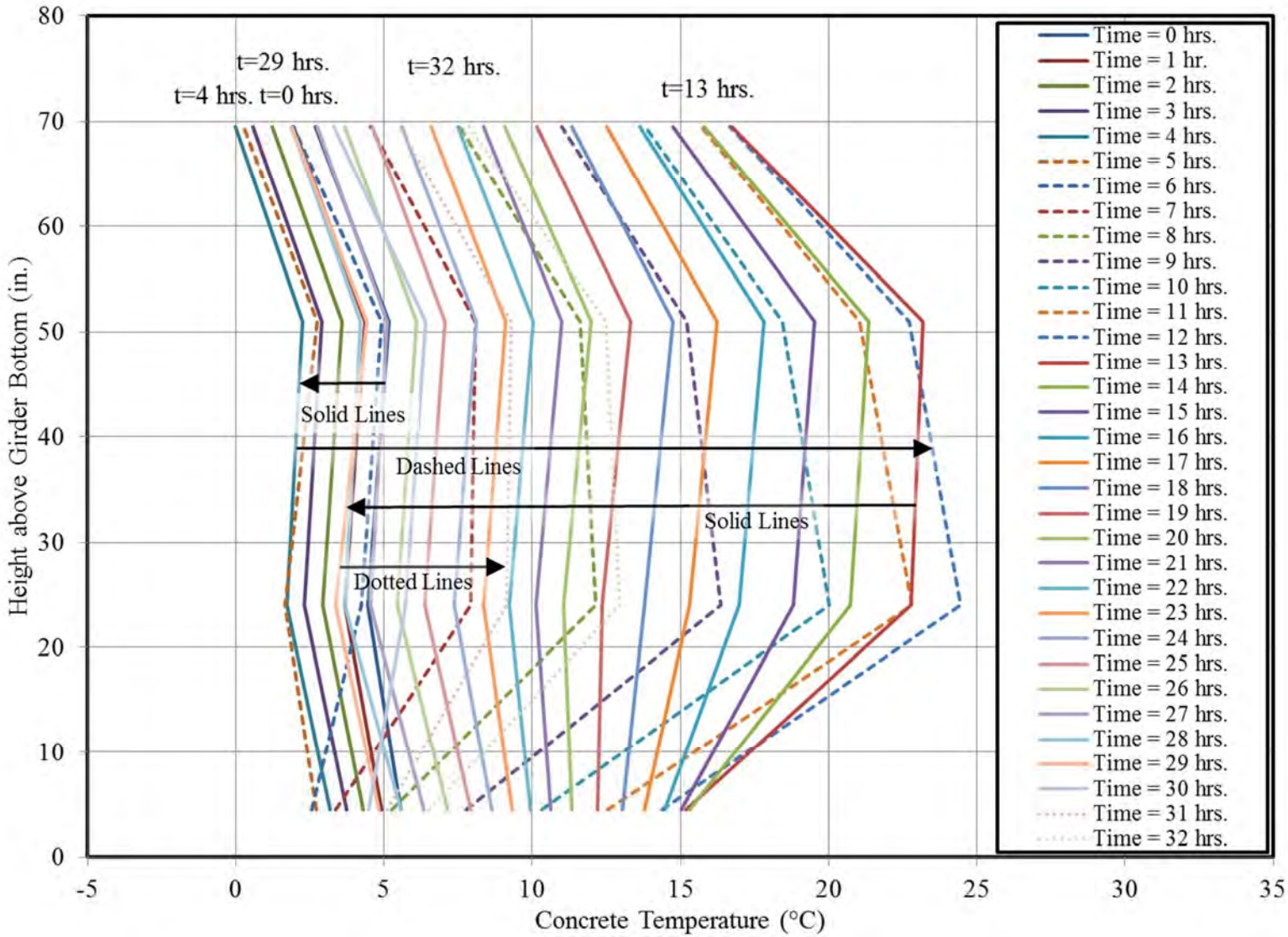

Figure 8-34: 1/6-Span Thermistor (TS6-Series) Results for Test #2

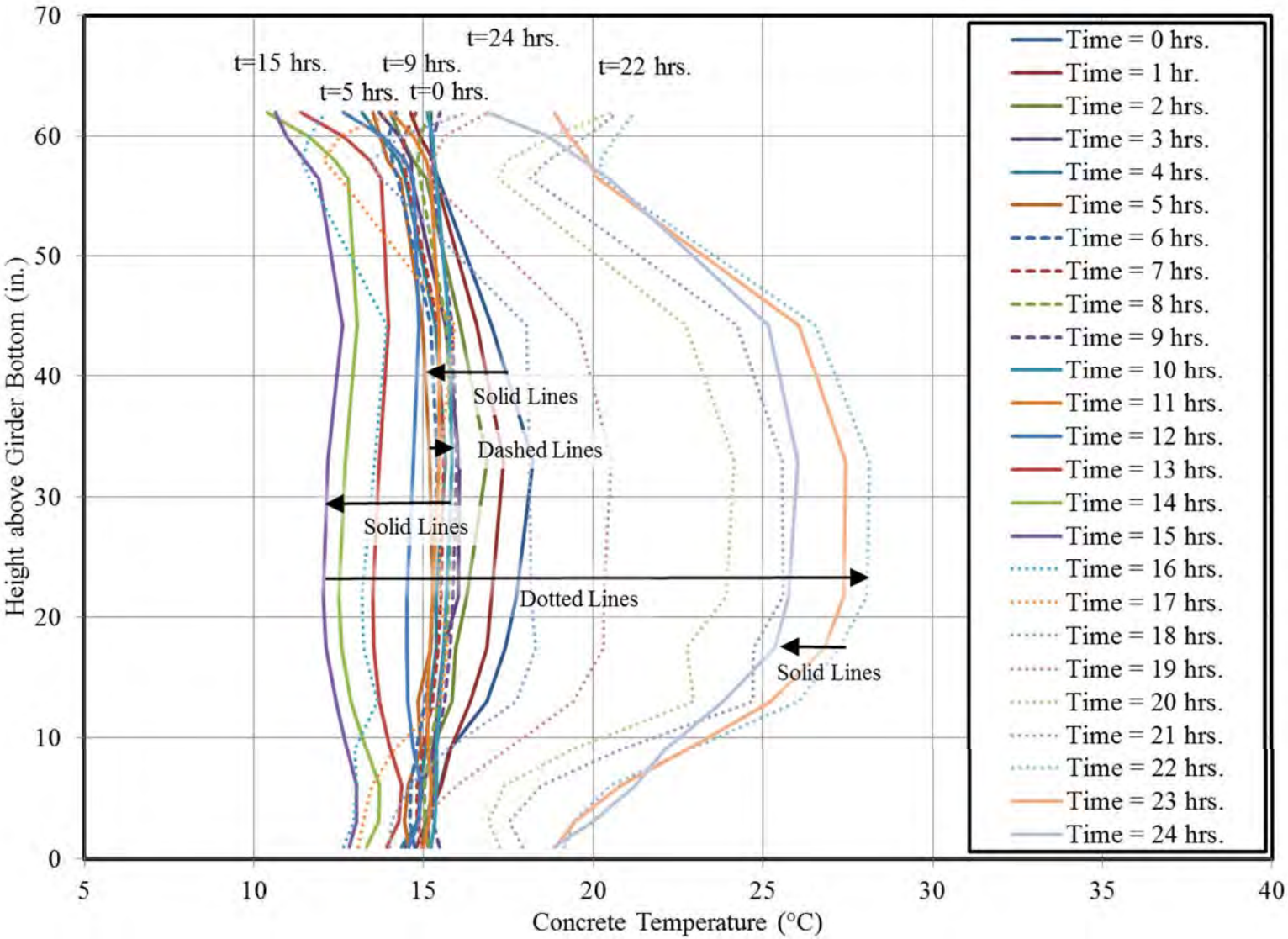

Figure 8-35: Midspan Thermocouple (TCM-Series) Results for Test #3

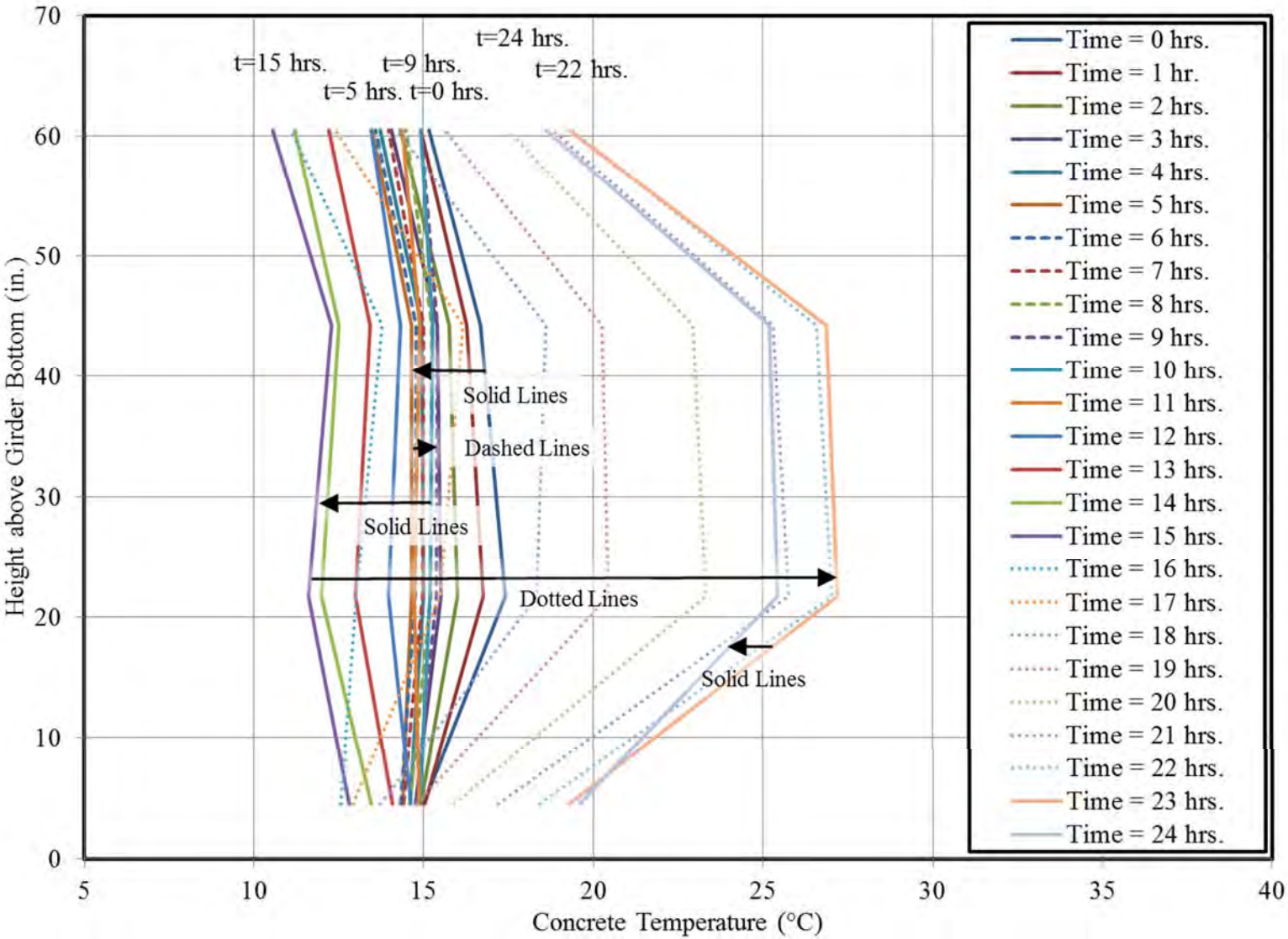

Figure 8-36: Midspan Thermistor (TSM-Series) Results for Test #3

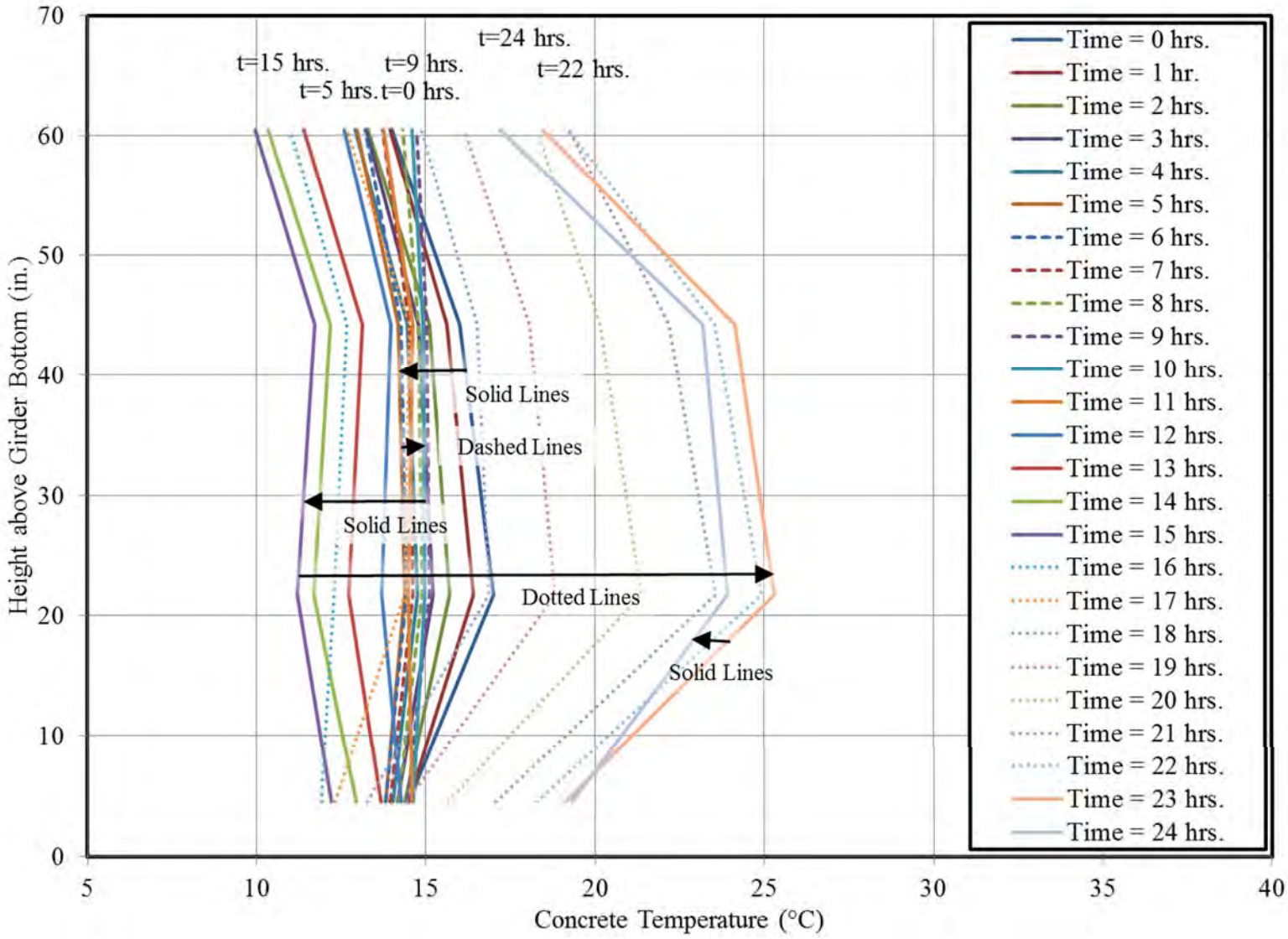

Figure 8-37: 1/6-Span Thermistor (TS6-Series) Results for Test #3

The following observations result from the inspection of Figures 8-29 through 8-37:

1. The general shape of temperature profiles at all locations (midspan and 1/6-span) are similar, with extreme temperature changes being induced in the girder web for all tests;
2. There is relatively close agreement between midspan gage groups (thermocouples and thermistors) for each of the three tests;
3. The positioning of the thermistor gages at one-quarter points within the girder web appear to approximate the reversals of the temperature profile occurring within the girder web relatively well;
4. The most detailed instrumentation (TCM-series) seem to better capture temperature trends at the extreme top and bottom depths within the girder when compared to the more limited in quantity midspan thermistor gages (TSM-series); and
5. Recorded temperature profiles from midspan and 1/6-span are similar in both relative shape and magnitude.

Further discussion of recommended gage locations for future work is presented later in this chapter in the context of the effect of gage location on the accuracy of temperature-correction procedures.

While the relative magnitudes of the temperatures observed in this study are similar to previous work by others (Kelly et al. [1987] and Lee [2010]), the shapes of the extreme temperature profiles observed during the tests differ from those previously reported. The typical shape for measured vertical temperature profiles in noncomposite bulb-tee girders as reported by Lee (2010) is shown in Figure 8-38. Previous results of Kelly et al. (1987) and Cook and Bloomquist (2005) also report similar temperature profile shapes for noncomposite girders in storage prior to erection. As shown, the top and bottom flanges typically reflect the highest recorded temperatures, with lesser or constant temperatures being reported throughout the girder web.

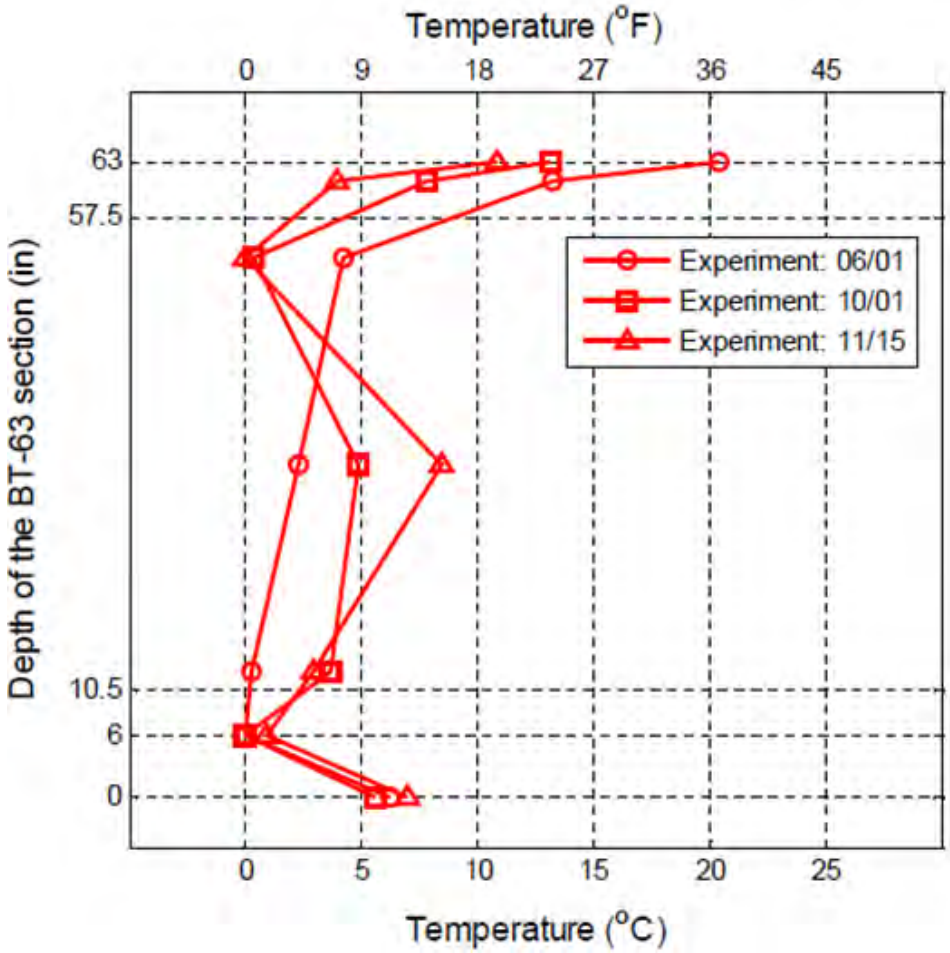

Figure 8-38: Measured Vertical Temperature Gradients in BT-63 Girder in Atlanta, Georgia (Lee 2010)

In the three tests conducted as part of the research effort of this report, a substantially different shape of induced temperature profile was observed than that reported by previous researchers. In this study, peak temperatures were typically observed within the girder web, with lesser temperatures reported in the girder top and bottom flanges. This unexpected temperature profile shape likely results from (a) the timing of the field-testing occurring during the colder winter months, (b) unseasonably cold ambient temperatures on testing days, (c) the reduced solar incident angle typical of winter months in the study region, (d) relatively unobstructed exposure of the girder webs to solar radiation (i.e. minimal shading by adjacent girders), and (e) orientation of the girders parallel to the direction of the sun's trajectory. It is likely that the lower incident angle of solar exposure caused disproportionate heating of the thinner girder web, while also minimizing solar exposure of the top and bottom flanges.

8.5 Analysis of Results

This section details the analyses conducted to (1) validate the use of the temperature-correction procedure, (2) solve for values of the effective concrete CTE for each field test, and (3) compare the effects of various simplifications on the accuracy of the temperature-correction algorithm.

8.5.1 Analytical Assumptions

The following assumptions are either explicitly or implicitly included in the analytical techniques used in this chapter:

- Where cross-sectional curvatures are computed from measured strain data, a linear regression of four strain gage readings is performed using the least-squares method of analysis;
- It is assumed that the effects of transverse temperature profiles can be decoupled from the effects of vertical temperature profiles, as verified analytically by Lee (2010);
- It is assumed that all cross sections along the girder length experience the same diurnal induced temperature profiles at a specific time; and
- In relating induced cross-sectional changes in curvature to global girder deformations, simple supports are assumed and elastic beam theory is relied on.

8.5.2 Analytical Iterations

Various analytical iterations are employed in this study and referenced throughout the remainder of this chapter. These iterations represent unique analysis procedures that rely on (a) differing analytical assumptions regarding cross-sectional girder shape and temperature profile shape, or (b) differing inputs of measured temperatures and measured concrete strains. These iterations are labelled in accordance with the convention shown in Figure 8-39, with a complete tabulated list of all considered iterations included in Table 8-4.

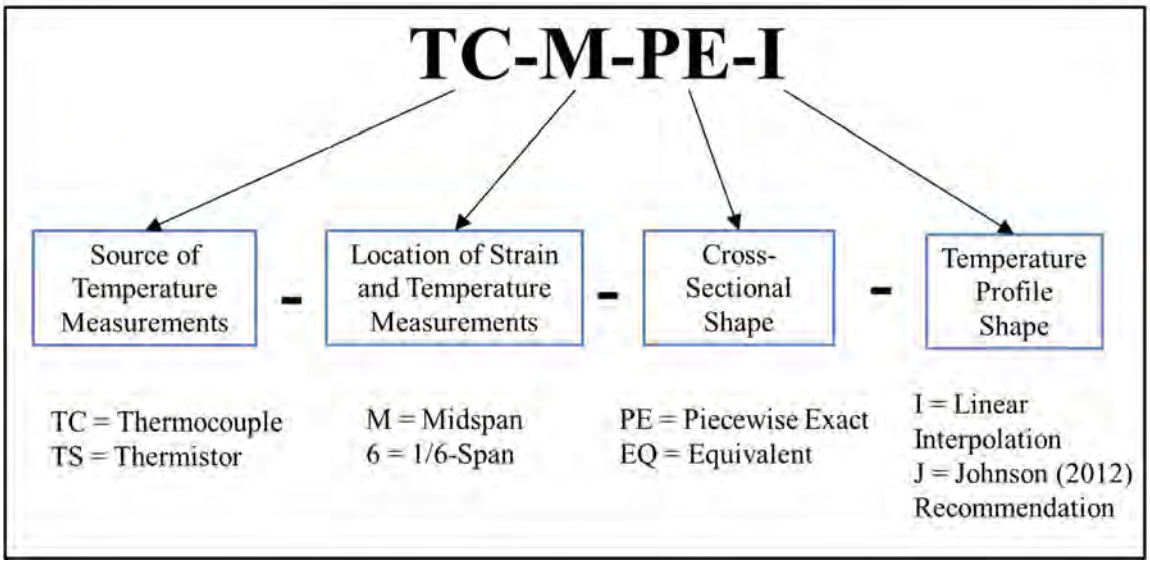

Figure 8-39: Analysis Procedure Labelling Convention

Table 8-4: Analytical Procedure Iterations

Iteration ID	Source of Temperature Measurements	Location of Strain and Temperature Measurements	Cross-Sectional Shape	Temperature Profile Shape
TC-M-PE-I	Thermocouples (TCM-Series)	Midspan	Piecewise Exact	Linear Interpolation
TS-M-PE-I	Thermistors (TSM-Series)	Midspan	Piecewise Exact	Linear Interpolation
TS-6-PE-I	Thermistors (TS6-Series)	1/6-Span	Piecewise Exact	Linear Interpolation
TS-M-EQ-I	Thermistors (TSM-Series)	Midspan	Equivalent Cross Section by Johnson (2012)	Linear Interpolation
TS-M-EQ-J	Thermistors (TSM-Series)	Midspan	Equivalent Cross Section by Johnson (2012)	Simplified Profile by Johnson (2012)

For each analytical iteration, the girder cross-sectional geometry is defined using one of two techniques:

6. *Piecewise Exact* (PE): The exact specified geometry of the girder cross section is utilized, programmed as a piecewise exact width function; or
7. *Equivalent Cross Section* (EQ): The simplified cross section comprising three rectangles as previously proposed by Johnson (2012) is utilized.

Similarly, the temperature profile shape is generated from recorded temperature data in one of the following two ways:

- *Linear Interpolation* (I): Adjacent measured temperatures at different depths are interpolated between, with results extrapolated linearly to the girder extreme surfaces (i.e. top or bottom) as shown in Figure 8-2; or
- *Simplified Profile* (J): The simplified profile[8] proposed by Johnson (2012), later used by Keske (2014), is utilized—resulting in uniform temperatures through each of the flanges and a single linear trend through the girder web as shown in Figure 8-1;

Iteration TC-M-PE-I represents the most detailed analysis performed in this investigation, relying on (a) between 11–13 thermocouple measurements from the midspan section, (b) four strain measurements from the midspan section, (c) a piecewise exact formulation of the girder cross section, and (d) linear interpolation to define the temperature profile shape. Iterations TS-M-PE-I and TS-6-PE-I represent the next most rigorous analytical iterations. Iteration TS-M-PE-I is identical to the most detailed iteration (TC-M-PE-I) with the exception that it relies on four thermistor measurements to define the temperature profile shape and magnitude instead of the more extensive thermocouple measurements. Iteration TS-6-PE-I is similar, except it relies on measurements of strain and temperature from the 1/6-span cross section. The TS-M-EQ-I iteration incorporates the simplification of girder cross section proposed by Johnson (2012), but is otherwise identical to iteration TS-M-PE-I. Finally, in an effort to replicate the temperature-correction procedure used by Johnson (2012), iteration TS-M-EQ-J incorporates both the effect of the simplified cross section and the effect of the assumed temperature profile assumed by Johnson.

8.5.3 Effective Coefficient of Thermal Expansion (CTE) Determination

To begin the analyses of this chapter, it was necessary to select one of the analysis iterations introduced in Section 8.5.2 for use in solving for an effective or apparent CTE observed during each field test. This apparent CTE represents the coefficient of thermal expansion that minimizes the error between the theoretical predicted response (caused by a measured temperature profile) and the observed girder

[8] The fitted temperature profile as used by Johnson (2012) and Keske (2014) relied on a bottom flange temperature reading taken at the centroid of the prestressing strand, whereas the bottom flange temperature measurement recorded in this study was located at the approximate centroid of the girder bottom flange.

response throughout each test. Iteration TC-M-PE-I was selected for this purpose because it represents the most detailed analytical method included in this study and utilizes data from the most detailed instrumentation included in this study. The procedure summarized in Figure 8-40, in conjunction with a GRG nonlinear solver, was used to systematically compute the effective CTE for each field test by minimizing the standard error of the estimate.

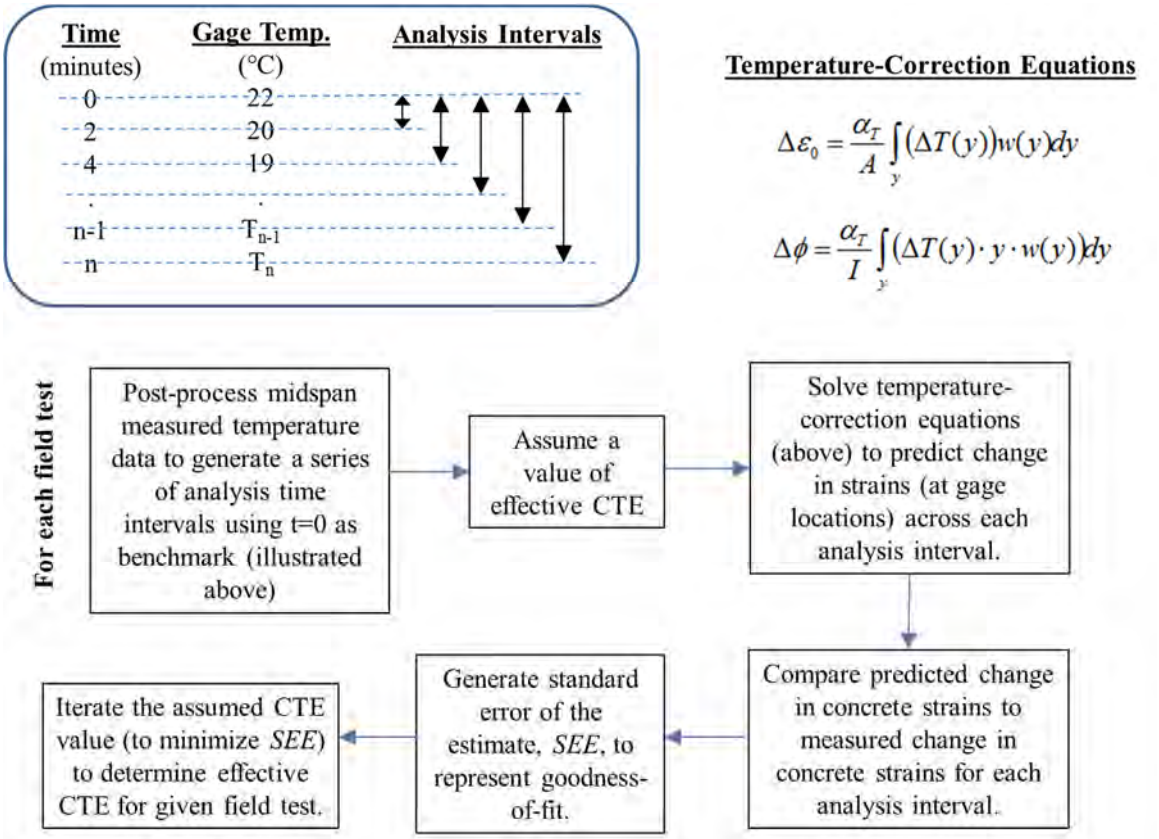

Figure 8-40: Analysis Procedure to Determine Effective CTE for each Field Test (using Iteration TC-M-PE-I)

Effective values for the concrete coefficient of thermal expansion, as determined by the procedure outlined above for the TC-M-PE-I analysis iteration, are tabulated in Table 8-5, along with corresponding values for the standard error of the estimate (*SEE*) for each strain gage.

Table 8-5: Effective CTE by Field Test (TC-M-PE-I)

Gage ID	Gage Location	Standard Error of the Estimate, *SEE*			
		Test #1	Test #2	Test #3	Units
eMTF	Top Flange	26.4	6.8	4.3	με
eMWT	Web Top	16.0	11.3	6.5	με
eMWB	Web Bottom	11.6	12.1	6.6	με
eMBF	Bottom Flange	4.9	10.6	6.8	με
Effective CTE (Determined by minimizing *SEE*)		**12.3**	**13.5**	**13.2**	($\mu\varepsilon/°C$)

While Schinder et al. (2010) recommend an average CTE value of 9.94 με/°C as a result of laboratory testing of regional dolomitic limestone concretes, the *effective* CTE values reported in Table 8-5 (12.3–13.5 με/°C) exceed this recommendation by up to 36 percent. Reasons for the disparity between laboratory-measured CTE values and the *effective* CTE values determined from field testing may include (a) the effect of varying moisture contents at the time and cross-sectional location of consideration, (b) inaccuracies related to assumptions of cross-sectional and longitudinal temperature profiles or other analytical procedures, or (c) other sources of variation inherent to full-scale field testing of concrete girders. For a more complete discussion of potential causes of variation in CTE values, readers are directed to the work of Keske (2014). Comparisons between predicted and measured concrete strains for each gage location are shown in Figures 8-41 through 8-43 for each field test.

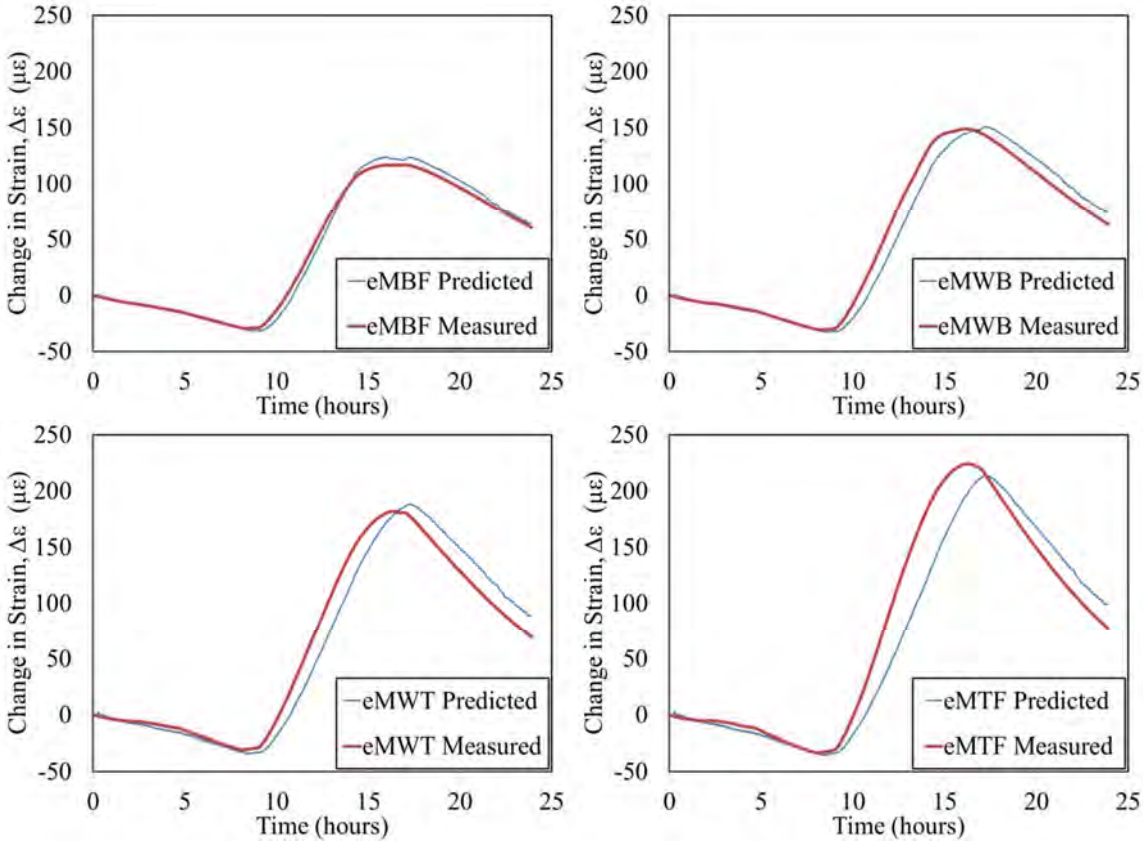

Figure 8-41: Predicted vs. Measured Strains for Test #1 (α_T=12.3)

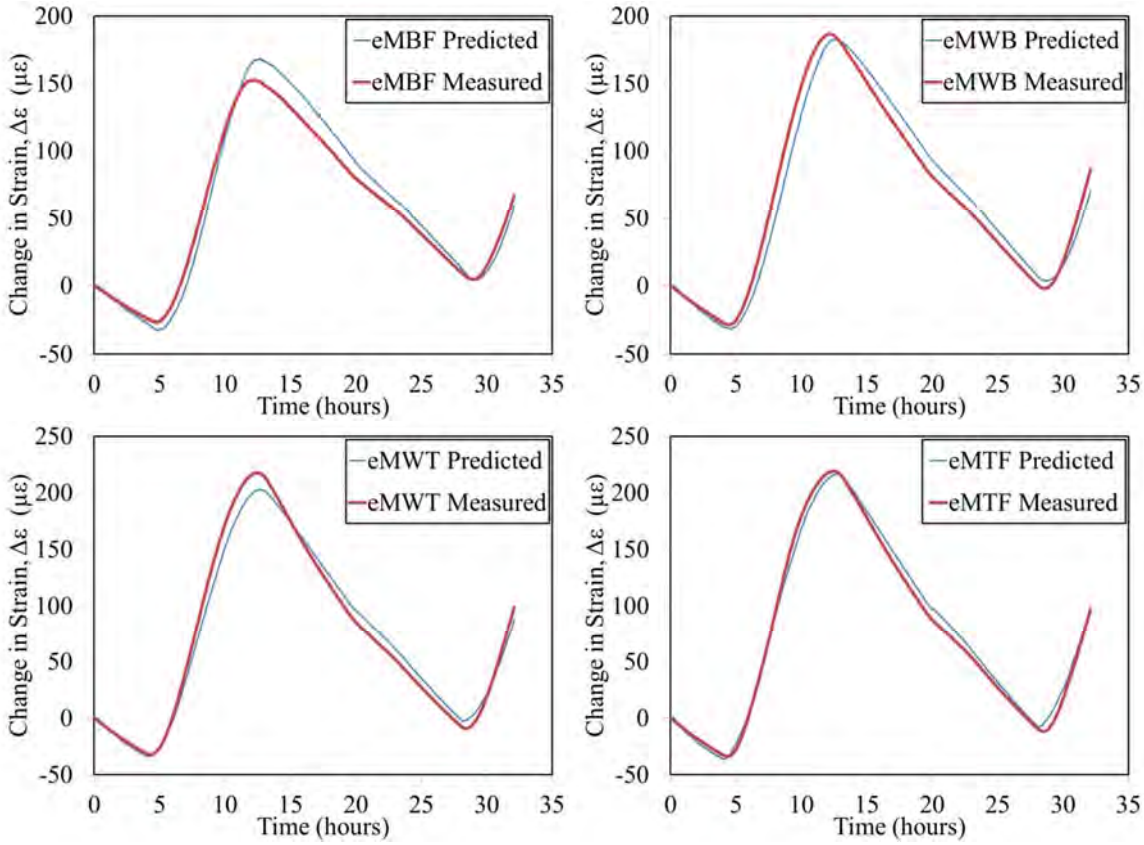

Figure 8-42: Predicted vs. Measured Strains for Test #2 (α_T=13.5)

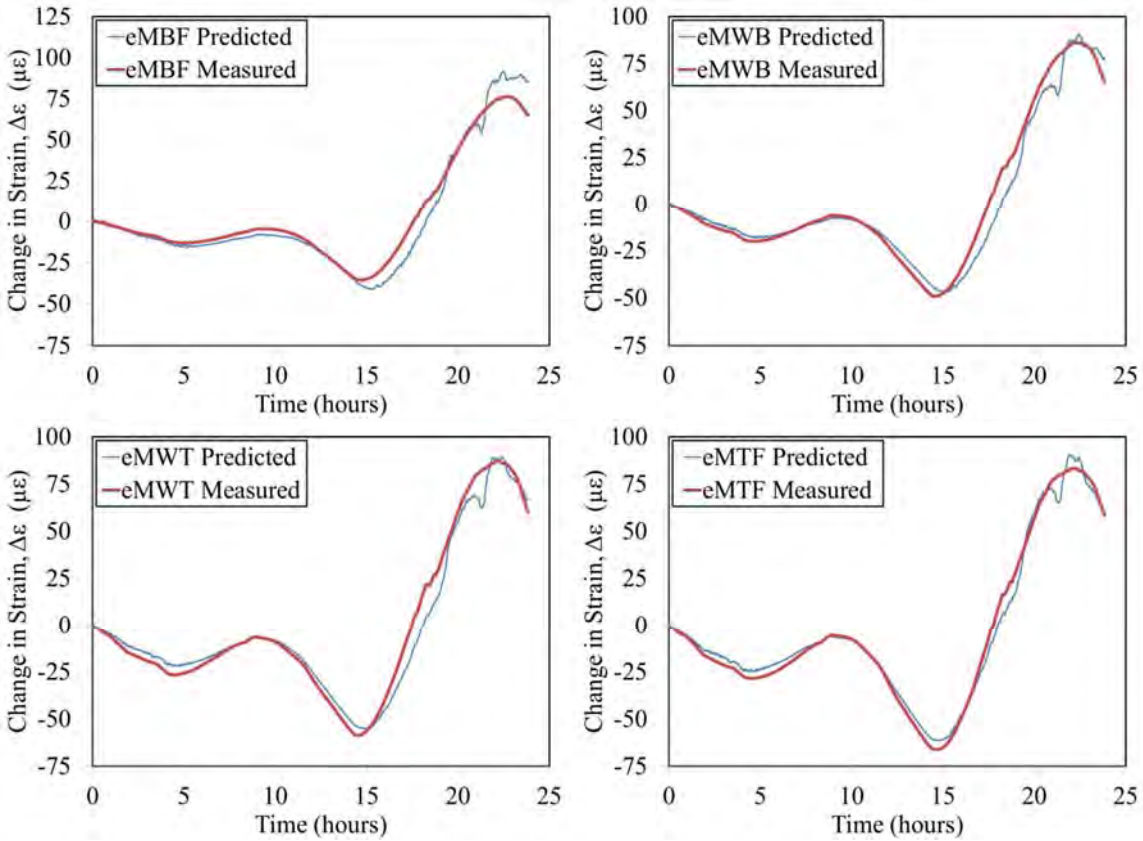

Figure 8-43: Predicted vs. Measured Strains for Test #3 (α_T=13.2)

As shown and indicated by the magnitude of the *SEE* in Table 8-5, the predicted and measured concrete strains show best agreement for Test #3 with a maximum *SEE* of 6.8 microstrain. Test #2 and #3 show the next best agreement between predicted and measured strains with maximum *SEE* of 12.1 microstrain and 26.4 microstrain, respectively. Although certain trends in curvature may be noted by inspection of concrete strain comparisons (i.e. strain comparisons becoming successively less accurate for gage readings towards the extreme top or bottom of section), inspection of concrete strains in this manner does not allow for direct comparisons of curvature—which is the parameter most closely tied to changes in girder camber. For this purpose, Figure 8-44 shows predicted and measured girder curvatures for each field test.

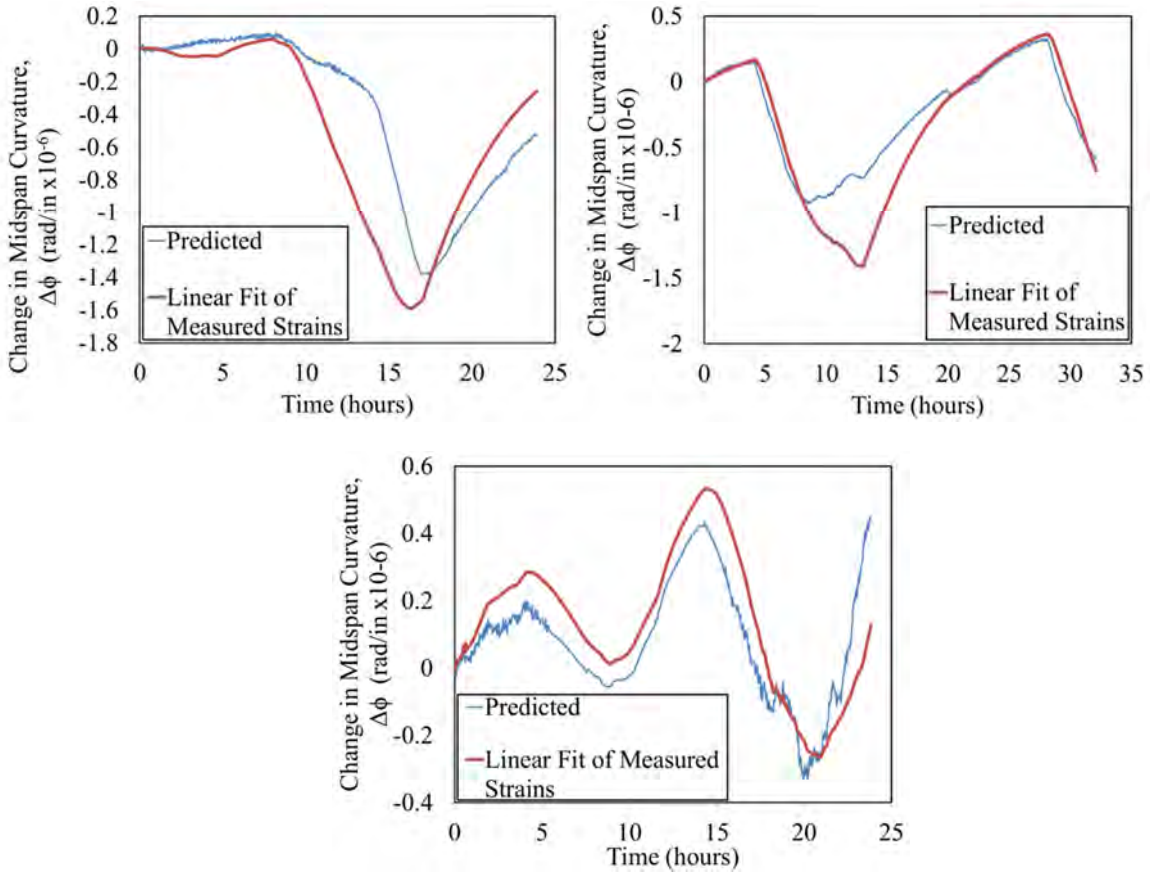

Figure 8-44: Predicted vs. Measured Midspan Curvatures for Test #1 (upper left), Test #2 (upper right), and Test #3 (bottom).

As shown, predicted curvatures for Tests #1–2 show some variations in shape from the measured responses, while predicted curvatures for Test #3 show good agreement with measured response. The discrepancy in curvature shape observed in Test #1 beginning approximately 10 hours into the test was apparently caused by the discrepancy between top flange temperature readings previously noted in Section 8.4.2. This topic is discussed further in Section 8.5.4.

In addition to the cross-sectional comparisons of girder strains and curvatures discussed above, corresponding global girder responses (e.g. vertical deflection at three girder cross sections) were computed using the tabulated expressions of Table 8-6 for comparison to measured girder vertical deflections.

Table 8-6: Engineering Beam Theory Relationships to Relate Cross-Sectional Curvature to Global Behavior

Test No.	Expression used to relate typical change in cross-sectional curvature to:		
	Midspan deflection	1/6-span deflection	One-third span deflection
1-2	$\Delta\phi\left(\frac{l^2}{8}\right)$	$\Delta\phi\left(\frac{5l^2}{72}\right)$	-
3	$\Delta\phi\left(\frac{l^2}{8}\right)$	-	$\Delta\phi\left(\frac{l^2}{9}\right)$

Note: 1. The length used for computation of global deflections is the actual span length.

Comparisons of predicted and measured girder deflections at girder midspan and 1/6-span for each of the three field tests are shown in Figures 8-45 through 8-47.

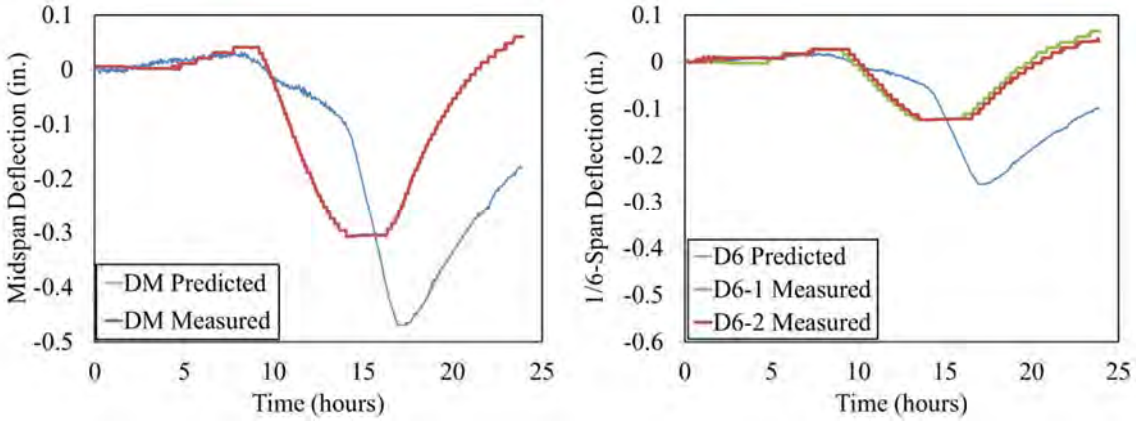

Figure 8-45: Predicted vs. Measured Deflections for Test #1 (α_T=12.3)

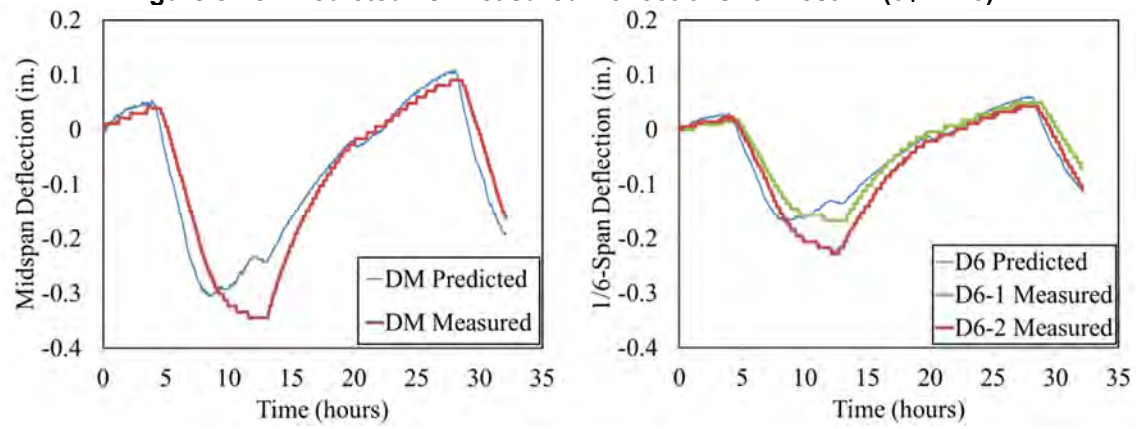

Figure 8-46: Predicted vs. Measured Deflections for Test #2 (α_T=13.5)

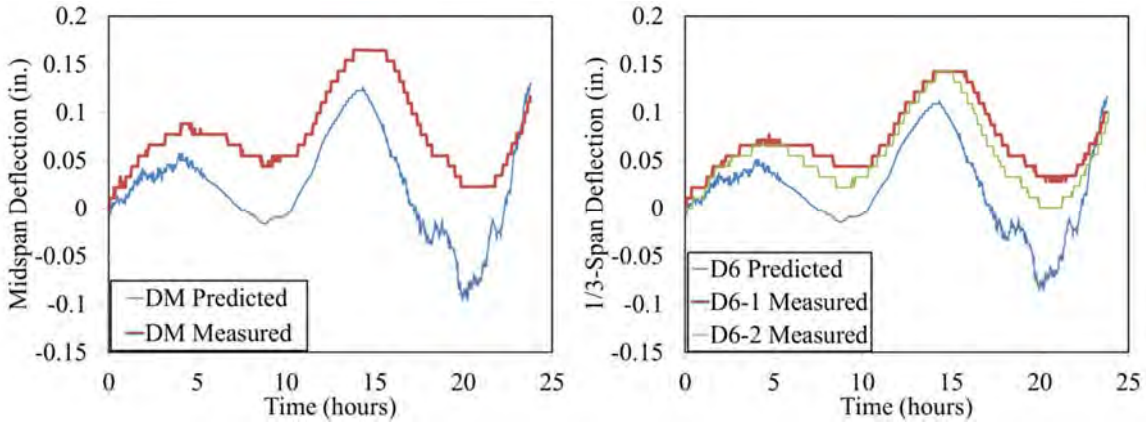

Figure 8-47: Predicted vs. Measured Deflections for Test #2 (α_T=13.2)

Relatively good agreement between predicted and measured vertical deflections is observed for Tests 2–3, although the previously-noted discrepancy in predicted curvature appears to negatively influence the accuracy of predictions for Test #1. The standard errors of the estimate, *SEE*, for each vertical deflection gage location are shown in Table 8-7.

Table 8-7: Standard Error of the Estimate for Global Deflections (TC-M-PE-I)

Gage ID	Gage Location	Standard Error of the Estimate, *SEE*			
		Test #1	Test #2	Test #3	Units
DM	Midspan	0.16	0.05	0.06	in.
D6-1	1/6-Span	0.10	0.03	0.06	in.
D6-2	1/6-Span	0.10	0.03	0.04	in.

As indicated by the small values of the standard errors for Tests #2–3 (between 0.04 and 0.06 in.), these tests represent the best fits between predicted and measured vertical deflections. The vertical deflections predictions for Test #1 are substantially less accurate than for the other two tests, with standard errors approaching triple those of the Tests #2–3.

The following observations regarding the implementation of the temperature-correction algorithm for the most detailed analysis iteration (TC-M-PE-I) are offered:

- The relative agreement between predicted and observed temperature-induced deformation in the precast, prestressed concrete girders included in this study provides support for the soundness and accuracy of the temperature-correction algorithm derived and implemented in this study;
- Best agreement between predicted and measured temperature-induced deformational responses were observed for Tests #2 and 3, with the predictions of Test #1 being less accurate and exhibiting an apparent discrepancy between predicted and measured curvature (and vertical deflection) shape;

- For the most accurate tests included in this study (Tests #2–3), effective CTE values of 13.5 and 13.2 με/°C were found to minimize the error between predicted and measured internal concrete strains;
- For Test #1, an effective CTE of 12.3 provided best agreement between predicted and measured internal concrete strains; and
- A previously noted discrepancy in top flange temperature readings for Test #1 may be to blame for the reduced accuracy of the predictions of temperature-induced deformational responses for this test. This hypothesis is explored further in Section 8.5.4, where comparisons are made to analytical iterations using alternate sources of measured temperatures.

The effective CTE values determined in this section are similar to—but slightly higher than—those values computed previously by the joint work of Keske (2014) and Neal (2015).

8.5.4 Effect of Varying Analytical Methods on Accuracy of Temperature-Correction Algorithm

A key task of this chapter was to evaluate the effect of various analytical simplifications and differing field-measured inputs on the accuracy of the temperature-correction effort implemented in this report. To this end, the various analytical iterations previously described in Section 8.5.2 (reproduced below) were implemented and standard errors of the estimate were computed for each field test and gage location to represent the goodness-of-fit to measured results. In the implementation of each of these iterations, the previously determined effective CTE for each field test was utilized.

Table 8-4: Analytical Procedure Iterations

Iteration ID	Source of Temperature Measurements	Location of Strain and Temperature Measurements	Cross-Sectional Shape	Temperature Profile Shape
TC-M-PE-I	Thermocouples (TCM-Series)	Midspan	Piecewise Exact	Linear Interpolation
TS-M-PE-I	Thermistors (TSM-Series)	Midspan	Piecewise Exact	Linear Interpolation
TS-6-PE-I	Thermistors (TS6-Series)	1/6-Span	Piecewise Exact	Linear Interpolation
TS-M-EQ-I	Thermistors (TSM-Series)	Midspan	Equivalent Cross Section by Johnson (2012)	Linear Interpolation

TS-M-EQ-J	Thermistors (TSM-Series)	Midspan	Equivalent Cross Section by Johnson (2012)	Simplified Profile by Johnson (2012)

Comparisons between predicted and measured bottom flange strains, top flange strains, and midspan vertical deflection are shown in Figures 8-48 through 8-56 for each iteration and test, with a summary of the standard errors of the estimate for each case tabulated in Table 8-8.

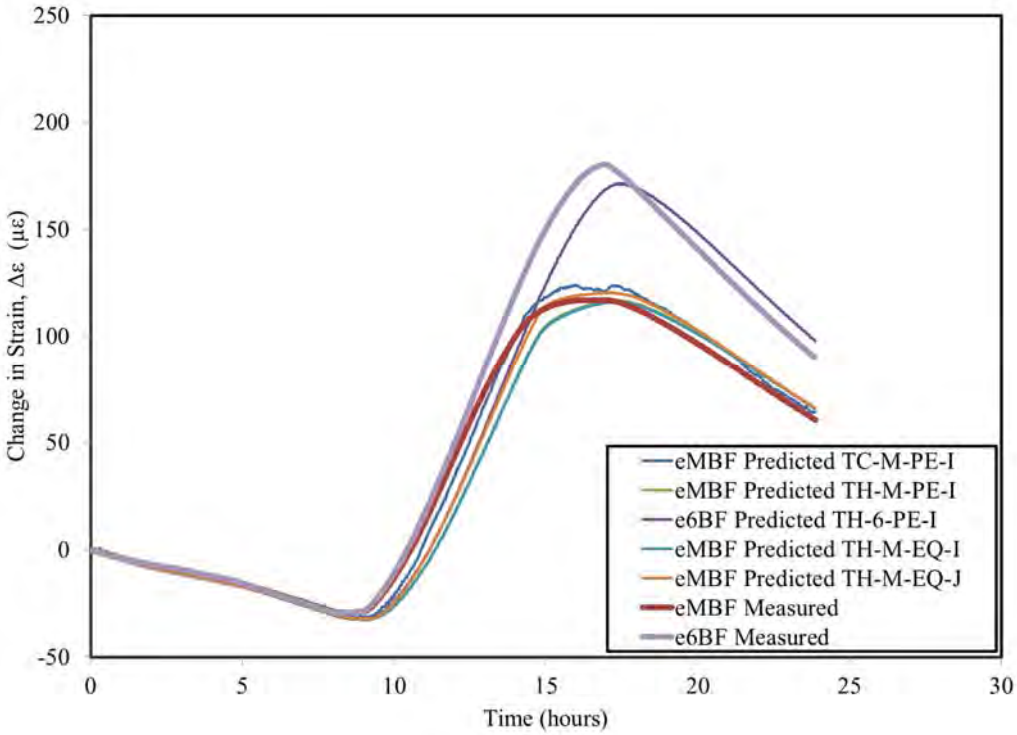

Figure 8-48: Predicted and Measured Bottom Flange Strains for Test #1 by Analysis Procedure (α_T=12.3)

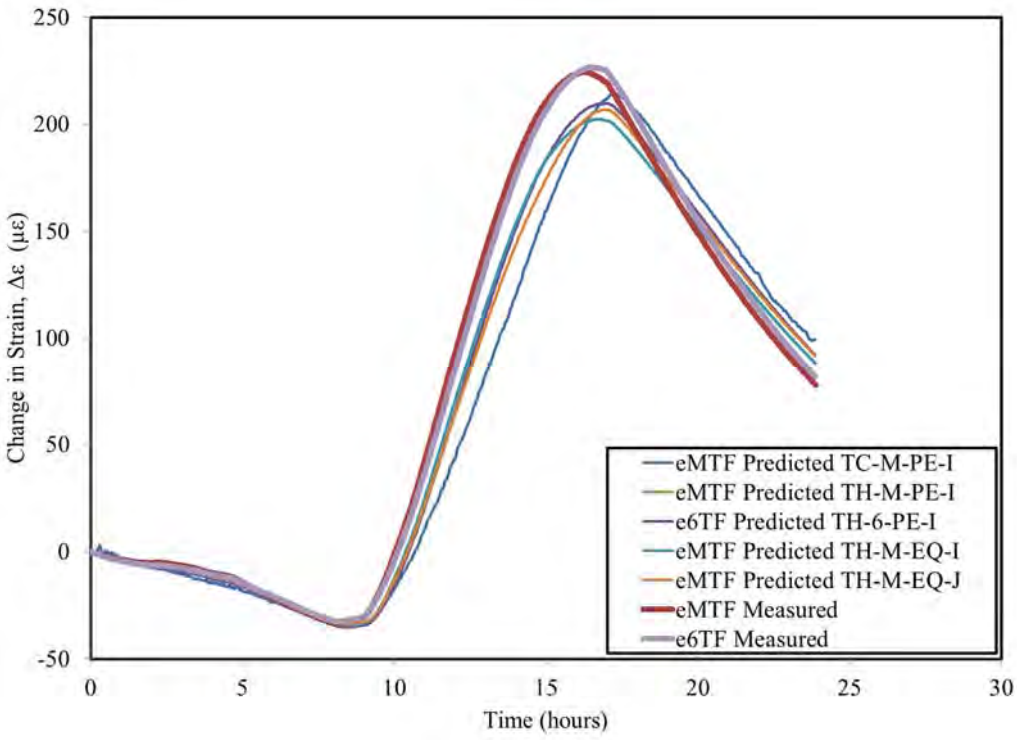

Figure 8-49: Predicted and Measured Top Flange Strains for Test #1 by Analysis Procedure (α_T=12.3)

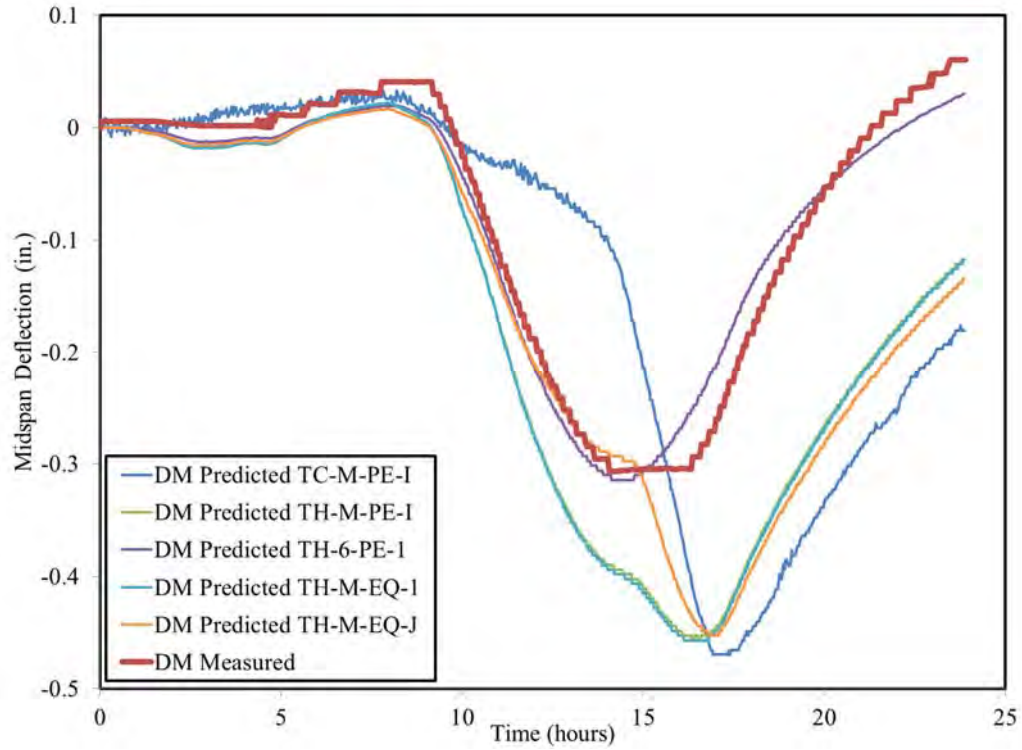

Figure 8-50: Predicted and Measured Midspan Deflection for Test #1 by Analysis Procedure (α_T=12.3)

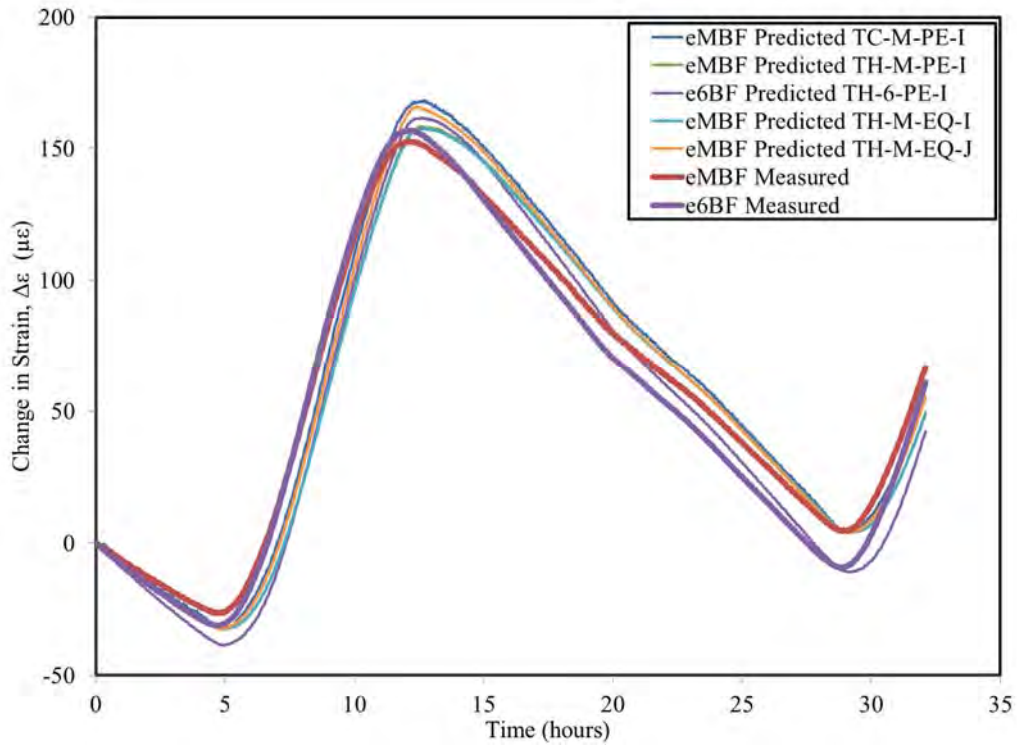

Figure 8-51: Predicted and Measured Bottom Flange Strains for Test #2 by Analysis Method (α_T=13.5)

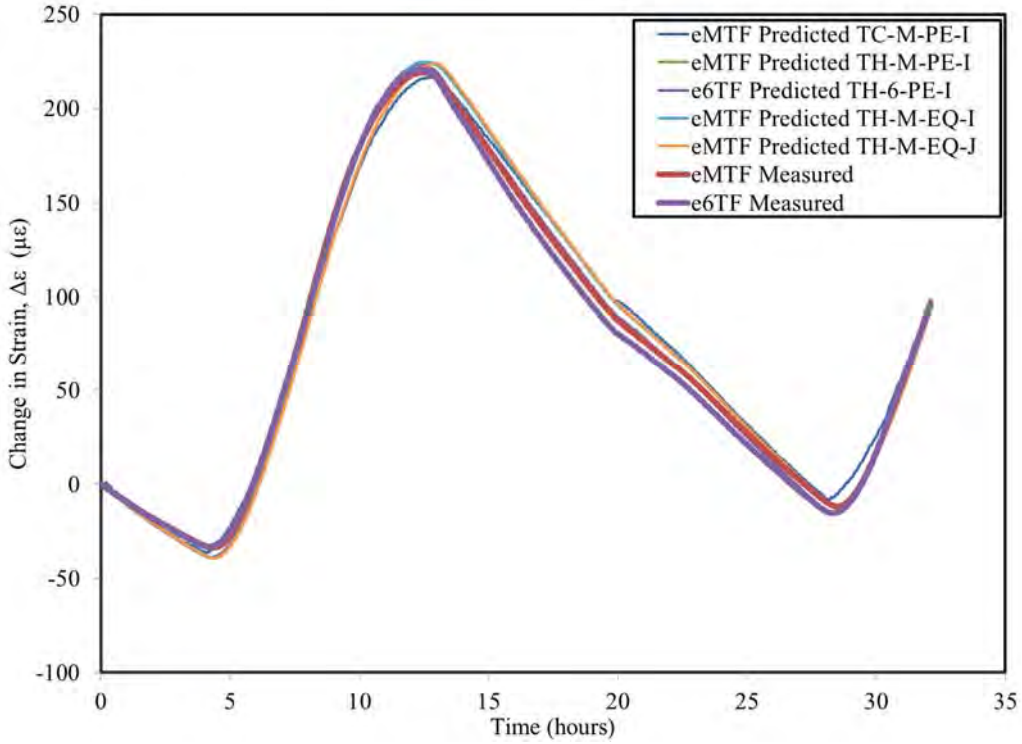

Figure 8-52: Predicted and Measured Top Flange Strains for Test #2 by Analysis Method (α_T=13.5)

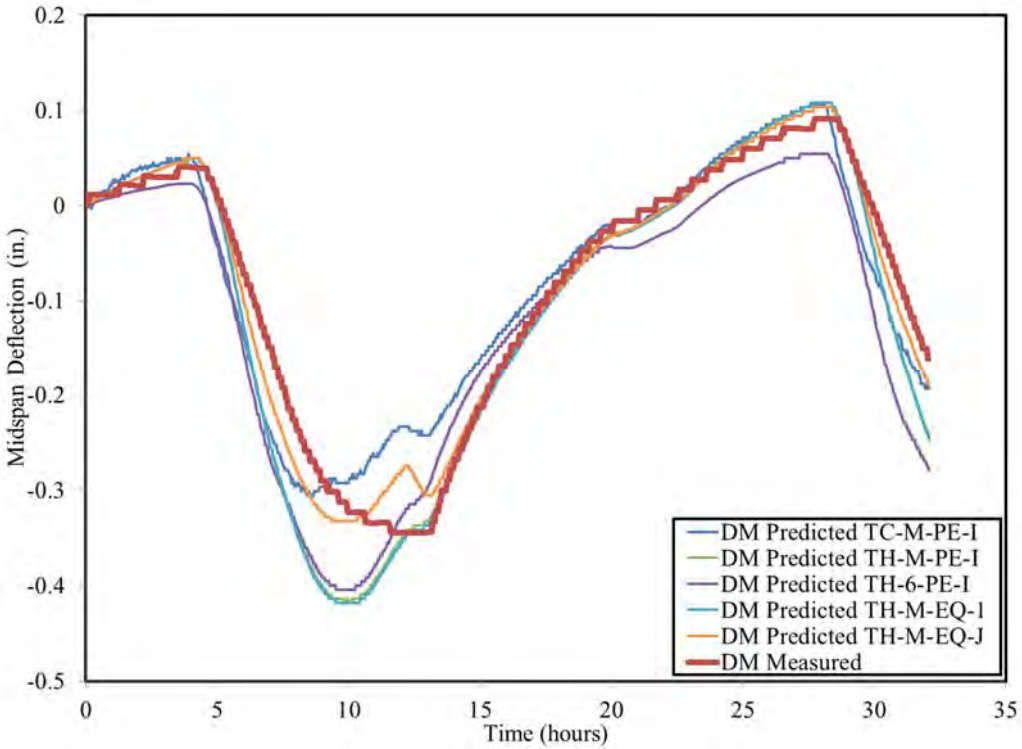

Figure 8-53: Predicted and Measured Midspan Deflection for Test #2 by Analysis Method (α_T=13.5)

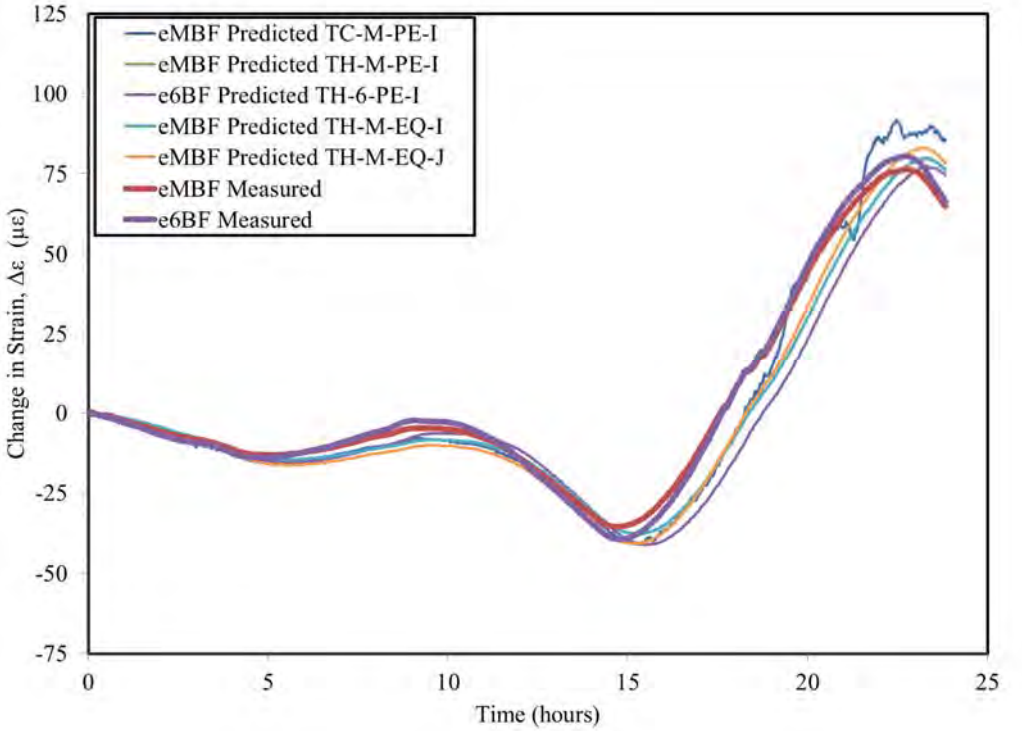

Figure 8-54: Predicted and Measured Bottom Flange Strains for Test #3 by Analysis Method (α_T=13.2)

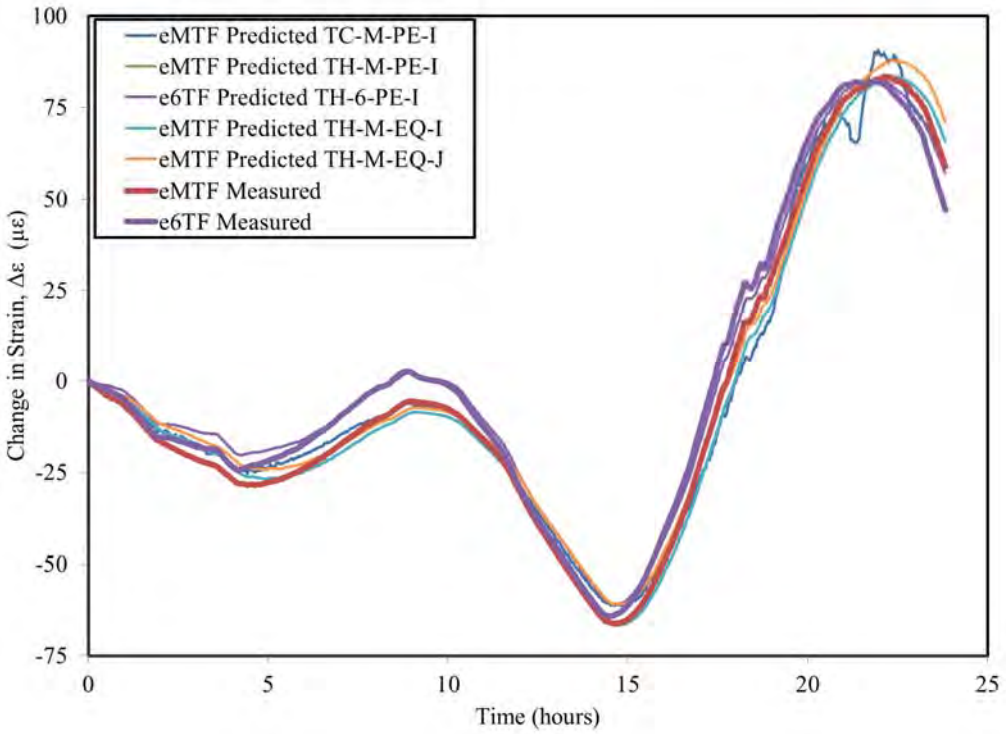

Figure 8-55: Predicted and Measured Top Flange Strains for Test #3 by Analysis Method (α_T=13.2)

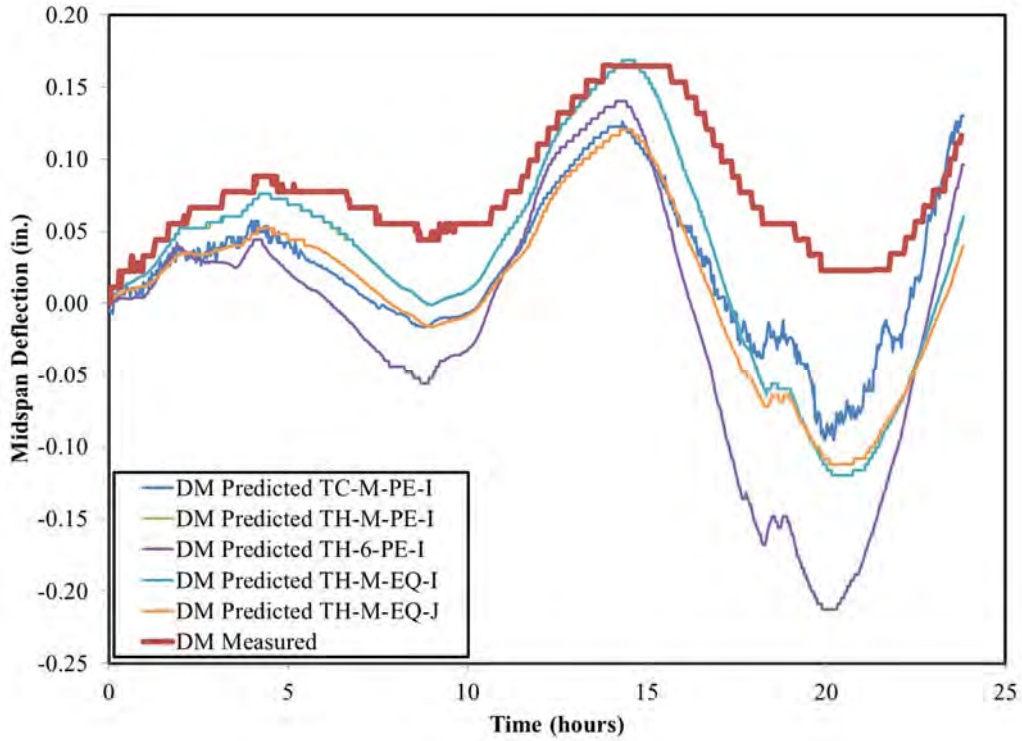

Figure 8-56: Predicted and Measured Midspan Deflection for Test #3 by Analysis Method (α_T=13.2)

Table 8-8: Standard Error of the Estimate for Various Analysis Iterations

Analysis Procedure	Gage ID	Standard Error of the Estimate, *SEE*			
		Test #1	Test #2	Test #3	Units
TC-M-PE-I (Most Detailed)	eMTF	26.4	6.8	4.3	με
	eMWT	16.0	11.3	6.5	με
	eMWB	11.6	12.1	6.6	με
	eMBF	4.9	10.6	6.8	με
	DM	0.16	0.05	0.06	in.
	D6-1	0.10	0.03	0.06	in.
	D6-2	0.10	0.03	0.04	in.
TH-M-PE-I	eMTF	13.7	6.4	3.3	με
	eMWT	8.3	10.1	7.2	με
	eMWB	12.7	14.5	8.5	με
	eMBF	10.6	12.4	6.6	με
	DM	0.12	0.04	0.07	in.
	D6-1	0.09	0.03	0.06	in.
	D6-2	0.09	0.02	0.05	in.
TH-6-PE-I	e6TF	12.0	6.3	3.1	με
	e6WT	18.3	9.6	4.9	με
	e6WB	15.0	14.7	4.7	με
	e6BF	13.1	13.1	10.2	με
	DM	0.02	0.06	0.12	in.
	D6-1	0.03	0.04	0.11	in.
	D6-2	0.03	0.03	0.09	in.
TH-M-EQ-I	eMTF	13.7	6.5	3.4	με
	eMWT	8.3	10.1	7.2	με
	eMWB	12.8	14.5	8.5	με
	eMBF	10.8	12.4	6.6	με
	DM	0.12	0.05	0.07	in.
	D6-1	0.09	0.04	0.06	in.
	D6-2	0.10	0.02	0.05	in.
TH-M-EQ-J	eMTF	17.0	8.1	4.0	με
	eMWT	10.2	11.2	6.2	με
	eMWB	11.7	13.4	7.2	με
	eMBF	8.2	11.3	6.5	με
	DM	0.12	0.02	0.08	in.
	D6-1	0.09	0.02	0.07	in.
	D6-2	0.09	0.02	0.05	in.

In consideration of the results presented in Figures 8-48 through 8-56 and summarized in Table 8-8, the following observations are offered:

- Relatively good agreement between predicted and measured deformations (e.g. strains and vertical deflection), in shape and magnitude, was observed for Tests #2 and 3 for each analytical iteration —with somewhat less accurate results evident for Test #1;
- Best agreement between predicted and measured cross-sectional strains was observed for Test #3, while most accurate predictions of vertical deflections were observed for Test #2;

- When comparing predicted and measured results between the midspan and 1/6-span analysis sections, the accuracy of strain, curvature, and deflection predictions were similar in shape and magnitude—with the exception of Test #1;
- The most detailed analysis iteration (TC-M-PE-I) used in this study (which relied on between 11–13 thermocouple measurements at midspan and an exact cross section definition) generated the most accurate predictions of girder deformations for Tests #2 and 3;
- The most detailed analysis iteration (TC-M-PE-I) generated the least accurate predictions of any analysis iteration in this study for Test #1—suggesting that the top flange thermocouple temperature measurements (previously noted to have differed from thermistor readings at the same location) were likely flawed. The effective CTE computed for Test #1 of 12.3 με/°C may have been affected by these flawed readings;
- Similar analytical iterations conducted using measured data from different cross sections (i.e. TH-M-PE-I at midspan and TH-6-PE-I at 1/6-span) generated largely similar results, with no consistent discernable trends evident with regards to prediction accuracy;
- By comparing similar analytical iterations using varying definitions of girder cross section (TH-M-PE-I and TH-M-EQ-I), it is evident that use of the simplified equivalent cross section proposed by Johnson (2012) resulted in negligible error when compared to use of an exact cross section definition;
- For tests where most significant top flange temperature gradients were observed (Tests #2–3), the use of the simplified temperature profile proposed by Johnson (TH-M-EQ-J) generated strain predictions only slightly less accurate than those of the most detailed analysis (TC-M-PE-I). For these same tests, a similar analytical iteration utilizing linear interpolation to define the temperature profile shape (TS-M-PE-I) resulted in predictions of strain and vertical deflection slightly less accurate than use of the temperature profile by Johnson; and
- The effective CTE values previously computed for Tests #2 and 3 (13.5 and 13.2 με/°C, respectively) generated satisfactory predictions of temperature-induced girder deformations for all analytical iterations included in this study. In the absence of more detailed information, an

effective CTE value of between 13.0 and 13.5 με/°C should be expected to yield sufficiently accurate results in conjunction with the analytical iterations utilized in this study.

8.6 Expected Magnitude of Transient Temperature-Induced Camber Variations For Girders in Storage

The shape of the extreme vertical temperature profiles observed during the three field tests performed in this study differed from the typical vertical temperature profile shape previously reported by others (e.g. Lee 2008, Barr et al. 2005, Kelly et al. 1987, and Neal 2015). Where others generally report extreme temperatures in the girder top flange, the vertical profiles observed in the three winter tests of this study were generally defined by extreme temperatures in the girder web. As a result, the limited temperature data compiled in this study is likely not representative of the most extreme temperature-induced girder camber variations. To explore this topic further, a design vertical temperature profile proposed by a previous researcher and the code-prescribed design profiles of AASHTO 2014 were used to estimate the magnitude of extreme temperature-induced camber variations to be expected for precast, prestressed concrete girders in storage.

The positive design profile[9] by Lee (2008) resulted from an extensive field study and corresponds to the maximum upward deflection expected in PCI bulb-tee girder shapes as a result of warming of the girder top flange. Lee's work was based on field observations of pre-erection behavior (i.e. during girder storage and transportation) and, thus, his design recommendations are useful to estimate the magnitude of temperature-induced camber variations for girders in storage. The AASHTO 2014 code-prescribed design profiles were also included in this analysis for comparison—although these vertical temperature profiles are primarily intended for use in girders with concrete decks. The three design vertical temperature profiles utilized in this analysis are shown in Figure 8-57.

[9] In agreement with AASHTO 2014 terminology, vertical temperature profiles corresponding to an increase in top flange temperature (e.g. 0 to 20 °C) are called "positive" temperature profiles.

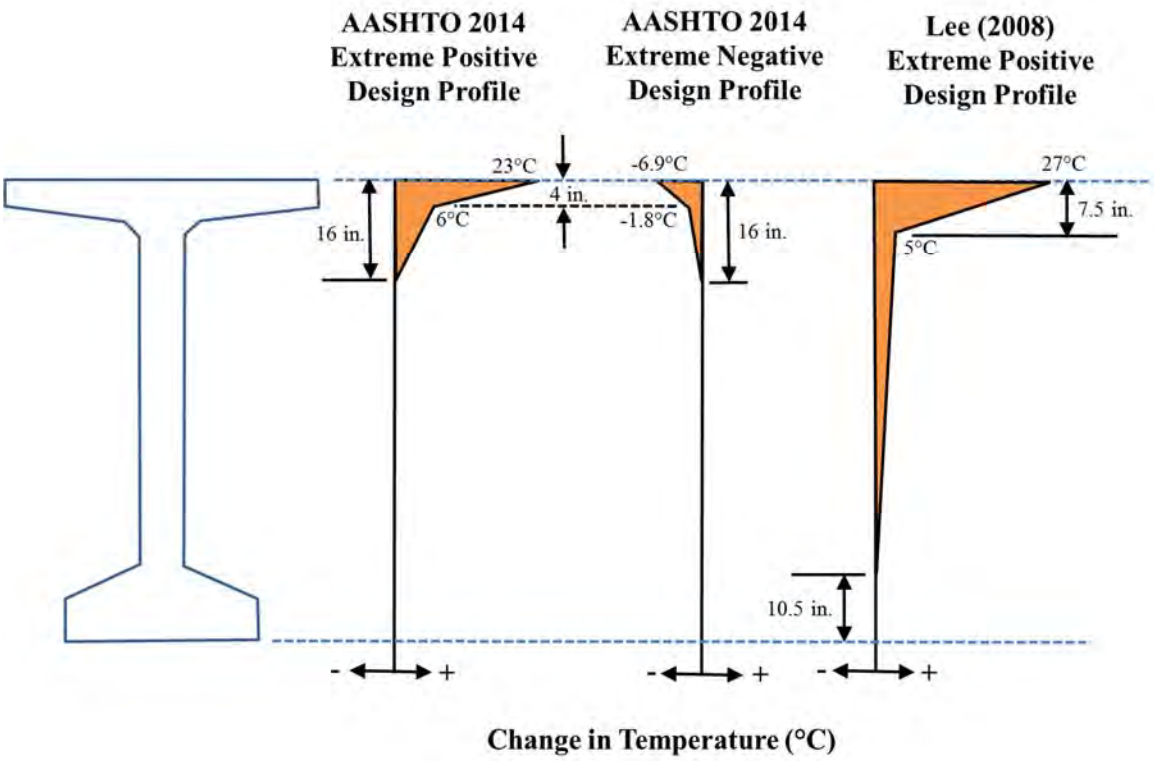

Figure 8-57: Extreme Positive and Negative Vertical Temperature Profiles

The positive design profiles (AASHTO and Lee [2008]) above tend to cause increases in girder camber, while the negative profile (AASHTO) tends to cause a decrease in girder camber. In general, positive design profiles are caused by exposure to solar radiation (i.e. heating of the top flange), while negative design profiles can be caused by other conditions (e.g. differential cooling due to wind or decreasing ambient temperature) in the absence of solar exposure. Using the temperature-correction algorithm implemented in this report, the curvature induced by each design vertical temperature profile was computed as shown in Table 8-9.

Table 8-9: Induced Curvature by Design Temperature Profile

Direction of Midspan Induced Deflection Change	Temperature Gradient Source	Deck Present?	Induced Curvature (x10^{-6} rad/in.)		
			BT-54	BT-63	BT-72
Upward	AASHTO 2014 (Positive)	Yes	-3.3	-2.7	-2.2
	Lee (2010)	No	-5.0	-4.1	-3.4
Downward	AASHTO 2014 (Negative)	Yes	<+1.0	<+1.0	<+1.0
Total Range	AASHTO 2014 (Computed)	Yes	4.3	3.7	3.2
	Observed in this Study	No	n/a	<1.0	<2.0

Notes:
1. An effective CTE of 13.0 με/°C was assumed.
2. Negative curvature corresponds to increased girder camber.

As shown, the design profile of Lee (2008) tended to induce the maximum changes in curvature—approximately 50 percent greater than those computed using the AASHTO 2014 positive design profile. The magnitude of the induced change in curvature corresponding to the negative AASHTO temperature profile was less than 1.0x10^{-6} rad/in. The total range of curvature change observed in this study was significantly less than the maximum computed using the AASHTO 2014 design profiles. Using assumed girder lengths and a transverse girder-to-girder spacing (each as noted in Table 8-10), changes to midspan camber were computed corresponding to the curvatures noted above and are shown in Table 8-10.

Table 8-10: Induced Changes in Midspan Camber by Design Temperature Profile

Direction of Midspan Induced Deflection Change	Temperature Gradient Source	Deck Present?	Induced Change in Midspan Camber (in.)		
			BT-54	BT-63	BT-72
Upward	AASHTO 2014 (Positive)	Yes	+0.9	+0.9	+1.0
	Lee (2010)	No	+1.3	+1.3	+1.5
Downward	AASHTO 2014 (Negative)	Yes	-0.3	-0.3	-0.4
Total Range	AASHTO 2014	Yes	1.2	1.2	1.4
	Observed in This Study	No	n/a	0.3	0.9

Notes:
1. Transverse girder-to-girder spacing of 6.5 ft is assumed.
2. Maximum span lengths for BT-54, BT-63, and BT-72 assumed as 120 ft, 135 ft, and 155 ft, respectively, in accordance with PCI design guidelines (PCI 2011).

A number of trends are evident from the results of Table 8-10:

- As a result of two opposing trends ([1] less deep girders exhibited more induced curvature than deeper girders for an identical vertical temperature profile, and [2] changes in cross-sectional curvature tended to cause larger changes in midspan camber for longer span lengths), expected temperature-induced changes in midspan camber are somewhat more independent of girder cross section than was the case for the curvatures previously reported in Table 8-9;
- The positive design temperature profiles of AASHTO 2014 and Lee (2010) are expected to cause maximum transient increases in midspan camber of 1.0 in. and 1.5 in., respectively, for typical PCI bulb-tee girders;
- The negative design temperature profile of AASHTO 2014 is expected to cause a maximum transient decrease in midspan camber of less than 0.5 in. for typical PCI bulb-tee girders; and
- The changes in midspan camber observed during the three field tests performed in this study were substantially less than the maximum values computed using the vertical design profiles of AASHTO or Lee (2008).

The transient change in upward camber computed from the design profile of Lee (2008) is most appropriate as an upper-bound estimate for expected upward camber variation because of the similarities between the experimental conditions used by Lee and typical girder storage practices (i.e. outdoor, unshaded ambient exposure with no concrete deck installed.) For the purpose of estimating the maximum expected downward transient change in midspan camber, use of the AASHTO negative profile is the default option. Although the AASHTO negative temperature profile is not strictly intended for application to girders without concrete decks, application as such is likely less error prone than if the AASHTO positive temperature profile were relied on similarly for a section without a concrete deck. As previously discussed, the heat transfer mechanisms associated with negative temperature profiles tend to be independent of solar exposure and, therefore, the presence of a concrete deck likely does little to change the magnitude or shape of the AASHTO negative temperature profile. Future research work may be justified in this area to better quantify negative temperature profiles in girders prior to concrete deck placement—although the resulting deformations are relatively small and likely of minimal consequence. Recommendations in agreement with the preceding discussion are summarized in Table 8-11.

Table 8-11: Transient Changes to Theoretical Midspan Camber

Expected Transient Temperature-Induced Changes to Theoretical Midspan Camber	
Upward	<+1.5 in.
Downward	<-0.5 in.

8.7 Summary and Conclusions

8.7.1 Summary

In this chapter, a curvature-based temperature-correction algorithm was developed and implemented to analytically predict the behavior of precast, prestressed concrete bridge girders upon exposure to vertical diurnal temperature variations. After derivation of the basic concept, results of a field-monitoring study were used to validate the algorithm and to calibrate values of an "effective" coefficient of thermal expansion providing best agreement between predicted and measured girder deformations. Finally, the magnitudes of expected transient changes in midspan girder camber were estimated using the temperature-correction procedure implemented in this chapter in conjunction with available design extreme vertical temperature profiles published by others.

8.7.2 Conclusions and Recommendations

Key observations and recommendations regarding the temperature-correction algorithm implemented in this report include the following:

7. As implemented in this study, the curvature-based temperature-correction algorithm demonstrated good agreement with field measured results—with the exception of where testing anomalies were detected (e.g. Field Test #1);
8. For the concrete girders monitored in this study, an effective CTE value of between 13.0 and 13.5 με/°C was found to provide best agreement between predicted and measured deformational responses for girders in unshaded outdoor storage;
9. Maximum temperature-induced changes to midspan camber of approximately 0.45 inches were observed in the field testing of this study;
8. The general shapes of vertical temperature profiles at all locations (midspan and 1/6-span) were similar, with extreme temperature changes being induced in the girder web for the field tests conducted in this effort;

9. Positioning of temperature gages at one-quarter points within the girder web of bulb-tee sections appeared to approximate the reversals of the temperature profile occurring within the girder web relatively well;
10. The most detailed analysis iteration (TC-M-PE-I) used in this study (which relied on between 11–13 thermocouple measurements at midspan and an exact cross section definition) tended to generate the most accurate predictions of girder deformations (with the exception of where testing anomalies were detected)—although at the greatest computational cost;
11. Analytical iterations conducted using measured data from different cross sections (i.e. TH-M-PE-I at midspan and TH-6-PE-I at 1/6-span), but identical analytical methods generated largely similar results;
12. Use of the simplified equivalent cross section proposed by Johnson (2012) resulted in negligible error when compared to use of an exact cross section definition;
13. Use of the simplified temperature profile proposed by Johnson (TH-M-EQ-J) generated strain predictions only slightly less accurate than those of the most detailed analysis included in this study (TC-M-PE-I). The use of linear interpolation to define the temperature profile shape (TS-M-PE-I) resulted in predictions of strain and vertical deflection only slightly less accurate than use of the temperature profile by Johnson (2012);
14. For the purposes of temperature-correction of field camber measurements, use of the temperature-correction algorithm derived in Section 8.2.2 is appropriate with either (a) the procedures and assumptions implemented by Johnson (2012), (b) the procedures and assumptions implemented in this study, or (c) any combinations thereof;
15. Maximum expected transient temperature-induced deformations for PCI bulb-tee girder sections (without decks) in unshaded outdoor storage are summarized in Table 8-11.

Table 8-11: Transient Changes to Theoretical Midspan Camber

Expected Transient Temperature-Induced Changes to Theoretical Midspan Camber	
Upward	<+1.5 in.
Downward	<-0.5 in.

Chapter 9: Camber Prediction Software (*ALCAMBER* v1.0) Development

9.1 Introduction

A key objective of this research effort was to publish a user-friendly camber prediction software capable of implementing the recommendations of this report with regards to predicting expected concrete strength (Chapter 5), concrete stiffness behavior (Chapter 6), and time-dependent concrete behavior (Chapter 7). This chapter serves as a basic introduction to the camber prediction software package, *ALCAMBER*, developed as part of this research project. Finer details of the software development have been documented by Schrantz (2012), Johnson (2012), and Isbiliroglu (2014).

9.1.1 Chapter Outline

First, a general background description of the incremental-time steps method for computing long-term girder deflections is discussed (Section 9.2). Next, various fundamental concepts and assumptions are utilized to derive the two governing equations for the incremental-time step method implemented in this research effort. Finally, the program algorithm is described along with the four key classes of computations performed.

9.2 Background

As introduced briefly in Chapter 2, the incremental time-steps method is an analysis method based on combining the computation of deformations with those of effective prestress and concrete stresses due to time-dependent creep, shrinkage, and relaxation (ACI Committee 435 2003). By dividing the life of the flexural element into discrete time increments, changes in shrinkage, creep, and relaxation can be computed for each time increment. Effective prestress force and deformations and stresses are then updated at the end of each time increment. By subdividing the flexural element into multiple cross sections and integrating the deformations along the length of the element, girder displacements and rotations can also be computed (ACI Committee 435 2003).

9.2.1 Application of Incremental Time-Steps Method

For the purposes of this research effort, the incremental time-steps method is applied to a simple-span, precast, prestressed concrete beam. Assuming symmetry about midspan, half of the girder is segmented by forty analysis cross sections. For each cross section, the initial strain distribution and corresponding curvature at the time immediately after prestress release is first computed from fundamental mechanics principles using transformed section properties to accurately include the steel stiffness. This initial strain distribution includes the effects of elastic shortening, pre-release relaxation of the prestressing strand, and the portion of concrete shrinkage occurring before prestress release.

The varying constituent girder materials (concrete and steel) exhibit time-dependent deformational tendencies—some of which begin as early as the time of initial strand tensioning. If fully unrestrained and independent of one another, the following responses from the girder constituent materials would be expected after prestress release:

- The tensile stresses (and corresponding forces) in the steel strands would reduce as a result of continued relaxation;
- Due to creep caused by a sustained stress, strains in the concrete would tend to increase in proportion to the relative magnitude of the sustained stress at a given depth within the section; and
- The strain in the concrete would tend to decrease (contract) as a result of unrestrained shrinkage of the concrete.

However, independent consideration of the material responses summarized above *would not* satisfy compatibility and equilibrium for a given cross section. Instead, these time-dependent material changes are interrelated and must be dealt with accordingly.

Two governing relationships can be used to compute the incremental change in cross-sectional strain and curvature that satisfy equilibrium and strain compatibility for a single time increment. Knowing the initial strain and curvature of each analysis section and the incremental change to these parameters within an increment (time step), the total strain and stresses can be updated for each cross section. By iterating this process, that is, using the results from the previous time step as the starting conditions for the subsequent time step, strains and curvatures can be computed at each analysis section for each time

step, while accurately incorporating the *interaction* of creep, shrinkage, and steel relaxation on the cross section. Finally, using moment-area theorems for flexural deformations, the cross-sectional stresses and curvatures for each analyzed cross section can be numerically integrated to compute camber at a considered time.

9.3 Derivation of Incremental Strain and Curvature Expressions

The incremental time-steps method, as implemented in this research effort, relies on two closed-form relationships to compute the incremental strain and curvature at a given cross section across a time step. Due to their importance to the development of the *ALCAMBER* software package, this section presents the derivations of these two governing equations beginning from basic principles of mechanics. These expressions, as derived by Schrantz (2012), are documented more thoroughly herein.

9.3.1 Key Assumptions

The following key assumptions are implicit to the *ALCAMBER* software package:

- Girders are assumed to be relatively slender, simply-supported, and symmetric about midspan;
- Deflections are computed from the time of prestress release until the estimated time of erection only, without consideration for post-erection behavior;
- Linear-elastic strain response to applied stress, as is uncracked section behavior;
- Strain compatibility between steel reinforcement and adjacent concrete is assumed; and
- The effect of prestressing strand transfer length is assumed to be limited to the end bonded segment of each group of strands (fully bonded or debonded) in the discretized girder.

9.3.2 Fundamental Principles

When the above assumptions are satisfied, it is permissible to utilize the fundamental principles listed here to derive the incremental strain and curvature equations: (1) plane sections remain plane and perpendicular to the longitudinal axis during deformation, (2) the total strain change in a material is equal to the sum of the stress-dependent (mechanical) strains and the stress-independent strains, and (3) cross-sectional equilibrium between internal stresses and external forces and moments.

9.3.3 Incremental Strain Expression Derivation

This section reviews the derivation of the equation for incremental strain as used in the incremental time-steps procedure implemented in the software *ALCAMBER*. The sign convention is as shown in Figure 9-1.

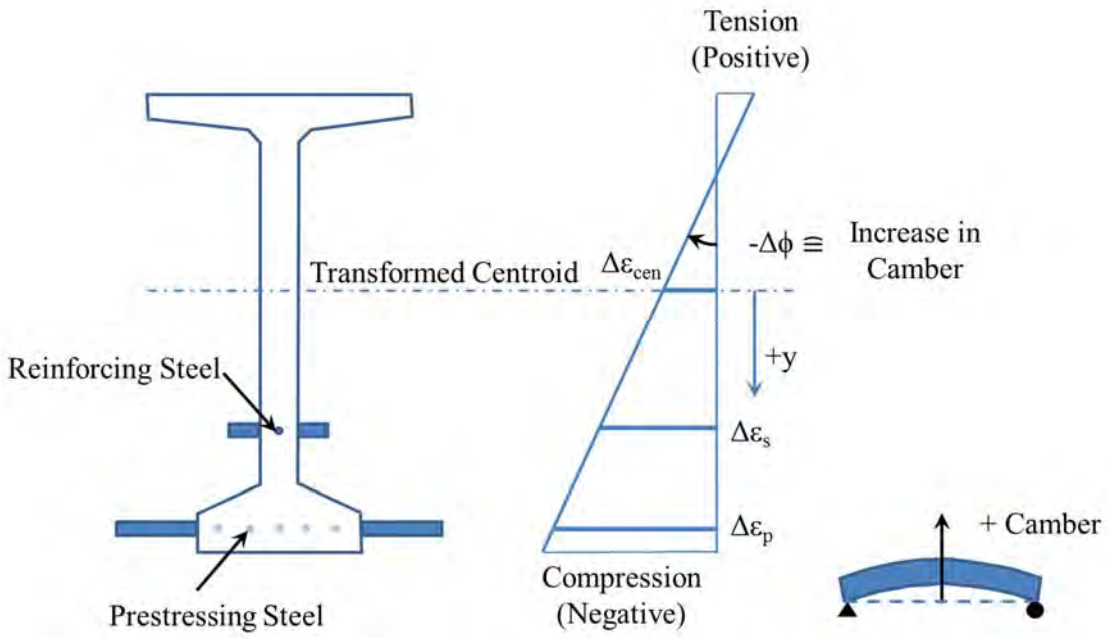

Figure 9-1: Sign Convention and Notation for Derivation

The strain profile shown is characteristic of a typical precast, prestressed girder at the time of prestress release. While the majority of the section remains in compression, any tensile strains at the top of the section remain below code-prescribed thresholds. Positive *y* is defined as downward from the transformed centroid, with negative *y* values upward. Using the fundamental principle of "plane sections remain plane", the following three equations describe the change in strain at all vertical locations in all constituent materials within a cross section:

$$\Delta\varepsilon_c = \Delta\varepsilon_{cen} + \Delta\phi(y) \tag{9-1}$$

$$\Delta\varepsilon_s = \Delta\varepsilon_{cen} + \Delta\phi(y_s) \tag{9-2}$$

$$\Delta\varepsilon_p = \Delta\varepsilon_{cen} + \Delta\phi(y_p) \tag{9-3}$$

where

$\Delta\varepsilon_c$ = change in concrete strain at a given depth within a cross section (in./in.);

$\Delta\varepsilon_{cen}$ = change in concrete strain at the transformed centroid (in./in.);

$\Delta\phi$ = change in curvature of a given cross section;

y = depth from the centroid of the transformed section to a given location within a cross section (in.);

$\Delta\varepsilon_s$ = change in strain in reinforcing steel (in./in.);

y_s = depth from the centroid of the transformed section to the steel location within a cross section (in.);

$\Delta\varepsilon_p$ = change in strain in prestressing steel (in./in.); and

y_p = depth from the centroid of the transformed section to the prestressing steel location within a cross section (in.).

Equilibrium with applied axial loads can be applied by integrating the changes in stress over the cross-sectional area:

$$\Delta N = \int_A \Delta\sigma dA = \int_{A_c} \Delta f_c dA_c + \int_{As} \Delta f_s dA_s + \int_{A_p} \Delta f_p dA_p \qquad (9\text{-}4)$$

where

f_x = the stress at a given height in a material [where x = c (concrete), s (steel), or p (prestressing steel)];

A_x = the total cross-sectional area of a material [same subscript convention used above for stress];

$\int_{A_c} \Delta f_c dA_c$ = representation of the change in cross sectional force in the concrete;

$\int_{As} \Delta f_s dA_s$ = representation of the change in cross-sectional force in the reinforcing steel; and

$\int_{A_p} \Delta f_p dA_p$ = representation of the change in cross sectional force in the prestressing steel.

Equilibrium of applied moments can be applied similarly, except with an added term to represent the distance from the transformed centroid:

$$\Delta M = \int_A y\Delta\sigma dA = \int_{A_c} y_c \Delta f_c dA_c + \int_{A_s} y_s \Delta f_s dA_s + \int_{A_p} y_p \Delta f_p dA_p \qquad (9\text{-}5)$$

For each time step in the analysis, the externally applied load and moments do not change for a given cross section. Therefore

$$\Delta N = 0 \;,\; \Delta M = 0 \tag{9-6}$$

Simplifying the integrals for reinforcing steel and prestressing steel terms into discrete sums to represent the discrete potential locations of steel within a cross section:

$$\Delta N = \int_{A_c} \Delta f_c dA_c + \sum \left(\Delta f_s A_s\right) + \sum \left(\Delta f_p A_p\right) = 0 \tag{9-7}$$

$$\Delta M = \int_{A_c} y \Delta f_c dA_c + \sum \left(y_s \Delta f_s A_s\right) + \sum \left(y_p \Delta f_p A_p\right) = 0 \tag{9-8}$$

Equations 9-7 and 9-8, currently written in terms of incremental stresses, can be written in terms of incremental strains using linear-elastic behavior assumptions and the definition of total strain. The total incremental strain in the concrete can be represented as the sum of the stress-dependent (mechanical) and stress-independent incremental strains as shown in Equation 9-9.

$$\Delta \varepsilon_c = \underbrace{\frac{\Delta f_c}{E_c}}_{\text{Stress Dependent}} + \underbrace{\Delta \varepsilon_{c,cr} + \Delta \varepsilon_{c,shr} + \Delta \varepsilon_{c,temp}}_{\text{Stress Independent}} \tag{9-9}$$

where

$\frac{\Delta f_c}{E_c}$ = the portion of change in concrete strain resulting from linear-elastic stress response;

$\Delta \varepsilon_{c,cr}$ = the portion of the change in concrete strain due to unrestrained creep;

$\Delta \varepsilon_{c,shr}$ = the portion of the change in concrete strain due to unrestrained shrinkage; and

$\Delta \varepsilon_{c,temp}$ = the portion of concrete strain due to unrestrained temperature effects.

Solving for the incremental stress in the concrete, Δf_c, and neglecting thermal strains yields:

$$\Delta f_c = E_c \left(\Delta \varepsilon_c - \Delta \varepsilon_{c,cr} - \Delta \varepsilon_{c,shr}\right) \tag{9-10}$$

Similarly, an expression for the incremental stress in the prestressing steel (considering relaxation) can be derived:

$$\Delta f_p = E_p \Delta \varepsilon_p + \Delta f_{p,relax} \tag{9-11}$$

where

$\Delta f_{p,relax}$ = the change in stress in prestressing steel due to steel relaxation.

Similarly, the stress in the reinforcing steel can be expressed as

$$\Delta f_s = E_s \Delta \varepsilon_s \tag{9-12}$$

Substitution of the three derived expressions for incremental stress (Equations 9-10, 9-11, and 9-12) into the incremental cross-sectional equilibrium equation for axial force (Equation 9-7) yields

$$\begin{aligned} &\int_{A_c} \left[E_c \left(\Delta \varepsilon_c - \Delta \varepsilon_{c,cr} - \Delta \varepsilon_{c,shr}\right)\right] dA_c + \sum \left(\left[E_s \Delta \varepsilon_s\right] A_s\right) + \\ &\sum \left(\left[E_p \Delta \varepsilon_p + \Delta f_{p,relax}\right] A_p\right) = 0 \end{aligned} \tag{9-13}$$

The incremental creep strain (which varies by cross-sectional height in proportion to stress) can be written similarly to Equation 9-1 as

$$\Delta \varepsilon_{c,creep} = \Delta \varepsilon_{cen,creep} + \Delta \phi_{creep}(y) \tag{9-14}$$

Combining Equations 9-1, 9-2, 9-3, and 9-14 with Equation 9-13 yields

$$\begin{aligned} &\int_{A_c} \left[E_c \left(\left(\Delta \varepsilon_{cen} + \Delta \phi(y)\right) - \left(\Delta \varepsilon_{cen,creep} + \Delta \phi_{creep}(y)\right) - \Delta \varepsilon_{c,shr}\right)\right] dA_c + \\ &\sum \left(\left[E_s \left(\Delta \varepsilon_{cen} + \Delta \phi(y_s)\right)\right] A_s\right) + \sum \left(\left[E_p \left(\Delta \varepsilon_{cen} + \Delta \phi(y_p)\right) + \Delta f_{p,relax}\right] A_p\right) = 0 \end{aligned} \tag{9-15}$$

Grouping curvature-dependent terms and those independent of location *y* yields

$$\begin{aligned} 0 = {} & E_c A_c \left[\Delta \varepsilon_{cen} - \left(\Delta \varepsilon_{cen,creep} + \varepsilon_{c,shr}\right)\right] + \sum \left(E_p A_p \Delta \varepsilon_{cen}\right) + \sum \left(E_s A_s \Delta \varepsilon_{cen}\right) + \\ & \sum \left(A_p \Delta f_{p,relax}\right) + E_c \Delta \phi \left[\int_{A_c} y dA_c + \left(\frac{E_p}{E_c}\right) \sum y_p A_p + \left(\frac{E_s}{E_c}\right) \sum y_s A_s\right] - E_c \Delta \phi_{creep} \int_{A_c} y dA_c \end{aligned} \tag{9-16}$$

Recognizing (1) that the bracketed portion of the following term is the first moment of area, and (2) that if y is measured relative to the centroid of the transformed section, the first moment of area is zero:

$$E_c \Delta \phi \left[\int_{A_c} y dA_c + \left(\frac{E_p}{E_c}\right) \sum y_p A_p + \left(\frac{E_s}{E_c}\right) \sum y_s A_s\right] = E_c \Delta \phi \int_{A_c} y dA_{tr} = 0 \tag{9-17}$$

Discarding the above term yields

$$0 = E_c A_c \left[\Delta\varepsilon_{cen} - \left(\Delta\varepsilon_{cen,creep} + \varepsilon_{c,shr}\right)\right] + \sum\left(E_p A_p \Delta\varepsilon_{cen}\right) + \sum\left(E_s A_s \Delta\varepsilon_{cen}\right) + \sum\left(A_p \Delta f_{p,relax}\right) - E_c \Delta\phi_{creep} \int_{A_c} y dA_c \quad (9\text{-}18)$$

Regrouping

$$0 = \Delta\varepsilon_{cen}\left[E_c A_c + \sum E_p A_p + \sum E_s A_s\right] - E_c A_c \left(\Delta\varepsilon_{cen,creep} + \Delta\varepsilon_{c,shr}\right) + \sum\left(A_p \Delta f_{p,relax}\right) - E_c \Delta\phi_{creep} \int_{A_c} y dA_c \quad (9\text{-}19)$$

Solving for $\Delta\varepsilon_{cen}$

$$\Delta\varepsilon_{cen} = \frac{E_c A_c \left(\Delta\varepsilon_{cen,creep} + \Delta\varepsilon_{c,shr}\right) - \sum\left(A_p \Delta f_{p,relax}\right) + E_c \Delta\phi_{creep} \int_{A_c} y dA_c}{\left[E_c A_c + E_p \sum A_p + E_s \sum A_s\right]} \quad (9\text{-}20)$$

Recognizing that the denominator is equal to $E_c A_{tr}$

$$\Delta\varepsilon_{cen} = \frac{A_c \left(\Delta\varepsilon_{cen,creep} + \Delta\varepsilon_{c,shr}\right) - \frac{1}{E_c}\sum\left(A_p \Delta f_{p,relax}\right) + \Delta\phi_{creep} \int_{A_c} y dA_c}{A_{tr}} \quad (9\text{-}21)$$

Here, the integral with respect to y is non-zero, because it is not defined in terms of the transformed section. Knowing that the transformed area is

$$A_{tr} = A_c + n_p A_p + n_s A_s \quad (9\text{-}22)$$

where

$n_p = \frac{E_p}{E_c}$ = the modular ratio of the prestressing steel, and

$n_s = \frac{E_s}{E_c}$ = the modular ratio of the reinforcing steel.

Solving for A_c

$$A_c = A_{tr} - n_p A_p - n_s A_s \quad (9\text{-}23)$$

Substituting into the integral of Equation 9-21

$$\int_{A_c} y dA_c = \int_{A_c} y d\left(A_{tr} - n_p A_p - n_s A_s\right) \quad (9\text{-}24)$$

Simplifying, recognizing the first term equals zero, and adding appropriate y-subscripts for context

$$\int_{A_c} y dA_c = -\sum n_p A_p y_p - \sum n_s A_s y_s \tag{9-25}$$

Substituting Equation 9-25 into 9-21 and simplifying yields

$$\Delta\varepsilon_{cen} = \frac{A_c}{A_{tr}}\left(\Delta\varepsilon_{cen,creep} + \Delta\varepsilon_{c,shr}\right) - \frac{\Delta\phi_{creep}\left(n_p\sum\left(A_p y_p\right) + n_s\sum\left(A_s y_s\right)\right)}{A_{tr}} - \frac{\frac{1}{E_c}\sum\left(A_p \Delta f_{p,relax}\right)}{A_{tr}} \tag{9-26}$$

Equation 9-26 is used in *ALCAMBER* at each analysis cross section and time step to compute the incremental strain at the centroid across each time increment.

9.3.4 Incremental Curvature Expression Derivation

This section reviews the derivation of the equation for incremental curvature as used in the incremental time-steps procedure implemented in the software *ALCAMBER*. This derivation is again based on the sign convention of Figure 9-1. Beginning with the incremental moment expression of Equation 9-8

$$\Delta M = \int_{A_c} y\Delta f_c dA_c + \sum\left(y_s \Delta f_s A_s\right) + \sum\left(y_p \Delta f_p A_p\right) = 0 \tag{9-8}$$

Substituting the incremental stress expressions of Equation 9-10, 9-11, and 9-12 and neglecting thermal strains;

$$\Delta M = \int_{A_c} y\left(E_c\left(\Delta\varepsilon_c - \Delta\varepsilon_{c,cr} - \Delta\varepsilon_{c,shr}\right)\right)dA_c + \sum\left(\left(E_s\Delta\varepsilon_s\right)y_s A_s\right) + \sum\left(\left(E_p\Delta\varepsilon_p + \Delta f_{p,relax}\right)y_p A_p\right) = 0 \tag{9-27}$$

Substituting the expressions for incremental strain (Equations 9-1, 9-2, 9-3, and 9-14) into Equation 9-27 yields

$$\Delta M = \int_{A_c} \left(E_c\left(\left[\Delta\varepsilon_{cen} + \Delta\phi(y)\right] - \left[\Delta\varepsilon_{cen,creep} + \Delta\phi_{creep}(y)\right] - \Delta\varepsilon_{c,shr}\right)\right)y dA_c + \sum\left(\left(E_s\left[\Delta\varepsilon_{cen} + \Delta\phi(y_s)\right]\right)y_s A_s\right) + \sum\left(\left(E_p\left[\Delta\varepsilon_{cen} + \Delta\phi\left(y_p\right)\right] + \Delta f_{p,relax}\right)y_p A_p\right) = 0 \tag{9-28}$$

Grouping Equation 9-28 into curvature-dependent and curvature-independent terms and simplifying yields

$$0 = \Delta\varepsilon_{cen} E_c \left[\left(\int_{A_c} y dA_c \right) + \frac{E_p}{E_c} \sum y_p A_p + \frac{E_s}{E_c} \sum y_s A_s \right] +$$
$$E_c \Delta\phi \left[\left(\int_{A_c} y^2 dA_c \right) + \frac{E_p}{E_c} \sum {y_p}^2 A_p + \frac{E_s}{E_c} \sum {y_s}^2 A_s \right] -$$
$$E_c \left[\Delta\varepsilon_{cen,creep} + \Delta\varepsilon_{c,shr} \right] \left[\int_{A_c} y dA_c \right] - E_c \Delta\phi_{cr} \int_{A_c} y^2 dA_c \qquad (9\text{-}29)$$
$$+ \sum \left(y_p A_p \Delta f_{p,relax} \right)$$

Recognizing that the bracketed portion of the first term is the first moment of area of the transformed section (which is zero) allows this term to be discarded as shown below.

$$0 = E_c \Delta\phi \left[\left(\int_{A_c} y^2 dA_c \right) + \frac{E_p}{E_c} \sum {y_p}^2 A_p + \frac{E_s}{E_c} \sum {y_s}^2 A_s \right] -$$
$$E_c \left[\Delta\varepsilon_{cen,creep} + \Delta\varepsilon_{c,shr} \right] \left[\int_{A_c} y dA_c \right] - \qquad (9\text{-}30)$$
$$E_c \Delta\phi_{cr} \int_{A_c} y^2 dA_c + \sum \left(y_p A_p \Delta f_{p,relax} \right)$$

The moment of inertia of the transformed section, I_{tr} is

$$I_{tr} = \int_{A_c} y^2 dA_c + n_p \sum {y_p}^2 A_p + n_s \sum {y_s}^2 A_s \qquad (9\text{-}31)$$

Simplifying 9-30 accordingly

$$0 = E_c \Delta\phi \left[I_{tr} \right] - E_c \left[\Delta\varepsilon_{cen,creep} + \Delta\varepsilon_{c,shr} \right] \left[\int_{A_c} y dA_c \right] -$$
$$E_c \Delta\phi_{cr} \int_{A_c} y^2 dA_c + \sum \left(y_p A_p \Delta f_{p,relax} \right) \qquad (9\text{-}32)$$

Combining Equation 9-25 with 9-32 yields

$$0 = E_c \Delta\phi \left[I_{tr} \right] - E_c \left[\Delta\varepsilon_{cen,creep} + \Delta\varepsilon_{c,shr} \right] \left[- n_p \sum A_p y_p - n_s \sum A_s y_s \right] -$$
$$E_c \Delta\phi_{cr} \int_{A_c} y^2 dA_c + \sum \left(y_p A_p \Delta f_{p,relax} \right) \qquad (9\text{-}33)$$

Next, the only remaining integral term, the second moment of area of concrete about the centroid of the transformed area, $\int_{A_c} y^2 dA_c$, must be evaluated. Solving Equation 9-31 for $\int_{A_c} y^2 dA_c$ yields

$$\int_{A_c} y^2 dA_c = I_{tr} - n_p \sum {y_p}^2 A_p - n_s \sum {y_s}^2 A_s \tag{9-34}$$

Substituting 9-41 into 9-40 and regrouping yields

$$\begin{aligned} 0 = {} & E_c \Delta\phi [I_{tr}] - E_c [\Delta\varepsilon_{cen,creep} + \Delta\varepsilon_{c,shr}] - n_p \sum A_p y_p - n_s \sum A_s y_s] - \\ & E_c \Delta\phi_{cr} \left(I_{tr} - \sum n_p {y_p}^2 A_p - \sum n_s {y_s}^2 A_s \right) + \sum \left(y_p A_p \Delta f_{p,relax} \right) \end{aligned} \tag{9-35}$$

Further regrouping, a final expression for incremental curvature can be obtained as follows:

$$\Delta\phi = \Delta\phi_{creep} \left[1 - \frac{\left(\{ n_p \sum A_p {y_p}^2 \} + \{ n_s \sum A_s {y_s}^2 \} \right)}{I_{tr}} \right] - \frac{\left(\Delta\varepsilon_{cen,cr} + \Delta\varepsilon_{c,shr} \right) \left(n_p \sum A_p y_p + n_s \sum A_s y_s \right)}{I_{tr}} - \frac{\frac{1}{E_p} n_p \sum \Delta f_{p,relax} A_p y_p}{I_{tr}} \tag{9-36}$$

In conjunction with the previously derived expression for incremental strain (Equation 9-26), the derived expression for incremental curvature (Equation 9-36) is used in *ALCAMBER* to completely define the incremental strains and curvature at each analysis cross section for each time step in the analysis, while satisfying equilibrium and compatibility conditions.

9.4 Software Algorithm Description

A brief description of the software algorithm is offered in this section. The *ALCAMBER* software algorithm is divided into four main categories: (1) initial calculations, (2) calculations for each time step and cross section, (3) updated strains and stresses, and (4) incremental and total camber as shown in Figures 9-2 and 9-3. Each of these categories is briefly discussed in this section. For a more complete description of the software algorithm, readers are referred to Isbiliroglu (2014).

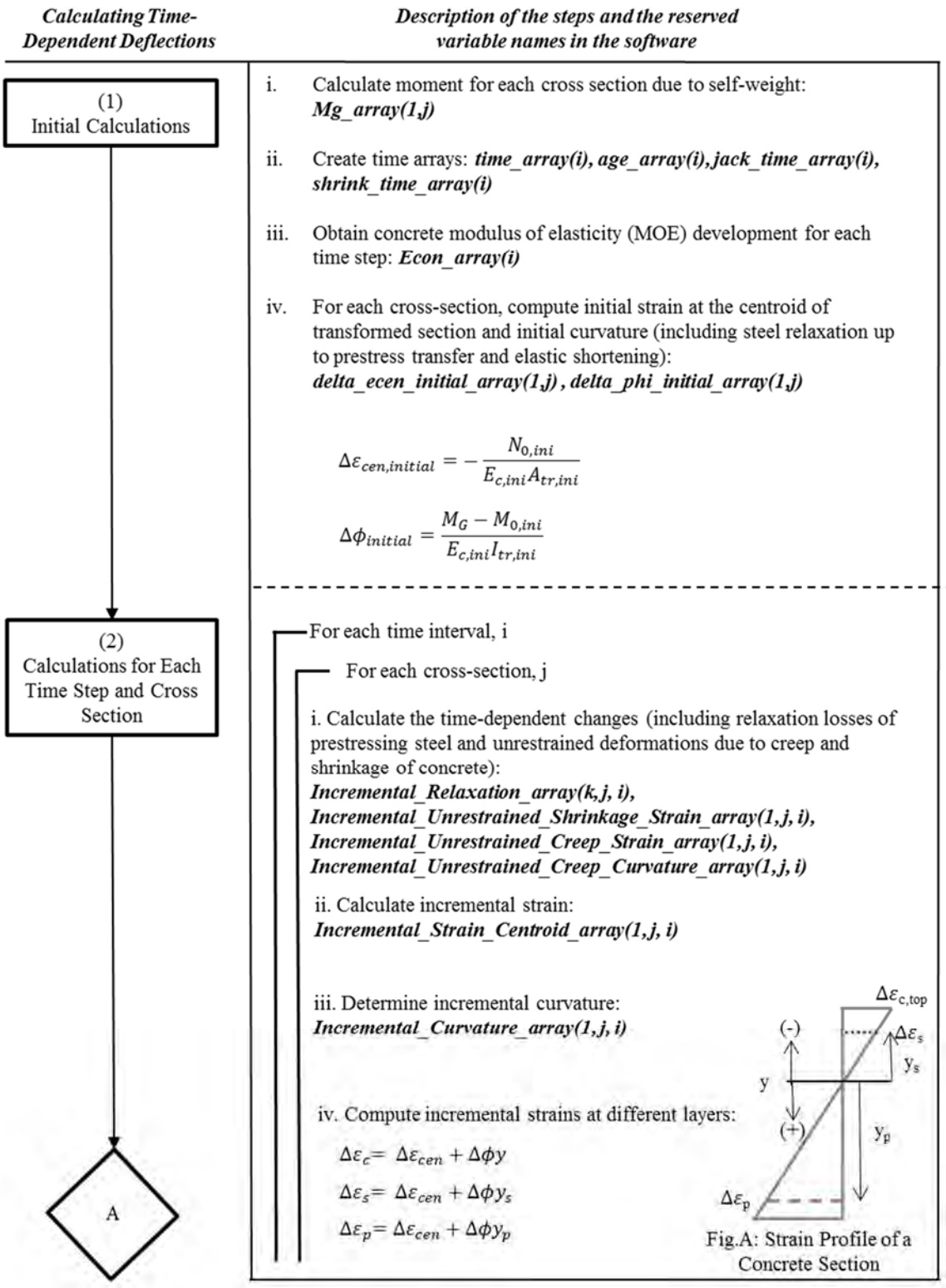

Figure 9-2: *ALCAMBER* Software Program Algorithm – Part 1

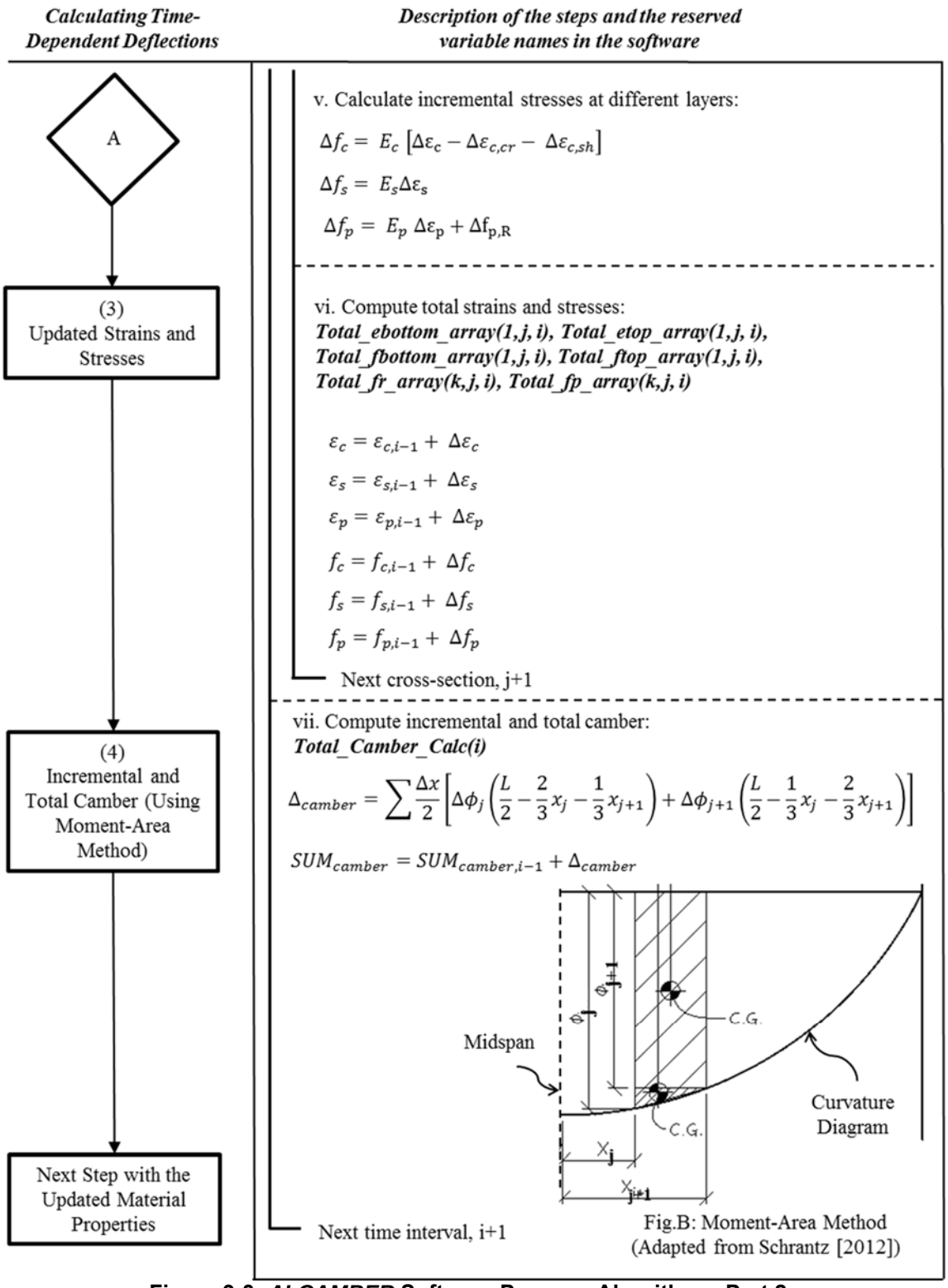

Figure 9-3: *ALCAMBER* Software Program Algorithm – Part 2

9.4.1 Initial Calculations

Prior to beginning the iterations typical of a time-steps analysis, it is first necessary for an analysis starting point to be defined by computing various quantities. First, the moment due to girder self-weight is computed for each cross section. Next, various time indices[10] or arrays are generated to define the progression of time within the program. These time indices are used to represent the chronological timing of construction events, the relative start and analysis end points for time-dependent changes (i.e. creep and shrinkage), and the maturity or equivalent age of concrete (if desired by the user). Next, the concrete modulus of elasticity is computed for each time step in accordance with the user-selected material model. Finally, initial strain and curvature are computed at the centroid of the transformed section at the time of prestress release. These initial strain and curvature computations include the effects of pre-release steel relaxation and elastic shortening. At this point, the initial computations, as necessary to define the starting point for the incremental analysis, are complete.

9.4.2 Calculations for Each Time Step and Cross Section

The next major category of the algorithm defines and executes the various logic loops of the program. As noted in Figure 9-2, there is an outer logic loop (the time loop) and an inner loop (for each cross section). Each of the computations discussed in this paragraph is completed within the inner loop, meaning that these computations are completed for each cross section at each time step. First, the time-dependent losses due to steel relaxation and the time-dependent deformation changes due to unrestrained creep and shrinkage of concrete are computed. Next, the incremental strain and curvature are computed using the previously derived expressions of Equation 9-26 and 9-36. Using the relationships of Equations 9-1, 9-2, and 9-3, the incremental strains at all locations within a given cross section are next computed. Finally, incremental stresses can be computed for constitutive materials at all layers within a given cross section.

[10] Schrantz (2012) details the time array functions utilized within *ALCAMBER* and also contains recommendations for the number of analysis increments and the corresponding effects on prediction accuracy.

9.4.3 Updated Strains and Stresses

Still within the inner logic loop, the next algorithm category is the computation of updated strains and stresses for each cross section. These updates strains and stresses are computed by adding the incremental change to the strains and stresses associated with a given time step to the values at the end of previous time step. It is critically important to update the strains and stresses at the end of each time step in order to ensure the accuracy of the time-dependent material reflects the new revised stresses over the next time step.

9.4.4 Incremental and Total Camber

The computations of the final category of the software algorithm are located within the outer logic loop (the time loop), but outside of the inner loop (the cross sectional loop). After all cross-sectional analyses are completed within a given time step (e.g. the inner time loop is completed), the fully-defined curvatures allow the use of the moment-area theorems to compute the incremental change in camber occurring across a given time step. By summing the previous incremental changes in camber, the total camber magnitude can be computed for any given age.

9.5 Summary

This chapter details the development of a user-friendly camber prediction software capable of implementing the recommendations of this report with regards to predicting expected concrete strength (Chapter 5), concrete stiffness behavior (Chapter 6), and time-dependent deformational behavior (Chapter 7). Using two key derived relationships, incremental values of centroidal strain and curvature are computed for each analysis cross section for each analysis time step. Using these key parameters, the collective girder deformational response is then defined—allowing predictions of girder camber.

Chapter 10: Selection and Validation of a Revised Camber Prediction Procedure by Limited In-Plant Testing

10.1 Introduction

Previous chapters have focused on systematically addressing inaccuracies intrinsic to the camber prediction problem in precast, prestressed concrete girders. The focus of this chapter is the implementation of the recommendations proposed thus far in this report (with respect to overstrength, modulus of elasticity, creep and shrinkage behavior, and thermal effects) and validation of these recommendations by comparisons to field measurements gathered during and after the production of ALDOT precast, prestressed concrete bridge girders.

10.1.1 Chapter Objectives

The primary objective of this chapter is to validate the effectiveness of various combinations of design recommendations resulting from the experimental work of this study—ultimately in pursuit of a single camber prediction procedure that results in improved predictions during initial girder design. Tasks completed in support of this primary objective include:

- For a variety of prediction trials, compare various metrics of field-observed girder deformation (i.e. camber, curvature, and cross-sectional concrete strains) to predicted girder behavior using different software packages;
- Modify field measurements using the temperature-correction procedure (detailed in Chapter 8) to analytically remove the effect of transient thermal exposure and facilitate appropriate comparisons among measurements;
- Explore the isolated and compounded effects of various design recommendations of previous report chapters; and

- Evaluate the appropriateness of the continued use of the simple multiplier method proposed by Martin (1977) for estimating changes in long-term deflections of Alabama precast, prestressed concrete bridge girders.

10.1.2 Chapter Outline

This chapter begins by detailing an experimental effort conducted on-site at girder production facilities within the study region. Included in the description of the experimental procedure are (1) details of the particular girder production cycles monitored in this study, (2) results of much of the on-site concrete material property testing conducted, and (3) details of techniques utilized to measure girder deformational behavior and internal concrete temperatures. Next, all gathered girder data is first presented unmodified, then subjected to post-processing efforts including (1) computation of concrete equivalent ages at the time of prestress release, (2) verification of the linearity of cross-sectional strain readings, and (3) application of the temperature-correction procedure to remove the effect of transient temperature variations from field measurements. Subsequently, a series of trial camber prediction procedures are implemented and then compared to the measured field responses. Based on these comparisons, the effects of various design recommendations (with respect to concrete overstrength, elastic modulus, and creep and shrinkage) on camber prediction accuracy are explored and a finalized design procedure is recommended. Finally, the appropriateness of the continued use (or modification) of the PCI multiplier method for predicting time-dependent deformations of Alabama precast, prestressed concrete bridge girders is explored.

10.2 Experimental Program

10.2.1 Summary

In this portion of the study, in-plant testing was conducted for nine girder production cycles, representing a total of twenty-two ALDOT precast, prestressed concrete bridge girders at two production facilities. In-plant testing efforts consisted of (1) measurement of various concrete material properties (e.g. concrete compressive strength and modulus of elasticity) at key ages for various curing conditions, (2) instrumentation of selected girders with internal strain and temperature sensors at the midspan cross section, and (3) measurement of girder camber using the surveying method at various key ages of

interest. Using the measured internal concrete temperatures, observed girder camber and internal strain (and curvature) measurements were then corrected to remove the effect of transient thermal effects.

10.2.2 Experimental Procedure

Due to the large number of simultaneous tasks involved in the on-site data gathering performed in this study, this section is divided into three main data collection efforts: (1) concrete material property testing, (2) measurement of girder camber by the surveying method, and (3) measurement of girder strains and temperatures. The experimental work described herein was conducted in parallel with a portion of the efforts discussed in Chapters 6 and 9.

Due to the vital role of concrete material properties in the camber prediction problem, concrete material testing was conducted during nine girder placement events occurring at two regional precast, prestressed concrete girder producers. This included testing concrete compressive strength and concrete elastic modulus in accordance with ASTM C39 and ASTM C469, respectively. The on-site material testing plan is outlined in Figure 10-1 and consisted of sampling 26 6”x12” cylinders for each girder production cycle, exposing these specimens to various curing conditions, and testing at key ages of interest. Additional considerations not explicitly noted in Figure 10-1 include the following:

- Fresh concrete properties, as tested by the girder producer, are also reported in this chapter;
- Field curing of cylinder specimens in this investigation was accomplished by locating cylinders within the girder formwork (between top- and bottom-flange projections) during accelerated curing, and then transferring specimens to preheated, shaded lime-baths exposed to ambient conditions. This method of field-curing cylinders was preferable because (1) it mitigated the rate of heat loss from cylinders upon removal from accelerated curing, thereby avoiding thermal shock, and (2) it avoided exposure of the specimens to direct solar radiation, which can result in artificially elevated temperatures in specimens with volumes substantially less than a girder;
- Hardened property testing consisted of using a cylinder to first conduct elastic modulus testing in accordance with ASTM C469, and then performing compressive strength testing (ASTM C39) on the same cylinder; and
- Concrete maturity, where necessary, was computed using measured internal girder temperatures.

For each of nine girder placement events

For each of two sampling locations, prepare twelve 6" x 12" cylinder specimens

Field cure nine cylinders inside formwork during accelerated curing, thereafter move to preheated[a] outdoor shaded lime bath until testing

Hardened testing[b] of three cylinders at time of prestress release

Hardened testing of three cylinders at 1-day

Hardened testing of three cylinders at 28-days

Standard cure three cylinders in laboratory until testing

Hardened testing of three cylinders at 28-days

Note:
[a] = Curing tank preheated by exposure to steam prior to insertion of cylinders.
[b] = Hardened testing consists of concrete compressive strength testing and modulus of elasticity testing in accordance with ASTM C39 and ASTM C469, respectively.

Figure 10-1: On-site Concrete Material Testing Procedure

Likely the most critical on-site data collection effort in this study was the measurement of girder camber at various key ages of interest. The procedure for camber measurement, as summarized in Figure 10-2, consisted of the measurement of girder camber by the surveying method. For each girder placement event, metal survey points were installed along the middle of the top flange of each girder during concrete placement in the positions shown in Figure 10-3. Using these permanently anchored points, a two-person team using a surveying instrument and prism rod measured girder camber. Midspan camber was computed as the deviation from a tangent connecting the two outer-most survey points.

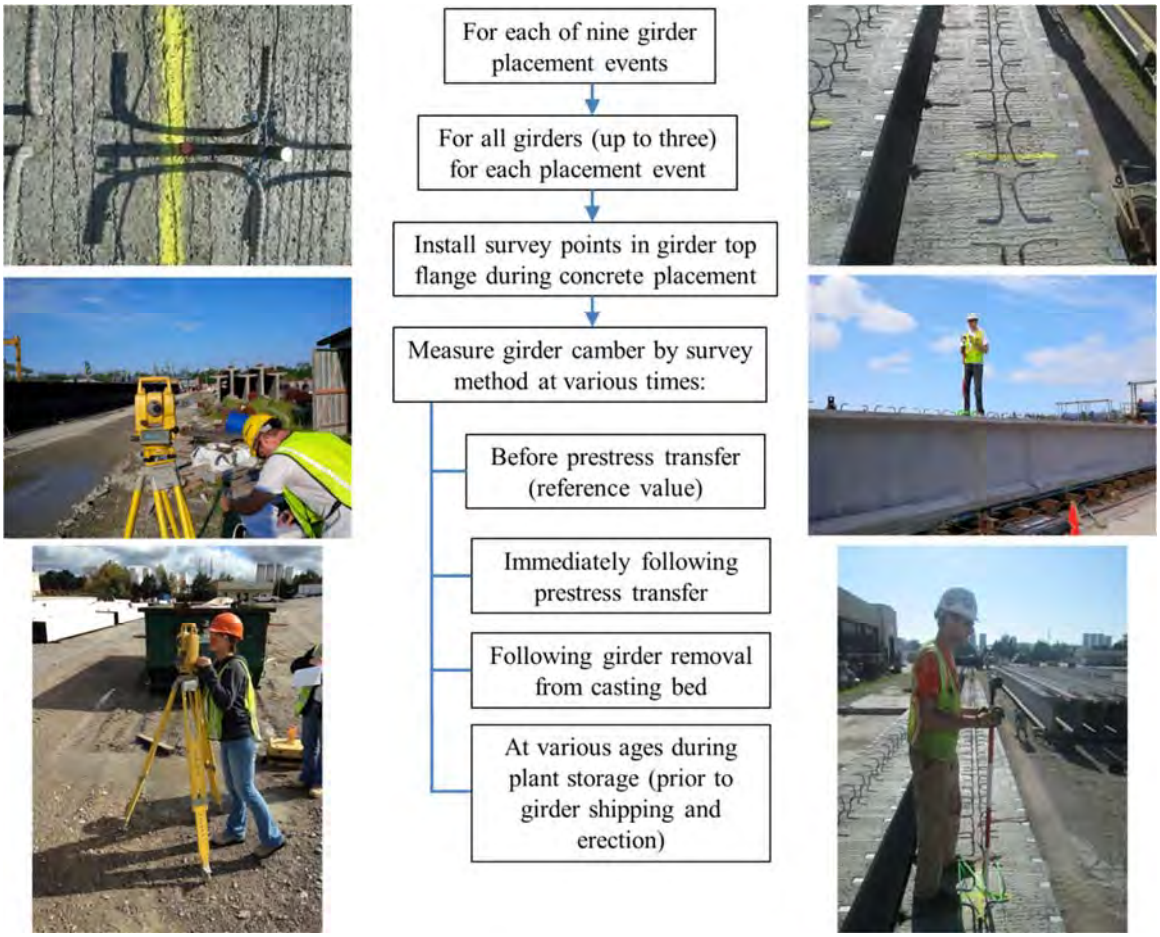

Figure 10-2: Procedure for On-Site Camber Measurement

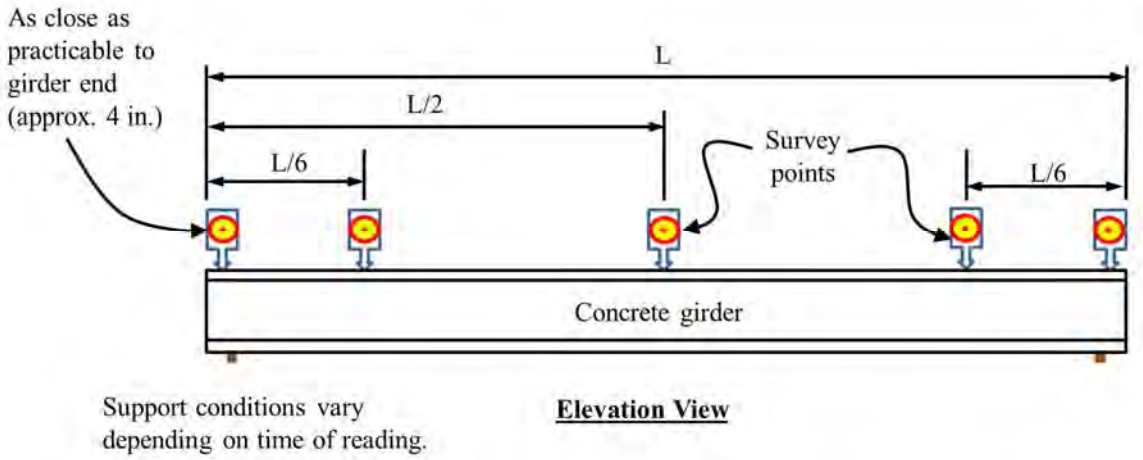

Figure 10-3: Typical Locations of Survey Points along Girder Top Flange

Camber measurements were taken both during the girder production process (to capture instantaneous camber) and also during girder storage (to capture camber growth). To properly measure camber using the survey method, benchmark measurements must be taken prior to the prestress transfer event.

Without these benchmark measurements, it is not possible to differentiate between the portion of elastic camber induced by the effective prestress force and the portion of apparent camber caused by any slope, crown, or other imperfections in the girder top flange concrete.

In order to offer meaningful comparisons among values of camber measured at differing times and ambient conditions, it was necessary to apply the temperature-correction procedure detailed in Chapter 8 of this report to all camber measurements. To perform this correction procedure, internal concrete strains and temperatures were measured at a typical cross section within a representative girder for each concrete placement event. The procedure for monitoring of internal concrete strain and temperatures is summarized in Figure 10-4. During girder production, four vibrating-wire strain gages with thermistors were placed within girder concrete at the midspan cross section in the typical locations shown in Figure 10-5. Then, strains and internal temperatures were monitored continuously during all steps of girder production and also at any time a follow-up measurement of girder camber was recorded. The concrete strain and temperature monitoring work described in this chapter utilized the same data collection system and vibrating-wire strain gage type as discussed in Section 8.3.3.

Figure 10-4: Procedure for On-Site Monitoring of Concrete Strain and Temperature

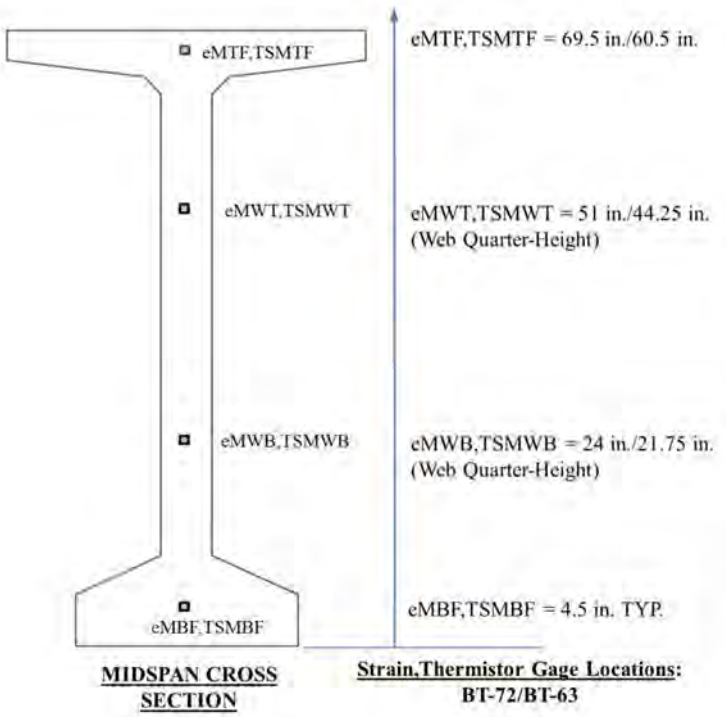

Figure 10-5: Locations of Midspan Concrete Strain and Temperature Sensors

10.2.3 Testing and Girder Details

Nine girder production events were monitored as part of this research effort. Included in this section are (1) general details regarding the girder production events and included girders, (2) timing of critical construction events, (3) girder cross section schematics and prestressing strand details, (4) specified concrete compressive strengths, and (5) concrete mixture designs used.

General details for each of the nine field tests, representing the production of twenty-two precast, prestressed girders, are summarized in Table 10-1. As shown, the girder production events occurred between July, 2013 and September, 2014. Two of the concrete placement events occurred on Mondays (following Friday strand tensioning), while the remainder were standard weekday placement events. There were twelve BT-63 girders and ten BT-72 girders of lengths varying from approximately 1360 in. (113 ft) to 1660 in. (138 ft).

Table 10-1: General Field Testing Information

Field Test ID	Production Date	Girder Cross Section	No. of Girders	Average Girder Length (in.)	Specified Release Strength (psi)	Specified 28-Day Strength (psi)
1[a]	7/8/13	BT-63	3	1357.8	5,600	6,000
2	7/24/13	BT-72	2	1641.0	5,500	7,250
3	7/25/13	BT-72	2	1631.4	5,500	7,250
4[a]	10/7/13	BT-72	2	1659.5	5,500	7,250
5	10/9/13	BT-72	2	1654.6	5,500	7,250
6	10/10/13	BT-72	2	1608.6	5,500	7,250
7	9/23/14	BT-63	3	1537.8	7,000	8,000
8	9/25/14	BT-63	3	1550.5	7,000	8,000
9	9/30/14	BT-63	3	1550.5	7,000	8,000

[a] = Production occurred on Monday following Friday strand tensioning

The timing of various construction events, as recorded by on-site research personnel, is shown in Table 10-2. Where values were not precisely known, estimates were made as noted. There are implicit difficulties encountered when attempting to document the timing of concurrent on-site production events—many with a duration exceeding 1-2 hours. For instance, while the transfer of the prestress force to the concrete occurs over a relatively short time period (approximately 5–30 minutes), the placement of girder concrete occurs gradually over a two hour period, resulting in girders with slightly different ages at the time of prestress release. To address this issue, a best effort was made to estimate average timings of each event and to select typical benchmark events (e.g. concrete placed at midspan gages of instrumented girder) for reporting construction timing.

Table 10-2: Construction Timing for Field Tests

Field Test ID	Age of Strand Tension Prior to Concrete Placement (hours)	Time from Concrete Placement to Prestress Transfer (hours)	Concrete Chronological Age at Prestress Transfer[b] (hours)	Curing Method	Curing Duration[c] (hours)
1	72[a]	42.7	43.0	Moist	40.7
2	24[a]	19.3	19.6	Steam	17.3
3	24[a]	16.1	16.4	Steam	15.1
4	72	19.0	19.3	Steam	17.9
5	24	19.8	20.1	Steam	18.4
6	26	17.7	18.0	Steam	16.4
7	24[a]	20.9	21.2	Steam	18.9
8	24[a]	19.8	20.1	Steam	17.8
9	24[a]	22.2	22.6	Steam	20.2

[a] = Estimated value.
[b] = Concrete mixing time estimated to be 20 minutes prior to placement based on experience.
[c] = Curing duration computed assuming tarp removal 2 hours prior to release unless otherwise documented by on-site researchers.

While the majority of field tests reflect relatively typical plant practices (similar to those reported in Chapter 4), the first production cycle included an abnormally long curing period due to production difficulties encountered by the girder producer. Concrete mixture designs for each girder production cycle, as initially shown in Table 6-3, are reproduced here for reference. Field Test #1 used a mixture similar to the ternary mixture (DL-FA/SF) from the laboratory investigation of Chapters 6 and 7, while the remaining tests used a mixture most similar to the slag SCM mixture (DL-SL) of Chapters 6 and 7. Finally, girder cross sections and prestressing strand details for the three typical girder designers included in this study are shown in Figures 10-6 through 10-8. Included in each figure is the sizing and arrangement of all prestressing strands, strand tensioning details, and strand draping and debonding lengths. For convenience in inputting strand position into design software, locations of each strand layer are provided relative to the girder bottom.

Table 6-3: Mixture Proportions for On-Site Production Cycles

Field Test ID	Type III Cement (pcy)	Grade 120 Slag Cement (pcy)	Class F Fly Ash (pcy)	Silica Fume (pcy)	Water (pcy)	*w/cm*	Coarse Agg. SSD (pcy)	Fine Agg. SSD (pcy)	*sand/total agg. (volume)*	*total agg. vol. (%)*	*paste vol.* (ft^3/cy)	HRWRA #1 (oz/cwt)	HRWRA #2 (oz/cwt)	HSA (oz/cwt)
Test 1	745	0	135 (14%)	75 (8%)	258	0.27	1,665 (#78 Dolomitic Limestone)	1,085 (#100 River Sand)	0.40	61	9.4	5.25	N/A	1.25
Tests 2-6	751	133 (15%)	0	0	282	0.32	1,861 (#67 Dolomitic Limestone)	1,048 (#100 Natural Sand)	0.37	62	9.1	6.0	4.50	1.0
Tests 7-9	751	133 (15%)	0	0	277	0.31	1,861 (#67 Dolomitic Limestone)	1,048 (#100 Natural Sand)	0.38	63	9.0	9.0	N/A	1.0

Notes:

1. Percent substitutions noted for supplementary cementing materials (SCMs) are by weight of total cementitious materials.
2. Test 1: HRWRA #1 = Glenium 7700 and HSA = Pozzolith 100-XR.
3. Tests 2-6: HRWRA #1 = ADVA Cast 575, HRWRA #2 = ADVA Cast 555, HSA = Recover
4. Tests 7-9: HRWRA #1 = Glenium 7700, HSA = Delvo

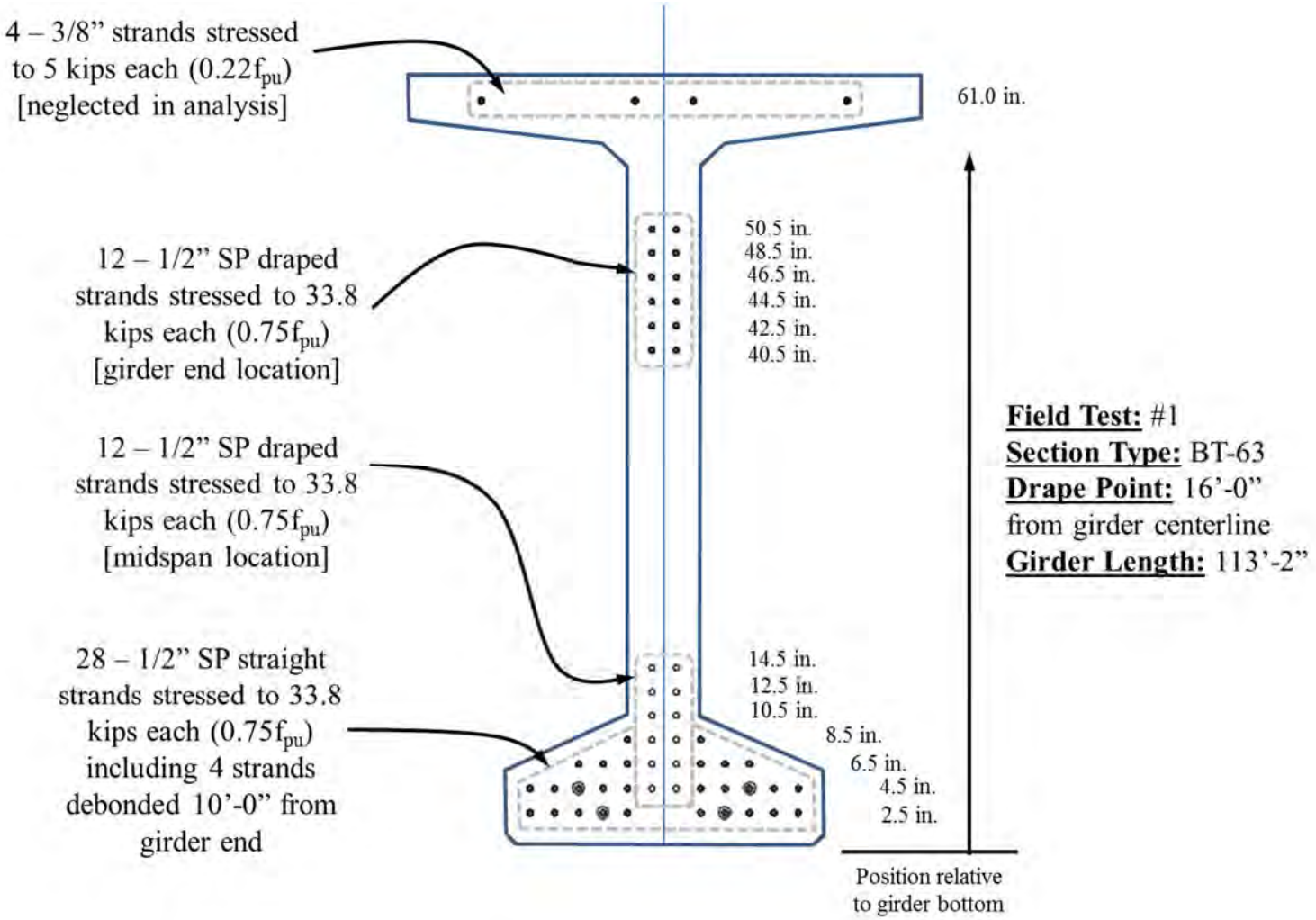

Figure 10-6: Girder and Prestressing Strand Details for Field Test #1

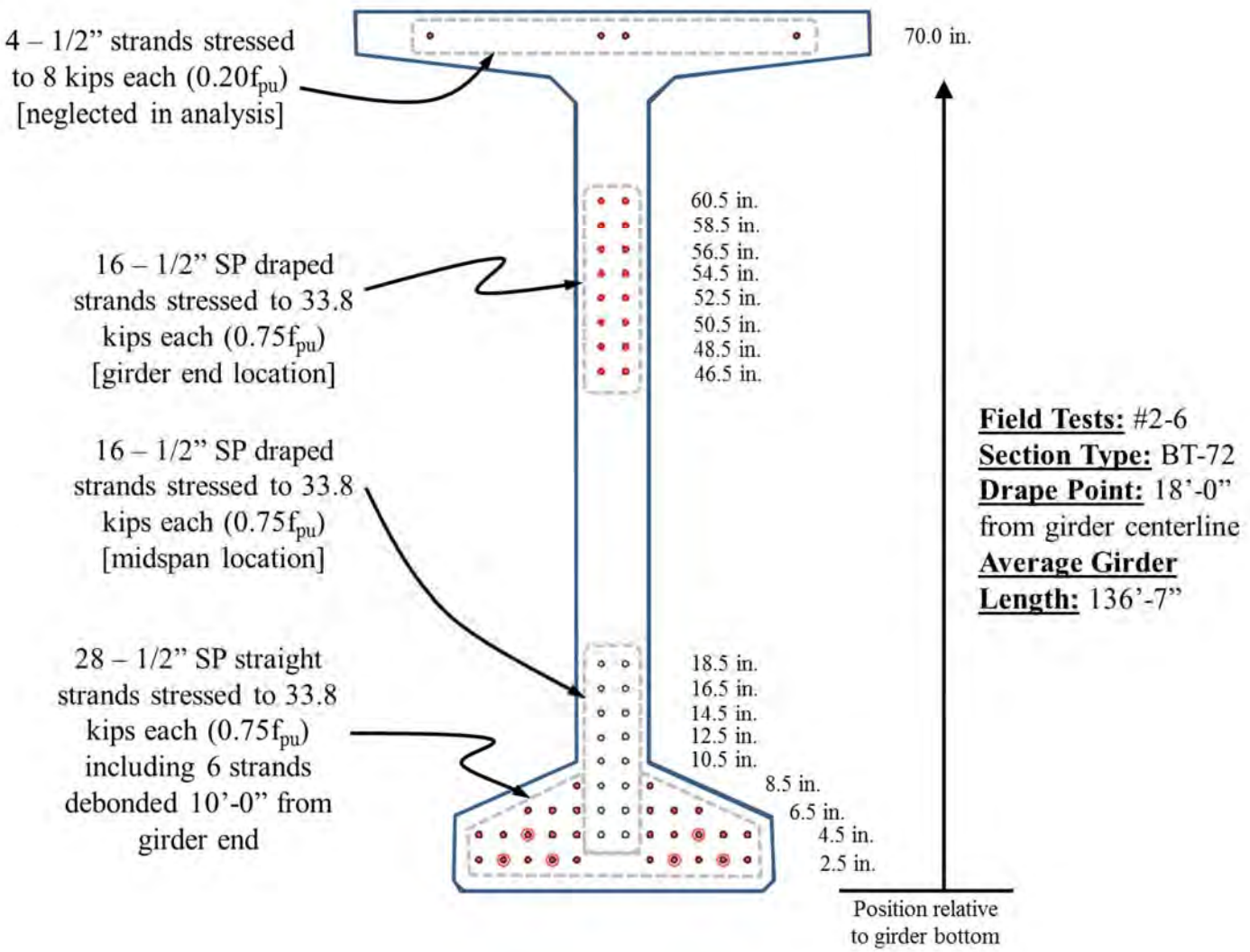

Figure 10-7: Girder and Prestressing Strand Details for Field Tests #2-6

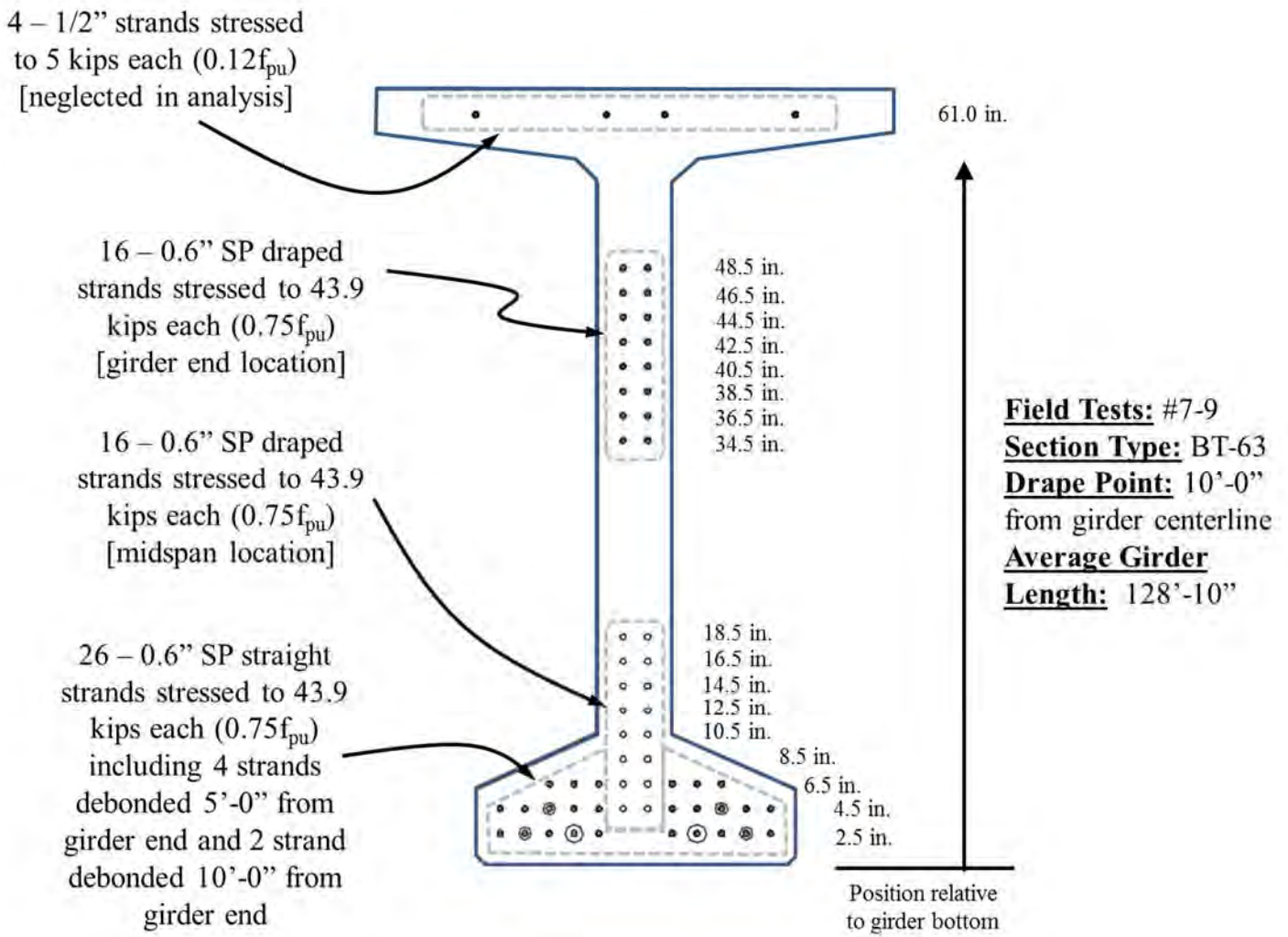

Figure 10-8: Girder and Prestressing Strand Details for Field Tests #7-9

10.3 Presentation and Post-Processing of Raw Field Data

This section begins with results of on-site concrete materials testing including fresh and hardened concrete properties. Next, internal girder temperature data is presented for each field test and computed concrete maturity at the time of prestress release is reported. Then, measured values of girder camber and cross-sectional deformation are presented for each field test. Finally, by applying the temperature-correction procedure previously implemented in Chapter 8, measured camber and cross-sectional deformation parameters are adjusted to values reflecting a standard reference temperature condition to allow for meaningful comparisons to predictions of girder behavior.

10.3.1 Fresh and Hardened Concrete Properties

Fresh concrete properties for each field test, as tested by producer staff and supervised by ALDOT inspectors, are shown in Table 10-3. The fresh properties observed during the on-site data gathering effort were in agreement with the historical observations and general comments offered in Chapter 4 of this report. Producers tend to target the upper limit of allowable slump (9 in.) and the lower allowable limit for air content (2.5 percent).

Table 10-3: Concrete Fresh Properties for Field Tests

Field Test ID	Concrete Temperature, (°F)	Slump (in.)	Air Content, (%)
1	89.5	7.0	3.3
2	88.0	9.0	2.8
3	88.0	8.5	3.3
4	84.0	8.5	2.8
5	82.5	9.0	3.3
6	87.0	8.0	4.2
7	83.0	9.0	2.7
8	86.0	9.0	3.5
9	86.0	8.5	2.7

Note: 1. All readings represent average of two sampling locations

Results of concrete compressive strength and elastic modulus testing for field-cured cylinders are summarized in Table 10-4. Measured compressive strengths for both the time of prestress release and 28 days after production well exceeded specified values. Additionally, as previously discussed in Chapter 4, concretes typical of the precast, prestressed concrete industry within the study region tend to exhibit relatively stiff behavior, with measured elastic moduli mostly greater than 6,000 ksi at transfer.

Table 10-4: Hardened Concrete Properties for Field-Cured Cylinders

Field Test ID	At Prestress Release			At 28 Days		
	Specified Strength, (psi)	Measured Strength (psi)	Measured Elastic Modulus (ksi)	Specified Strength (psi)	Measured Strength (psi)	Measured Elastic Modulus (ksi)
1	5,600	6,770	5,100	6,000	9,420	6,250
2	5,500	8,450	6,700	7,250	11,160	7,650
3	5,500	7,570	5,900	7,250	10,780	7,850
4	5,500	9,280	6,700	7,250	11,040	7,650
5	5,500	8,510	6,500	7,250	10,180	7,200
6	5,500	8,330	6,450	7,250	9,860	6,750
7	7,000	8,300	6,400	8,000	10,960	7,250
8	7,000	8,310	6,350	8,000	10,250	7,500
9	7,000	8,470	6,600	8,000	10,940	7,550

Notes: 1. Strength and modulus testing cylinders field-cured in shaded lime bath.
2. Measured values represent averages of two sampling locations.

The results from the standard-cured cylinders, summarized in Table 10-5, reflect largely similar trends to the field-cured cylinders—although greater 28-day strengths and moduli are attained. The relatively high strengths and stiffnesses obtained during the materials testing portion of this study reflect the properties of the dolomitic limestone coarse aggregate available within the study region. As shown, certain 28-day test results unexpectedly exceeded the 12,000 psi limit for the use of unbonded caps in accordance with ASTM C1231.

Table 10-5: Hardened Concrete Properties for Standard-Cured Cylinders

Field Test ID	At 28 Days		
	Specified Strength (psi)	Measured Strength (psi)	Measured Elastic Modulus (ksi)
1	6,000	10,040	6,500
2	7,250	12,750	8,100
3	7,250	11,990	7,900
4	7,250	12,610	7,900
5	7,250	11,430	7,450
6	7,250	11,710	7,750
7	8,000	12,200	7,800
8	8,000	11,590	7,750
9	8,000	12,410	8,000

Notes: 1. Cylinders cured in temperature-controlled limebath at producer facilities, then transported to AU laboratory and stored in curing room.
2. Measured values represent averages of two sampling locations.

10.3.2 Measured Girder Temperatures and Computed Equivalent Age

In order to compute the equivalent age of girder concrete at the time of prestress release, a complete temperature-history record of the girder concrete is needed beginning at the time of initial concrete mixing. These required temperature records were established using the following procedure:

- The fresh concrete temperature (as reported in Table 10-3) was assumed to extend for a 20-minute period from mixing until the time the concrete was placed in the girder formwork at the midspan of the instrumented girder; and
- The average of the four thermistor measurements (located across the depth at midspan of each instrumented girder) was assumed to be a representative temperature for use in computing concrete maturity for the entire girder.

Complete concrete temperature history plots for each field test are shown in Figure 10-9. Peak average girder temperatures approached, but did not exceed, the ALDOT maximum allowable curing temperature of 160°F. Recall, field test #1 was not steam cured and included an abnormally long curing period due to difficulties encountered by the girder producer.

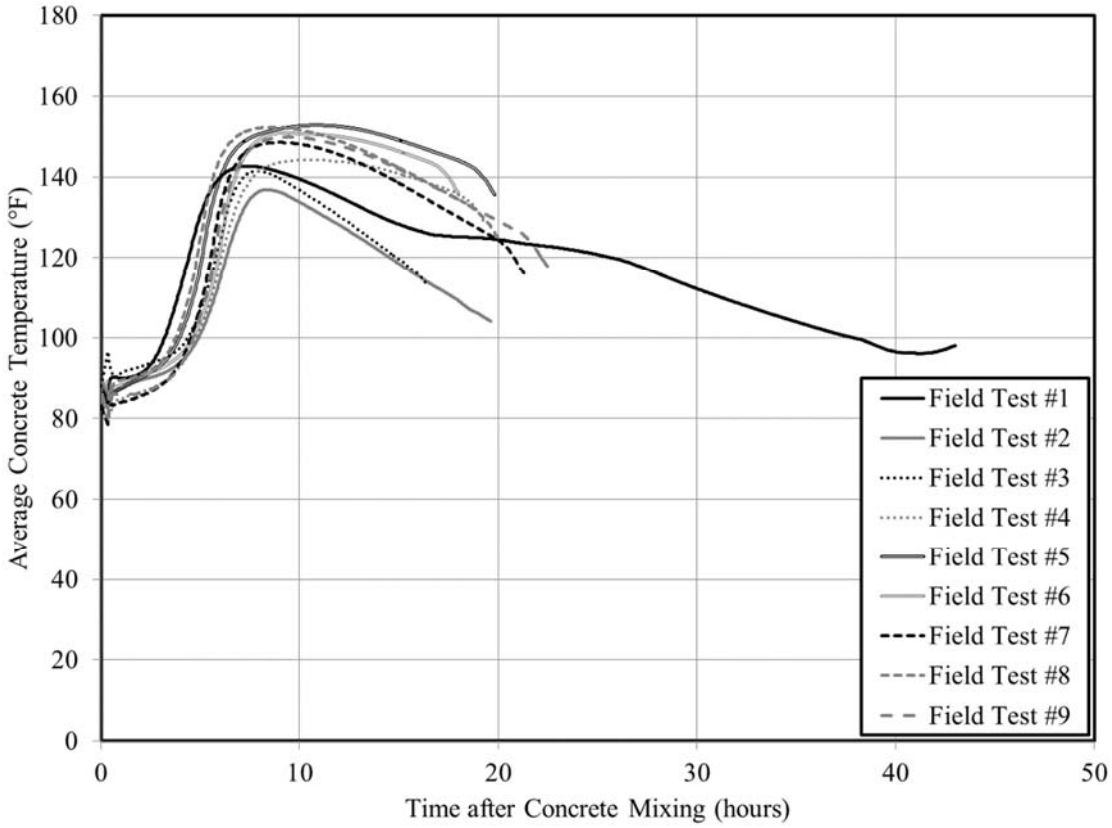

Figure 10-9: Temperature Histories of Girder Concrete

Values from the above-referenced temperature-history plots were used to compute the equivalent age of girder concrete at the time of prestress release yielding results shown in Table 10-6. Recall, for the purposes of camber prediction, equivalent age maturity is only used for the time-dependent portion of the

fib MC 2010 provisions, as the other time-dependent models rely on chronological concrete age. Accordingly, maturity computations were conducted (similarly to those discussed in Chapter 7) in accordance with the requirements of MC 2010 utilizing a datum temperature of 20°C and an activation energy of 33.2 kJ/mol. The equivalent ages computed here range from 2.4 to 6.0 days and show good agreement with those reported earlier.

Table 10-6: Maturity of Girder Concrete for Field Tests

Field Test ID	Chronological Time from Concrete Placement to Prestress Transfer (hours)	Concrete Chronological Age at Prestress Transfer (hours)	MC2010 Temperature-Adjusted Concrete Age, t_T, at Prestress Transfer[a] (days)	MC2010 Adjusted Equivalent Age at Prestress Transfer[b], t_o (days)
1	42.7	43.0	6.0	11.1
2	19.3	19.6	2.6	7.1
3	16.1	16.4	2.4	6.8
4	19.0	19.3	3.3	8.1
5	19.8	20.1	4.1	9.1
6	17.7	18.0	3.4	8.3
7	20.9	21.2	3.7	8.6
8	19.8	20.1	3.9	8.9
9	22.2	22.6	4.1	9.0

[a] = Computed from datum temperature = 20°C and AE = 33.2 kJ/mol
[b] = Accounting for cement type and curing temperature.

In addition to monitoring temperature during concrete placement for the purpose of computing concrete maturity at the time of prestress release, the experimental plan called for the monitoring of internal girder temperatures each time camber was measured to allow for temperature correction of measured deformations. This practice generated a large amount of data that is presented in its entirety in Mante (2016).

10.3.3 Raw Measurements of Girder Deformations

The raw measurements of girder deformations recorded in the field-monitoring portion of this study included midspan camber and midspan concrete strains. Similarly to the temperature data previously mentioned, strain readings were recorded each time camber was measured. Because it is difficult to present the large amount of compiled data in a space-conscious manner, the full raw data set, as directly output from the data collection system is included in Mante (2016). All raw strain measurements were well within the measurable range of the sensors utilized in the investigation. Prior to displaying a condensed tabulated version of the full data set, the data set was processed in a number of ways. First,

the manufacturer's gage temperature correction was applied to all recorded strain measurements. Next, strain readings were zeroed to the pre-release survey event to provide a consistent reference for comparison of future measurements to. Then, using the least-squares method of linear fit and relying on the principle that plane sections remain plane, the linearity of measured strain profiles was evaluated for each instrumented girder at the time of maximum induced curvature. Finally, the two key cross-sectional parameters necessary to fully define midspan strains at a given time (strain at the centroid of the section and curvature) were computed.

Girder deformations, as modified by the above procedure, are shown in Tables 10-7 and 10-8. Bottom flange centroid strain readings are intended as an indication of the accuracy of prestress loss computations. The values displayed in Tables 10-7 and 10-8 are referred to as "unadjusted" measurements, as they have yet to be temperature corrected according to the analytical procedures of Chapter 8.

Table 10-7: Measurements of Girder Deformations–Tests 1-5

Field Test ID	Girder No.	Verification of Linearity of Strain Gages[a]	Time After Release (days)	Midspan Camber[b] (in.)	Computed Midspan Curvature[c] ($x10^{-6}$ rad/in.)	Computed Midspan Centroidal Strain[d] (με)	Computed Midspan Bottom Flange Centroidal Strain[d] (με)
1[d]	1	0.99	0.0	2.05	-8.52	-314	-546
			0.1	2.53	-10.05	-323	-598
	2		0.0	2.00	-8.36	-311	-538
			0.1	2.30	-10.11	-322	-599
	3		0.0	1.97	-7.87	-321	-535
			0.1	2.34	-9.62	-334	-596
2	1	0.99	0.0	1.18	-5.76	-285	-487
			0.1	2.04	Data Collection System Malfunction		
			74.0	2.41	-10.70	-845	-1,232
			231.2	2.93	-11.63	-930	-1,358
	2		0.0	0.95	-5.66	-285	-484
			0.1	1.56	Data Collection System Malfunction		
			74.0	2.16	-10.65	-850	-1,236
			145.2	2.65	-11.97	-887	-1,327
			231.2	2.70	-11.58	-936	-1,364
3	1	0.99	0.0	0.79	-4.01	-378	-503
			0.1	1.39	-5.70	-463	-642
			73.2	1.70	-7.61	-999	-1,231
			230.3	2.38	-9.17	-1,108	-1,386
	2		0.0	0.52	-4.07	-383	-510
			0.1	1.12	-5.76	-459	-641
			73.2	1.38	-7.65	-993	-1,226
			230.3	1.94	-9.21	-1,102	-1,382
4	1	0.90	0.0	0.74	-3.68	-345	-441
			0.1	1.19	-5.44	-424	-576
			156.3	2.46	-9.62	-1,030	-1,298
	2		0.0	1.03	-3.89	-346	-449
			0.1	1.51	-5.58	-417	-574
			156.3	3.00	-9.73	-1,018	-1,295
5	1	0.99	0.0	1.09	-3.04	-328	-431
			0.1	1.33	-4.77	-397	-555
			67.1	2.16	-7.05	-1,087	-1,322
			154.2	2.69	-8.58	-1,029	-1,313
	2		0.0	0.98	-3.24	-327	-437
			0.1	1.55	-4.90	-386	-548
			154.2	2.81	-8.69	-1,013	-1,300

[a] = Linearity verification performed for maximum observed curvature for each instrumented girder.
[b] = Positive camber corresponds to upward deflection
[c] = Negative curvature corresponds to concave-down flexure.
[d] = Negative concrete strain corresponds to a relative shortening of girder concrete.

Table 10-8: Measurements of Girder Deformations–Tests 6-9

Field Test ID	Girder No.	Verification of Linearity of Strain Gages	Time After Release (days)	Midspan Camber[a] (in.)	Computed Midspan Curvature[b] (x10^{-6} rad/in.)	Computed Midspan Centroidal Strain[c] (με)	Computed Midspan Bottom Flange Centroidal Strain[c] (με)
6	1	0.99	0.0	1.22	-4.24	-362	-497
			0.1	1.67	-5.61	-434	-612
			153.3	2.70	-8.89	-1,072	-1,342
	2		0.0	1.13	-4.00	-358	-485
			0.1	1.42	-5.50	-445	-620
			153.3	3.10	-8.77	-1,084	-1,350
7[d]	1	0.99	0.0	1.74	-8.24	-458	-678
			0.1	2.39	-10.28	-542	-818
			43.0	3.07	-14.34	-1,020	-1,408
			82.1	3.14	-14.71	-1,144	-1,544
	2		0.0	1.76	-8.64	-465	-696
			0.1	2.10	-10.41	-537	-816
			43.0	2.93	-14.42	-1,010	-1,400
			82.2	3.13	-14.94	-1,130	-1,536
	3		0.0	1.92	-8.77	-450	-685
			0.1	2.34	-10.56	-524	-808
			43.0	3.14	-14.55	-996	-1,390
			82.2	3.38	-15.14	-1,114	-1,525
8[d]	1	0.99	0.0	2.00	-7.96	-458	-664
			0.1	2.59	-9.26	-518	-759
			41.1	3.62	-13.07	-1,047	-1,388
			80.2	3.80	-13.33	-1,076	-1,428
	2		0.0	2.11	-8.24	-459	-672
			0.1	2.38	-9.42	-512	-757
			41.1	3.42	-13.20	-1,037	-1,382
			80.2	3.74	-13.49	-1,064	-1,420
	3		0.0	2.03	-8.50	-458	-679
			0.1	2.38	-9.56	-504	-754
			41.1	3.54	-13.33	-1,028	-1,377
			80.2	3.95	-13.62	-1,053	-1,413
9[d]	1	0.99	0.0	1.86	-7.21	-484	-680
			0.1	2.47	-9.27	-553	-804
			36.1	3.68	-14.10	-1,059	-1,434
			75.3	3.79	-15.00	-1,121	-1,527
	2		0.0	1.72	-7.54	-500	-704
			0.1	2.36	-9.41	-542	-798
			36.1	3.26	-14.23	-1,043	-1,422
			75.3	3.55	-15.08	-1,110	-1,518
	3		0.0	1.24	-7.52	-479	-683
			0.1	1.96	-9.53	-532	-791
			36.1	2.88	-14.33	-1,031	-1,413

Note: Subscript definitions provided in Table 10-7 apply here also.

The following summarizing remarks are offered as a result of the review of the data presented in Tables 10-7 and 10-8:

- Several girders (Field Tests #1, 7, 8, and 9) shipped without notice prior to final measurement of pre-shipping camber;
- The linearity of midspan strain gages installed in each test was good to excellent with values ranging from 0.90 to 0.99—suggesting that gages remained in intended locations and were largely undisturbed by concrete placement activities; and
- The longest period of camber measurement included in this study was 231 days after the prestress transfer event.

10.3.4 Temperature Correction of Field-Measured Values

Using the recorded internal temperatures and measurements of girder deformations discussed in the preceding two sections, the temperature-correction procedure described in Chapter 8 was used to adjust measured values to reflect a standard uniform vertical temperature profile of 20°C. Recall, as shown in Figure 10-10, the temperature-correction procedure consists of two governing equations (Equation 8-17 and 8-25, reproduced below) that jointly define changes in girder cross-sectional centroidal strain and curvature attributed to a given change in vertical temperature profile.

$$\Delta\varepsilon_0 = \frac{\alpha_T}{A}\int_y \left(\Delta T(y)\right) w(y)\,dy \tag{8-17}$$

$$\Delta\phi = \frac{\alpha_T}{I}\int_y \left(\Delta T(y)\cdot y\cdot w(y)\right) dy \tag{8-25}$$

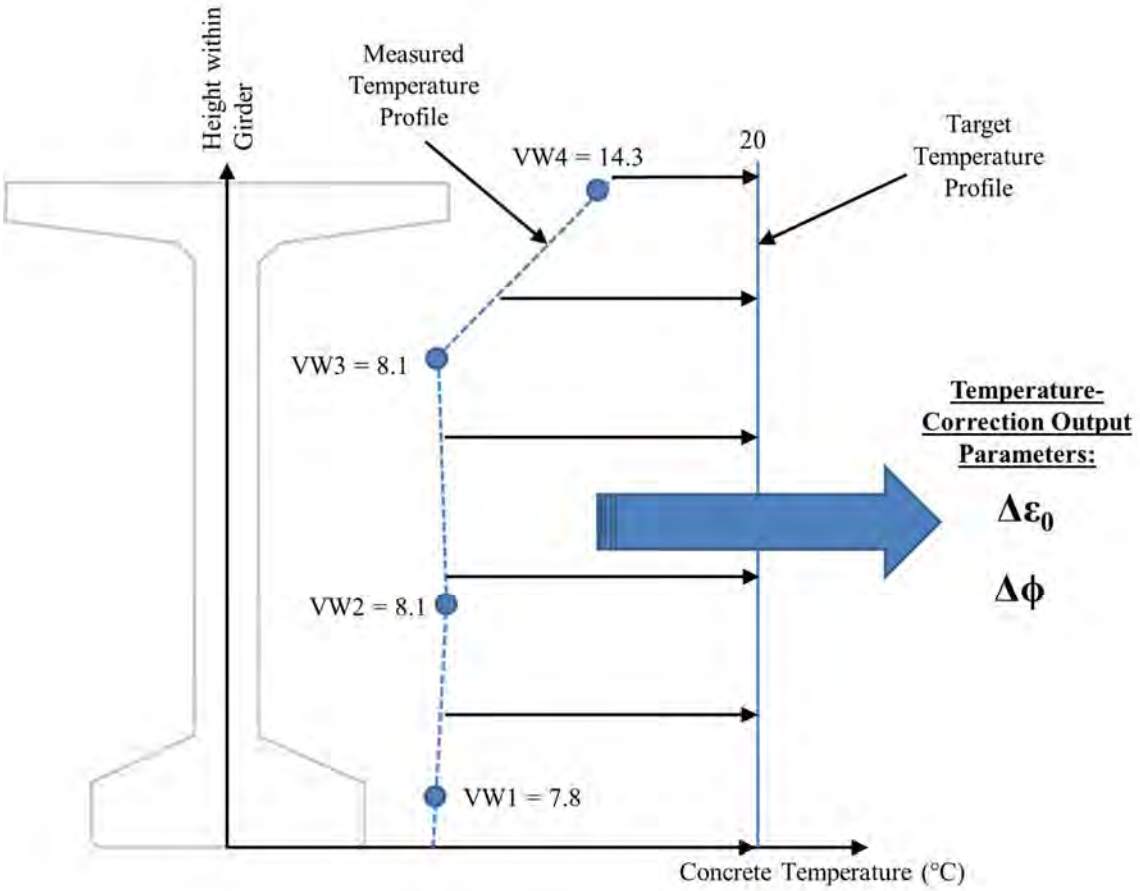

Figure 10-10: Temperature Correction of Field-Measured Girder Deformation Parameters

For the temperature correction performed in this section, the following analytical assumptions and procedures (in agreement with the recommendations of Chapter 8) were used:

- An effective CTE value of 13.0 με /°C was assumed;
- A piecewise-exact cross-sectional shape definition was assumed; and
- Linear interpolation between adjacent temperature measurements was used to define the vertical temperature profile.

Final values of temperature-corrected girder deformations are displayed in Tables 10-9 and 10-10. Where measurements of internal concrete strains and temperatures were not available due to data collection system malfunction (e.g. Field Test #2, t=0.1 hours), missing values were estimated using the following procedure: (1) the ratio of each deformation metric (e.g. camber, curvature, bottom flange strain, or centroidal strain) was computed for other similar field tests between adjacent ages (0 and 0.1 days), and (2) the average of the computed ratios was used to modify the intact reading (t=0 hours) to estimate

the missed reading (t=0.1 hours). The magnitude of the temperature-corrected values observed here are in agreement with those expected by the previous analyses conducted in Chapter 8 of this report.

Table 10-9: Temperature-Corrected Measurements of Girder Deformations–Tests 1-5

Field Test ID	Girder No.	Time After Release (days)	Midspan Camber (in.)	Computed Midspan Curvature (x10^{-6} rad/in.)	Computed Midspan Centroidal Strain (με)	Computed Midspan Bottom Flange Centroidal Strain (με)
1	1	0.0	1.89	-7.82	-332	-544
		0.1	2.27	-8.90	-358	-602
	2	0.0	1.84	-7.67	-327	-536
		0.1	2.03	-8.90	-359	-602
	3	0.0	1.76	-6.98	-338	-527
		0.1	2.01	-8.21	-371	-595
2	1	0.0	1.17	-5.74	-273	-474
		0.1[a]	2.03	-8.33	-290	-559
		74.0	2.39	-10.60	-537	-923
		231.2	2.82	-11.30	-519	-937
	2	0.0	0.94	-5.64	-268	-466
		0.1[a]	1.55	-8.18	-286	-550
		74.0	2.14	-10.60	-536	-921
		145.2	2.17	-10.60	-503	-897
		231.2	2.59	-11.30	-518	-935
3	1	0.0	0.86	-4.22	-354	-485
		0.1	1.53	-6.11	-387	-579
		73.2	2.03	-8.60	-632	-895
		230.3	2.32	-9.01	-616	-890
	2	0.0	0.58	-4.27	-361	-494
		0.1	1.22	-6.09	-389	-580
		73.2	1.68	-8.54	-634	-895
		230.3	1.86	-8.97	-618	-890
4	1	0.0	0.85	-3.99	-310	-415
		0.1	1.35	-5.91	-330	-496
		156.3	1.91	-8.03	-432	-654
	2	0.0	1.12	-4.15	-314	-425
		0.1	1.64	-5.96	-329	-498
		156.3	2.44	-8.10	-431	-655
5	1	0.0	1.19	-3.34	-297	-410
		0.1	1.50	-5.27	-324	-498
		67.1	1.99	-6.55	-330	-549
		154.2	2.20	-7.16	-376	-615
	2	0.0	1.04	-3.41	-307	-422
		0.1	1.66	-5.23	-324	-497
		154.2	2.24	-7.04	-378	-612

Note: A coefficient of thermal expansion of 13.0 με /°C was used in the temperature-correction procedure as determined in the analysis of Chapter 8.

[a] = For analysis purposes, missed values were estimated from similar field tests.

Table 10-10: Temperature-Corrected Measurements of Girder Deformations–Tests 6-9

Field Test ID	Girder No.	Time After Release (days)	Midspan Camber (in.)	Computed Midspan Curvature (x10^{-6} rad/in.)	Computed Midspan Centroidal Strain (με)	Computed Midspan Bottom Flange Centroidal Strain (με)
6	1	0.0	1.31	-4.49	-337	-480
		0.1	1.86	-6.19	-356	-554
		153.3	2.46	-8.14	-441	-687
	2	0.0	1.23	-4.31	-327	-465
		0.1	1.65	-6.21	-356	-554
		153.3	2.91	-8.19	-440	-687
7	1	0.0	1.89	-8.74	-407	-641
		0.1	2.56	-10.90	-435	-726
		43.0	3.01	-14.10	-574	-956
		82.1	3.18	-14.80	-572	-975
	2	0.0	1.88	-9.04	-418	-660
		0.1	2.22	-10.80	-435	-726
		43.0	2.83	-14.10	-575	-955
		82.2	3.07	-14.70	-574	-973
	3	0.0	1.98	-8.97	-422	-662
		0.1	2.40	-10.80	-438	-727
		43.0	2.99	-14.00	-578	-957
		82.2	3.24	-14.60	-577	-975
8	1	0.0	2.14	-8.41	-410	-628
		0.1	2.81	-9.97	-428	-688
		41.1	3.70	-13.30	-551	-899
		80.2	3.89	-13.60	-545	-905
	2	0.0	2.23	-8.62	-417	-640
		0.1	2.56	-10.00	-429	-691
		41.1	3.46	-13.30	-552	-901
		80.2	3.79	-13.60	-548	-908
	3	0.0	2.12	-8.81	-422	-652
		0.1	2.52	-10.00	-431	-694
		41.1	3.55	-13.30	-554	-904
		80.2	3.95	-13.60	-551	-912
9	1	0.0	2.00	-7.67	-435	-643
		0.1	2.66	-9.89	-459	-727
		36.1	3.54	-13.60	-623	-985
		75.3	3.62	-14.40	-651	-1,040
	2	0.0	1.84	-7.95	-448	-664
		0.1	2.49	-9.84	-461	-728
		36.1	3.05	-13.50	-625	-984
		75.3	3.34	-14.40	-653	-1,040
	3	0.0	1.30	-7.74	-448	-658
		0.1	2.03	-9.79	-465	-731
		36.1	2.61	-13.40	-629	-986

Note: A coefficient of thermal expansion of 13.0 με /°C was used in the temperature-correction procedure.

Percent differences between temperature-corrected data (Tables 10-9 and 10-10) and unadjusted measured data (Tables 10-7 and 10-8) for each time of measurement are displayed in Tables 10-11 and

10-12. The denominator in the percent differences computed below is the temperature-corrected value—meaning the percent differences indicate the variation that would remain unaccounted for if a temperature correction was not performed.

Table 10-11: Percent Difference of Temperature-Corrected Girder Deformations–Tests 1-5

Field Test ID	Girder No.	Time After Release (days)	Change in Midspan Camber (%)	Change in Midspan Curvature (%)	Change in Midspan Centroidal Strain (%)	Change in Midspan Bottom Flange Centroidal Strain (%)
1	1	0.0	8.5	9.0	-5.4	0.4
		0.1	11.5	12.9	-9.8	-0.7
	2	0.0	8.7	9.0	-4.9	0.4
		0.1	13.3	13.6	-10.3	-0.5
	3	0.0	11.9	12.8	-5.0	1.5
		0.1	16.4	17.2	-10.0	0.2
2	1	0.0	0.9	0.3	4.4	2.7
		0.1	0.5	Initial Readings Unavailable		
		74.0	0.8	0.9	57.4	33.5
		231.2	3.9	2.9	79.2	44.9
	2	0.0	1.1	0.4	6.3	3.9
		0.1	0.6	Initial Readings Unavailable		
		74.0	0.9	0.5	58.6	34.2
		145.2	22.1	12.9	76.3	47.9
		231.2	4.2	2.5	80.7	45.9
3	1	0.0	-8.1	-5.0	6.8	3.7
		0.1	-9.2	-6.7	19.6	10.9
		73.2	-16.3	-11.5	58.1	37.5
		230.3	2.6	1.8	79.9	55.7
	2	0.0	-10.3	-4.7	6.1	3.2
		0.1	-8.2	-5.4	18.0	10.5
		73.2	-17.9	-10.4	56.6	37.0
		230.3	4.3	2.7	78.3	55.3
4	1	0.0	-12.9	-7.8	11.3	6.3
		0.1	-11.9	-8.0	28.5	16.1
		156.3	28.8	19.8	138.4	98.5
	2	0.0	-8.0	-6.3	10.2	5.6
		0.1	-7.9	-6.4	26.7	15.3
		156.3	23.0	20.1	136.2	97.7
5	1	0.0	-8.4	-9.0	10.4	5.1
		0.1	-11.3	-9.5	22.5	11.4
		67.1	8.5	7.6	229.4	140.8
		154.2	22.3	19.8	173.7	113.5
	2	0.0	-5.8	-5.0	6.5	3.6
		0.1	-6.6	-6.3	19.1	10.3
		154.2	25.4	23.4	168.0	112.4

Table 10-12: Percent Difference of Temperature-Corrected Girder Deformations Tests–6-9

Field Test ID	Girder No.	Time After Release (days)	Change in Midspan Camber (%)	Change in Midspan Curvature (%)	Change in Midspan Centroidal Strain (%)	Change in Midspan Bottom Flange Centroidal Strain (%)
6	1	0.0	-6.9	-5.6	7.4	3.5
		0.1	-10.2	-9.4	21.9	10.5
		153.3	9.8	9.2	143.1	95.3
	2	0.0	-8.1	-7.2	9.5	4.3
		0.1	-13.9	-11.4	25.0	11.9
		153.3	6.5	7.1	146.4	96.5
7	1	0.0	-7.9	-5.7	12.5	5.8
		0.1	-6.6	-5.7	24.6	12.7
		43.0	2.0	1.7	77.7	47.3
		82.1	-1.3	-0.6	100.0	58.4
	2	0.0	-6.4	-4.4	11.2	5.5
		0.1	-5.4	-3.6	23.4	12.4
		43.0	3.5	2.3	75.7	46.6
		82.2	2.0	1.6	96.9	57.9
	3	0.0	-3.0	-2.2	6.6	3.5
		0.1	-2.5	-2.2	19.6	11.1
		43.0	5.0	3.9	72.3	45.2
		82.2	4.3	3.7	93.1	56.4
8	1	0.0	-6.5	-5.4	11.7	5.7
		0.1	-7.8	-7.1	21.0	10.3
		41.1	-2.2	-1.7	90.0	54.4
		80.2	-2.3	-2.0	97.4	57.8
	2	0.0	-5.4	-4.4	10.1	5.0
		0.1	-7.0	-5.8	19.3	9.6
		41.1	-1.2	-0.8	87.9	53.4
		80.2	-1.3	-0.8	94.2	56.4
	3	0.0	-4.2	-3.5	8.5	4.1
		0.1	-5.6	-4.4	16.9	8.6
		41.1	-0.3	0.2	85.6	52.3
		80.2	0.0	0.1	91.1	54.9
9	1	0.0	-7.0	-6.0	11.3	5.8
		0.1	-7.1	-6.3	20.5	10.6
		36.1	4.0	3.7	70.0	45.6
		75.3	4.7	4.2	72.2	46.8
	2	0.0	-6.5	-5.2	11.6	6.0
		0.1	-5.2	-4.4	17.6	9.6
		36.1	6.9	5.4	66.9	44.5
		75.3	6.3	4.7	70.0	46.0
	3	0.0	-4.6	-2.8	6.9	3.8
		0.1	-3.4	-2.7	14.4	8.2
		36.1	10.3	6.9	63.9	43.3

As shown, the largest percent differences (in magnitude) are observed in midspan strains (up to 229 percent), while corresponding temperature-induced changes to camber and midspan curvature tended to be significantly less—approaching maximum percent differences of 30 and 25 percent, respectively.

10.4 Comparison of Field Measurements to Design Prediction Trials

This section focuses primarily on comparisons among various trial camber prediction procedures and temperature-corrected measured field results for considered deformation metrics. First, the analytical procedure—including various trial camber prediction procedures utilized in this investigation—is presented and described in Section 10.4.1. Next, a summary of any relevant material model inputs used within prediction trials is provided. Finally, relevant comparisons are made for each prediction trial for four key midspan parameters of girder deformation (camber, curvature, centroidal strain, and bottom flange strain) to identify the isolated and compounded (combined) effects of varying camber prediction practices.

10.4.1 Analytical Procedure and Details

Trial camber prediction procedures, as utilized in this research effort, are labelled in accordance with the notation of Figure 10-11. The full list of considered trial prediction procedures—accompanied by an outline of the analytical logic implemented herein—is shown in Figure 10-12. The various trial camber prediction procedures considered in this chapter were selected (1) to identify a best prediction procedure for use in ALDOT girder design, and (2) to evaluate the relative effects of varying assumptions (e.g. analysis method, concrete compressive strength, elastic modulus, and creep and shrinkage) on camber prediction accuracy.

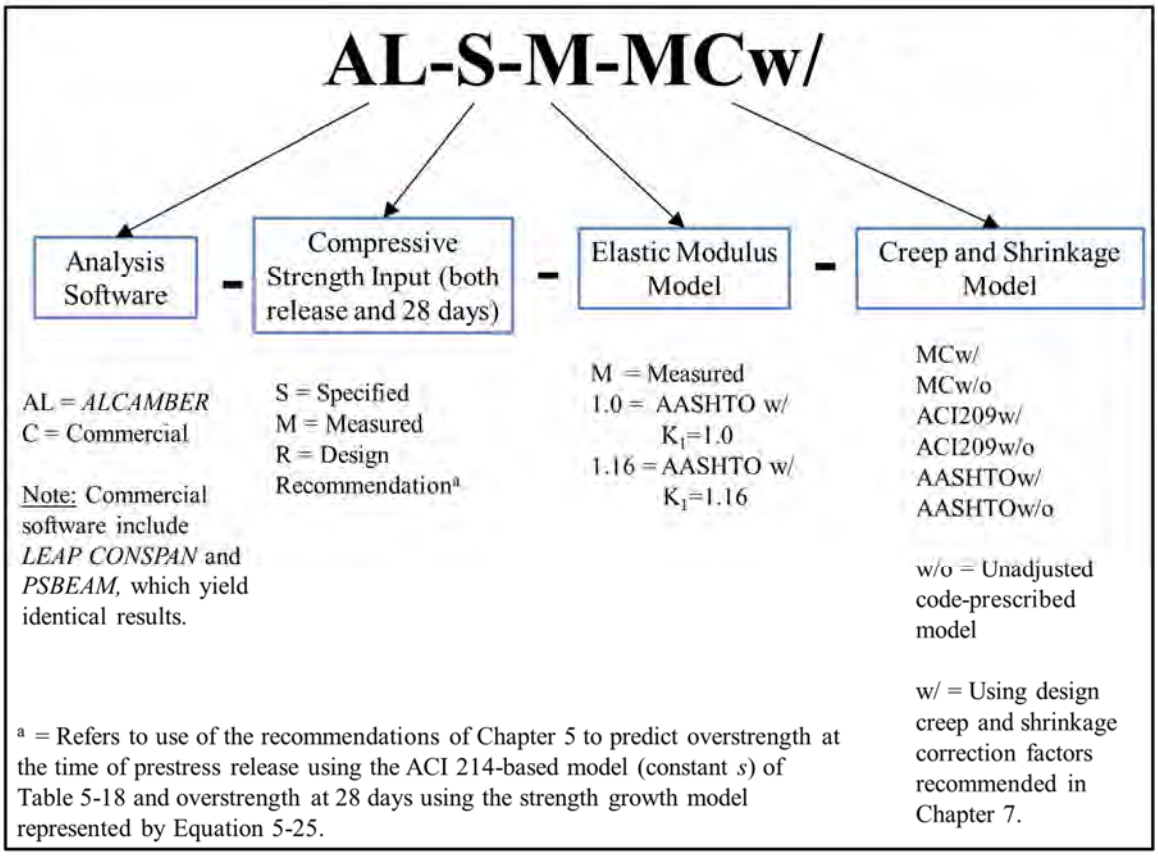

Figure 10-11: Trial Camber Prediction Procedure Labelling Notation

Step 1: Generate best predictions of girder deformations using measured on-site data and three calibrated creep and shrinkage models.

AL-M-M-MCw/ **AL-M-M-ACI209w/** **AL-M-M-AASHTOw/**

Step 2: Compare above predictions to measured deformations to determine *best overall prediction procedure* (including best time-dependent model[a]), to provide benchmark for comparison to subsequent trial procedures–likely **AL-M-M-MCw/**.

Step 3: Generate predictions of girder deformations using measured on-site data and three *uncalibrated* creep and shrinkage models to isolate effect of calibration of models.

AL-M-M-MCw/o **AL-M-M-ACI209w/o** **AL-M-M-AASHTOw/o**

Step 4: Generate predictions of girder deformations necessary to isolate effect of various elastic modulus predictions [on predominately instantaneous deformations].

AL-M-1.16-MCw/ **AL-M-1.0-MCw/**

Step 5: Generate predictions of girder deformations necessary to isolate effect of various compressive strength predictions.

AL-S-M-MCw/ **AL-R-M-MCw/**

Step 6: Generate predictions of deformations [using trial procedures] to capture the compounded (combined) effects of selected changes in compressive strength, elastic modulus, and time-dependent models prediction practices–relative to the previously selected benchmark procedure (likely **AL-M-M-MCw/**).

AL-S-1.16-MCw/	Captures effect of various compressive strength and elastic modulus prediction practices [on both instantaneous and time-dependent behavior].
AL-S-1.0-MCw/	
AL-R-1.16-MCw/	Likely design recommendation.
AL-S-1.0-AASHTOw/o	Most similar to current design practice.

Step 7: Using commercial software, generate predictions of initial deformations to capture the compounded effects of selected changes in compressive strength, elastic modulus, and time-dependent models prediction practices.

C-R-1.16	Using recommended estimate of overstrength and aggregate stiffness modifier.
C-S-1.16	Using only aggregate stiffness modifier.
C-S-1.0	Current design practice.

[a] = MC2010w/ assumed as most accurate time-dependent model for illustration purposes.

Figure 10-12: Analysis Procedure and Trial Prediction Procedures

Predictions of girder deformations (e.g. midspan camber, curvature, bottom flange strain, and centroidal strain) were generated for 17 trial prediction procedures for each of nine field tests using a combination of the following design software programs: *ALCAMBER*, *LEAP CONSPAN*, or *PSBEAM.*

In order to compare the accuracy of predicted girder deformations to observed field behavior for each trial prediction procedure, a standard metric of prediction accuracy is required. Where the standard error of the estimate, *SEE*, was used in previous chapters for similar purposes, the standard error of the estimate fails to indicate if predictions tend to fall above or below the observed response. For this reason, the metric of percent difference from observed values was selected as the preferred metric of prediction procedure accuracy—computed as follows for each time of field measurement:

$$\%Diff = \left[\frac{D_{predicted} - D_{observed}}{D_{observed}} \right] * 100 \qquad (10\text{-}1)$$

where

$D_{predicted}$ = the predicted response of a selected deflection metric (e.g. camber, curvature, bottom flange strain, or centroidal strain) for a given trial prediction procedure; and

$D_{observed}$ = the observed response (either measured or computed from measurements) of the same deflection metric considered above.

A positive percent difference computed in accordance with Equation 10-1 indicates an overprediction of a given parameter.

A final analytical assumption was necessary to facilitate comparisons between predicted and observed early life girder deformations. Recall, in this study, midspan deformation measurements (e.g. camber and concrete strains) were recorded immediately after prestress release (on the prestressing bed), and shortly thereafter, following girder relocation to a finishing station. For the comparisons of this chapter, the first deformation reading is taken as the average of the reading taken on the prestressing bed and the subsequent reading after girder relocation. It is assumed that by virtue of (1) initial readings likely underestimating deformations due to friction with the prestressing bed (as noted by Rosa et al. [2007]) and (2) readings taken after girder relocation likely overestimating deformations due to the

inclusion of a portion of early-age creep and shrinkage deformations, these opposing trends largely cancel and provide a consistent indicator of initial girder deformations.

10.4.2 Prediction Model Summary of Inputs

Various inputs and details regarding the implementation of code-prescribed models are displayed in Tables 10-13 through 10-15. Collectively, the data contained in these tables (and referenced previous tables) represent all input data necessary to generate camber predictions for each trial prediction procedure.

Table 10-13: Elastic Modulus Model Summary of Inputs

AASHTO 2014	
Input	***Justification***
K_1 = 1.16	Recommendation of Ch. 6
Concrete unit weight = 150 pcf	In accordance with ALDOT standard practice and current design practice review of Ch. 4
Strength growth development (where necessary) = Backcalculated using ACI 209R-92 formulation by Isbiliroglu[a] (2014)	Yields most accurate prediction of elastic modulus growth at release and 28 days

[a] = Isbiliroglu (2014) derived a function within the *ALCAMBER* software to backcalculate the concrete strength growth curve based on known concrete strengths at two times (typically prestress release and 28 days after production).

Table 10-14: Creep Prediction Model Summary of Inputs

AASHTO 2014		ACI 209		Model Code 2010	
Input	***Justification***	***Input***	***Justification***	***Input***	***Justification***
Relative humidity = 70 percent	AASHTO / ALDOT Recommendation	Relative humidity = 70 percent	AASHTO / ALDOT Recommendation	Relative humidity = 70 percent	AASHTO / ALDOT Recommendation
Volume-to-surface ratio = 3.01 in.	Computed by girder geometry (same for BT-54, BT-63, and BT-72)	Volume-to-surface ratio = 3.01 in.	Computed by girder geometry (same for BT-54, BT-63, and BT-72)	Notional size = 6.02 mm.	Computed per MC 2010 provisions
Chronological age at loading	Table 10-2	Slump = 0.5 in.	Assumed pre-admixture slump in agreement with Keske (2014) and Ellis (2012)	MC2010 concrete maturity at loading, t_t [a]	Table 10-6
Compressive strength at loading	Table 10-4	Sand-to-aggregate weight ratio	Computed from Table 6-3	28-day measured compressive strength	Table 10-4
Creep coefficient correction factor = 1.00	Recommendations of Ch. 7 (for unknown mixture compositions)	Cement factor	Assumed total powder content, Table 6-3	Rapid-hardening high-strength cement assumed	Per Keske (2014) and recommendations of ACI 209 (2008).
		Air content	Table 10-3	Creep coefficient correction factor = 0.80	Recommendations of Ch. 7 (for unknown mixture compositions)
		Creep coefficient correction factor = 1.15	Recommendations of Ch. 7 (for unknown mixture compositions)		

[a] = The *ALCAMBER* software computes the MC2010 cement- and temperature-adjusted age, t_o, based on (1) input of concrete maturity, t_t, and (2) selection of cement properties.

Table 10-15: Shrinkage Prediction Model Summary of Inputs

AASHTO 2014		ACI 209		Model Code 2010	
Input	***Justification***	***Input***	***Justification***	***Input***	***Justification***
Relative humidity = 70 percent	AASHTO / ALDOT Recommendation	Relative humidity = 70 percent	AASHTO / ALDOT Recommendation	Relative humidity = 70 percent	AASHTO / ALDOT Recommendation
Volume-to-surface ratio for cylinder = 3.01 in.	Computed by girder geometry (same for BT-54, BT-63, and BT-72)	Volume-to-surface ratio = 3.01 in.	Computed by girder geometry (same for BT-54, BT-63, and BT-72)	Notional size =6.02 mm	Computed per MC 2010 provisions
Chronological age at loading	Table 10-2	Slump = 0.5 in.	Assumed pre-admixture slump in agreement with Keske (2014) and Ellis (2012)	28-day measured compressive strength	Table 10-4
Compressive strength at loading	Table 10-4	Sand-to-aggregate weight ratio	Computed from Table 6-3	MC2010 concrete maturity at loading, t_t [a]	Table 10-6
Shrinkage correction factor = 0.80	Recommendations of Ch. 7 (for unknown mixture compositions)	Cement factor	Assumed total powder content, Table 6-3	Rapid-hardening high-strength cement assumed	Per Keske (2014) and recommendations of ACI 209 (2008).
		Air content	Table 10-3	Concrete age at beginning of drying for cylinders	Table 10-2
		Shrinkage correction factor = 0.75	Recommendations of Ch. 7 (for unknown mixture compositions)	Shrinkage correction factor = 0.70	Recommendations of Ch. 7 (for unknown mixture compositions)

[a] = The *ALCAMBER* software computes the MC2010 cement- and temperature-adjusted age, t_o, based on (1) input of concrete maturity, t_t, and (2) selection of cement properties.

10.4.3 Estimate of Girder Deformations Using Measured Material Properties and Calibrated Time-Dependent Models

It is logical to assume that the most accurate predictions of girder deflections will result from use of measured concrete compressive strength, elastic modulus, and creep and shrinkage behavior. In this section, results of on-site material testing and calibrated laboratory creep and shrinkage models (representative of girder concretes) are used to generate predictions of girder deformations. The focus of the analyses of this chapter remains predominately on midspan camber—although average percent differences (from observed) for midspan curvature, bottom flange strain, and centroidal strain are also reported. Percent differences from observed midspan camber (averaged for up to three girders in a single field test and measurement time) are shown for the three most comprehensive prediction trials in Figure 10-13.

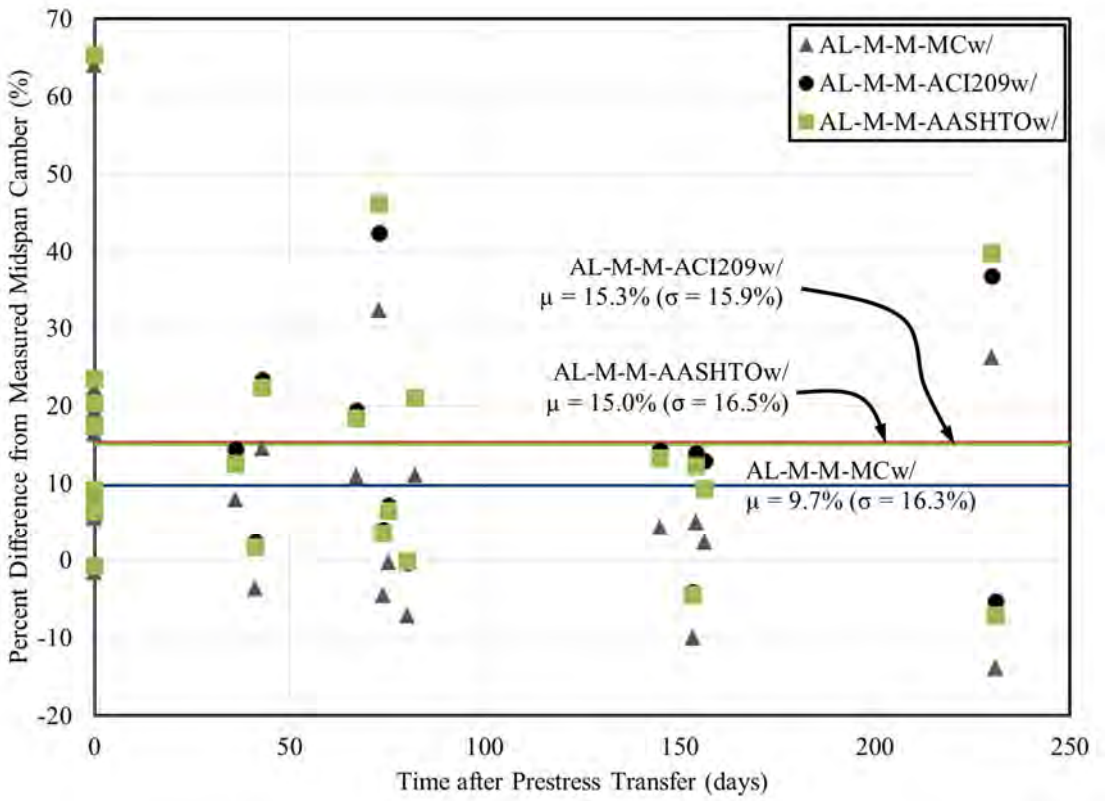

Figure 10-13: Accuracy of Girder Camber Predictions for Selected Trial Procedures

Averages and standard deviations (of percent difference) are also shown on the plot for each prediction trial. Use of the calibrated MC2010 creep and shrinkage model with measured material properties (AL-M-M-MCw/) yielded the overall most accurate prediction of camber—averaging 9.7 percent greater than

measured for the girder production cycles monitored in this study. Use of the calibrated AASHTO and ACI 209 creep and shrinkage models yielded somewhat less accurate results—tending to overestimate camber, on average, by approximately 15 percent. Similar average summary statistics are shown in Table 10-16 for other considered metrics of deformation including midspan (a) curvature, (b) bottom flange strain, and (c) centroidal strain.

Table 10-16: Accuracy of Deflection Predictions for Selected Prediction Trials

Trial Prediction Procedure	Percent Difference from Measured Values for All Midspan Measurements (%)							
	Camber		Curvature		Bottom Flange Strain		Centroidal Strain	
	μ	σ	μ	σ	μ	σ	μ	σ
AL-M-M-MCw/	+9.7	+16.3	-12.7	+12.8	+5.5	+16.1	+16.9	+24.6
AL-M-M-ACI209w/	+15.3	+15.9	-8.2	+12.1	+0.1	+14.9	+5.5	+20.7
AL-M-M-AASHTOw/	+15.0	+16.5	-8.7	+12.3	+8.3	+19.9	+19.0	+30.6

Predictions of midspan bottom flange strains tended to be the most accurate of any predicted deformation metric for all considered prediction trials, with lesser levels of accuracy observed for midspan curvatures and centroidal strains. The largest variability in results (as represented by the standard deviation) was observed in centroidal strain comparisons. Where most metrics tended to be overpredicted (e.g. camber, and cross-sectional strains), curvature tended to be underpredicted. For the remainder of this analysis, the most accurate of the above prediction trials (AL-M-M-MCw/) is used for comparison to subsequent prediction trials implementing varying levels of approximations of measured materials properties.

10.4.4 Effect of Calibration of Time-Dependent Models on Prediction Accuracy

To isolate the influence of the calibration of creep and shrinkage models on prediction accuracy for the metrics of deformation considered in this study, prediction trials similar to those discussed in Section 10.4.3 were generated, except omitting creep and shrinkage correction factors. Results for both calibrated and uncalibrated prediction trials for each of the three creep and shrinkage models considered in this study are shown in Figures 10-14 through 10-17.

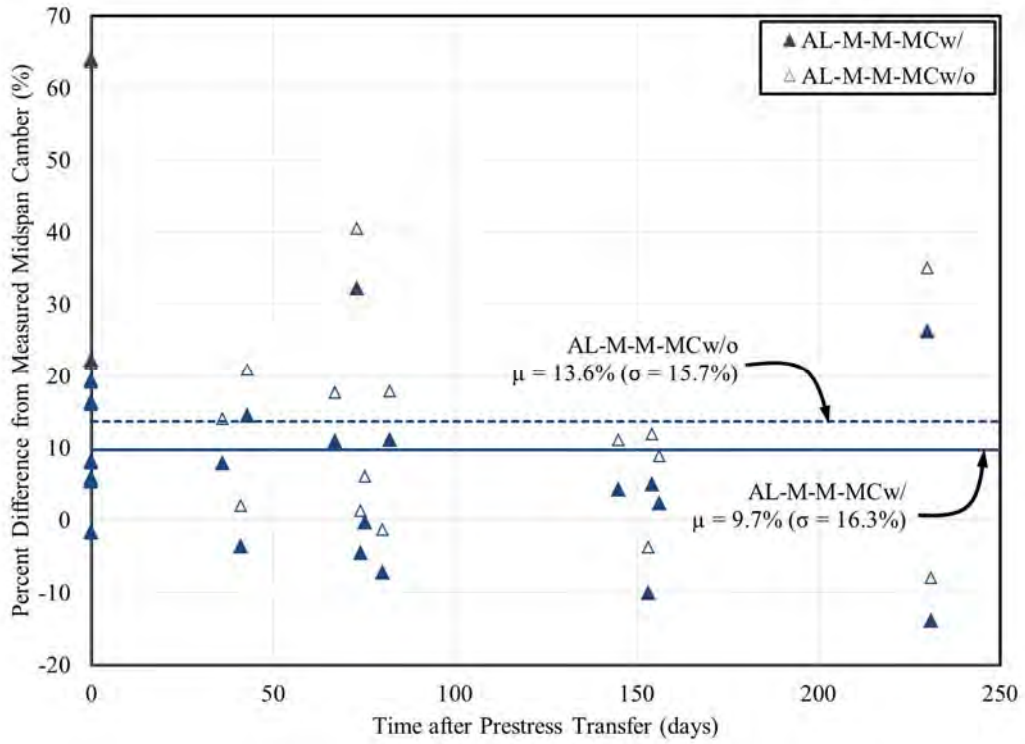

Figure 10-14: Effect of Calibration of MC2010 Creep and Shrinkage Models on Prediction Accuracy

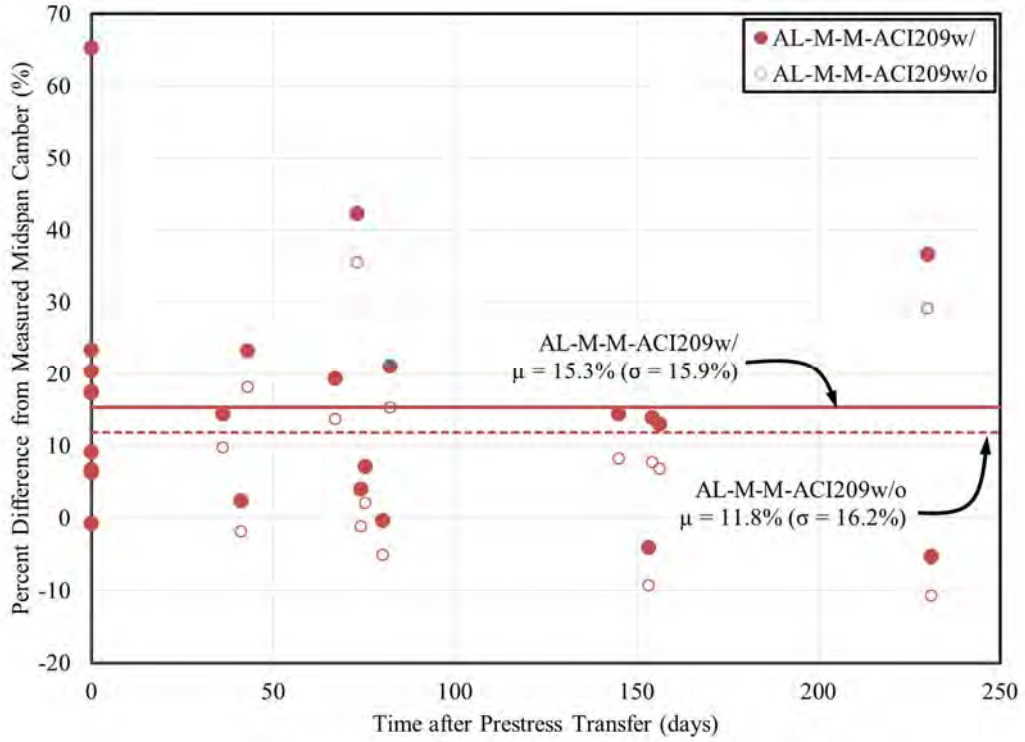

Figure 10-15: Effect of Calibration of ACI 209 Creep and Shrinkage Models on Prediction Accuracy

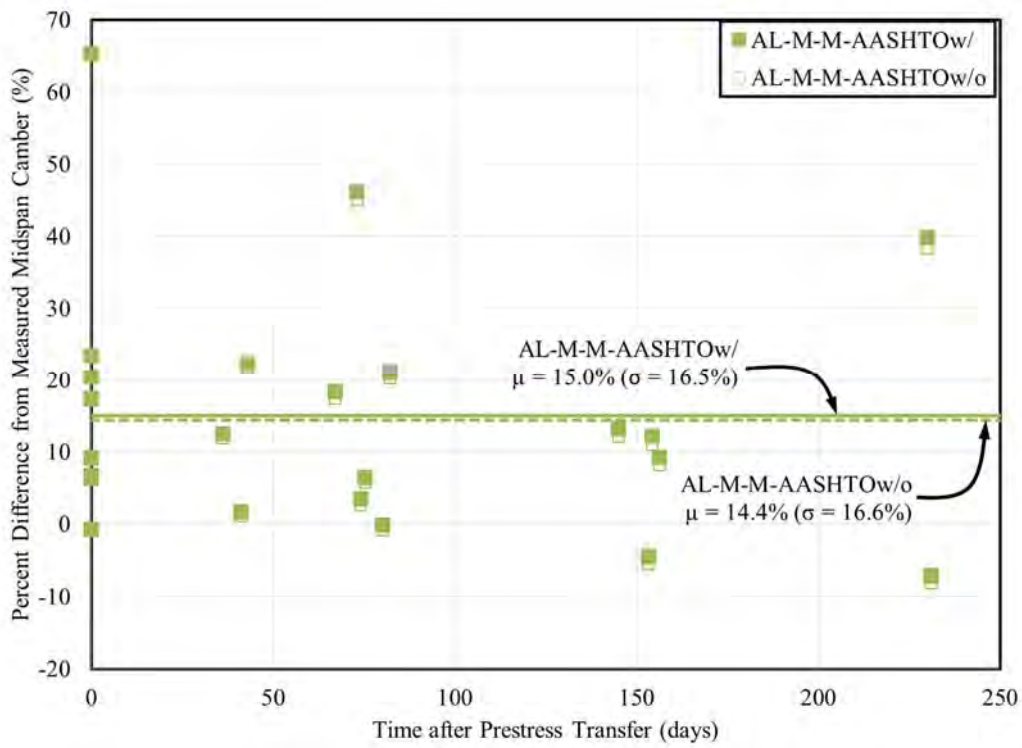

Figure 10-16: Effect of Calibration of AASHTO Creep and Shrinkage Models on Prediction Accuracy

Calibration of the MC2010 creep and shrinkage model tended to increase the accuracy of camber predictions by, on average, approximately 4 percent, while calibration of the ACI 209 creep and shrinkage models tended to reduce camber prediction accuracy by approximately 3.5 percent for the production cycles monitored in this study. Use of the calibrated AASHTO creep and shrinkage models tended to have little effect when compared to use of the uncalibrated models. Average percent differences for other metrics of deformation for the three prediction trials included in this section are summarized in Table 10-17.

Table 10-17: Effect of Calibration of Creep and Shrinkage Models on Deflection Prediction Accuracy

Trial Prediction Procedure	Percent Difference from Measured Values for All Midspan Measurements (%)							
	Camber		Curvature		Bottom Flange Strain		Centroidal Strain	
	μ	σ	μ	σ	μ	σ	μ	σ
AL-M-M-MCw/	+9.7	+16.3	-12.7	+12.8	+5.5	+16.1	+16.9	+24.6
AL-M-M-MCw/o	+13.6	+15.7	-9.8	+12.3	+15.9	+21.8	+31.9	+33.8
AL-M-M-ACI209w/	+15.3	+15.9	-8.2	+12.1	+0.1	+14.9	+5.5	+20.7
AL-M-M-ACI209w/o	+11.8	+16.2	-10.9	+12.4	-1.5	+14.1	+4.6	+20.3
AL-M-M-AASHTOw/	+15.0	+16.5	-8.7	+12.3	+8.3	+19.9	+19.0	+30.6
AL-M-M-AASHTOw/o	+14.4	+16.6	-9.2	+12.3	+11.1	+22.0	+23.9	+34.5

In the above analysis, the differences observed between similar prediction trials reflect differences in only time-dependent behavior, because the initial predictions of girder deformations (at prestress release) remain unaffected by choice of time-dependent model.

10.4.5 Effect of Varying Elastic Modulus Assumptions on Prediction Accuracy

The next series of prediction trials enables investigation of the influence of varying approximations of elastic modulus—independent of approximations in concrete strength or time-dependent behavior. Percent differences from observed midspan camber are shown in Figure 10-17, with summary statistics for other metrics of deformation displayed in Table 10-18.

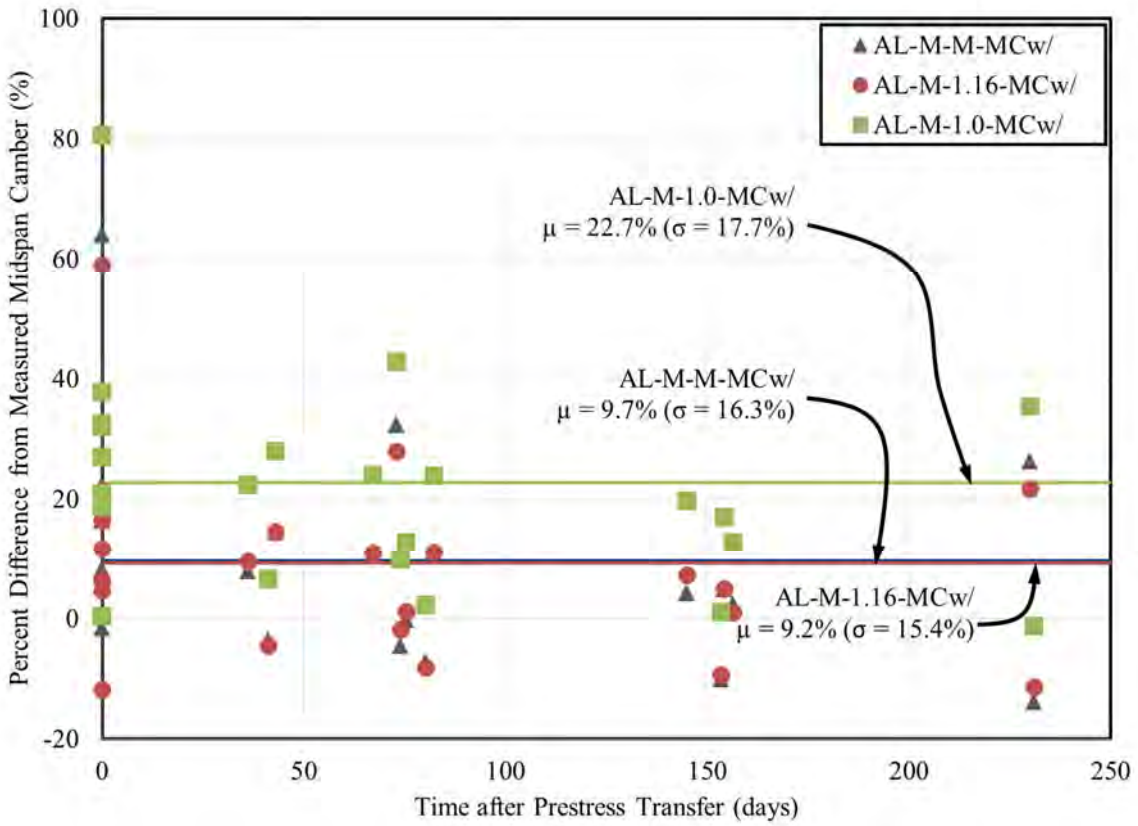

Figure 10-17: Effect of Varying Modulus Assumptions on Camber Prediction Accuracy

Table 10-18: Effect of Varying Modulus Assumptions on Deflection Prediction Accuracy

Trial Prediction Procedure	Percent Difference from Measured Values for All Midspan Measurements (%)							
	Camber		Curvature		Bottom Flange Strain		Centroidal Strain	
	μ	σ	μ	σ	μ	σ	μ	σ
AL-M-M-MCw/	+9.7	+16.3	-12.7	+12.8	+5.5	+16.1	+16.9	+24.6
AL-M-1.16-MCw/	+9.2	+15.4	-13.2	+11.7	+5.1	+15.9	+16.6	+25.0
AL-M-1.0-MCw/	+22.7	+17.7	-2.8	+13.6	+17.2	+16.9	+29.8	+26.6

As shown in Figure 10-17, the computation of elastic modulus with a K_1 factor of 1.16 (using measured strength) yielded results nearly identical to use of measured elastic modulus. Computation of elastic modulus with a K_1 factor of 1.0 (using measured strength) yielded camber predictions that were, on average, 13 percent greater than the most accurate predictions of camber (AL-M-M-MCw/).

10.4.6 Effect of Varying Strength Assumptions on Prediction Accuracy

To explore the effect of varying approximations of concrete compressive strength independent of approximations of elastic modulus, three additional prediction trials were generated. In these cases, changes to the concrete compressive strength tended to only influence the time-dependent deformation

predictions due to the inclusion of concrete strength in various creep and shrinkage models. Percent differences for camber predictions for each of the three prediction trials are shown in Figure 10-18, with summary results for other metrics of deformation shown in Table 10-19.

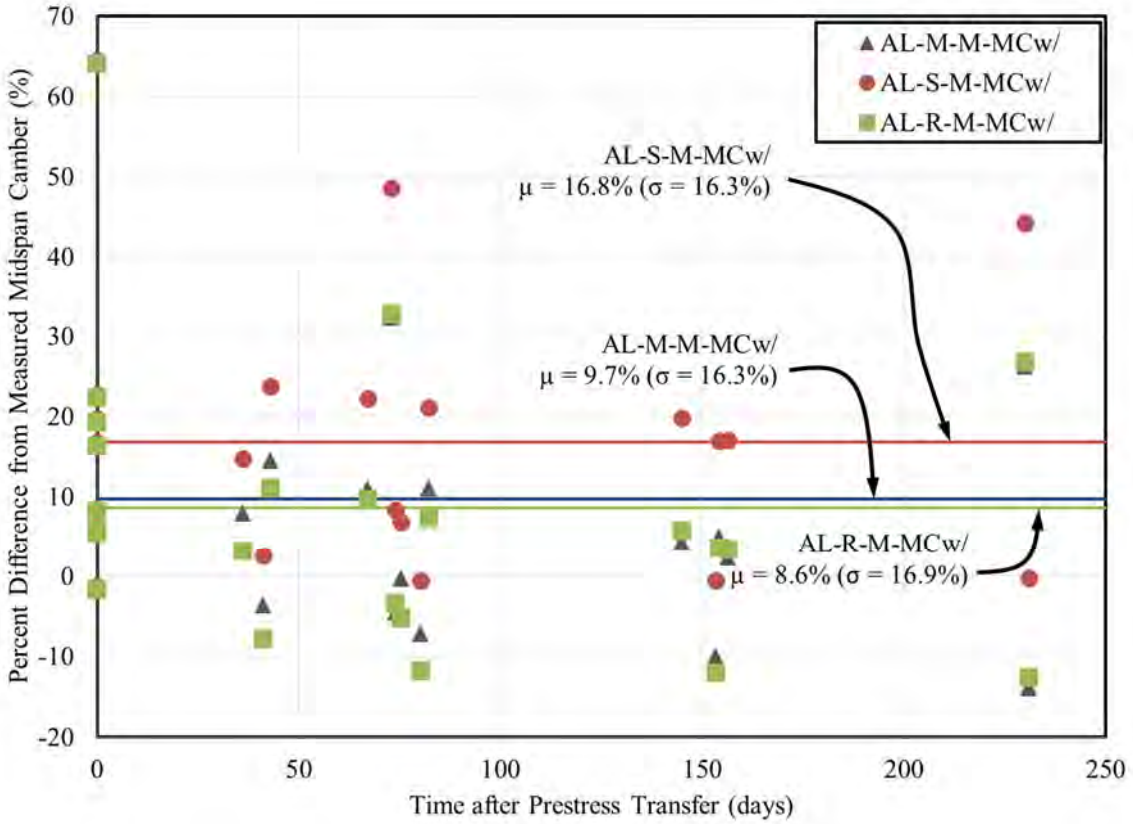

Figure 10-18: Effect of Varying Concrete Strength Assumptions on Camber Prediction Accuracy

Table 10-19: Effect of Varying Concrete Strength Assumptions on Deflection Prediction Accuracy

Trial Prediction Procedure	Percent Difference from Measured Values for All Midspan Measurements (%)							
	Camber		Curvature		Bottom Flange Strain		Centroidal Strain	
	μ	σ	μ	σ	μ	σ	μ	σ
AL-M-M-MCw/	+9.7	+16.3	-12.7	+12.8	+5.5	+16.1	+16.9	+24.6
AL-S-M-MCw/	+16.8	+16.3	-7.3	+11.6	+11.2	+20.4	+22.9	+30.8
AL-R-M-MCw/	+8.6	+16.9	-13.7	+12.5	+4.7	+15.6	+16.2	+24.0

Use of the overstrength recommendations of Chapter 5 in Trial AL-R-M-MCw/ yielded predictions with accuracy similar to those of the overall most accurate prediction trial (AL-M-M-MCw/), while use of specified concrete strengths in prediction trials corresponded to roughly double the percent difference of the overall most accurate prediction trial of this study.

10.4.7 Effects of Selected Compounded Errors Using *ALCAMBER* Software

Where previous sections of this analysis focused on uncoupled (isolated) effects of various approximations of concrete strength, elastic modulus, and creep and shrinkage, this section explores the effect of selected combinations of these approximations. The first two combinations (AL-S-1.16-MCw/ and AL-S-1.0-MCw/) enable investigation of prediction errors associated with approximations of both concrete strength and elastic modulus, while the latter two combinations (AL-R-1.16-MCw/ and AL-S-1.0-AASHTOw/o) correspond to potential and current camber prediction procedures, respectively. Percent differences for camber predictions for each prediction trial are shown in Figure 10-19.

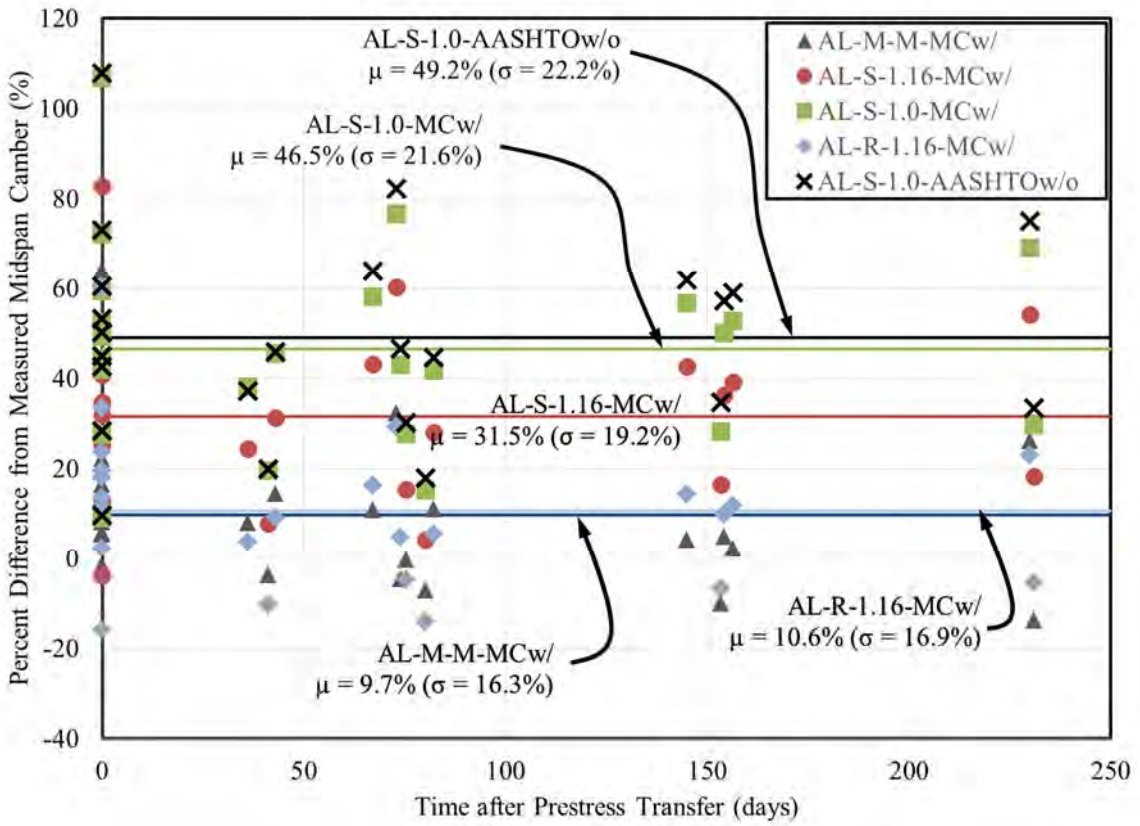

Figure 10-19: Effect of Selected Compounded Approximations on Camber Prediction Accuracy

As shown, the use of specified concrete strength (a lower bound value) with a recommended approximation of elastic modulus (K_1 = 1.16) yields predictions roughly 22 percent less accurate than the best trial procedure (AL-M-M-MCw/) in this study. Use of specified strength and an unadjusted approximation of elastic modulus (K_1 = 1.0), regardless of the choice of time-dependent model, yields camber predictions that are, on average, 40 percent less accurate than best predictions of girder camber. Finally, use of (a) the overstrength recommendations of Chapter 5, (b) a recommended approximation of

elastic modulus (K_1 = 1.16), and (c) a calibrated MC2010 time-dependent model yields camber prediction accuracy approximately identical to the best predictions of camber observed in this study. For reference, tabular results for average percent difference for camber and other metrics of girder deformation are displayed in Table 10-20.

Table 10-20: Effect of Selected Compounded Approximations on Deflection Prediction Accuracy Using *ALCAMBER*

Trial Prediction Procedure	Percent Difference from Measured Values for All Midspan Measurements (%)							
	Camber		Curvature		Bottom Flange Strain		Centroidal Strain	
	μ	σ	μ	σ	μ	σ	μ	σ
AL-M-M-MCw/	+9.7	+16.3	-12.7	+12.8	+5.5	+16.1	+16.9	+24.6
AL-S-1.16-MCw/	+31.5	+19.2	+3.5	+12.4	+25.0	+24.6	+38.7	+37.6
AL-S-1.0-MCw/	+46.5	+21.6	+14.9	+14.2	+39.1	+26.0	+54.5	+40.1
AL-R-1.16-MCw/	+10.6	+16.9	-12.4	+11.6	+6.5	+17.4	+18.5	+27.1
AL-S-1.0-AASHTOw/o	+49.2	+22.2	+16.7	+14.6	+49.2	+37.3	+69.8	+58.4

10.4.8 Effects of Selected Compounded Errors on Initial Camber Prediction Using Commercial Design Software

The previous analyses of this section utilized the *ALCAMBER* analysis software to generate predictions of girder deformations at various ages up to an assumed age of girder erection (250 days). This section details a similar limited analysis performed using *LEAP CONSPAN* and *PSBEAM* to explore the effect of various assumptions of concrete strength and elastic modulus on camber prediction accuracy. The comparisons of this section are focused exclusively on *camber* prediction at the time of prestress release because these commercial software programs (a) output only a single time-dependent camber prediction at an approximate age between 30–60 days after production,

and (b) do not directly output other metrics of deformations (e.g. curvature or internal concrete strains). Average summary statistics for the percent difference from measured midspan camber for the three trial prediction procedures included in this analysis are shown in Table 10-21.

Table 10-21: Effect of Selected Compounded Errors on Camber Prediction Accuracy using Commercial Software

Trial Prediction Procedure	Percent Difference from Measured Values for Initial Midspan Camber Measurements (%)	
	μ	σ
C-R-1.16	+25.6	+23.8
C-S-1.16	+41.4	+27.8
C-S-1.0 [Current Practice]	+68.3	+42.7

As shown, the current practice of using specified concrete strength and an unmodified elastic modulus equation (K_1 = 1.0) tended to overpredict initial camber by approximately 68 percent when using commercial design software. The use of a recommended elastic modulus equation (K_1 = 1.16) tended to reduce the magnitude of the overestimate by 27 percent, while use of both the recommended elastic modulus equation and the Chapter 5 overstrength recommendations tended to reduce the magnitude of the overestimate by 43 percent—to a net overprediction of 25 percent when compared to the field measurements of camber included in this study.

10.5 Design Recommendations

In the above analysis, it is evident that most accurate predictions of girder camber are furnished when using measured material properties for a given production cycle (e.g. concrete compressive strength and elastic modulus) and laboratory calibrated creep and shrinkage models. However, at the time of girder design, these measured properties are not yet available. As an alternative, the trial prediction procedure AL-R-1.16-MCw/ incorporates the design recommendations of Chapters 5, 6, and 7 of this report to predict expected material properties and yields camber predictions nearly as accurate as those computed using measured material properties. For this reason, the trial prediction procedure AL-R-1.16-MCw/, as summarized in Table 10-22, is proposed for use during initial girder design.

Table 10-22: Proposed Camber Prediction Procedure (AL-R-1.16-MCw/) for ALDOT Girder Design

Material Property	**Recommendation**	**Equation(s)**
Concrete Compressive Strength	Estimate expected concrete strength at release, f_{ci}^{*}, using the ACI 214-based overstrength model (constant *s*).	$f_{ci}^{*} = f'_{ci} + 1{,}950$ psi when $f'_{ci} \le 5{,}000$ psi $f_{ci}^{*} = 0.9 f'_{ci} + 2{,}450$ psi otherwise
	Estimate expected concrete strength at 28 days, f_{c}^{*}, using the derived strength-growth model.	$f_{c}^{*} = 1.30 f'_{ci} + 3{,}530$ psi
Modulus of Elasticity	Use the AASHTO modulus of elasticity prediction equation with K_1 **= 1.16** for typical regional aggregates for predictions at both release and 28 days.	$E_c = 33{,}000 \cdot K_1 \cdot w^{1.5} \sqrt{f'_c}$ where E_c = static elastic modulus of concrete (ksi); K_1 = correction factor for source of aggregate; = 1.16 for typical regional aggregates;
	Backcalculate the strength-growth curve from computed values at release and 28 days within *ALCAMBER*.	
Creep and Shrinkage Behavior	Use the Model Code 2010 creep prediction model with a creep coefficient correction factor of **0.80.**	---
	Use the Model Code 2010 shrinkage prediction model with a shrinkage correction factor of **0.70.**	---
	In the absence of more detailed information, an MC2010 concrete maturity, t_t, of **3.5** days[a] may be used as *ALCAMBER* input.	---

[a] = Represents the average MC 2010 maturity, t_t, computed for typical field tests of this study.

Summary statistics regarding the accuracy of the proposed camber prediction procedure and a trial procedure similar to current design practice are shown in Table 10-23.

Table 10-23: Summary Statistics for Key Prediction Trials

Trial Prediction Procedure	Percent Difference from Measured Values for All Midspan Measurements (%)							
	Camber		Curvature		Bottom Flange Strain		Centroidal Strain	
	μ	σ	μ	σ	μ	σ	μ	σ
AL-R-1.16-MCw/ **[Proposed Camber Prediction Procedure]**	+10.6	+16.9	-12.4	+11.6	+6.5	+17.4	+18.5	+27.1
AL-S-1.0-AASHTOw/o **[Most Similar to Current Design Practice]**	+49.2	+22.2	+16.7	+14.6	+49.2	+37.3	+69.8	+58.4

As shown above, for the girder production events monitored in this study, use of the proposed camber prediction procedure (AL-R-1.16-MCw/) tended to reduce the net overprediction of girder camber (for all ages) from 49.2 percent to 10.6 percent—thereby eliminating nearly 80 percent of the average error associated with camber prediction by current design practice.

Despite the calibrated MC 2010 creep and shrinkage models providing best agreement with time-dependent behavior observed in both the laboratory portion of this study (Chapter 7) and the field-monitoring portion of this study (Chapter 10), there may be some reluctance regarding the implementation of a camber prediction procedure that relies on MC 2010 time-dependent provisions. In this case, use of the AASHTO creep and shrinkage models (either calibrated or uncalibrated) are an acceptable alternative expected to generate camber predictions that, on average, are approximately 5 percent less accurate than those generated using MC 2010 provisions (as evident from Figures 10-14 and 10-16)—thereby tending to overpredict observed girder camber by approximately 15 percent instead of the 10.6 percent characteristic of the use of MC 2010 time-dependent provisions.

Despite the analyses of this report thus far confirming that (a) the time-steps analysis approach implemented in the *ALCAMBER* software generates most accurate predictions of girder deformations, and (b) the MC2010 shrinkage provisions (implemented in the *ALCAMBER* software) tend to most closely match early-age shrinkage of typical precast, prestressed concrete girders, certain designers may desire to continue use of existing commercial software for the purposes of camber prediction. In this case, designers are encouraged to manually implement the recommendations of Table 10-22 with regards to

computing concrete overstrength and elastic modulus. For the girder production events monitored in this study, manual implementation of these recommendations in commercial software tended to reduce the magnitude of overprediction for camber at prestress transfer from 68 percent to 26 percent—thereby eliminating approximately 60 percent of the average error associated with prediction of camber at prestress transfer by current practice. The next section will briefly examine the suitability of using the PCI multiplier method, as implemented within existing commercial software, for the prediction of time-dependent camber for those who may prefer not to use the *ALCAMBER* software.

10.6 Comparison of PCI Multiplier Method to Recommended Camber Prediction Procedure

The two primary design software programs currently in use by ALDOT bridge designers (*LEAP CONSPAN* and *PSBEAM*) rely on the approximate PCI multiplier method to compute time-dependent midspan camber. This section briefly examines the appropriateness of the continued use of the PCI multiplier by comparing the prediction results obtained from a commercial design software (*LEAP CONSPAN*) to those predictions generated by the camber prediction procedure (implemented within the *ALCAMBER* software) recommended in Section 10.5. For each of the three typical girder designs observed in the field monitoring effort of this study, predictions of midspan camber are shown in Figure 10-20 for a) the recommended camber prediction procedure (AL-R-1.16-MCw/) and the most similar commercial design prediction procedure (C-R-1.16).

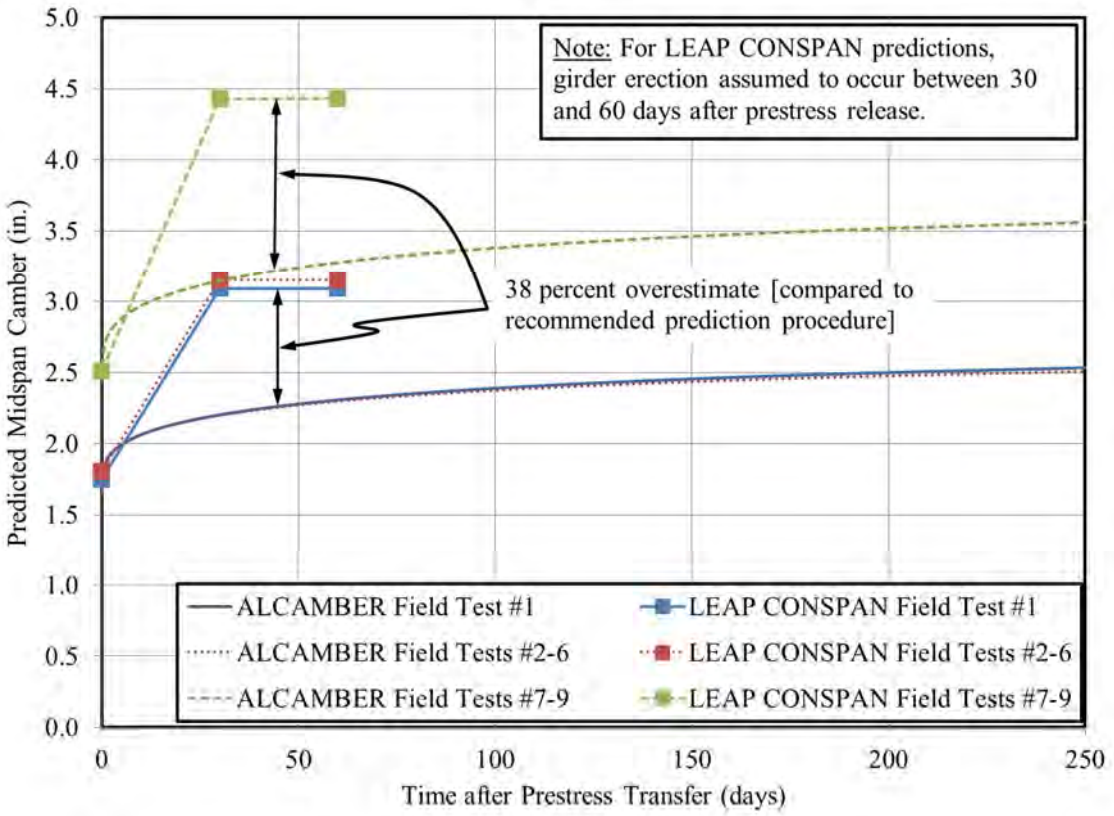

Figure 10-20: Comparison of Predictions by ALCAMBER Recommended Procedure (AL-R-1.16-MCw/) and Commercial Software (C-R-1.16) for Field Test Groups

Predictions of initial camber (t=0 days) were nearly identical for both methods for a given girder design—due to the inclusion of identical overstrength and aggregate stiffness modifiers in each prediction procedure. However, the predictions of time-dependent camber generated using the approximate PCI multiplier method (for t=40 days) exceeded those predictions generated using the recommended *ALCAMBER* prediction procedure by approximately 38 percent. Because of this discrepancy, use of the PCI multiplier method for the prediction of time-dependent girder deformations is cautioned against—particularly in circumstances where most accurate predictions of girder camber are required to ensure constructability (i.e. midspan camber).

10.7 Summary and Conclusions

10.7.1 Summary

This chapter focused on implementation of the design recommendations of previous chapters (Chapters 5–7) and comparisons of predictions to field measurements of girder deformations for 22 bridge girders

produced within the study region. While the beginning portions of this chapter served largely as a compilation of pertinent information from field tests, field results were then post-processed in preparation for comparisons to various trial prediction procedures. By comparing predicted and measured deformational responses for various trials, recommendations were made for the use of a revised camber prediction procedure that is expected to significantly increase the accuracy of initial design predictions of girder deformations.

The following conclusions regarding prediction of girder deformations (at all ages) for the nine girder production events monitored in this study result from the analyses of Chapter 10 conducted within the *ALCAMBER* software:

1. Most accurate predictions of girder camber were furnished using measured concrete properties (compressive strength and elastic modulus) for a given field test and a calibrated MC 2010 creep and shrinkage model—resulting in a net overprediction of girder camber (at all ages) of 10 percent. Similar predictions generated using the calibrated ACI 209 and AASHTO creep and shrinkage models yielded slightly less accurate results (approximately 15 percent overprediction);
2. Calibration of creep and shrinkage models tended to, on average, affect prediction accuracy by less than 5 percent;
3. Independent of changes in other input variables (e.g. concrete strength and creep and shrinkage models), the use of appropriate stiffness modifiers (K_1 = 1.16) tended to yield prediction accuracies approximately equal to those generated using measured elastic moduli, while omission of stiffness modifiers (K_1 = 1.0) tended to result in predictions 13 percent less accurate than those generated using measured elastic moduli;
4. Independent of changes in other variables (e.g. concrete modulus and creep and shrinkage models), the use of recommended overstrength provisions (Ch. 5) tended to yield prediction accuracies on par with those generated using measured compressive strength, while use of specified concrete strength tended to generate predictions roughly half as accurate as those generated using measured compressive strength;

5. Use of both appropriate stiffness modifiers (K_1 = 1.16) and recommended overstrength provisions (Ch. 5) tended to generate predictions with accuracy nearly identical to those generated using corresponding measured properties—resulting in a net overprediction of girder camber of approximately 10 percent;
6. Use of appropriate stiffness modifiers (K_1 = 1.16), but specified concrete strength (a lower bound value) tended to result in prediction accuracies roughly 22 percent less accurate than those generated using measured material properties; and
7. Use of specified strength and an unadjusted approximation of elastic modulus (K_1 = 1.0), regardless of the choice of time-dependent model, tended to yield camber predictions that were, on average, 40 percent less accurate than best predictions observed in this study and represent overpredictions of roughly 50 percent when compared to field measured values.

The following conclusions regarding predictions of girder deformations at prestress transfer for the nine girder production events monitored in this study result from the analyses of Chapter 10 conducted using commercial design software:

- Current design practice tended to overpredict midspan camber at prestress release by approximately 68 percent when compared to field measured values;
- Implementation of an appropriate stiffness modifier (K_1 = 1.16)—while still relying on specified concrete strength—tended to improve the accuracy of initial camber predictions by approximately 27 percent;
- Implementation of both an appropriate stiffness modifier (K_1 = 1.16) and recommended overstrength recommendations (Ch. 5) tended to improve the accuracy of initial camber predictions by approximately 45 percent.

The following conclusions regarding use of the PCI multiplier method result from the analysis of Section 10.6:

- For the three girder designs observed in the field monitoring portion of this study, use of the approximate PCI multiplier method tended to yield predictions of midspan girder camber (at erection) that exceeded best refined predictions (generated using the *ALCAMBER* software) by approximately 38 percent; and

- Use of the PCI multiplier method for the prediction of time-dependent girder deformations is cautioned against—particularly in circumstances where most accurate predictions of camber are required to ensure constructability (i.e. midspan camber).

10.7.2 Design Recommendations

To improve the accuracy of design camber predictions in Alabama, the following design recommendations are proposed:

1. The revised camber prediction procedure summarized in Table 10-24 (and implemented within the *ALCAMBER* software) is recommended for use at the time of girder design to predict girder camber through the time of girder erection. For the nine girder production events monitored in this study, use of the revised camber prediction procedure—in conjunction with the time-steps analysis procedure of the *ALCAMBER* software—eliminated, on average, approximately 80 percent of the error associated with current ALDOT camber prediction practices.

   As an alternative to the revised prediction procedure summarized in Table 10-24, designers may instead utilize AASHTO creep and shrinkage models (either calibrated or uncalibrated) within the *ALCAMBER* software—although the accuracy of camber prediction results are expected to be somewhat less accurate (approximately 5 percent);

Table 10-24: Recommended Camber Prediction Procedure (AL-R-1.16-MCw/) for ALDOT Girder Design

Material Property	**Recommendation**	**Equation(s)**
Concrete Compressive Strength	Estimate expected concrete strength at release, f_{ci}^{*}, using the ACI 214-based overstrength model (constant *s*).	$f_{ci}^{*} = f'_{ci} + 1{,}950$ psi when $f'_{ci} \le 5{,}000$ psi $f_{ci}^{*} = 0.9 f'_{ci} + 2{,}450$ psi otherwise
	Estimate expected concrete strength at 28 days, f_{c}^{*}, using the derived strength-growth model.	$f_{c}^{*} = 1.30 f'_{ci} + 3{,}530$ psi
Modulus of Elasticity	Use the AASHTO modulus of elasticity prediction equation with K_1 **= 1.16** for typical regional aggregates for predictions at both release and 28 days.	$E_c = 33{,}000 \cdot K_1 \cdot w^{1.5} \sqrt{f'_c}$ where E_c = static elastic modulus of concrete (ksi); K_1 = correction factor for source of aggregate; = 1.16 for typical regional aggregates;
	Backcalculate the strength-growth curve from computed values at release and 28 days within *ALCAMBER*.	
Creep and Shrinkage Behavior	Use the Model Code 2010 creep prediction model with a creep coefficient correction factor of **0.80.**	---
	Use the Model Code 2010 shrinkage prediction model with a shrinkage correction factor of **0.70.**	---
	In the absence of more detailed information, an MC2010 concrete maturity, t_t, of **3.5** days[a] may be used as *ALCAMBER* input.	---

[a] = Represents the average MC 2010 maturity, t_t, computed for typical field tests of this study.

2. Designers who prefer to continue use of existing commercial software for camber prediction should consider manual implementation of the overstrength and modulus of elasticity adjustments included in Table 10-24. Manual implementation of these recommendations is expected to eliminate approximately 60 percent of the average error associated with current design practice. Designers should also be aware that use of the PCI multiplier, as implemented in existing commercial design software, may tend to overpredict camber at girder erection by approximately 40 percent when compared to predictions of camber furnished by the recommended procedure of Table 10-24.

Chapter 11: Summary, Conclusions, and Recommendations

11.1 Summary of Work

In precast, prestressed concrete construction, the eccentricity of the prestressing force typically results in a net upward girder deflection known as camber. Camber is first observed at the time of prestress transfer and tends to increase thereafter as a function of time-dependent material properties. While accurately predicted levels of camber are desirable to concrete bridge construction, inaccuracies in design camber estimates can result in construction difficulties and the need to modify bridge designs to ensure proper girder fit. To mitigate such troublesome issues, the Alabama Department of Transportation (ALDOT) sponsored an investigation to develop a suggested procedure for use during girder design to more accurately predict pre-erection camber in precast, prestressed concrete bridge girders.

In support of this objective, various laboratory and field studies were conducted to explore relevant regionally-variable concrete material properties (e.g. concrete compressive strength, concrete elastic modulus, and creep and shrinkage behavior), as well as the effect of varying temperature conditions on girder camber. Then, a revised camber prediction procedure was developed, implemented in a standalone computer program (*ALCAMBER*), and validated by comparison to multiple production events of ALDOT precast, prestressed concrete girders. Use of the revised camber prediction procedure developed in this study—in conjunction with the time-steps analysis procedure of the *ALCAMBER* software—eliminated, on average, approximately 80 percent of the error associated with current ALDOT camber prediction practices for the girder production events monitored in this study.

11.2 Research Conclusions and Recommendations

Conclusions and recommendations are grouped by chapter title—with recommendations of Chapter 10 incorporating relevant design recommendations from earlier chapters.

11.2.1 Current Design and Construction Practices for ALDOT Precast, Prestressed Concrete Bridge Girders

A recommended change to girder design practice supported by work presented in Chapter 4:

- In addition to the 60-day erection midspan camber currently noted on design drawings, ALDOT bridge design plans should also include estimated camber at the time of prestress transfer, thereby facilitating earlier detection of any significant deviations from predicted camber.

11.2.2 Accurately Predicting Expected Concrete Compressive Strength

Conclusions and recommendations are supported by research presented in Chapter 5:

1. For design deflection computations, it is appropriate to use an estimate of the "expected" concrete compressive strength rather than the current practice of using the specified strength.
2. The existing provisions of ACI 301 and ACI 214R-11 are an appropriate and convenient method for estimating the expected concrete compressive strength as a function of the specified strength.
3. The "difference statistic" and the concept of preservation of standard deviation (as summarized below) offer a convenient method to compute a standard deviation from a historical data set with varying specified concrete strengths that is appropriate for use within the provisions of ACI 301 and ACI 214R-11:

   For an assumed (or approximated) constant standard deviation value at all considered strength levels, the distribution of the difference statistic is identical regardless of the number of constitutive mixtures or the relative mean strength levels of each mixture.

Recommendations for use by girder designers, supported by the historical data set compiled in Chapter 5, include the following:

1. To predict the expected concrete compressive strength at the time of prestress release, f_{ci}^{*}, the overstrength provisions of ACI 301 and ACI 214 should be applied with a standard deviation as determined by the distribution of the difference statistic for historical records from production events of precast, prestressed products within the region.
   a. In the absence of historical data, the standard deviation, *s*, may be assumed to be 1,050 psi based on the results of this study—resulting in the following relationships:

For 4,000 psi $\leq f_{ci} \leq 5{,}000$ psi $\qquad f_{ci}^{*} = f'_{ci} + 1{,}950$ psi

For 5,000 psi $< f_{ci} \leq 9{,}000$ psi $\qquad f_{ci}^{*} = 0.9 f'_{ci} + 2{,}450$ psi

2. The overstrength factor at release, OS_i, corresponding to the above expressions (for concrete strengths exceeding 5,000 psi) can be expressed as

$$OS_i = \frac{f_{ci}^{*}}{f'_{ci}} = 0.9 + \frac{2{,}450}{f'_{ci}}$$

where

OS_i^{*} = expected overstrength factor at prestress release;

f_{ci}^{*} = the expected concrete strength at prestress release (psi); and

f'_{ci} = the specified concrete strength at prestress release (psi).

3. To predict expected compressive strength at the age of 28 days (for accelerated cured concretes typical of the precast, prestressed industry), the following expression is recommended:

$$f_c^{*} = 1.3 f'_{ci} + 3{,}500 \text{ psi}$$

where

f'_{ci} = the specified concrete strength at prestress release (psi).

4. The expected overstrength at 28 days, OS_{28}^{*}, corresponding to the above expressions can be computed as

$$OS_{28}^{*} = 1.3\left(\frac{f'_{ci}}{f'_c}\right) + \frac{3{,}500}{f'_c}$$

where

$\left(\frac{f'_{ci}}{f'_c}\right)$ = the ratio of specified strength at prestress release to 28 days as selected by design engineer; and

f'_c = specified compressive strength at 28 days.

11.2.3 Concrete Modulus of Elasticity Relationships

Conclusions and recommendations are supported by research presented in Chapter 6:

1. No statistical difference in elastic modulus was detectable among three laboratory mixtures containing various SCMs (fly ash, slag cement, or silica fume) in typical percent replacements used in Alabama.
2. The use of two regional dolomitic limestone aggregates (acquired from an ALDOT-approved source) resulted in concrete stiffnesses greater than those predicted by unmodified AASHTO equations by 16 percent at the time of prestress transfer and by 13 percent 28 days after production.
3. The use of a regional crushed granite aggregate (acquired from an ALDOT-approved source) resulted in concretes with less than expected E_c values (K_1 values between 0.68–0.72).
    a. Requirements of the *ALDOT Standard Specification for Highway Construction* (ALDOT 2012), specifically with regards to the permissible levels of deleterious substances within coarse aggregate, should continue to be enforced to ensure acceptable concretes for precast, prestressed applications.
4. Concrete cylinder temperature (at the time of hardened testing) is a potential source of uncontrolled variability in this research study and, perhaps a cause of the varying K_1 factors observed at different ages of testing.

Recommendations for use by girder designers supported by the research reflected in Chapter 6:

5. The AASHTO LRFD Bridge Design Specifications (AASHTO 2014) prediction equation, with the assumptions and calibrations noted below, is most appropriate for design predictions of the elastic modulus for precast, prestressed concrete.

$$E_c = 33{,}000 \cdot K_1 \cdot w^{1.5} \sqrt{f'_c}$$

where

E_c = static elastic modulus of concrete (ksi);

K_1 = correction factor for source of aggregate;

= 1.16 for dolomitic limestone at release;

= 1.13 for dolomitic limestone at 28 days;

w = unit weight of concrete (kcf);

= assumed equation to 0.150 kcf for design purposes; and

f'_c = concrete compressive strength (ksi).

6. For simplicity, the above K_1 factors may be approximated as $K_1 = 1.15$ in design applications incompatible with the implementation of unique K_1 factors for different ages.

11.2.4 Creep and Shrinkage Behavior of Alabama Precast, Prestressed Concretes

Conclusions and recommendations regarding concrete creep are supported by research presented in Chapter 7:

1. No significant difference in concrete creep was detected between the two regional dolomitic limestone aggregates included in this study.
2. Concrete mixtures using crushed granite aggregate exhibited 55–58 percent more compliance than corresponding dolomitic limestone control mixtures. However, this difference was primarily due to the reduced elastic modulus of the crushed granite aggregate and is not attributable to a significant difference in time-dependent creep behavior.
3. Specimens loaded at 24 hours appeared to exhibit slightly reduced creep in comparison to specimens loaded at 18 hours, although approaching the limits of experimental precision.
4. The use of slag cement (15 percent substitution) had a negligible effect on creep, while the use of fly ash (15 percent substitution) may have caused a slight reduction in creep.
5. The use of fly ash and silica fume (18 percent and 8 percent substitution, respectively) resulted in a reduced creep tendency of between 9–12 percent.
6. Of the unadjusted creep prediction models, the ACI 209 and AASHTO 2014 models provided relatively accurate predictions for the typical regional prestressed concretes considered in this

study, with BP coefficients of variation of 10.3 and 12.9, respectively. Of these models, AASHTO LRFD is the simplest.

7. Elastic moduli, as computed from creep frame loadings in accordance with ASTM C512, tended to be 14 percent lower than those measured in companion cylinders by ASTM C469 at the time of loading—suggesting that a small portion of early creep is "missed" during typical ASTM C512 testing.
8. The "missed" portion of early creep corresponded to negligible differences in compliance, and thus, affirms the preference to consider compliance as the primary metric of time-dependent load-induced deformation.

Conclusions and recommendations regarding concrete shrinkage are supported by research presented in Chapter 7:

1. No significant difference in shrinkage behavior was detectable between the two regional dolomitic limestones included in this study.
2. Crushed granite mixtures tended to exhibit between 40–70 percent increased shrinkage when compared to dolomitic limestone mixtures.
3. Specimens loaded at 18 hour ages exhibited a slightly increased shrinkage tendency when compared to specimens loaded at 24 hour ages, although approaching experimental precision.
4. No significant effect of fly ash or slag (for typical regional substitution percentages) on shrinkage behavior was detectable in comparison to control mixtures.
5. The ternary mixture (containing fly ash and silica fume) exhibited slightly decreased shrinkage in comparison to control mixtures, although approaching experimental precision.
6. Of the three unadjusted candidate prediction models, the AASHTO 2014 method is most accurate of the considered models with a BP coefficient of variation of 36 percent.

The following summarize recommendations for future researchers:

1. The use of sound post-processing techniques to eliminate erroneous data points and to detect loading anomalies is encouraged.

2. Experimental precisions and repeatability of measurements should be determined by duplicate tests to allow identification of significant experimental trends.
3. If conducting testing intended to simulate precast, prestressed concrete element production, an accelerated curing system should be used to introduce expected temperature profiles before and at the time of creep loading.
4. The comparison of concrete elastic modulus as computed by loading frame data and also by companion material testing can be used to affirm the soundness of testing procedures and validate the accuracy of benchmark readings.

Recommendations for use by girder designers, supported by the laboratory testing conducted in Chapter 7, include the following:

1. For best estimates of creep, the following creep coefficient modifications may be applied to the unadjusted models—with most accurate predictions offered by the Model Code 2010 method:

Table 7-22: Design Recommendations for Creep Coefficient Modification Factors

	Proposed Creep Coefficient Modification Factors	
Prediction Model	**When ternary mixtures are used**	**For all other mixture compositions (or unknown)**
AASHTO LRFD	**0.80**	1.00
ACI 209[b]	**0.95**	**1.15**
Model Code 2010[c]	**0.65**	**0.80**

[a] = Ternary mixtures refer to those mixtures containing fly ash and silica fume.
[b] = Requires mixture-specific input parameters including fine aggregate percent, slump, air content.
[c] = Requires estimate of adjusted maturity at the time of prestress transfer.

2. For best predictions of concrete shrinkage, the following shrinkage modification factors are suggested for use with each considered prediction model:

Table 7-20: Design Recommendations for Shrinkage Modification Factors

	Proposed Shrinkage Modification Factors	
Prediction Model	**For use with slag and ternary[a] mixtures with limestone coarse aggregate (or unknown)**	**For use with crushed granite aggregate**
AASHTO LRFD	**0.80**	1.6
ACI 209[b]	0.75	1.5
Model Code 2010[c]	0.70	1.4

[a] = Ternary mixtures refer to those containing fly ash and silica fume.
[b] = Requires mixture-specific input parameters including fine aggregate percentage, cement content, slump, and air content.
[c] = Requires estimate of adjusted maturity at the time of prestress release and cement type.

11.2.5 Effect of Diurnal Temperature Changes on Girder Camber

Conclusions and recommendations are supported by research presented in Chapter 8:

1. The curvature-based temperature-correction algorithm, as implemented in this study, demonstrated good agreement with field measured results—with the exception of where testing anomalies were detected (e.g. Field Test #1).
2. For the concrete girders monitored in this study, an effective CTE value of between 13.0 and 13.5 με/°C was found to provide best agreement between predicted and measured deformational responses for girders in unshaded outdoor storage.
3. Maximum diurnal temperature-induced changes to midspan camber of approximately 0.45 inches were observed in the field testing of this study.
4. The general shapes of vertical temperature profiles at all locations (midspan and 1/6-span) were similar, with extreme temperature changes being induced in the girder web for the field tests conducted in this effort.
5. Positioning of temperature gages at one-quarter points within the girder web of bulb-tee sections appeared to approximate observed reversals of the temperature profile occurring within the girder web relatively well.
6. The most detailed analysis iteration used in this study (which relied on between 11–13 thermocouple measurements at midspan and an exact cross section definition) tended to generate the most accurate predictions of temperature-induced girder deformations (with the exception of where testing anomalies were detected)—although at the greatest computational cost.
7. Analytical iterations conducted using measured data from different cross sections (i.e. measured temperatures and strains from midspan and 1/6-span) generated largely similar results.
8. Use of the simplified equivalent cross section proposed by Johnson (2012) resulted in negligible error when compared to use of an exact cross section definition.
9. Use of the simplified temperature profile proposed by Johnson (2012) generated strain predictions only slightly less accurate than those of the most detailed analysis included in this study.

10. The use of direct linear interpolation between measurements to define vertical temperature profile shape resulted in predictions of strains and vertical deflections only slightly less accurate than use of the temperature profile by Johnson (2012).
11. For the purposes of temperature-correction of field camber measurements, use of the temperature-correction algorithm derived in Section 8.2.2 is appropriate with either (a) the procedures and assumptions implemented by Johnson (2012), (b) the procedures and assumptions implemented in this study, or (c) any combinations thereof.
12. Maximum expected transient temperature-induced deformations for PCI bulb-tee girder sections (without decks) in unshaded outdoor storage are summarized in Table 8-11.

Table 8-11: Transient Changes to Theoretical Midspan Camber

Expected Transient Temperature-Induced Changes to Theoretical Midspan Camber	
Upward	<+1.5 in.
Downward	<-0.5 in.

11.2.6 Selection and Validation of a Revised Camber Prediction Procedure by Limited In-Plant Testing

Conclusions and recommendations are supported by research presented in Chapter 10:

1. Most accurate predictions of girder camber were furnished using the *ALCAMBER* software, measured concrete properties (compressive strength and elastic modulus) for a given field test, and calibrated MC 2010 creep and shrinkage models. For the girder production events monitored in this study, use of this procedure resulted in a net overprediction of midspan camber of 10 percent compared to field-observed values.
2. Prediction trials generated using measured concrete properties and either the calibrated ACI 209 or AASHTO creep and shrinkage models tended to yield slightly less accurate results (approximately 15 percent greater than field-observed values).
3. In comparison to the use of uncalibrated creep and shrinkage models, use of calibrated models tended to affect prediction accuracy, on average, by less than 5 percent.
4. The use of appropriate stiffness modifiers (K_1 = 1.16), independent of changes to other input variables (e.g. concrete strength and creep and shrinkage models), tended to yield prediction accuracies approximately equal to those generated using measured elastic moduli, while

omission of stiffness modifiers (K_1 = 1.0) tended to result in predictions 13 percent less accurate than those generated using measured elastic moduli.

5. The use of recommended overstrength provisions (Ch. 5), independent of changes in other variables (e.g. concrete modulus and creep and shrinkage models), tended to yield prediction accuracies on par with those generated using measured compressive strength, while use of specified concrete strength tended to generate predictions roughly half as accurate as those generated using measured compressive strength.
6. Use of appropriate stiffness modifiers (K_1 = 1.16) and recommended overstrength provisions (Ch. 5) tended to generate predictions with accuracy nearly identical to those generated using corresponding measured properties—resulting in a net overprediction of observed girder camber by approximately 10 percent.
7. Use of appropriate stiffness modifiers (K_1 = 1.16), but specified concrete strength (a lower bound value) tended to result in prediction accuracies roughly 22 percent less accurate than those generated using measured material properties.
8. Use of specified strength and an unadjusted approximation of elastic modulus (K_1 = 1.0), regardless of the choice of time-dependent model, tended to yield camber predictions that were, on average, 40 percent less accurate than best predictions observed in this study (and represent overpredictions of roughly 50 percent when compared to field observed values).
9. Current design practice (using commercial design software) tended to overpredict midspan camber at the time of prestress release by approximately 68 percent when compared to field observed values.
10. Implementation of an appropriate stiffness modifier (K_1 = 1.16) in commercial design software—while relying on specified concrete strength—tended to improve the accuracy of initial camber predictions by approximately 27 percent when compared to current design practice.
11. Implementation of both an appropriate stiffness modifier (K_1 = 1.16) and recommended overstrength recommendations (Ch. 5) in commercial design software tended to improve the accuracy of initial camber predictions by approximately 45 percent when compared to current design practice.

12. For the three girder designs observed in the field monitoring portion of this study, use of the approximate PCI multiplier method tended to yield predictions of midspan girder camber (at erection) that exceeded best refined predictions (generated using the *ALCAMBER* software) by approximately 38 percent.
13. Use of the PCI multiplier method for the prediction of time-dependent girder deformations is cautioned against—particularly in circumstances where most accurate predictions of deformations are required to ensure constructability (i.e. midspan camber).

To improve the accuracy of design camber predictions in Alabama, the following design recommendations, supported by the complete work of this report, are recommended:

1. The revised camber prediction procedure summarized in Table 10-24 (as implemented within the *ALCAMBER* software) is recommended for use at the time of girder design to predict midspan camber through girder erection. For the nine girder production events monitored in this study, use of the revised camber prediction procedure—in conjunction with the time-steps analysis procedure of the *ALCAMBER* software—eliminated, on average, approximately 80 percent of the error associated with current ALDOT camber prediction practices.
    a. As an alternative to the revised prediction procedure summarized in Table 10-24, designers may instead utilize AASHTO creep and shrinkage models (either calibrated or uncalibrated) within the *ALCAMBER* software if preferred—although the accuracy of camber prediction results is expected to be somewhat less (by approximately 5 percent).

    Designers who prefer to continue use of existing commercial software for camber prediction should consider manual implementation of the overstrength and modulus of elasticity adjustments included in Table 10-24. Manual implementation of these recommendations is expected to eliminate approximately 60 percent of the average error associated with initial camber predictions by current design practice. Designers should also be aware that use of the PCI multiplier, as implemented in existing commercial design software, may tend to overpredict camber at girder erection (by up to 40 percent) when compared to predictions of camber furnished by the recommended procedure of Table 10-24.

Table 10-24: Recommended Camber Prediction Procedure (AL-R-1.16-MCw/) for ALDOT Girder Design

Material Property	**Recommendation**	**Equation(s)**
Concrete Compressive Strength	Estimate expected concrete strength at release, f_{ci}^{*}, using the ACI 214-based overstrength model (constant *s*).	$f_{ci}^{*} = f'_{ci} + 1{,}950$ psi when $f'_{ci} \le 5{,}000$ psi $f_{ci}^{*} = 0.9 f'_{ci} + 2{,}450$ psi otherwise
	Estimate expected concrete strength at 28 days, f_{c}^{*}, using the derived strength-growth model.	$f_{c}^{*} = 1.3 f'_{ci} + 3{,}500$ psi
Modulus of Elasticity	Use the AASHTO modulus of elasticity prediction equation with K_1 **= 1.16** for typical regional aggregates for predictions at both release and 28 days.	$E_c = 33{,}000 \cdot K_1 \cdot w^{1.5} \sqrt{f'_c}$ where E_c = static elastic modulus of concrete (ksi); K_1 = correction factor for source of aggregate; = 1.16 for typical regional aggregates;
	Backcalculate the strength-growth curve from computed values at release and 28 days within *ALCAMBER*.	
Creep and Shrinkage Behavior	Use the Model Code 2010 creep prediction model with a creep coefficient correction factor of **0.80.**	---
	Use the Model Code 2010 shrinkage prediction model with a shrinkage correction factor of **0.70.**	---
	In the absence of more detailed information, an MC2010 concrete maturity, t_t, of **3.5** days[a] may be used as *ALCAMBER* input.	---

[a] = Represents the average MC 2010 maturity, t_t, computed for typical field tests of this study.

11.3 Recommendations for Future Research

Based on the research presented in this report, the following recommendations are given for potential future research:

1. The temperature of concrete cylinders at the time of hardened testing was identified as a possible reason for the time-dependent nature of aggregate stiffness factors, K_1, as observed in this study and also noted by previous researchers. Future work is recommended in this area to identify potential trends significant to the precast, prestressed concrete community.
2. Recalibration of the existing PCI multiplier method to better match the refined predictions of *ALCAMBER* may be useful for preliminary estimates of time-dependent girder camber.
3. Public distribution of the *ALCAMBER* v1.0 software at the conclusion of this study will provide a convenient platform for conducting parametric studies regarding the prediction of pre-erection time-dependent girder deformations. Potential topics of future study include the following:
    a. The effect of non-standard production schedules (i.e. weekend pours) on predicted camber, and
    b. The effect of selected variable concrete properties (e.g. concrete compressive strength, elastic modulus, and creep and shrinkage) on predicted camber.

References

AASHTO. 2014. *AASHTO LRFD Bridge Design Specifications*. 7th ed. Washington, DC: American Association of State Highway and Transportation Officials.

AASHTO. 2012. *AASHTO LRFD Bridge Design Specifications*. 6th ed. Washington, DC: American Association of State Highway and Transportation Officials.

Abrams, D.A. 1927. Water-Cement Ratio as Basis of Concrete Quality. *ACI Journal Proceedings* 23 (2): 452-457.

ACI Committee 211. 2008. Guide for Selecting Proportions for High-Strength Concrete Using Portland Cement and Other Cementitious Materials (ACI 211.4R-08). Farmington Hills, MI: American Concrete Institute.

ACI Committee 301. 2010. Specifications for Structural Concrete (ACI 301-10). Farmington Hills, MI: American Concrete Institute.

ACI Committee 363. 2010. Report on High-Strength Concrete (ACI 363R-11). Farmington Hills, MI: American Concrete Institute.

ACI Committee 209. 2005. Factors Affecting Shrinkage and Creep of Hardened Concrete (ACI 209.1R). Farmington Hills, MI: American Concrete Institute.

ACI Committee 209. 2008. Guide for Modeling and Calculating Shrinkage and Creep of Concrete (ACI 209.2R-08). Farmington Hills, MI: American Concrete Institute.

ACI Committee 209. 2008. Prediction of Creep, Shrinkage, and Temperature Effects in Concrete Structures (ACI 209R-92/08). Farmington Hills, MI: American Concrete Institute.

ACI Committee 214. 2011. Guide to Evaluation of Strength Test Results of Concrete (ACI 214R-11). Farmington Hills, MI: American Concrete Institute.

ACI Committee 216. 2014. Code Requirement for Determining the Fire Resistance of Concrete and Masonry Construction Assemblies (ACI 216.1-14). Farmington Hill, MI: American Concrete Institute.

ACI Committee 318. 2014. Building Code Requirements for Structural Concrete (ACI 318-14). Farmington Hills, MI: American Concrete Institute.

ACI Committee 318. 1971. Building Code Requirements for Reinforced Concrete (ACI-318-71). Detroit, MI: American Concrete Institute.

ACI Committee 435. 1997. Report on Temperature-Induced Deflections of Reinforced Concrete Members (ACI 435.7R-85). Farmington Hills, MI: American Concrete Institute.

ACI. 2013. ACI Concrete Terminology (ACI CT-13). Farmington Hills, MI: American Concrete Institute.

ACI Committee 318. 2011. Building Code Requirements for Structural Concrete (ACI 318-11). Farmington Hills, MI: American Concrete Institute.

ACI Committee 435. 2003. Control of Deflection in Concrete Structures (ACI 435R), Farmington Hills, MI: American Concrete Institute.

ACI Committee 435/Subcommittee 5. 1963. Deflections of Prestressed Concrete Members. *Journal of the American Concrete Institute* 60 (12): 1697-1728.

Adam, I., and M. M. R. Taha. 2011. Identifying the Significance of Factors Affecting Creep of Concrete: A Probabilistic Analysis of RILEM database. *International Journal of Concrete Structures and Materials* 05 (2): 97-111.

Aitcin, P.C., and P.K. Mehta. 1990. Effect of Coarse-Aggregate Characteristics on Mechanical Properties of High-Strength Concrete. *ACI Materials Journal* 82 (2): 103-107.

ALDOT. 2014. Structural Design Manual. Montgomery, AL: Alabama Department of Transportation.

ALDOT. 2014. Bridge Plans Detailing Manual. Montgomery, AL: Alabama Department of Transportation.

ALDOT. 2009. Method of Controlling Concrete Operations for Structural Portland Cement Concrete (Procedure 170). Montgomery, AL: Alabama Department of Transportation.

ALDOT. 2015. Production and Inspection of Precast Non-Prestressed and Prestressed Concrete (Specification ALDOT-367-89). Montgomery, AL: Alabama Department of Transportation.

ALDOT. 2012. Standard Specifications for Highway Construction. Montgomery, AL: Alabama Department of Transportation.

Alexander, M.G., and T.I. Milne. 1995. Influence of Cement Blend and Aggregate Type on Stress-Strain Behavior and Elastic Modulus of Concrete. *ACI Materials Journal* 92 (3): 227-235.

Al-Omaishi, N, M.K. Tadros, and S.J. Seguirant. 2009. Elasticity, Modulus, Shrinkage, and Creep of High-Strength Concrete as Adopted by AASHTO. *PCI Journal* 54 (3):44-63.

Al-Omaishi, N. 2001. *Prestress Losses in High Strength Pretensioned Concrete Girders*. PhD Dissertation, University of Nebraska – Lincoln.

Aly, T. and Sanjayan, J.P. 2008. Factors Contributing to Early Age Shrinkage Cracking of Slag Concretes Subjected to 7-days Moist Curing. *Materials and Structures Journal*: 41(4):633-624.

ASTM C1074. 2011. Standard Practice for Estimating Concrete Strength by the Maturity Method. *ASTM International*. West Conshohocken, PA.

ASTM C192. 2014. Standard Practice for Making and Curing Concrete Test Specimens in the Laboratory. *ASTM International*. West Conshohocken, PA.

ASTM C31. 2009. Standard Practice for Making and Curing Concrete Test Specimens in the Field. *ASTM International*. West Conshohocken, PA.

ASTM C157. 2008. Standard Test Method for Length Change of Hardened Hydraulic-Cement Mortar and Concrete. *ASTM International*. West Conshohocken, PA.

ASTM C512. 2002. Standard Test Method for Creep of Concrete in Compression. *ASTM International*. West Conshohocken, PA.

ASTM C39. 2010. Standard Test Method for Compressive Strength of Cylindrical Concrete Specimens. *ASTM International*. West Conshohocken, PA.

ASTM C469. 2010. Standard Test Method for Static Modulus of Elasticity and Poisson's Ratio of Concrete in Compression. *ASTM International*. West Conshohocken, PA.

Barr, P.J., and F. Angomas. 2010. Differences between Calculated and Measured Long-Term Deflections in a Prestressed Concrete Girder Bridge. *ASCE J. Perform. Constr. Facil,* 24 (6), 603-609.

Barr, P.J., J.F. Stanton, and M.O. Eberhard. 2005. Effects of Temperature Variations on Precast, Prestressed Concrete Bridge Girders." *ASCE Journal of Bridge Engineering*, 10 (2): 186-194.

Baughn, J. 2014. Searchable National Bridge Inventory Data. http://www.uglybridges.com (accessed February 2, 2015).

Bazant, Z.P., and L. Panula. 1980. Creep and Shrinkage for Analyzing Prestressed Concrete Structures." *PCI Journal* 25 (3): 68-117.

Bentley Systems, Inc. 2012. *LEAP CONSPAN User Manual*. Exton, PA.

Boehm, K. 2008. *Structural Performance of Self-Consolidating Concrete*. MS Thesis, Auburn, AL: Auburn University.

Boehm, K.M., R.W. Barnes, and A.K. Schindler. 2010. *Performance of Self-Consolidating Concrete in Prestressed Girders*. Final Project Report, Auburn University Highway Research Center.

Boresi, Arthur P., and Richard J. Schmidt. 2003. *Advanced Mechanics of Materials*. Hoboken, NJ: John Wiley and Sons, Inc.

Branson, D.E. 1977. *Deformations of Concrete Structures*. New York, NY: McGraw-Hill Book Co.

Branson, D.E., and A.M. Ozell. 1961. Camber in Prestressed Concrete Beams. *Journal of the American Concrete Institute* 57 (12): 1549-1574.

Brooks, J.J. 1999. How Admixtures Affect Shrinkage and Creep. *Concrete International*, 21 (4): 35-38.

Brown, K.M. 1998. *Camber Growth Prediction in Precast Prestressed Concrete Bridge Girders*. PhD Dissertation, University of Idaho, Ann Arbor, MI.

Buettner, D.R., and J.R. Libby. 1979. Camber Requirements for Pretensioned Members. *Concrete International* 1 (2): 66-72.

Carino, N.J., and R.C. Tank. 1992. Maturity Functions for Concrete Made with Various Cements and Admixtures. *ACI Materials Journal* 89 (2): 188-196.

Carrasquillo, R.L., A.H. Nilson, and F.O. Slate. 1981. Properties of High Strength Concrete Subject to Short-Term Loads. *ACI Journal* 78(3): 171-177.

Chern, J., and Y. Chan. 1989. Deformations of Concretes Made with Blast-Furnace Slag Cement and Ordinary Portland Cement. *ACI Materials Journal* 86 (4): 372-382.

Collins, M.P., and D. Mitchell. 1991. *Prestressed Concrete Structures.* Englewood Cliffs, NJ: Prentice Hall.

Cook, J.E. 1989. 10,000 psi Concrete. *Concrete International* 11 (10): 67-75.

Cook, J.E. 1982. Research and Application of High-Strength Concrete Using Class C Fly Ash. *Concrete International* 4 (7): 72-80.

Cook, R.A., and D. Bloomquist. 2005. *Field Verification of Camber Estimates for Prestressed Concrete Bridge Girders*. Final Project Report, University of Florida, Tallahassee, FL: Florida Department of Transportation.

Davis, R.E., and H.E. Davis. 1931. Flow of Concrete Under the Action of Sustained Loads. *ACI Journal Proceedings* 27 (3):837-901.

Davison, B. 2014. *Prediction of Time-Dependent Stresses and Deflections in Prestressed, Concrete Girders: From Start of Fabrication to End of Service Life.* MS Thesis, Seattle Washington: University of Washington.

Donza, H., O. Cabrera, and E.F. Irassar. 2002. High-strength Concrete with Different Fine Aggregates. *Cement and Concrete Research* (Pergamon) 32: 1755-1761.

Dunham, E.L. 2011. *Transfer Length in Bulb-Tee Girders Constructed with Self-Consolidating Concrete*. MS Thesis, Auburn, AL: Auburn University.

Ellis, M.A. 2012. *Time-Dependent Deformations of Concrete for Precast/Prestressed Bridge Components*. MS Thesis, Auburn, AL: Auburn University.

Fawzy, F. and K.E. Hanna. 2011. Precast, Prestressed Girder Camber Variability. *PCI Journal* 56 (1): 135-154.

fib. *Model Code 2010*. Design Code, Lausanne, Switzerland: International Federation for Structural Concrete, 2010.

French, C.E., and C. O'Neill. 2012. *Validation of Prestressed Concrete I-Beam Deflection and Camber Estimates*. Final Report, University of Minnesota, St. Paul, MN: Minnesota Department of Transportation.

Freskakis, G.N., R.C. Burrow, and E.B. Debbas. 1979. Strength Properties of Concrete at Elevated Temperatures. *Proceedings of ASCE National Convention Civil Engineering Nuclear Power*. Boston, Massachusetts: American Society of Civil Engineers.

Ghosh, R.S., and J. Timusk. 1981. Creep of Fly Ash Concrete. *ACI Journal* 78 (5): 351-357.

Haranki, B. 2009. *Strength, Modulus of Elasticity, Creep, and Shrinkage of Concrete Used in Florida*. MS Thesis, Gainesville, FL: University of Florida.

He, W. 2013. *Creep and Shrinkage of High Performance Concrete and Prediction of the Long-term Camber of Prestressed Bridge Girders*. MS Thesis, Ames, Iowa: Iowa State University.

Hibbeler, R. C. 2011. *Mechanics of Materials*. Upper Saddle River, NJ: Pearson Prentice Hall.

Hibbeler, R.C. 2006. *Structural Analysis*. Upper Saddle River, NJ: Pearson Prentice Hall.

Hinkle, S.D. 2006. *Investigation of Time-Dependent Deflection in Long Span, High Strength, Prestressed Concrete Bridge Beams*. MS Thesis, Blacksburg, VA: Virginia Polytechnic Institute and State University.

Hofrichter, A. 2014. *Compressive Strength and Modulus of Elasticity Relationships for Alabama Prestressed Concrete Bridge Girders*. MS Thesis, Auburn, AL: Auburn University.

Holland, R.C. 2005. *Silica Fume User's Manual*. Lovettsville, VA: Silica Fume Association.

Holt, R. 1996. *Implementation Program on High Performance Concrete Guidelines for Instrumentation of Bridges*. Research Report, Washington, DC: Federal Highway Administration.

Hubler, M.H., Wendner, R., Bazant, Z.P. 2015. Comprehensive Database for Concrete Creep and Shrinkage: Analysis and Recommendations for Testing and Recording. *American Concrete Institute Materials Journal* 112 (4): 547-558.

Huo, X.S., N. Al-Omaishi, and M.K. Tadros. 2001. Creep, Shrinkage, and Modulus of Elasticity of High Performance Concrete. *ACI Materials Journal* 98 (6): 440-449.

Imbsen, R.A., D.E. Vandershaf, R.A. Schamber, and R.V. Nutt 1985. *Thermal Effects in Concrete Bridge Superstructures* (NCHRP Report 276). Washington, DC: Transportation Research Board.

Isbiliroglu, L. 2014. *Predicting Time-Dependent Deformations in Prestressed Concrete Girders*. MS Thesis, Auburn, AL: Auburn University.

Jayaseelan, H., and B.W. Russell. 2007. *Prestress Losses and the Estimation of Long-Term Deflections and Camber for Prestressed Concrete Bridges*. Final Report, Stillwater, OK: Oklahoma State University.

Johnson, Brandon Ray. 2012. *Time-Dependent Deformation in Precast, Prestressed Bridge Girders*. MS Thesis, Auburn, AL: Auburn University.

Kavanaugh, B.P. 2008. Creep Behavior of Self-Consolidating Concrete. MS Thesis, Auburn, AL: Auburn University.

Kelly, D.J., T.E. Bradberry, and J.E. Breen. 1987. *Time Dependent Deflections of Pretensioned Beams* (Research Report 381-1). The University of Texas at Austin, Austin, TX: Center for Transportation Research.

Keske, S.D. 2014. *Use of Self-Consolidating Concrete in Precast, Prestressed Girders*. PhD Dissertation, Auburn, AL: Auburn University.

Khatri, B.P., and V. Sirivivatnanon. 1995. Effect of Different Supplementary Cementitious Materials on Mechanical Properties of High Performance Concrete. *Cement and Concrete Research* (Elsevier Science Ltd.) 25 (1): 209-220.

Lane, R.O., and J.F. Best. 1982. Properties and Use of Fly Ash in Portland Cement Concrete. *Concrete International* 4 (7): 81-92.

Lee, J.H. 2010. *Experimental and Analytical Investigations of the Thermal Behavior of Prestressed Concrete Bridge Girders Including Imperfections*. PhD Dissertation, Atlanta, GA: Georgia Institute of Technology.

Levy, K. 2007. *Bond Behavior of Prestressed Reinforcement in Beams Constructed with Self-Consolidating Concrete*. MS Thesis, Auburn, AL: Auburn University.

Levy, K., Barnes, R.W., Schindler, A.K. 2010. *Time-Dependent Deformations of Pretensioned, Self-Consolidating Concrete*. Proceedings of the 3rd *fib* International Congress, May 29–June 2, 2010: Washington, DC.

Limeria, J., M. Etxeberria, and D. Molina. 2011. Mechanical and Durability Properties of Concrete Made with Dredged Marine Sand. *Journal of Construction and Building Products* (Elsevier) 25: 4165-4174.

Liu, Yanjan, and Mang Tia. 2012. Creep Property of Concretes with Different Types of Coarse Aggregates. *Journal of Applied Mechanics and Materials* (Trans Tech Publications) 174-177: 308-313.

Magura, D.D., M.A. Sozen, and C.P. Seiss. 1964. A Study of Stress Relaxation in Prestressing Reinforcement. *PCI Journal* 9 (2): 13-57.

Mahmood, O.I. 2013. *Camber Control in Simply Supported Prestressed Concrete Bridge Girders.* MS Thesis, Lexington, KY: University of Kentucky.

Mante, D.M. 2016. *Improving Camber Predictions for Precast, Prestressed Concrete Bridge Girders.* PhD Dissertation, Auburn AL: Auburn University.

Martin, L.D. 1977. A Rational Method for Estimating Camber and Deflection of Precast Prestressed Members. *PCI Journal* 22 (1):100-108.

Mehta, P.K., and P.J.M. Monteiro. 2014. *Concrete Microstructure, Properties, and Materials*. 4th ed. McGraw-Hill Education.

Muller, H.S., I. Anders, R. Breiner, and M. Vogel. 2013. Concrete: Treatment of types and properties in fib Model Code 2010. *Journal of Structural Concrete* (Ernst and Sohn) 4: 320-334.

Naaman, A.E. 2004. *Prestressed Concrete Analysis and Design: Fundamentals*. 2nd ed. Ann Arbor, MI: Techno Press 3000.

Nawy, E.G. 2010. *Prestressed Concrete - A Fundamental Approach*. Upper Saddle River, NJ: Pearson Education, Inc.

Nervig, J. 2014. *Improving Predictions of Instantaneous Camber for Prestressed Concrete Bridge Girders* (Paper 13817). MS Thesis. Iowa State University.

Neville, A.M. 2013. *Properties of Concrete*. New Delhi, India: Dorling Kindersley.

Noguchi, T., F Tomosawa, K.M. Nemati, B.M. Chiaia, and A.P. Fantill. 2009. A Practical Equation for Elastic Modulus of Concrete. *ACI Structural Journal* 106 (5): 690-696.

Omar, W., T. Pui Lai, L. Poh Huat, and R. Omar. 2008. Improved Prediction of Pre-Camber of Post-Tensioned Prestressed I-Beam. *Journal of the Institution of Engineers* 69 (1):32-37.

Pauw, Adrian. 1960. Static Modulus of Elasticity of Concrete as Affected by Density. *Journal of the American Concrete Institute* 57 (2): 679-688.

Philleo, R.E. 1981. Increasing the Usefulness of ACI 214: Use of Standard Deviation and a Technique for Small Sample Sizes. *Concrete International* 3 (9): 71-74.

PCI Committee on Bridges. 2012. Camber FAST Team. Chicago, IL: Precast Prestressed Concrete Institute.

PCI. 2011. *Precast Prestressed Concrete Bridge Design Manual* 3rd ed. Chicago, IL: Precast/Prestressed Concrete Institute.

Rizkalla, S., P. Zia, and T Storm. 2011. *Predicting Camber, Deflection, and Prestress Losses in Prestressed Concrete Members*. Final Project Report, Raleigh, NC: North Carolina State University.

Roller, J.J., H.G. Russell, R.N. Bruce, and B. Hasset. 2003. Effect of Curing Temperature on High Strength Concrete Bridge Girders. *PCI Journal* 48 (2): 72-79.

Rosa, M.A., J. F. Stanton, and M.O. Eberhard. 2007. *Improving Predictions for Camber In Precast, Prestressed Concrete Bridge Girders*. Research Report, University of Washington, Seattle, WA: Washington State Transportation Center (TRAC).

Schindler, A.K, M.L. Hughes, R.W. Barnes, and B.E. Byard. 2010. *Evaluation of Cracking of the US 331 Bridge Deck*. ALDOT Project Report 930-645. Auburn University, Auburn AL: Highway Research Center.

Schrantz, C.E. 2012. *Development of a User-Guided Program for Predicting Time-Dependent Deformations in Prestressed Bridge Girders*. MS Thesis, Auburn, AL: Auburn University.

Schuster, R.L. 1957. *A Review of Research on Deleterious Substances in Concrete Aggregates*. Joint Highway Research Project, Lafayette, Indiana: Purdue University.

Shi-Cong, K., and P. Chi-Sun. 2009. Properties of Concrete Prepared with Crushed Fine Stone, Furnace Bottom Ash, and Fine Recycled Aggregate as Fine Aggregate. *Journal of Construction and Building Materials* (Elsevier) 23:2877-2886.

Stallings, J.M., and S. Eskildsen. 2001. *Camber and Prestress Losses in High Performance Concrete Bridge Girders*. Final Research Report: Project 930-373, Auburn, AL: Auburn University Highway Research Center.

Stallings, J.M., R.W Barnes, and S. Eskildsen. 2003. Camber and Prestress Losses in Alabama HPC Bridge Girders. *PCI Journal* 48 (5): 2-16.

Storm, T.K., S.H. Rizkalla, and P.Z. Zia. 2013. Effects of Production Practices on Camber of Prestressed Concrete Bridge Girders. *PCI Journal* 58 (1): 96-111.

Svirsky, A. National Bridges. 2015. www.nationalbridges.com (accessed February 2, 2015).

Tadros, M.K, N. Al-Omaishi, S.J Seguirant, and J.G. Gallt. 2003. *Prestress Losses in Pretensioned High-Strength Concrete Bridge Girders* (NCHRP Report 496), Washington, DC: National Cooperative Highway Research Program, Project 18-07.

Tadros, M.K., A. Ghali, and A.W. Meyer. 1985. Prestressed Loss and Deflection of Precast Concrete Members. *PCI Journal* 30 (1): 114-141.

Tadros, M.K., F. Fawzy, and K.E. Hanna. 2011. Precast, Prestressed Girder Camber Variability. *PCI Journal* 56 (1): 135-154.

Thoman, W.H., and W. Raeder. 1934. Ultimate Strength and Modulus of Elasticity of High-Strength Portland Cement Concrete. *Journal of the American Concrete Institute* 30 (1).

Tia, M., Y Liu, and D. Brown. 2005. *Modulus of Elasticity, Creep, and Shrinkage of Concrete*. Final Project Report, University of Florida, Tallahassee, FL: Florida Department of Transportation.

Troxell, G.E., J.M. Raphael, and R.E. Davis. 1958. Long-Term Creep and Shrinkage Tests of Plain and Reinforced Concrete. *Proceedings of ASTM Annual Meeting 1958*: 1101-1120.

Vardeman, S.B. and Jobe, J.M. 2001. Basic Engineering Data Collection and Analysis. Pacific Grove, CA: Duxbury Thompson Learning.

Wu, K., B. Chen, W. Yao, and D. Zhang. 2001. Effect of Coarse Aggregate Type on Mechanical Properties of High-Performance Concrete. *Journal of Cement and Concrete Research* (Pergamon) 31: 1421-1425.

Wyffels, T.A., C.E. French, and C.K. Shield. 2000. *Effects of Pre-Release Cracks in High-Strength Prestressed Concrete*. Final Project Report, University of Minnesota, St. Paul, MN: Minnesota Department of Transportation Office of Research Administration.